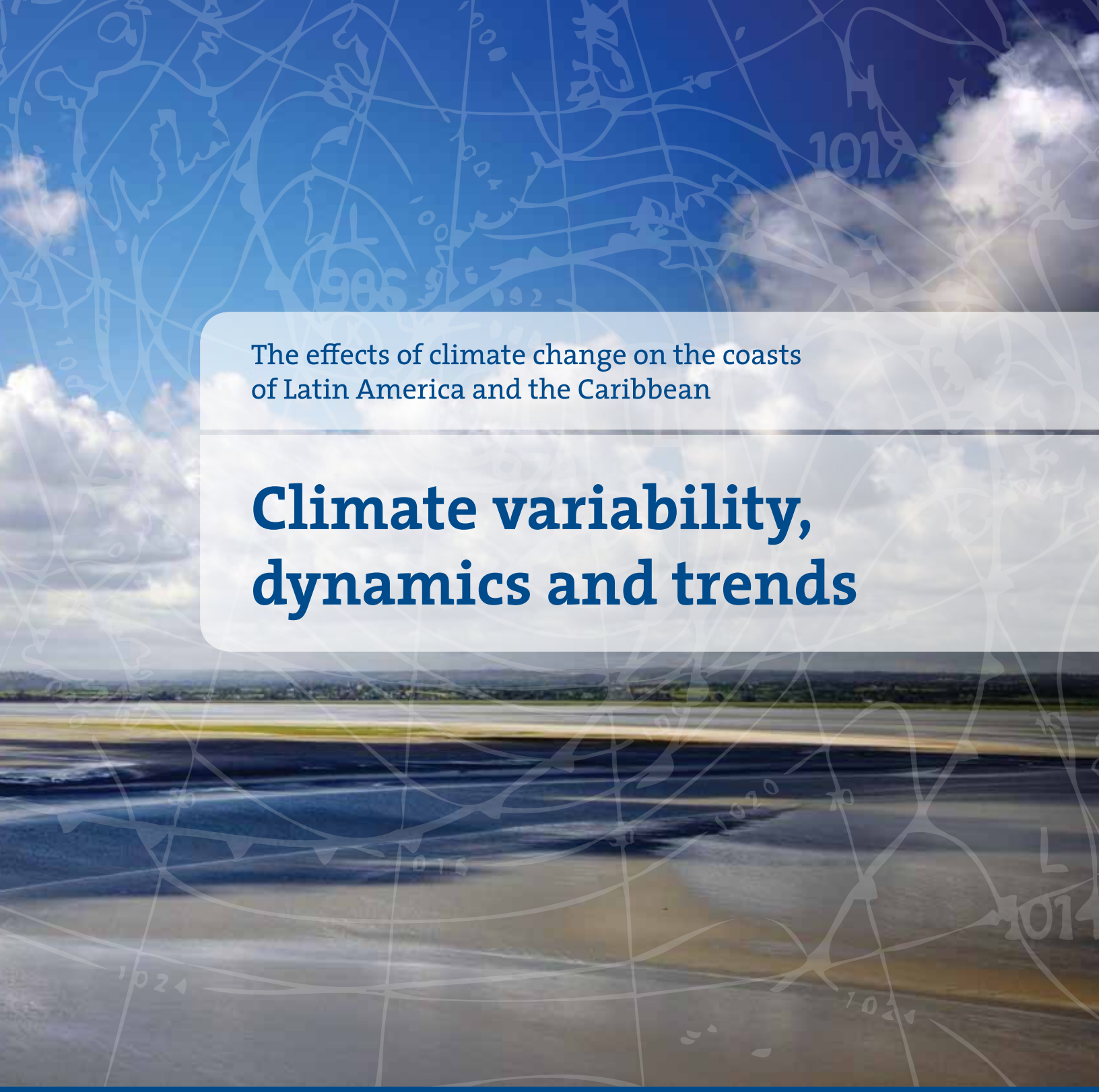

The effects of climate change on the coasts of Latin America and the Caribbean

Climate variability, dynamics and trends

UNITED NATIONS

ECLAC

GOBIERNO DE ESPAÑA
MINISTERIO DE AGRICULTURA, ALIMENTACIÓN Y MEDIO AMBIENTE
MINISTERIO DE ASUNTOS EXTERIORES Y DE COOPERACIÓN

UC UNIVERSIDAD DE CANTABRIA
IH cantabria
INSTITUTO DE HIDRÁULICA AMBIENTAL
UNIVERSIDAD DE CANTABRIA

The effects of climate change on the coasts of Latin America and the Caribbean

CLIMATE VARIABILITY, DYNAMICS AND TRENDS

Alicia Bárcena
Executive Secretary

Antonio Prado
Deputy Executive Secretary

Joseluis Samaniego
Chief, Sustainable Development and Human Settlements Division

Ricardo Pérez
Chief, Publications and Web Services Division

Copies of this publication may be obtained from:
Sustainable Development and Human Settlements Division, ECLAC, webpage: www.cepal.org/ddsah.

Cover photo © Gabriel Barajas Ojeda
United Nations publication

LC/W.447

S.14-20914

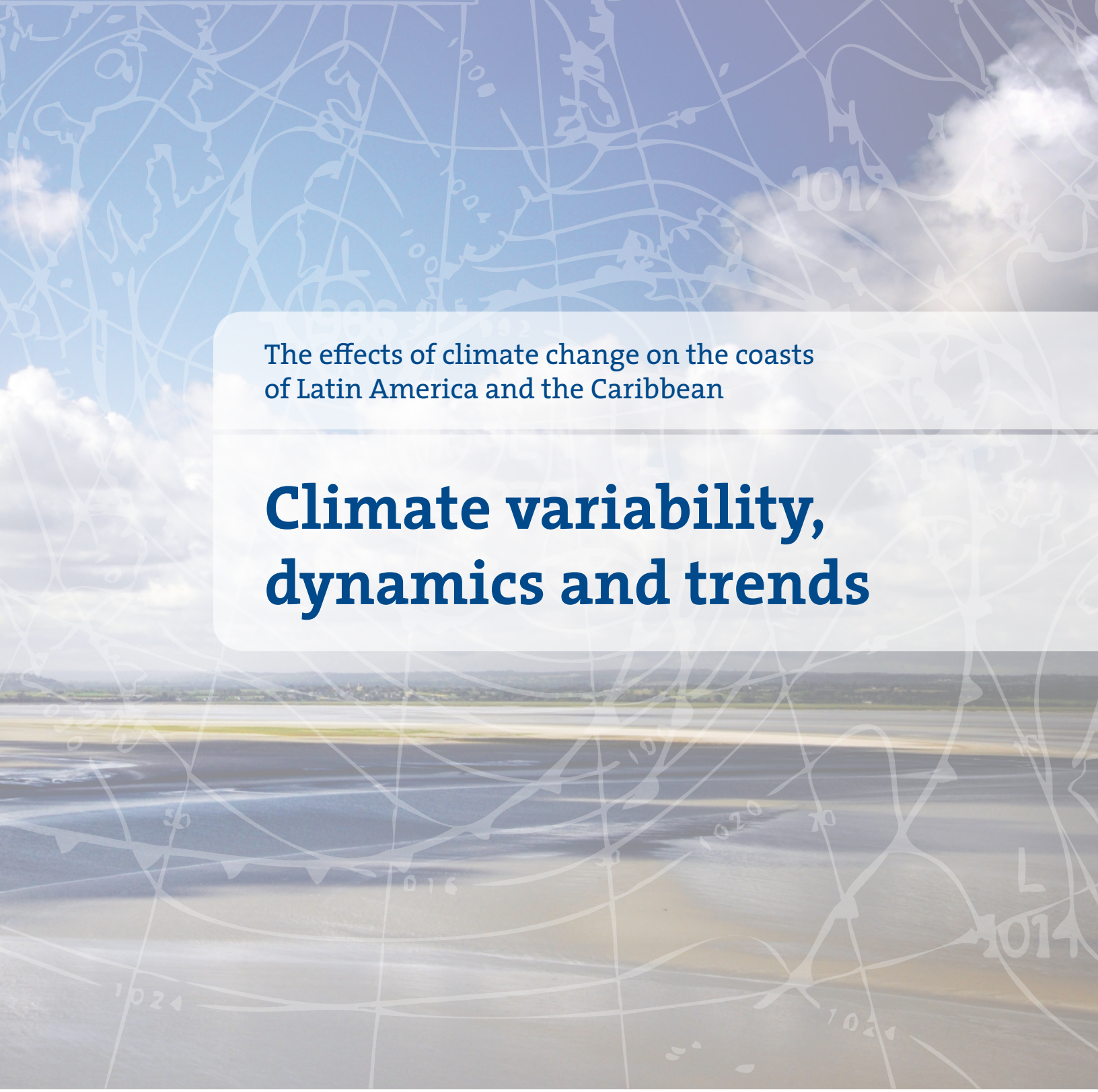

The effects of climate change on the coasts of Latin America and the Caribbean

Climate variability, dynamics and trends

NACIONES UNIDAS

CEPAL

GOBIERNO DE ESPAÑA
MINISTERIO DE AGRICULTURA, ALIMENTACIÓN Y MEDIO AMBIENTE
MINISTERIO DE ASUNTOS EXTERIORES Y DE COOPERACIÓN

UC UNIVERSIDAD DE CANTABRIA
IH cantabria
INSTITUTO DE HIDRÁULICA AMBIENTAL
UNIVERSIDAD DE CANTABRIA

This document was prepared by the Environmental Hydraulics Institute of the University of Cantabria under the direction of Iñigo Losada Rodríguez and coordinated by Fernando J. Méndez Incera. The following researchers took part in the work: Borja González Reguero, Sonia Castanedo Bárcena, Gabriel Díaz Hernández, Raúl Medina Santamaría, Pedro Díaz Simal, Bárbara Ondiviela Eizaguirre, Roberto Mínguez Solana, Ana J. Abascal Santillana, Antonio Espejo Hermosa, Cristina Izaguirre Lasa, Paula Camus Braña, Oscar García Aguilar, Pino González-Riancho Calzada, Melisa Menéndez García, José Antonio Juanes de la Peña and Antonio Tomás Sampedro The ECLAC team that coordinated and supervised the study was composed of the following staff members of the Sustainable Development and Human Settlements Division: Carlos de Miguel, Environmental Affairs Officer, José Javier Gómez, Economic Affairs Officer, Karina Martínez and Mauricio Pereira Research Assistants. This document forms part of a larger regional study of the effects of climate change in the coastal areas of Latin America and the Caribbean which is being funded by the Government of Spain. The study is being conducted under the Ibero-American Programme on Adaptation to Climate Change (PIACC) and is one of the priority lines of action identified by the member countries of the Ibero-American Network of Climate Change Offices (RIOCC).

Special thanks are owed to the staff of the Spanish Climate Change Office of the Ministry of Agriculture, Food and the Environment of Spain and particularly to Paz Valiente, Ana Pintó, José Ramón Picatoste and Alfonso Gutiérrez.

The authors also wish to express their gratitude for the valuable contributions made by Felipe Fernández Pérez, Sheila Abad Herrero, Patricia Fernández Quintana, Felipe Maza and Nabil Kakeh Burgada, experts with the Environmental Hydraulics Institute of the University of Cantabria, and for the comments of Rodrigo Cienfuegos, a researcher with the Hydraulics and Environmental Engineering Department of the Catholic University of Chile.

Contents

Figures

Tables

Acronyms and abbreviations

A1B	The balance across all sources group in the IPCC A1 storyline and scenario family
A1T	The non-fossil energy sources group in the IPCC A1 storyline and scenario family
A1F1	The fossil-intensive group in the IPCC A1 storyline and scenario family
A2	The IPCC A2 storyline and scenario family
AR4	Fourth Assessment Report of the Intergovernmental Panel on Climate Change (IPCC)
ARMA	Auto-Regressive Mean Average model
AMO	Atlantic Multidecadal Oscillation
AO	Arctic Oscillation
AOGCM	Atmosphere-Ocean General Circulation Model
B1	The IPCC B1 storyline and scenario family
B2	The IPCC B2 storyline and scenario family
BODC	British Oceanographic Data Centre
CAR	Caribbean sea surface temperature (SST) index
CORR	Pearson correlation coefficient (0-1)
COADS	Comprehensive Ocean-Atmosphere Data Set
CSIRO	Commonwealth Scientific and Industrial Research Organisation of Australia (www.csiro.au)
DINAS	Dynamic and Interactive Assessment of National, Regional and Global Vulnerability of Coastal Zones to Climate Change and Sea Level Rise
DIVA	Dynamic Interactive Vulnerability Assessment
DMI	Dipole Mode Index

EA	East Atlantic pattern
EA/WR	East Atlantic/Western Russian pattern
ECLAC	Economic Commission for Latin America and the Caribbean
ENSO	El Niño Southern Oscillation
EOF	Empirical orthogonal function
EP/NP	East Pacific-North Pacific pattern
ERS-2	Europe Remote Sensing 2
ERSST	Extended Reconstructed Sea Surface Temperature
ETOPO	Earth Topography Digital Dataset (A global relief model of Earth's surface that integrates land topography and ocean bathymetry)
GCM	General Circulation Model
GEBCO	General Bathymetric Chart of the Oceans
GEV	Generalized extreme value
GHG	Greenhouse gases
GIA	Glacial Isostatic Adjustment
GFO	Geosat Follow-On
GISS	Goddard Institute for Space Studies
GMSL	Global mean sea level
GODAS	Global Ocean Data Assimilation System
GOS	Global Ocean Surges database
GOT	Global Ocean Tides database
GOW	Global Ocean Waves reanalysis
GPD	Generalized Pareto Distribution
IHC	Environmental Hydraulics Institute of the University of Cantabria
IOD	Indian Ocean Dipole
IPCC	Intergovernmental Panel on Climate Change
ITCZ	Intertropical Convergence Zone
JMA	Japan Meteorological Agency
MSL	Mean sea level
NAO	North Atlantic Oscillation
NASA	National Aeronautics and Space Administration
NCAR	National Center for Atmospheric Research
NCEP	National Centers for Environmental Prediction
NOAA	National Oceanic and Atmospheric Administration
NPI	North Pacific Index

OECC	Climate Change Office of Spain
OGCM	Ocean General Circulation Model
OPPE	State Port Administration
PCs	Principal components
PDO	Pacific Multidecadal Oscillation
PNA	Pacific/North American Index
POT	Peak Over Threshold
PSMSL	Permanent Service for Mean Sea Level
QBO	Quasi-Biennial Oscillation (the “Singapore winds”)
QQ	Quantile-quantile
R2	Symmetrical regression coefficient
RBF	Radial basis function
REDEXT	OPPE deep-water buoy
REDMAR	OPPE network of tide gauges
RMSE	Root mean square error
RSLR	Relative sea level rise
SAL	Salinity
SAM	Southern Annular Mode
SAT	Surface air temperature
SCA	Scandinavian pattern
SI	Scatter Index
SLP	Sea level pressure
SLR	Sea level rise
SOI	Southern Oscillation Index
SOM	Self-organizing maps
SPM	Shore Protection Manual
SST	Sea surface temperature
SWAN	Simulating WAves Nearshore
T-EOF	Trend empirical orthogonal function (Trend-EOF)
TOPEX/Poseidon	French-United States spatial oceanographic satellite (1997-2003)
TPXO	Global model of ocean tides based on altimetric data from the TOPEX/POSEIDON mission
TNA	Tropical North Atlantic Index
TSA	Tropical South Atlantic Index
UHSLC	University of Hawaii Sea Level Center

UNEP	United Nations Environment Programme
WAM	WAve Model
WMO	World Meteorological Organization
WP	Western Pacific index
WW III	Wave Watch III

Symbols

β_{LT}	Long-term slope (extreme events)
Dir	(Wave) direction
Hs	Significant wave height
Hs_{95}	95th percentile of significant wave height
Hs_{12}	Significant wave height exceeded 12 hours per year
P	Pressure
pdf	Probability density function
Prob	Probability
q_n	Quantile n
R^2	Coefficient of determination
σ	Standard deviation
Tm	Mean wave period
Pp	Peak wave period
Tr	Return period
W	Wind speed (at 10 m)

Units

g	Grams / gravitational acceleration
kg	Kilograms
km	Kilometres
m	Metres
mb	Millibars
mm	Millimetres
m/s	Metres / second
º	Sexagesimal degrees
ºC	Degrees Celsius
psu	Practical salinity units

1. Introduction

1.1. Background

This effort to study the effects of climate change in the coastal areas of Latin America and the Caribbean has been divided into four main parts in line with the comprehensive risk-assessment methodology developed. The outputs of this regional study are presented in four core documents: an analysis of coastal dynamics and climate variability, a study on the vulnerability of coastal areas, an evaluation of the impacts of climate change and an exploration of how all these different factors can be brought together in an assessment of the risks of the impacts of climate change on the region's coastal areas.

Supplementary documents include a manual that sets out the theoretical approaches to the effects of climate change and the concepts and details relating to coastal phenomena and processes, among many other factors, that were analysed in the study. This manual also covers the expressions that can be used to arrive at approximate impact assessments (the disturbance method) when conducting initial baseline analyses for future local and regional research projects. In addition, the approach that was developed for arriving at a comprehensive risk assessment is described in a methodological handbook. Finally, a web viewer has been developed in order to make this project's findings as widely available as possible to readers in the countries of the region. In sum, the project documents are as follows:

• Document 1: Climate variability, dynamics and trends in Latin America and the Caribbean

• Document 2: Vulnerability and exposure of Latin American and Caribbean coastal areas to the effects of climate change

• Document 3: Impacts of climate change in the coastal areas of Latin America and the Caribbean

• Document 4: A climate change risk assessment for the coastal areas of Latin America and the Caribbean

• Theoretically derived effects of climate change in coastal areas (supplementary document)

• Methodological handbook of risk assessment (supplementary document)

• Web viewer of project findings

Table 1.1 provides an overview of the project's structure and outputs. This study, which is the first of the project documents, focuses on coastal dynamics, the changes that have been observed and how climate variability is influencing coastal areas.

TABLE 1.1
PROJECT STRUCTURE AND DOCUMENTS

Climate change in Latin American and Caribbean coastal areas			
Document 1: Coastal agents	**Document 2: Vulnerability**	**Document 3: Impact**	**Document 4: Risks**
• Dynamics • Trends • Climate variability in coastal areas			

Supplementary documents		
Theoretically derived effects of climate change in coastal areas	Methodological handbook	Project findings web viewer

Source: Prepared by the authors.

1.2. Project background

The local-level analyses undertaken as part of the Regional Study on the Economics of Climate Change in Latin America and the Caribbean (ERECC) initiative, for which ECLAC provides technical coordination, furnish countries and regions with the information they need to gauge what the implications of climate change may be for their economies and for specific socioeconomic groups. The ERECC initiative is designed to assist the countries of Latin America and the Caribbean to assess their capacity for dealing with the problems associated with climate change.

The areas bordering the world's oceans are extremely vulnerable to the potential impacts of climate change, as has been demonstrated by numerous studies and research papers in recent years (Nicholls *et al.* 1999 and 2010, IPCC 2007). The socioeconomic scenarios developed by the Intergovernmental Panel on Climate Change (IPCC) all provide for varying but considerable increases in the population in coastal areas as people move to these zones in search of resources and as various types of socioeconomic activities located along the coasts flourish. This increase is expected to go hand in hand with the construction of new infrastructure, the introduction of extractive industries, and a reduction in the supply of fresh water and sedimentation in coastal zones, along with other factors that may interfere with the conservation of coastal habitats. The problem of coastal erosion and the damage caused by coastline retreat and flooding affects all countries and will no doubt grow worse as a result of climate change, as has been demonstrated by various studies (Bird, 1985, Zhang *et al.* 2004).

Maritime transport is a key factor in any country's economic system. The development of a port system and the associated industries entails the use of portions of the coastline in ways that are not always compatible with the preservation of coastal ecosystems. Climate change is expected to lead to a decrease in port operationality and safety and to do damage to infrastructure, which will make it necessary to reassess port functionality and evaluate the various options and adaptation costs.

A similar type of problem will arise in coastal cities, most of whose seawalls and other fortifications, modes of transport, and sanitation, energy and water supply systems have been designed in line with climatic conditions that are going to undergo substantial changes. It is important to have the necessary data, tools and methodologies to determine which cities and which areas will need to adopt adaptation strategies so that the necessary investments can be made.

There is still a great deal of uncertainty about how the tourism industry will be affected because it is not yet known how or to what extent demand will be influenced by climate change, but the sector will no doubt be strongly affected in a number of Latin American and Caribbean countries.

The reports of the Intergovernmental Panel on Climate Change (IPCC) have systematically pointed out the risks associated with climate change in coastal areas, and these risks have also been discussed in numerous scientific journals. Most of the problems that are being foreseen have to do with the impact of climate change on marine dynamics. In most cases, the focus has been limited to problems caused by rising sea levels, but the climate risks posed by changes in temperature, precipitation patterns, wave activity, storm surge and wind also need to be evaluated. These risks have to be assessed within the context of the extreme vulnerability of coastal zones as the interface between land and sea in which a natural system encompassing important ecosystems and a wealth of biodiversity exist side by side with a socioeconomic system in which human beings are exerting more and more pressure on the environment as they compete for resources.

All of the ERECC studies for any of the coastal countries in Latin America or the Caribbean should therefore include a targeted analysis of climate risks in coastal zones.

Because of Spain's geographic position and the nature of its economic status and activities, it is one of the European countries whose coasts and associated socioeconomic resources are most seriously threatened by climate change. In response to this situation, the Climate Change Office of the Ministry of Agriculture, Food and the Environment worked with the Environmental Hydraulics Institute of the University of Cantabria to develop a special methodology (hereafter referred to as the UC/CCO methodology) for assessing the impact of climate change in coastal areas. This methodology has provided the foundation for the National Climate Change Adaptation Plan and has been highly acclaimed by a number of international organizations. The Government of Spain would like to make this methodology and the related tools available to other countries, since it provides a means of compiling information that can be extremely useful in assessing climate impacts, devising adaptation measures and evaluating their economic implications.

This study provides a preliminary analysis of the application of the UC/CCO methodology to the coasts of Latin America and the Caribbean. The following sections describe the general and specific objectives of this effort.

1.3. Study objectives

The overall objective of this study is to compile the specific types of information required in order to analyse the economic impacts of climate change in the coastal areas of Latin America and the Caribbean.

In order to attain this overall objective, the following specific objectives have been defined on a preliminary basis:

- Develop methodologies and techniques for compiling a high-resolution (in both temporal and spatial terms) numerical database on the maritime climate, both past and future
- Generate a database on deep-sea marine dynamics (sea levels, storm surges, swells) at the highest possible level of spatial and temporal resolution
- Apply downscaling and classification techniques and algorithms for the database
- Use a variety of techniques for arriving at forecasts/projections for future maritime climates (extrapolation of trends based on a non-stationary statistical analysis, dynamic downscaling and statistical downscaling) to analyse maritime climate variability
- Develop and identify coastal-zone impact indicators covering flooding, erosion and impacts on transport, supply and tourism infrastructure
- Prepare an atlas of deep-sea coastal impacts for Latin America and the Caribbean (generally depths greater than 100 m)
- Develop a manual on possible climate-change adaptation measures that provides indicators for the associated economic cost of such measures
- Help to integrate this information with the proposed ERECC economic analysis
- Develop training initiatives that will help to transfer the tools and methodologies applied in this project and that will be conducive to the development of local projects in the future.

In addition to the actions taken to meet the objectives that were defined at the outset, a comprehensive methodology for assessing **vulnerability** and **risk** was developed that yielded results for various spatial scales (5 km, 50 km and by country).

1.4. Study area

The area covered by the study encompasses the coastlines of Latin America and the Caribbean (an area totalling approximately 72,182 km in length). In the following overview of the geomorphological and ecological features of this area, it is divided into four geographic zones: North America, Central America, South America and the Caribbean islands (see figure 1.1).

FIGURE 1.1
STUDY AREA

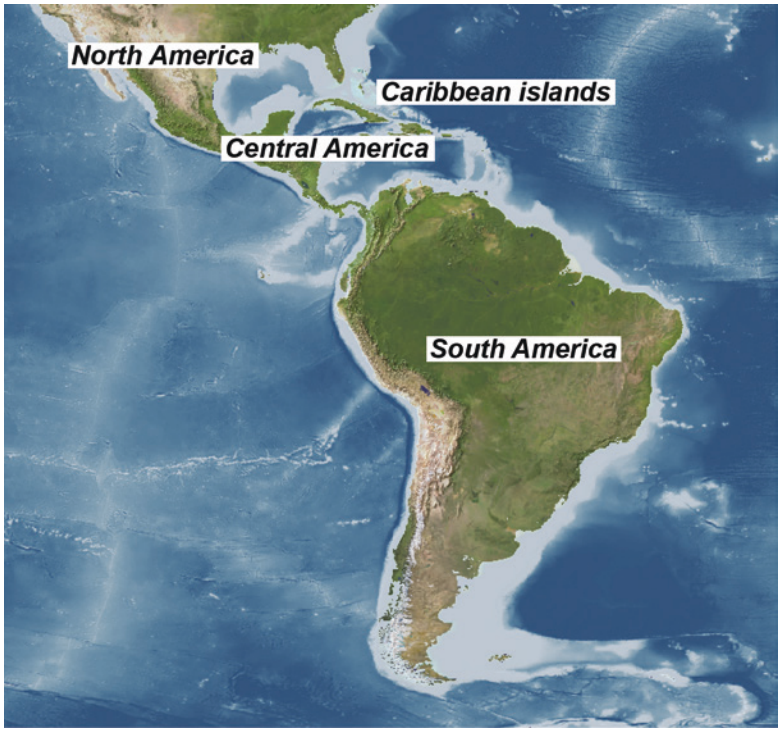

Source: Prepared by the authors.

1.4.1. Description of the study area

1.4.1.1. North America

The portion of the North American coastline covered by this study corresponds to the Mexican coast. The western coastline falls within what is known as the Pacific Rim Province (Schwartz, 2005), which stretches from the Guatemalan border to the Alaskan Peninsula. This is a tectonically active region located in the convergence zone between the Pacific, Juan de Fuca and Cocos plates and the North American plate. The general morphology of this province is marked by a narrow continental shelf and a narrow or absent coastal plain that immediately gives way to mountain chains. Steep slopes or cliffs predominate, with the sandbanks or shoals found along the coast of the Gulf of California being an exception. In the northern part of this gulf, the Colorado River forms a delta that is riddled with channels, estuaries, marshes and saltwater lagoons. The eastern coastline of Baja California is bounded by mountains to the north and south of the peninsula. The main geomorphological features of the eastern coast of this peninsula are Magdalena Bay and Vizcaíno Bay. Further south, along the coast in the vicinity of Guatemala, sandbars and lagoons are found, with dunes forming along the sandbars and mangrove swamps intermingling with most of the lagoons. Coral reefs are found in very few places along this coastline. The spring tide ranges from 0.5 m along the coast near Acapulco to 7 m in the northern part of the Gulf of California near the mouth of the Colorado River. Most of the wave energy along this coast takes the form of swells and the storm surges driven by tropical storms and hurricanes in the August-January hurricane season.

The Atlantic coast is classified as part of the Gulf of Mexico. This area has a number of well-developed sandbar/marsh/lagoon systems. To the south of the Río Grande delta, Laguna Madre is one of the largest bird refuges in Mexico. Further to the south, discontinuous sandbar/lagoon systems lead down to the vast delta and estuaries of the Pánuco River. To the south of this system, the dunes and beaches that shelter the Laguna Tamiahua are found. This coastal area is located in a tropical coral reef habitat. Coral is also found along the coast of Veracruz, as are vast stretches of marshlands, lagoons and sandbars spotted with dunes and mangrove swamps. Finally, the western coast of the Yucatán Peninsula is dominated by the sedimentation deposited by major drainage systems that empty into the sandbars and shoals of the deltas. Coral reefs and mangrove swamps predominate in sheltered areas. This is a micro-tidal area, and the level of wave energy is generally low, but it is exposed to tropical storms that sometimes reach hurricane force.

1.4.1.2. Central America

Central America is made up of the following countries: Belize, Guatemala, Honduras, El Salvador, Nicaragua, Costa Rica and Panama. It accounts for approximately 12% of the entire length of the coastline of Latin America and the Caribbean. Tectonic activity in this area has resulted in a narrow continental shelf all along the Pacific coast. Along the Atlantic, the Caribbean archipelago shields the coastline from wave action and has made it possible for wider continental shelves to form. Contrary to popular belief, continental shelves dominated by the effects of mangrove swamps or coral reefs are the exception rather than the rule in this area. The Central American coast encompasses numerous peninsulas, gulfs and bays that give rise to a marked degree of physiographic diversity, along with extensive inter-tidal areas and well-developed sandbar systems. Along the Pacific coast, steeply sloping areas and cliffs are pronounced in Costa Rica and somewhat less so in El Salvador and Panama, but no such slopes are found off the coast of Nicaragua. Along the Atlantic, coastal areas tend to be quite flat, and there are no cliffs except in Guatemala. Numerous large lagoon/estuary systems are found in this area, including the Amatique Bay (Guatemala), the Gulf of Fonseca (El Salvador/Honduras/Nicaragua), the Gulf of Nicoya and Golfo Dulce (Costa Rica) and Panama Bay (Panama). The patterns observed along the two coasts differ markedly: whereas, along the Pacific, the spring tide ranges up to 6 m, along the Atlantic it amounts to some 30 cm.

The prevailing winds generate waves of up to 3 m high in the Caribbean. Wave heights are lower for the Pacific Ocean, although this region is also hit by hurricanes.

1.4.1.3. South America

South America includes climates that range from tropical zones (12º30'N) to polar regions (around 55ºS) and thus has a great variety of coastal and marine ecosystems, including: sandy beaches, rocky terrain, coral reefs, mangrove swamps, inter-tidal zones and seagrass habitats. It is divided into two tectonic zones: the Andes Mountains in the west, and a broad shelf to the east. The Pacific Andean coast is very rugged terrain, has a fairly narrow continental shelf bordering a deep trench and small drainage basins. The Atlantic coast, on the other hand, has much more even terrain, a broader continental shelf and large river basins and alluvial deposits. Most of the South American coastline is composed of sandy beaches. The range of morphodynamic variation is quite large, with the continuum running from sandy beaches in small coves, rocky shores and mangrove swamps and marshes along the Pacific coasts of the Bolivarian Republic of Venezuela, Colombia and Ecuador to broad exposed, dissipative, micro-tidal beaches, such as the beach that stretches for 640 km from Río Grande do Sul (in southern Brazil) to the north-eastern portion of Uruguay. South of 43ºS, the Patagonian coast is mainly composed of sandy lowlands, pebble beaches, and cliffs and steep slopes. South America's coral reefs are more prominent along the Atlantic coast then along the Pacific. More specifically, these ecosystems are found primarily along the coasts of Colombia, the Bolivarian Republic of Venezuela and Brazil.

Mangrove swamps are found in protected areas along the entire length of the South American coast with the exception of Chile, Argentina and Uruguay. Large estuary ecosystems are also found along this coast in areas such as the Gulf of Guayaquil in Ecuador, which is the largest system of this type along the Pacific coast of South America, and in the deltas/estuaries of the three main rivers that empty into the Atlantic: the Amazon (Brazil), the Orinoco (Bolivarian Republic of Venezuela) and the Paraná, which helps to form the estuary of the Plate River (Argentina and Uruguay).

1.4.1.4. Caribbean islands

Most of the Caribbean islands are in the tropics (between latitudes 10ºN and 23ºN, with the latter parallel being the Tropic of Cancer), although some of the islands of the Bahamas are further north. The Greater Antilles (Cuba, Jamaica, Hispaniola and Puerto Rico) are, with the exception of Cuba, quite mountainous and have narrow coastal plains, while Cuba is flatter. The Lesser Antilles are made up of two archipelagos: the low-lying Windward Islands, which stretch from Barbados up to Anguilla and then continue north up to the Bahamas, and the mountainous, volcanic Leeward Islands, which run from Grenada northward. The same coastal and marine environments are found in these islands as on the mainland. The morphology of the beaches vary markedly depending on the type of sediment, the presence or absence of rivers, the degree of wave energy, the presence or absence of coral reefs, etc. There are straight sandy beaches of several kilometres in length, such as those found along the eastern coast of Barbados, and sandy coves just a few hundred metres long. Most of the coastlines of the volcanic islands such as Montserrat and Dominica are made up of steep cliffs. Mangrove swamps are found in areas that are sheltered from wave action, such as estuaries, lagoons and mudflats. Long stretches of mangrove swamps are found, for example, along the coastline of the Gulf of Trinidad and the southern coast of Jamaica. Coral reefs have played an important role in the formation and protection of many of the Caribbean islands. There are three main types of reefs in the Caribbean: strip reefs, such as those that fringe the western coast of Barbados; coral barrier reefs, such as those along the eastern coast of Andros Island in the Bahamas, and patch reefs, which are small isolated colonies that may be no larger than a few metres in diameter. Seagrass “meadows” are another important island ecosystem and are generally located between beaches and coral reefs. The climate of the Caribbean is governed by the trade winds, which blow from the northeast year round. Many of the islands are located in what is known as the Caribbean Hurricane Belt. The mean tide is around 30 cm, and high tides are up to 50 cm. Waves generally come from the east, but vary depending on the pattern of the trade winds. Extreme wave regimes are associated with the passage of hurricanes.

1.5. Objectives and structure

This research effort seeks to provide much-needed data in three specific areas. First, data have been compiled or generated, as appropriate, to augment the existing level of knowledge regarding the various dynamics and phenomena that affect the coasts of Latin America and the Caribbean, since, in many cases, the available information is insufficient and inhomogeneous and does not cover all the relevant variables. This type of information is a crucial input for coastal and harbor engineering and for integrated environmental management systems. Second, given the threat posed by climate change, an effort has been made to learn more about how these changes are being brought about and to determine what types of alterations can be expected in the future by extrapolating long-term trends in coastal dynamics. And third, in view of the importance of certain types of weather patterns in the region, such as El Niño, the ways in which coastal dynamics are influenced by these patterns is analysed by exploring the effects of climate variability in the region.

This study is structured as follows:

Section 1. Introduction, setting out the objectives of the study and an outline of how the document is structured.

Section 2. Information sources and databases consulted and generated by the Environmental Hydraulics Institute of the University of Cantabria (IHC) in Latin America and the Caribbean in order to determine the nature of coastal dynamics and to extrapolate long-term trends.

Section 3. Analysis and description of coastal dynamics in Latin America and the Caribbean. Current conditions were determined with the help of existing databases (which are specified in each case) and/or databases constructed for use in this study (in these cases, the way in which they were developed and validated, as well as the results, are described).

Section 4. Methodologies employed in the analysis of long-term trends in coastal dynamics and their impacts.

Section 5. Analysis of long-term trends in coastal dynamics in Latin America and the Caribbean. This section describes future dynamics along the region's coasts, gives mean values and gauges the degree of uncertainty or variability that is to be expected.

Section 6. Description of the model used to analyse year-on-year variability. Analyses of inter-annual variability based on climate indices are used to describe the way in which coastal dynamics in Latin America and the Caribbean are influenced by variations in weather patterns from year to year.

Section 7. General conclusions concerning dynamics and trends in Latin America and the Caribbean.

Annex 1. Description, calibration and validation of databases on waves, storm surges and tides compiled by IHC.

Annex 2. Hurricanes in Latin America and the Caribbean.

2. Databases and other information sources

2.1. Introduction

Information from various organizations across the world has been drawn upon in order to develop a suitable definition, in both spatial and temporal terms, of the physical factors that influence the coastal areas of Latin America and the Caribbean. In order to be useful, the information has to be comparative in nature and must cover a suitable time span to allow for a trend analysis of the variables in question. Despite the wealth of information that is available, as may be seen from table 1.2, there is a significant shortfall of data on storm surges, tides and swells. The reason for this is that the available data, as collected, for example, by means of instrumental buoys, are not homogeneous or available for the entire study area, while the data that are available for the entire area, such as satellite data, do not afford a suitable temporal resolution (data sampled at random intervals of time and data series that are relatively short and thus insufficient for conducting an analysis of trends over the long term). IHC has therefore developed numerically derived high-resolution data in temporal terms on the study area along the Latin American and Caribbean coasts. These data have been calibrated and validated for the three above-mentioned variables (see table 1.3).

TABLE 1.2
EXISTING DATABASES

Type of information	Time period covered	Spatial resolution	Source
Mean sea level (MSL)	1950-2009 / monthly	Global, 1º	CSIRO—Commonwealth Scientific and Industrial Research Organisation.
	Variable	Global, dispersed	Tide gauges UHSLC—University of Hawaii Sea Level Center.
Subsidence	-	Variable	DIVA—Dynamic Interactive Vulnerability Assessment. (Peltier *et al.* 2000)
Tides	Harmonic constants	Global, 0.25º	TPXO—Global model of ocean tides based on altimetric data from the TOPEX/POSEIDON mission.
Salinity (SAL)	1980-2009 / monthly	Global, 1ºx0.333º	NCEP - GODAS—National Centers for Environmental Prediction (USA), Global Ocean Data Assimilation System.
	1948-2011 / monthly	Global, 2.5º (Gaussian grid)	NCEP - NCAR—National Centers for Environmental Prediction (USA), National Center for Atmospheric Research.
Sea surface temperature (SST)	1950-2009 / monthly	Global, 2º	ERSSTv3 - NOAA—Extended Reconstructed Sea Surface Temperature, National Oceanic and Atmospheric Administration (USA).
Air temperature anomaly	1950-2005 / monthly	Global, 2º	GISS - NASA—Goddard Institute for Space Studies, National Aeronautics and Space Administration (USA).
Air temperature	1948-2009 / monthly	Global, 2.5º (Gaussiana grid)	NCEP - NCAR
Atmospheric pressure	1948-2009 / 6h	Global, 2.5º (Gaussian grid)	NCEP - NCAR
Wind	1948-2009 / 6h	Global, 2.5º (Gaussian grid)	NCEP - NCAR
Hurricanes	1950-2010	Global, dispersed	National Hurricane Center, NOAA
Swells	Variable	Global, dispersed	CSIRO satellite data
	Variable	Global, dispersed	NOAA buoys
	Variable	Global, dispersed	State port buoys
Bathymetry	-	Global, 2´	ETOPO—Earth Topography Digital Dataset. A global relief model of the Earth's surface that integrates land topography and ocean bathymetry.
	-	Global, 0.5´	GEBCO—General Bathymetric Chart of the Oceans.

Source: Prepared by the authors.

TABLE 1.3
DATABASES GENERATED BY IHC

Type of information generated by IHC	Period of time covered	Spatial resolution	Source
Swells	1948-2010	Global, Latin America and the Caribbean 0.5º and Caribbean 0.25º	GOW-IHC
Storm surges	1948-2010	Global, Latin America and the Caribbean 0.25º	GOS-IHC
Tides	1948-2010	Global, Latin America and the Caribbean 0.25º	GOT-IHC

Source: Prepared by the authors.

Section 2.2 describes the information sources from which each variable is derived and the characteristics of these sources. In each case, a brief overview of the data generated by IHC is given in the sections on the different variables, as well as in the annexes to the main document. Since this description is very brief, a full explanation of both the methodology and the process used to generate the data is included in an annex (annex 1).

2.2. Existing databases

2.2.1. Global mean sea level (MSL) data

Sea level data have been obtained from the Commonwealth Scientific and Industrial Research Organisation (CSIRO): http://www.cmar.csiro.au/sealevel/sl_data_cmar.html.

FIGURE 1.2
RISING GLOBAL MEAN SEA LEVELS (GMSL): 1870-2008
(Millimetres)

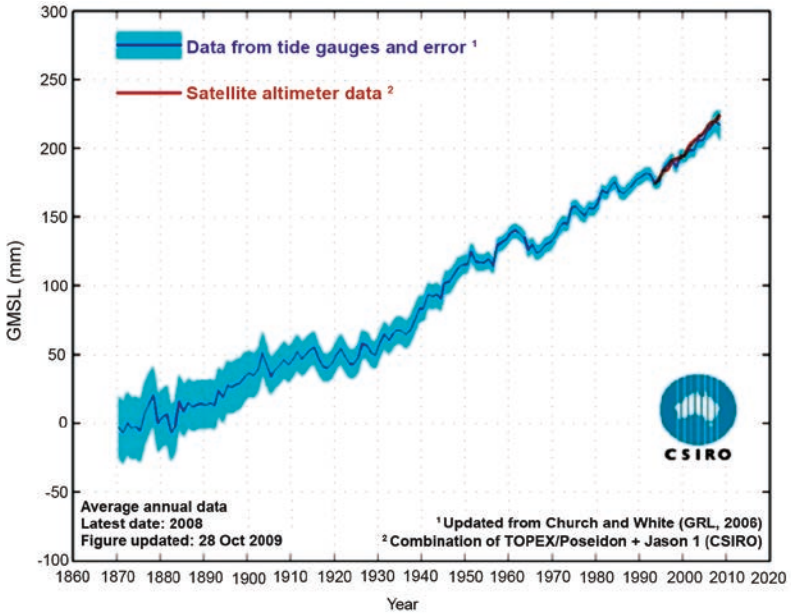

Source: CSIRO.

The latest estimates of changes occurring in the global mean seal level (figure 1.2) are based on satellite data collected since 1993 (shown in red in figure 1.2) and data gathered since 1870, which are a combination of on-site tide gauge levels and spatial patterns of variability as determined by satellite data (in blue). For the sake of clarity, the confidence interval is not shown for the satellite data, but its value is around ±5 mm.

Two different types of data for two different periods of time –from 1950 to 2001 and from 1993 to 2009– have been used for this study; they include an eight-year overlap.

1950-2001:

Sea level data for this period have been reconstructed using the method proposed by Church *et al.* (2004); the period has been extended up to 2001.

These data exhibit the following characteristics:

- The spatial resolution grid is 1º x 1º and extends between latitudes 65°S and 65°N; temporal coverage is from January 1950 to December 2001; the temporal resolution is at the one-month level.
- The data have been deseasonalized.
- The inverse barometer correction has been applied to the data.
- The Glacial Isostatic Adjustment (GIA) correction (Mitrovica) has been applied to tide gauge data.

1993-2009:

Data were taken from TOPEX/POSEIDON, Jason-1 and Jason-2/OSTM satellite altimetry, with the following characteristics:

- Spatial resolution for these data is 1º x 1º; the coverage is from 65°S to 65°N.
- The data reflect the monthly average of measurements taken from January 1993 until August 2009; the database is updated periodically as new information becomes available.

The available versions are as follows:

—Versions with or without inverse barometer corrections.

—Versions with or without seasonality adjustments (annual or semi-annual signals).

—Versions with or without a GIA correction.

It is worth discussing the relationship between these data and rises in sea level due to tectonic shifts. Movements of landmasses fall into two categories: slow and monotonic movements, such as the Glacial Isostatic Adjustment (GIA), and swift, irregular movements, such as the tectonic shifts observed in Chile, which are seismic in nature.

Seismic activity is not affected by climate change. It is true that a large-scale earthquake, in and of itself, or the tsunamis that it generates, may alter the coastline considerably (as was seen, for example, with the Indian Ocean earthquake of 2004 or the 2010 earthquake in Chile), thereby modifying the extent of a given area's vulnerability to climate change. However, it is not within the scope of this study to analyse effects of this nature, given that, from the standpoint of climate change risks, the macro-configuration of the coastline is assumed to be invariable in the long run. This type of consideration is more appropriate in studies concerned with tsunami- and natural-disaster-related risk analyses.

The sea level database used in this study to gauge slow changes in land elevations or subsidence contains measurements of the rise in sea levels relative to the land, and the analysis therefore takes into account these kinds of tectonic movements. Examples showing various trends in the relative rise and fall of sea levels as measured by different gauges are presented in figure 1.3:

• Glacial Isostatic Adjustment (GIA) (e.g., Stockholm) or Post Glacial Rebound (PGR): The level of the land is rising at a faster rate than the level of the sea.

• Earthquakes (e.g., Nezugaseki, Japan): There has been a sudden rise in sea level since the 1964 earthquake. This indicates that, in this region, the Earth's crust is sinking relative to the sea.

• Extraction of groundwater (e.g., Bangkok, Thailand): The level of the land is sinking with respect to the level of the sea due to the excessive extraction of groundwater since 1960.

• Sedimentation (e.g., Manila): Sedimentation from river discharge and land reclamation are triggering a rise in sea levels.

• Long-run trend (e.g., Hawaii): This area is located far from the effects of the GIA, and no seismic activity has been recorded during the period for which records have been kept.

FIGURE 1.3
FIVE MEAN SEA LEVEL GAUGES
(Millimetres)

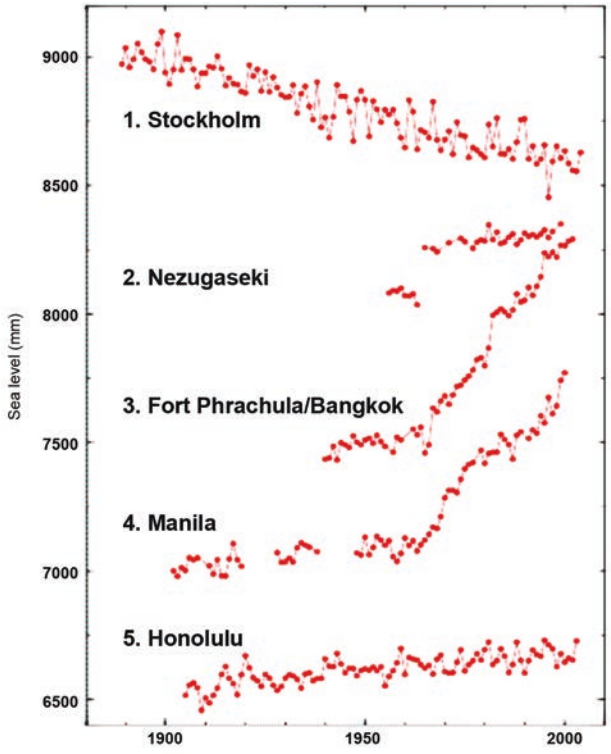

Source: Permanent Service for Mean Sea Level (PSMSL).

These differences arise because the tide gauge monitoring stations measure changes in sea levels but are located on the surface of the sea therefore and measure changes in sea level relative to a fixed position on land. Thus, regardless of whether the landmass moves with respect to the sea or vice-versa, the gauge will show a relative change in sea level. Therefore, the effects of these two phenomena cannot be isolated from each other using tide gauge data alone, as is the case of the data used in this study. The movements of landmasses could be registered using GPS (Global Positioning System) receivers positioned near tide gauges, which would make it possible to isolate the effects of such movements on sea level data.

Furthermore, changes in atmospheric pressure also influence changes in sea level. For this reason, baroclinic corrections have also been made.

The database used here to derive trends in rising mean sea levels is widely employed by the scientific community.

Section 3 provides results for the mean sea level distribution and current seasonal variations in the mean.

2.2.2. Tide data

Tide data for the Latin American and Caribbean coasts have been generated by IHC using harmonic constants derived from the TPXO global model of ocean tides (version 7) developed at Oregon State University (Egbert *et al.*, 1994; Egbert and Erofeeva, 2002). The TPXO model incorporates data from the TOPEX/POSEIDON missions and from tide gauges (Ardalan and Hashemi-Farahani, 2007) and is one of the most accurate global tide models of all (http://www.esr.org/polar_tide_models/Model_TPXO71.html).

The database includes eight harmonic constants for principal tide constituents (M2, S2, N2, K2, K1, O1, P1, Q1) and two for long-period tides (Mf y Mm) on a global grid of 1440 x 721 points, with a 0.25º spatial resolution (http://volkov.oce.orst.edu/tides/global.html).

Figure 1.4 shows a map for the M2 constituent calculated using the above model.

FIGURE 1.4
MAP OF THE M2 TIDAL CONSTITUENT CALCULATED USING THE TPXO MODEL
(Metres)

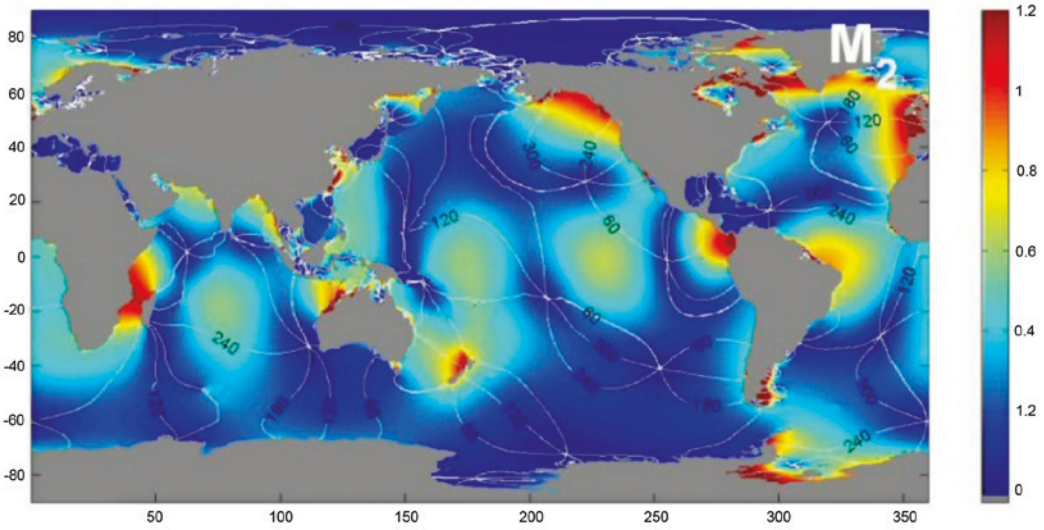

Source: http://volkov.oce.orst.edu/tides/global.html.

Series of time slots of tides along the Latin American and Caribbean coasts have been generated for the period from January 1948 until December 2099 based on the above data. Possible long-term tidal variations caused by rising mean sea levels are not reflected in this database. The results for tidal range (the range between maximum and minimum values) along the length of the coast are presented in the section devoted to the characterization of the coastal environment (chapter 4).

2.2.3. Salinity data (SAL)

The salinity data used in this study has been drawn from the reanalysis of the NCEP-Global Ocean Data Assimilation System (GODAS) maintained by NOAA. These data has been applied at a depth of 5 m (http://www.esrl.noaa.gov/psd/data/gridded/data.godas.html).

The new GODAS system was developed as a replacement for RA6 in order to provide the appropriate initial conditions for the Global Climate Forecast System (CFS) developed in the course of the NCEP reanalysis (Saha *et al.,* 2006). More detailed information regarding this model can be found in Behringer and Xue (2004).

GODAS is based on a quasi-global configuration of the GFDL MOM.v3 model. The area covered by the model extends from 75°S to 65°N and has a resolution of 1°, which is increased to 1/3° along the N-S axis starting from 10º from the equator. The model has 40 levels with a resolution of 10 m up to a maximum of 230 m. GODAS is forced by the momentum flux, heat flux and fresh water flux from the NCEP atmospheric reanalysis 2 (R2).

The data are as follows:

- Temporal coverage: monthly resolution from January 1980 to November 2009.
- Spatial coverage: latitudinal resolution of 0.333º and 1º longitudinal resolution on a global grid of 418 x 360 nodes.

The results for the salinity distribution and its current mean seasonal variations are presented in section 3 of this chapter.

2.2.4. Sea surface temperature (SST) data

Sea surface temperature data have been obtained from NOAA (Extended Reconstructed Sea Surface Temperature, ERSST): https://www.ncdc.noaa.gov/data-access/marineocean-data/extended-reconstructed-sea-surface-temperature-ersst-v3b

The database coverage is as follows:

- Temporal coverage: monthly resolution from 1950 to 2009.
- Spatial coverage: global resolution of 2º x 2º.

The most recent version of the ERSST is v3b. The analysis is based on version 2.4 of the International Comprehensive Ocean-Atmosphere Data Set (ICOADS). At the end of each month, the ERSST analysis is updated using available information from ships and buoys for that month. The anomalies are calculated for monthly weather data for the period 1971-2000 (Xue *et al.,* 2003).

The ERSST.v3b database is generated using discontinuous on-site SST data which are then rounded using a statistical method that makes it possible to arrive at a stable reconstruction based on spatially disperse data. The monthly analysis covers the period from January 1854 to the present. However, given the disperse nature of the instrumental information, the signal that can be analysed starts in 1880. From 1880 on, the signal is more consistent in time (figure 1.5). The ERSST is suitable for spatially and temporally large-scale studies, since local and short term variations have been smoothed out.

FIGURE 1.5
ANNUAL ERSST.V3B ANOMALY FOR 1880-2009
FROM 60°S TO 60°N WITH 95% CONFIDENCE INTERVAL (IN BLUE)
(Centigrade)

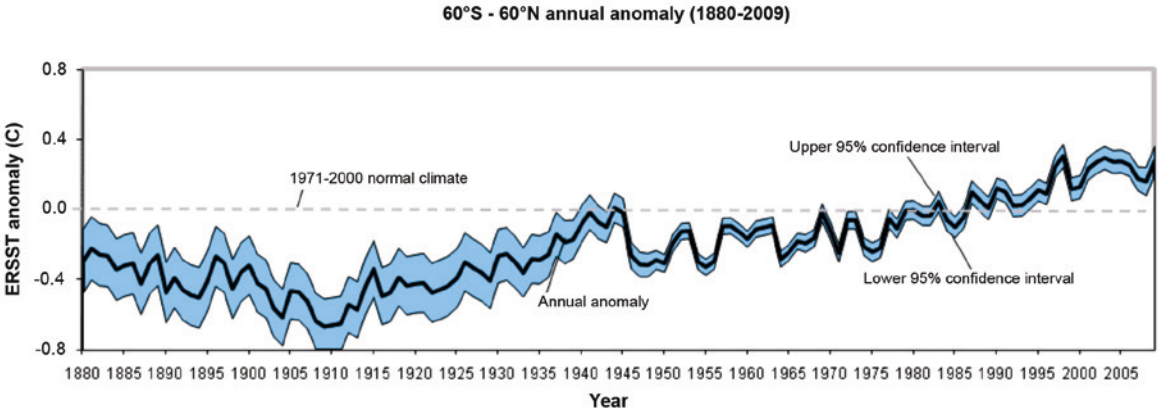

Source: NOAA-NCDC.
Note: There is a higher confidence level for data after 1940.

As can be seen in figure 1.5, the temperature increase in recent decades far outweighs the uncertainty limits of the data.

The results for the spatial distribution and its current mean seasonal variations are presented in section 3 of this chapter.

2.2.5. Pressure and wind databases

Pressure and wind data were used in generating the storm surge and wave activity data used in this study. The data were obtained from the reanalysis project run by the National Centers for Environmental Prediction (NCEP) and National Center for Atmospheric Research (NCEP/NCAR) of the Physical Sciences Division (NOAA/ESRL). These data provide global coverage and suitable spatial and temporal resolutions, since they include atmospheric data from 1948 until the present and have been regularly updated. The data can be accessed on the following website: http://www.esrl.noaa.gov/psd/data/reanalysis/reanalysis.shtml.

The maximum wind speeds at an elevation of 10 m on a global scale over the last 10 years of the NCEP reanalysis are shown in figure 1.6.

FIGURE 1.6
NCEP REANALYSIS: MAXIMUM WIND SPEEDS AT AN ELEVATION OF 10 M (1998-2008)
(Millimetres/seconds)

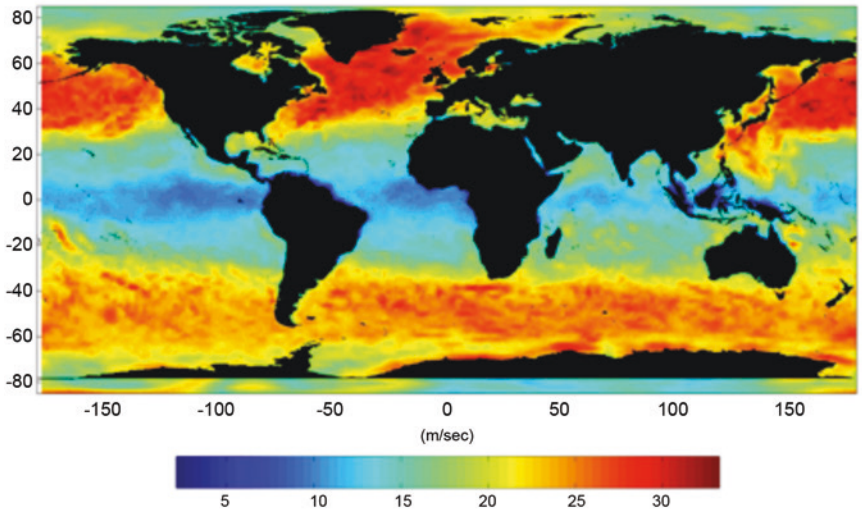

Source: Prepared by the authors based on NCEP/NCAR reanalysis project data.

2.2.6. Instrumental swell gauge databases

As was discussed in chapter 4, instrumental gauge data were used to validate and calibrate numerical results for wave activity. Two data sources have been used for this purpose: satellite measurements and buoy data.

Wave height data from 1992 to 2009 are available for the regions shown in figure 1.7. The data have been processed based on information gathered by various altimeter-equipped missions: Jason-2 (since late 2009), Jason-1, TOPEX/POSEIDON, ERS-2, Envisat and GFO.

FIGURE 1.7
SATELLITE DATA FOR THE LATIN AMERICAN AND CARIBBEAN STUDY

Source: Prepared by the authors based on the Archiving, Validation and Interpretation of Satellite Oceanographic Data (AVISO) network.

These are AVISO network databases: http://www.aviso.oceanobs.com/.

Satellite data are homogeneously distributed in space but not in time due to the fact that there is a gap of several days between passes of a satellite over a specific area. For this reason, buoy records have been used to validate the swell data. The two sources for these buoy records are the Spanish government's *Puertos de Estado* webpage (http://www.puertos.es/es-es/oceanografia/Paginas/portus.aspx) and the NOAA National Data Buoy Center (http://www.ndbc.noaa.gov). Figure 1.8 shows the buoys used in validating the swell data generated for this study (see the annex 1).

FIGURE 1.8
BUOYS USED IN GLOBAL OCEAN WAVE (GOW) DATA VALIDATION

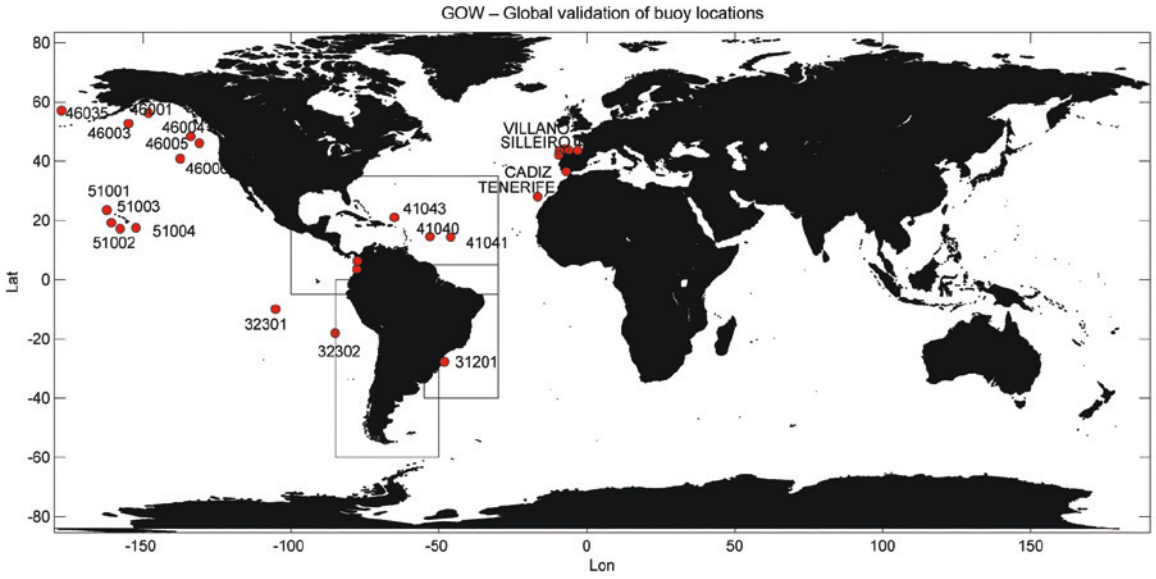

Source: *Puertos de Estado* (Spanish government) and NOAA.

2.2.7. Instrumental sea level gauge databases

Tide gauge data have been obtained from the University of Hawaii Sea Level Center (UHSLC), which compiles tide gauge data from around the world from regional and national sea level networks. These data are available at: http://ilikai.soest.hawaii.edu/uhslc/rqds.html.

These tide gauges are part of the UHSLC research quality sea level station database, and the data they provide have been checked and quality-controlled. The data series have an hourly temporal resolution, while the length of the series varies from one tide gauge station to the next.

Figure 1.9 shows the gauges located in the study area which were used to validate the numerical data generated for storm surges and tides (see annex 1.2). There are a total of 179 gauges.

FIGURE 1.9
UHSLC GAUGES IN THE STUDY AREA

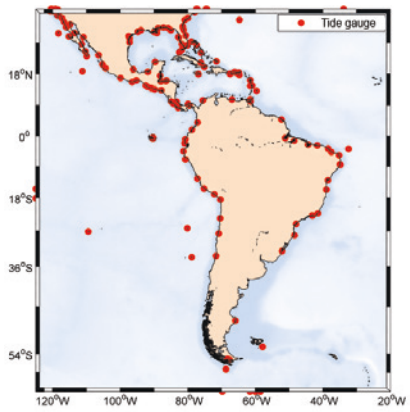

Source: Prepared by the authors.

2.2.8. Air temperature

Air temperatures have been derived from NCEP-NCAR reanalysis data and have a monthly temporal resolution and a spatial resolution of approximately 1.875º x 1.9º. This data source has been chosen for its spatial and temporal coverage, which is more suitable for the purposes of this study than other sources available through the network, such as the Hadley Center or NASA.

2.2.9. Mean sea level projections

One of the first databases on projected sea level rise for the different socioeconomic scenarios was published in the third IPCC report (2001). In that report seven Atmosphere Ocean General Circulation Models (AOGCMs) are aggregated (see figure 1.10), to deduce the increase in global mean sea levels from 1990 to 2100 for six socioeconomic scenarios (coloured lines) and the corresponding confidence intervals (grey shading).

Based on these projections, it can be determined, for example, that the average rise (average of all the projected scenarios) in the mean sea level for 2050 (based on 2010 levels) will be approximately 12 cm, while by 2100 (based on 2010 levels), levels will have risen by 30 cm. The latest results have been published in the fourth IPCC report (2007) and are shown in table 1.4.

FIGURE 1.10
MEAN SEA LEVEL RISE SCENARIOS
(Metres)

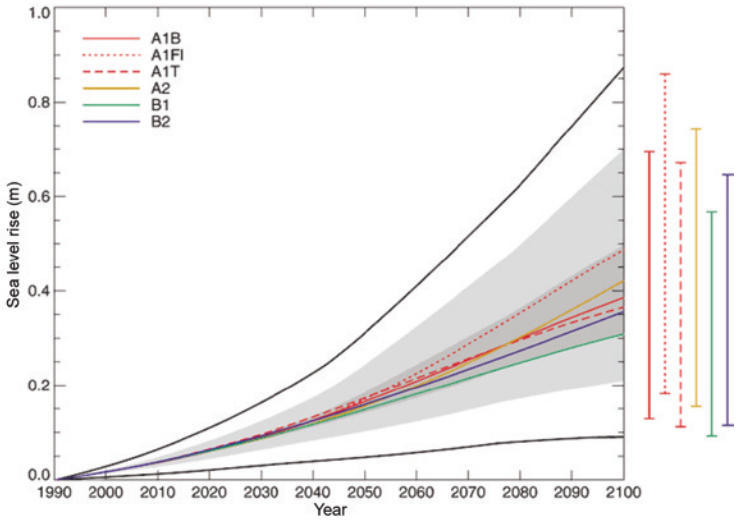

Source: IPCC, TAR, 2001.

TABLE 1.4
MEAN SEA LEVEL RISE SCENARIOS
(Millimetres)

Year	A1B	A1T	A1FI	A2	B1	B2
1990	0	0	0	0	0	0
2000	10	11	9	9	12	11
2010	21	23	19	20	26	24
2020	35	42	32	32	44	42
2030	55	63	48	47	64	63
2040	77	86	69	67	84	83
2050	102	112	96	89	105	103
2060	126	135	130	115	127	125
2070	150	156	165	142	145	146
2080	173	173	200	173	161	168
2090	192	186	234	203	175	190
2100	208	194	266	237	185	210

Adjusted projections of sea level for 5-percentile minimum, derived by adjusting the TAR-IPCC projections to correspond to the AR4-IPCC projections at 2095.

Year	A1B	A1T	A1FI	A2	B1	B2
1990	0	0	0	0	0	0
2000	27	26	28	27	25	26
2010	59	59	60	60	56	58
2020	96	100	99	97	92	97
2030	143	149	146	139	132	142
2040	200	208	204	190	178	192
2050	266	272	278	251	227	247
2060	337	342	368	320	279	307
2070	413	413	471	401	333	369
2080	493	482	584	490	388	435
2090	571	548	701	588	444	504
2100	649	611	819	692	496	576

Adjusted projections of sea level for 95-percentile maximun, derived by adjusting the TAR-IPCC projections to correspond to the AR4-IPCC projections at 2095.

Source: Hunter, J., (2010), "Estimating sea-level extremes under conditions of uncertain sea-level rise", *Climatic Change.*

The values obtained from the AR4-IPCC projections are similar, although the uncertainty level for each socioeconomic scenario is somewhat lower. The IPCC report (2007) specifies that future fast-paced changes in the dynamic of ice flows are not taken into consideration. Glacier melt and the contribution of Antarctica and Greenland to rising sea levels are some of the factors that have caused

the scientific community to reformulate many of the hypotheses underlying the findings published by IPCC. Figure 1.11, for example, compares the sea level rise data obtained from tide gauge and satellite measurements (3.3 mm/year) with average IPCC model projections (Rahmstorf *et al.,* 2007).

FIGURE 1.11
COMPARING IPCC SCENARIO MODEL RESULTS AND INSTRUMENTAL VALUES

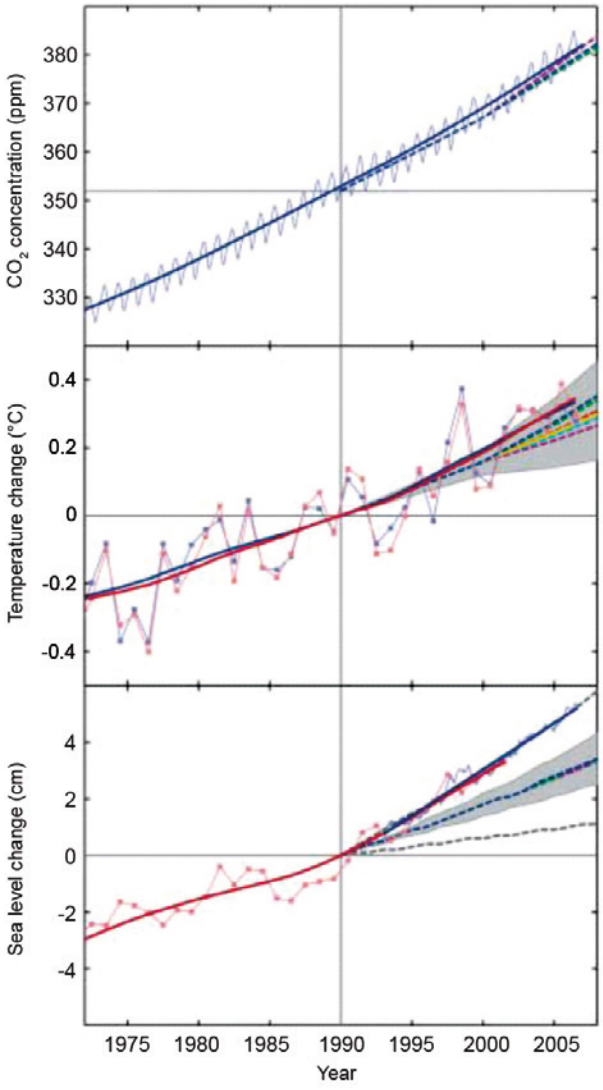

Changes in important climate parameters since 1973 as compared with IPCC scenarios (represented here with dotted lines and grey shading) (upper panel). Monthly carbon dioxide concentrations and trends in Mauna Loa, Hawaii (blue) up to January 2007 as obtained from Scripps in collaboration with NOAA in parts per million (ppm) (middle panel). Mean annual global (land and sea) surface temperature data and trends obtained from GISS (red) and the Hadley Centre/Climate Research Unit (blue) up to 2006 (bottom panel). Sea level data and trends primarily based on tide gauge records (annual data in red) and satellite altimeters (trimonthly data up to 2006 in blue). All the trends observed here are non-linear and have an 11-year overlap, with the roughness criterion being applied except in the case of the altimeter data, where a linear trend was used due to the shortness of the series. Temperature and sea level data are shown as deviations from the 1990 trend values (the base year for IPCC scenarios).

Source: Rahmstorf and others, 2007.

Clearly, there are significant differences in the figures; numerous researchers have attempted to resolve the issue of rising sea levels by using semi-empirical approaches (simple statistical models that represent the relationship between the increase in mean global temperature and rising sea levels). Following this line of thought, Rahmstorf (2007), Vermeer and Rahmstorf (2009), Horton and others (2008), and Gringsted and others (2009) have arrived at estimates for sea levels in the year 2100 that are higher than those obtained by the IPCC-AR4 (2007). Figure 1.12 shows an example of the results obtained by Vermeer and Rahmstorf (2009), which predict an increase in the global mean sea level of 1 m by the year 2100.

FIGURE 1.12
PROJECTED RISE IN MEAN SEA LEVELS FROM 1990 TO 2100 BASED ON TEMPERATURE PROJECTIONS FOR THE A2, B1 AND A1F1 SCENARIOS

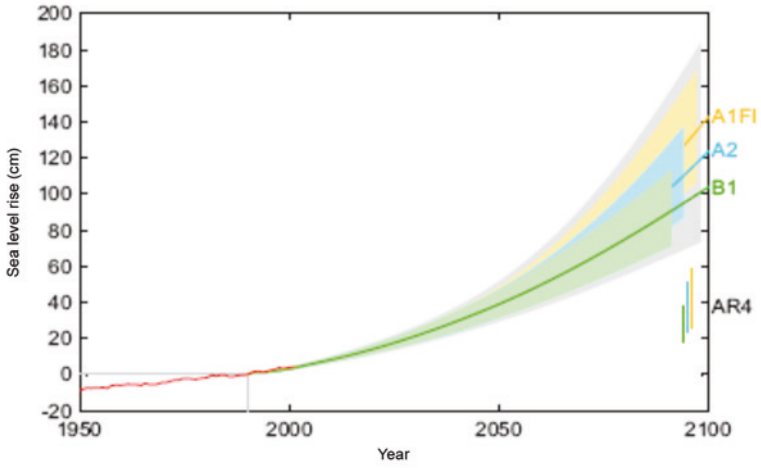

Source: Vermeer and Rahmstorf (2009).
Note: The range of IPCC-AR4 results are also shown.

Other studies conducted by Dutch experts (Dutch Delta Committee, *Exploring High-End Climate Change Scenarios for Flood Protection of the Netherlands,* 2008), however, conclude that the global mean sea level will rise by between 0.55 and 1.1 m by the year 2100.

In the chapters on impacts and risks, the sea level rise and underlying emissions scenarios to be covered in this study will be defined on the basis of all the available information.

2.2.10. Climate model projection databases

Information pertaining to the AOGCM climate models that were used in the IPCC-AR4 (2007) can be accessed at: http://www-pcmdi.llnl.gov/. This information is summarized in figure 1.13.

FIGURE 1.13
AOGCM CLIMATE MODELS IN IPCC-AR4

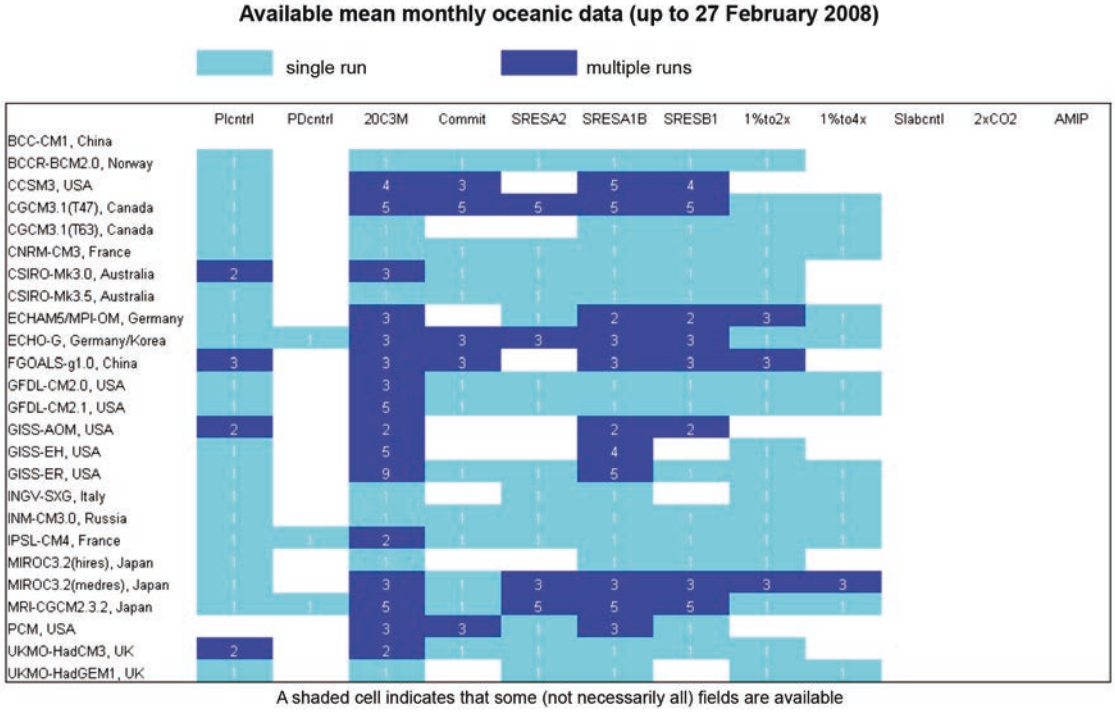

Source: http://www-pcmdi.llnl.gov/

In order to determine the suitability of the available climate model data for this study, the scientific literature on modeling and projections of the ENSO (El Niño–Southern Oscillation) phenomenon for different climate change scenarios was reviewed. The conclusion reached was that, as things stands today, there is a great deal of uncertainty as to the AOGCM climate models' ability to accurately model ENSO events, and there is as yet no consensus as to whether these events are more or less intense and/or frequent than before (see, for example, M.A. Cane (2005), N. Nicholls (2008), Van Oldenborgh and others (2005), M. Collins and others (2005)). For this reason, and considering the scope of this study, projected AOGCM climate models from the IPCC covering the twenty-first century will not be utilized. Instead, the analysis will be conducted on the basis of the correlations between the factors considered in this study and known climate indices (NIÑO3, SAM, etc.). Using short-term predictions (one year or less) of an ENSO event, the results will allow the risks associated with a particular value of, for example, the NIÑO3 index to be evaluated. As an example, the influence reflected on the NIÑO3 index of sea level anomalies is shown in figure 1.14. As the reader will see, the southern Pacific coast is strongly influenced by ENSO. Section 6 describes the influence on the various factors (sea level, swell intensity, swell directionality, storm surges) exerted by the agents reflected in the climate indices for the oceanic climate in Latin America and the Caribbean.

FIGURE 1.14
INFLUENCE AS MEASURED BY THE NIÑO3 INDEX ON MONTHLY SEA LEVEL ANOMALIES

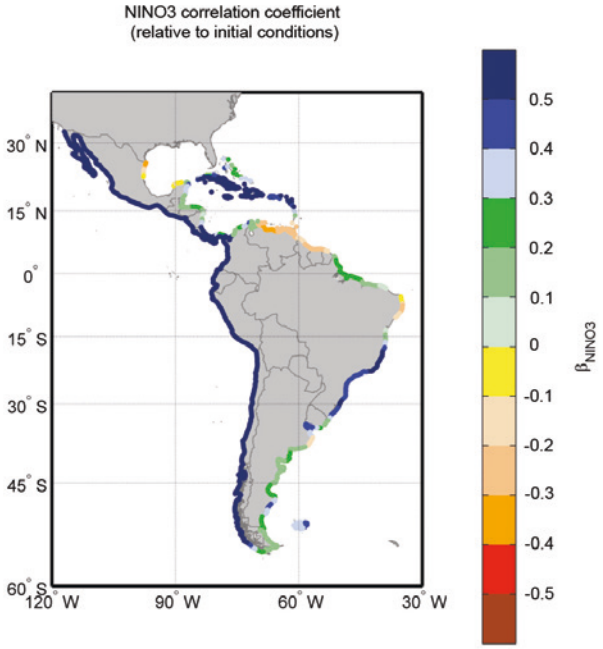

Source: Prepared by the authors.

3. Coastal dynamics in Latin America and the Caribbean

An overview of the dynamics dealt with in this study is provided in table 1.5. Descriptions of these variables are given in the sections that follow.

TABLE 1.5
OVERVIEW OF COASTAL VARIABLES DEALT WITH IN THIS STUDY

Meteo-oceanographic variables	Coastal dynamics (IHC)	Extreme events	Hurricane events
• Mean sea level (MSL) • Sea surface temperature (SST) • Salinity (SAL) • Air surface temperature (AST) • Wind (W)	• Waves (monthly mean, monthly peak, height exceeded 12 hours per year and mean wave direction) • Storm surge • Tide	• Waves • Storm surges	• Winds • Waves • Storm surges

Source: Prepared by the authors.

3.1. Meteo-oceanographic dynamics

3.1.1. Mean sea level

Global mean sea level data were used to obtain seasonal figures (monthly means) worldwide and specifically for the Latin America and Caribbean region. At the world level, there is a very noticeable degree of spatial variability, with peak levels of variation in the northern Pacific Ocean and in more enclosed seas, such as the Tasman Sea and the Mediterranean. For Latin America and the Caribbean (see figure 1.16), seasonal variations between the northern and southern hemispheres are observable, with the sharpest variations being seen along the northern coast of Brazil and the Pacific coast of Central America.

FIGURE 1.15
SEASONAL DIFFERENCES IN MEAN SEA LEVELS WORLDWIDE
(Millimetres)

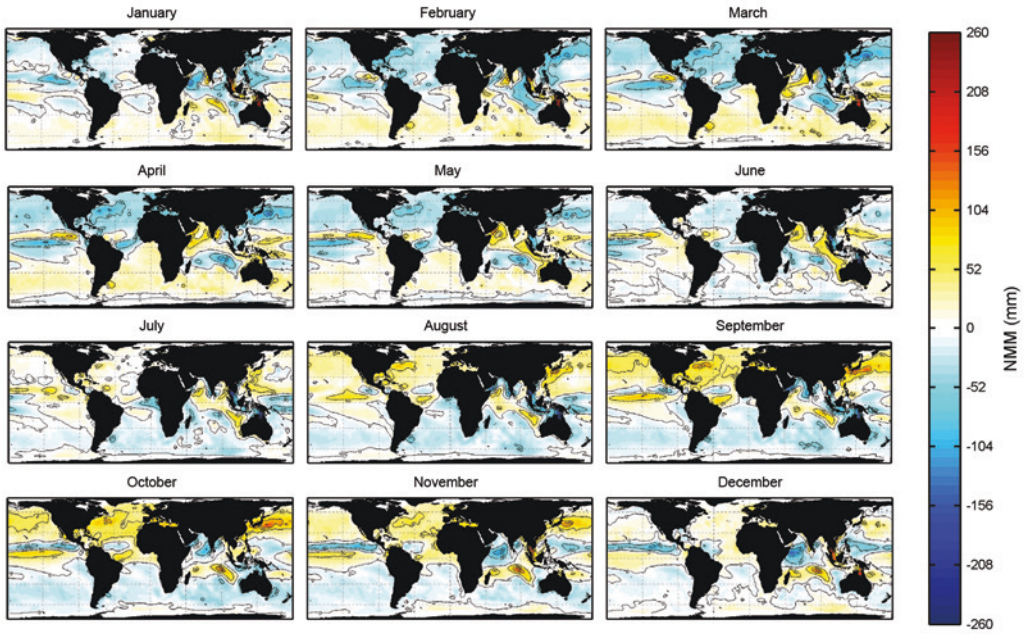

Source: Prepared by the authors.

FIGURE 1.16
SEASONAL DIFFERENCES IN MEAN SEA LEVELS IN LATIN AMERICA AND THE CARIBBEAN
(Millimetres)

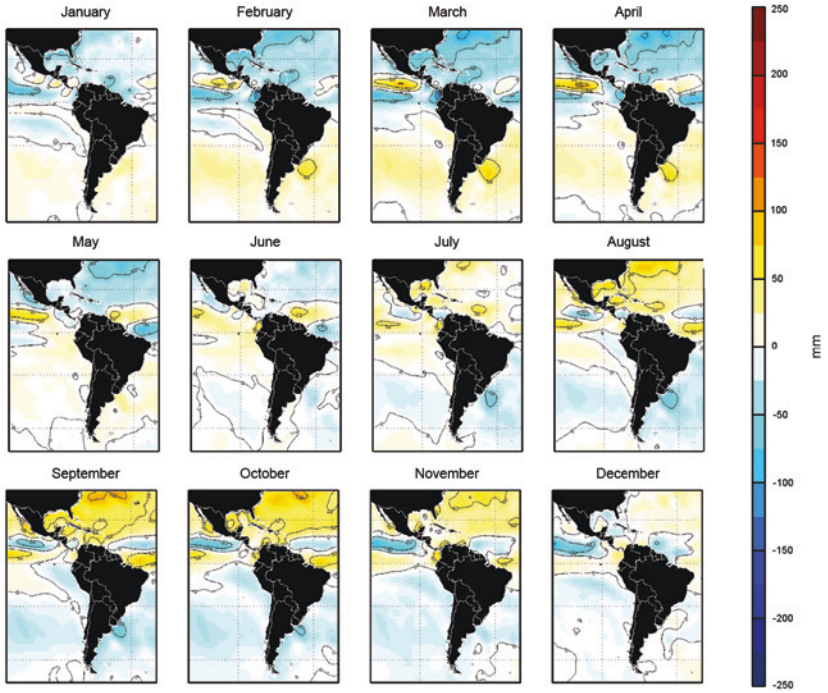

Source: Prepared by the authors.

3.1.2. Salinity

The data indicate that, at the global level (see figure 1.17), the Atlantic Ocean has a higher degree of salinity than the Pacific Ocean does and that the degree of salinity of enclosed seas such as the Mediterranean is especially high. The seasonality of this variable is less marked than it is for some of the other variables.

FIGURE 1.17
SEASONAL DIFFERENCES IN SALINITY WORLDWIDE
(Kilograms /kilograms)

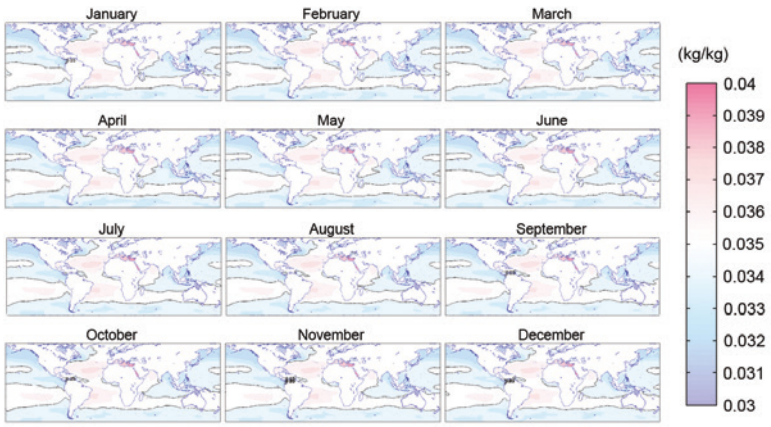

Source: Prepared by the authors.

3.1.3. Sea surface temperatures

At the global level, the sea temperature gradient is linked to latitude. There is a seasonal shift in isotherms from north to south in the summer months in the southern hemisphere and a shift in the other direction during the winter.

FIGURE 1.18
SEASONAL DIFFERENCES IN SEA SURFACE TEMPERATURES WORLDWIDE
(Centigrade)

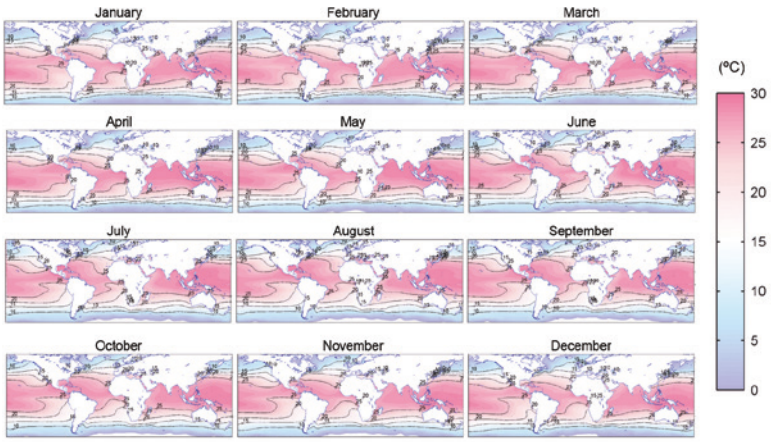

Source: Prepared by the authors.

FIGURE 1.19
SEASONAL DIFFERENCES IN SEA SURFACE TEMPERATURES IN LATIN AMERICA AND THE CARIBBEAN
(Centigrade)

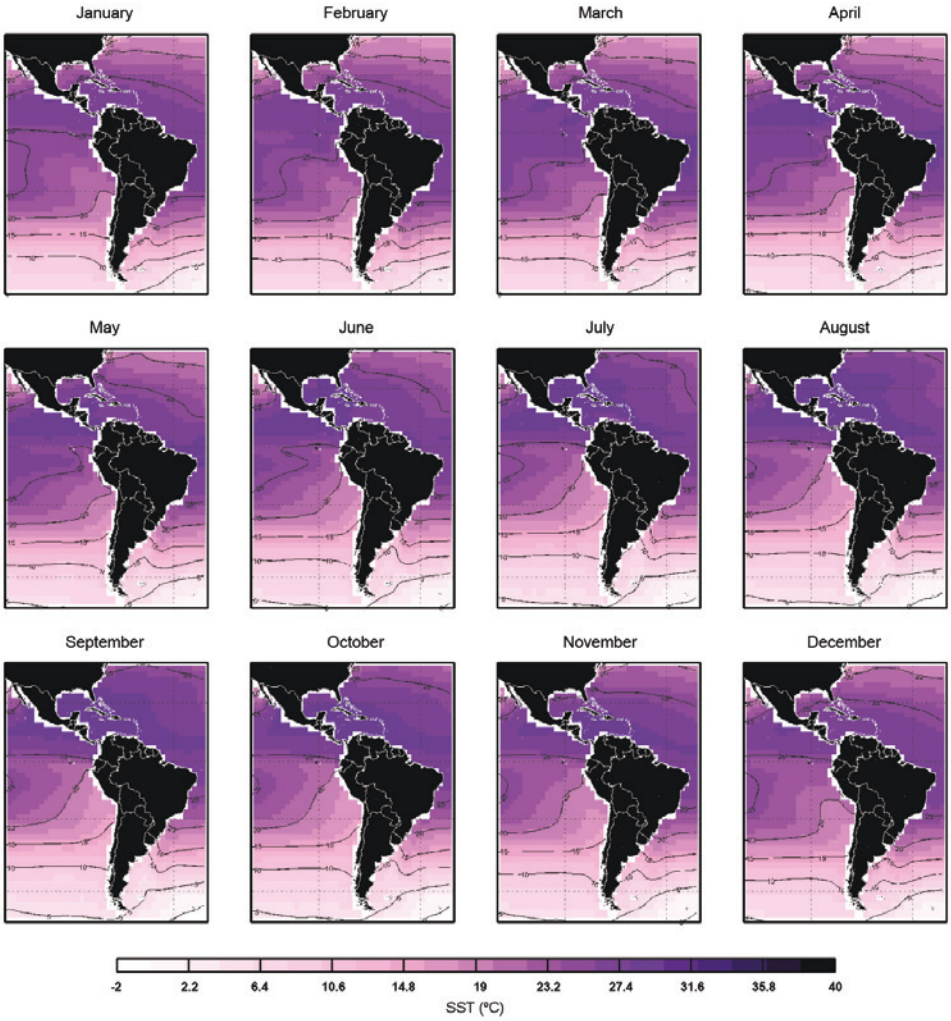

Source: Prepared by the authors.

3.1.4. Air temperatures

As is also the case with the preceding variables, temperature shifts are associated with the winter/summer cycles in the northern and southern hemispheres.

FIGURE 1.20
SEASONAL DIFFERENCES IN SURFACE AIR TEMPERATURES WORLDWIDE
(Centigrade)

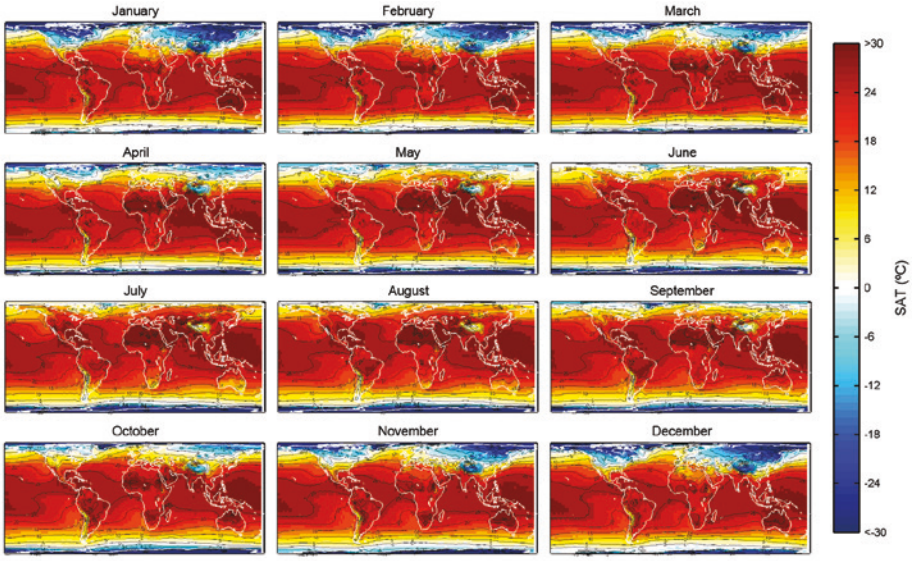

Source: National Centers for Environmental Prediction (NCEP)/National Center for Atmospheric Research (NCAR) reanalysis.

FIGURE 1.21
SEASONAL DIFFERENCES IN SURFACE AIR TEMPERATURES IN LATIN AMERICA AND THE CARIBBEAN
(Centigrade)

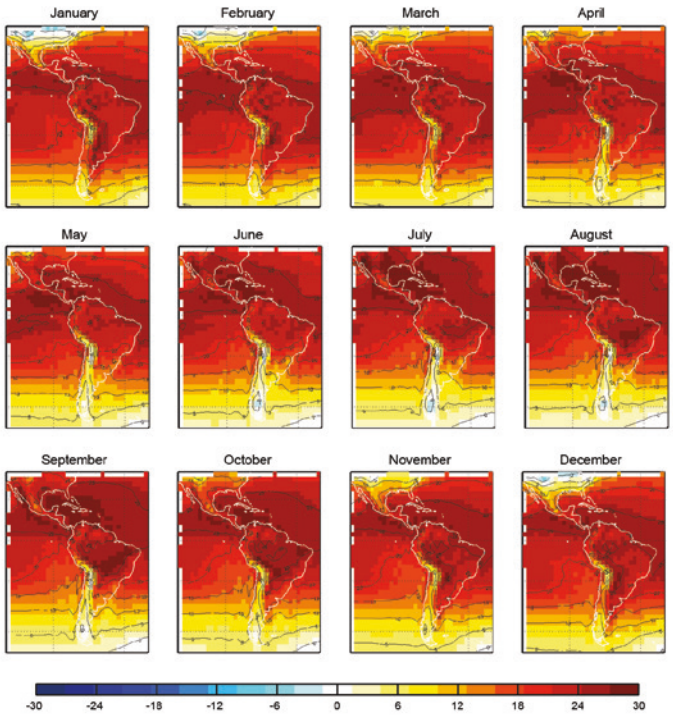

Source: National Centers for Environmental Prediction (NCEP)/ National Center for Atmospheric Research (NCAR) reanalysis.

3.1.5. Wind

Annual 90th percentiles have been used to gauge high-end (but not extreme) wind velocities. The National Centers for Environmental Prediction (NCEP)/National Center for Atmospheric Research (NCAR) reanalysis is the information source used for this purpose; due to its resolution, tropical storms are not properly reflected in the data, although they do appear as high-intensity winds. The 90th percentile therefore provides a measurement of the high end of the spectrum of strong winds in the area. As shown in figure 1.23, the strongest winds occur in the southern portion of the continent (the westerlies) and in the Caribbean (tropical winds). The doldrums (Intertropical Convergence Zone (ITCZ)) are also clearly visible.

Global wind patterns (see figure 1.22) are such that north-easterly winds predominate in the northern-hemisphere portions of Latin America and the Caribbean, while south-easterly winds make up the predominate pattern in the subtropical regions of the southern hemisphere. Starting from about 30ºS, the winds are generally from the north-west, but the pattern then switches to south-easterlies in the low-pressure polar regions.

FIGURE 1.22
THEORETICAL (A) AND ACTUAL (B) GLOBAL WIND CIRCULATION PATTERNS IN THE AMERICAS

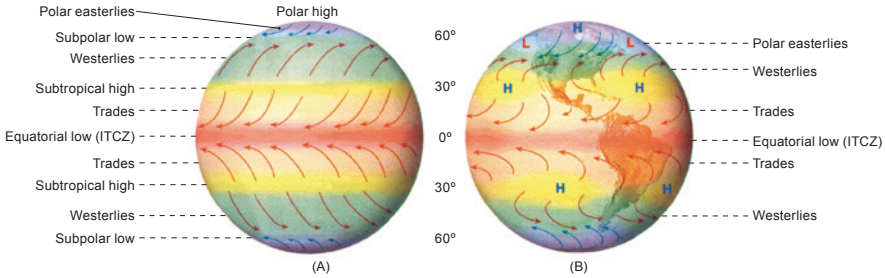

Source: Atmospheric Chemistry Department of the Max Planck Institute.

FIGURE 1.23
0.9 QUANTILE OF WIND VELOCITIES: 1948-2008
(Metre/second)

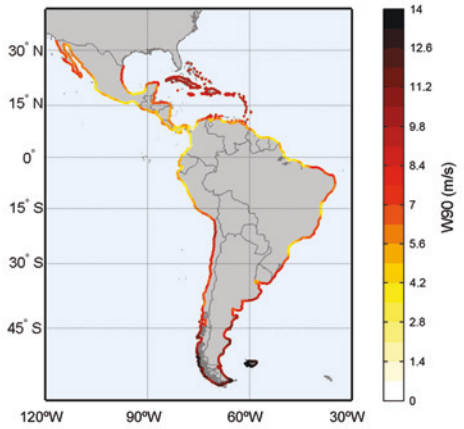

Source: Prepared by the authors on the basis of the National Centers for Environmental Prediction (NCEP)/National Center for Atmospheric Research (NCAR) reanalysis.

Figure 1.24 shows the effects during the northern-hemisphere winter, where values exceed the 90th percentile; the inter-seasonal variation in the southern hemisphere is less marked.

FIGURE 1.24
SEASONAL DIFFERENCES IN MEAN WIND SPEEDS: 1948-2008
(Metre/second)

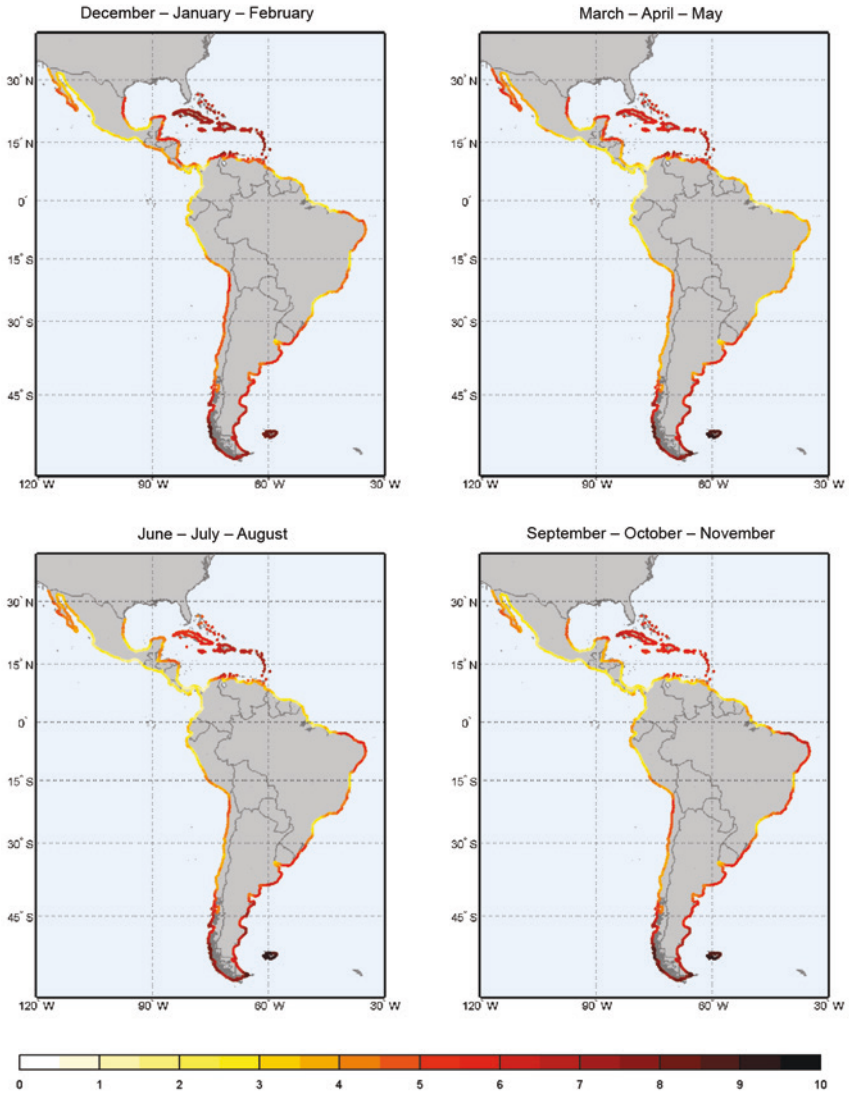

Source: Prepared by the authors on the basis of the National Centers for Environmental Prediction (NCEP)/National Center for Atmospheric Research (NCAR) reanalysis.

The effect of global wind patterns is also reflected in mean wind directions. As shown in figure 1.25, onshore winds prevail in both the Atlantic and the Pacific, except in Central America, southern Mexico and Panama, where northerly winds prevail along both coasts due to the narrowness of the land mass and the low elevations found in this part of the world.

FIGURE 1.25
MEAN WIND DIRECTIONS: 1948-2008

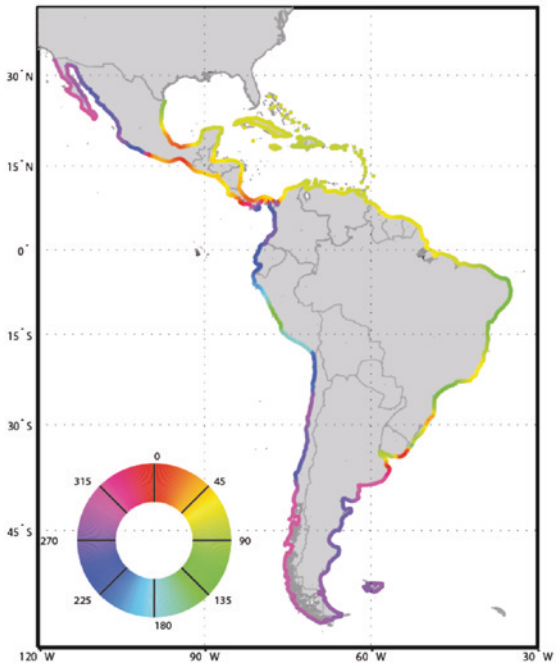

Source: Prepared by the authors on the basis of the National Centers for Environmental Prediction (NCEP)/National Center for Atmospheric Research (NCAR) reanalysis.

3.2. Coastal dynamics

This section deals with coastal variables, such as waves, tides and storm surges. Very little information or research on these types of variables is available, and this is especially true in the specific case of Latin America and the Caribbean and, more generally, the southern hemisphere as a whole.

3.2.1. Waves

As this study focuses on variables in the region about which relatively little is known, such as wave patterns, statistical data on waves and their seasonal distribution will be analysed here.

Wave data have been obtained by means of a numerical simulation that provides a basis for a reanalysis of the IHC Global Ocean Waves (GOW) database. Descriptive wave variables include the monthly mean value for **significant wave height** (Hs), or the average height of the highest one-third of waves, as an indicator of mean monthly conditions; the **monthly peak significant wave height,** which reflects the most severe wave conditions in each month; the **significant wave height likely to be exceeded during 12 hours per year** (Hs_{12}), which is extremely important when defining equilibrium beach profiles, since it provides information about the depth at which the transport of sediments ceases to be dominated by wave action and represents a quantile for the high end of annual wave conditions (see figure 1.29); and the **mean wave direction,** which is the predominant direction from which the wave energy is flowing (see figure 1.28). Mean and peak wave heights are analysed in spatial terms and in terms of their temporal distribution over the four seasons of the year (see figures 1.26. and 1.27).

FIGURE 1.26
MEAN SEASONAL SIGNIFICANT WAVE HEIGHT
(Metres)

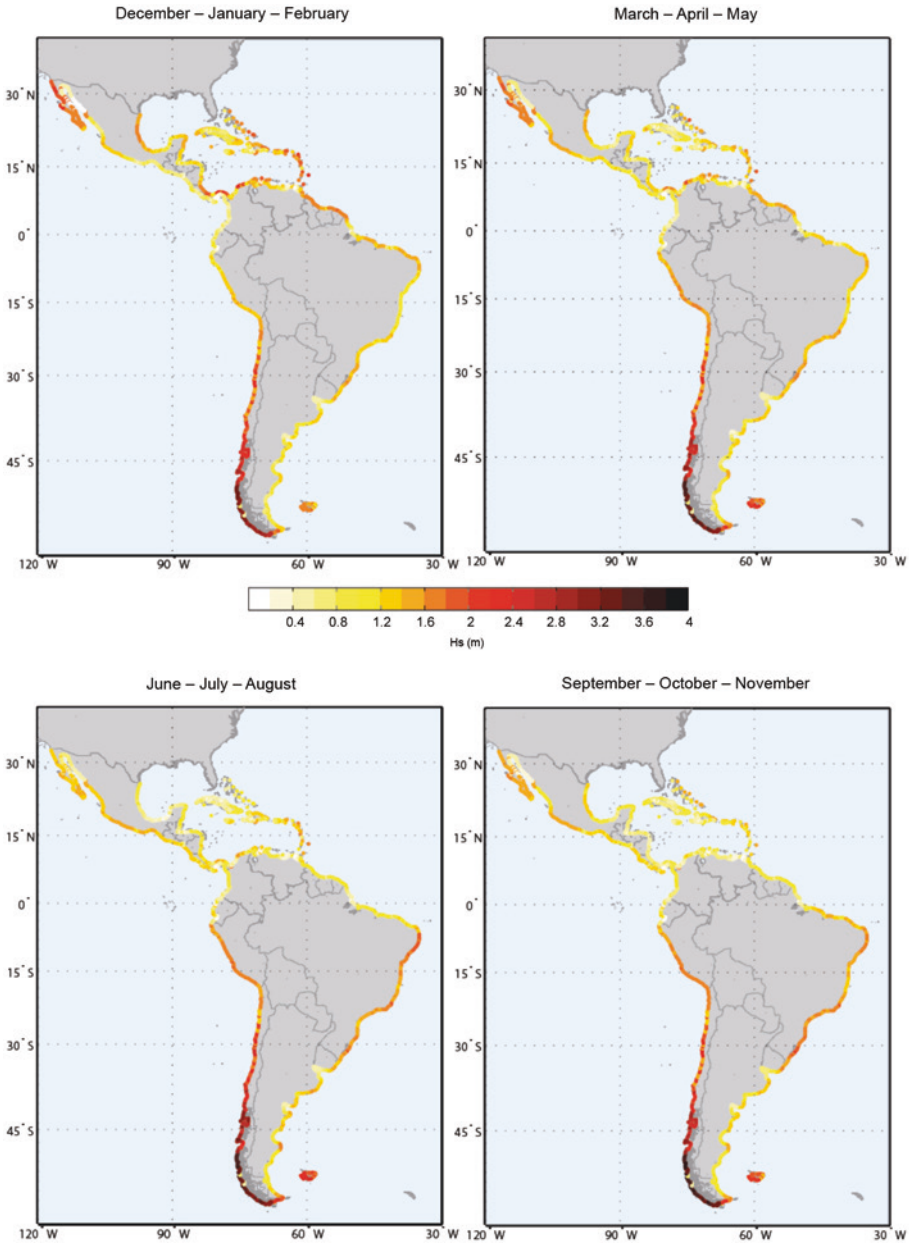

Source: Global Ocean Waves (GOW) reanalysis.

The greatest mean wave heights in the part of the Latin American and Caribbean region that is located in the northern hemisphere are found along the peninsula of Baja California, Mexico, where mean significant wave heights of around 2 m are recorded. The wave heights for the Caribbean islands are around 1 m in the Caribbean Sea itself and between 1.6 m and 2 m on the Atlantic side of the islands down to the border of Brazil, the northern part of the Gulf of Mexico and the northern shores of Costa Rica and Panama, which are exposed to larger waves generated in the Atlantic. Seasonal variations are quite sharp, with significant heights declining from about 2 m to 1 m in the summer. Seasonal peak heights of around 4.5 m are observed in the Gulf of Mexico in the winter.

In the southern hemisphere, there are clear differences between the Atlantic and Pacific coasts. Along the Atlantic coast, the monthly mean significant wave heights (Hs) hover around 1m except along the Brazilian coast, where they are about 2 m. Seasonal peaks along the southern coast of Brazil and the coast of Uruguay are approximately 3.5 m. Mean peak heights along the rest of the Atlantic coast are below 2.5 m. Peak values along the southern portion of the Pacific coast go from up to 8.5 m for southern Chile down to 5 m for northern Chile and around 3 m for Peru. Seasonal means are about 4 m for southern Chile and then gradually decline as one moves north, reaching values of approximately 1.8 m along the Peruvian coast. Seasonal variations in both peak and mean Hs are quite pronounced, with higher waves in June, July and August in the southern hemisphere and higher values in December, January and February in the northern hemisphere.

FIGURE 1.27
SEASONAL PEAK SIGNIFICANT WAVE HEIGHT
(Metres)

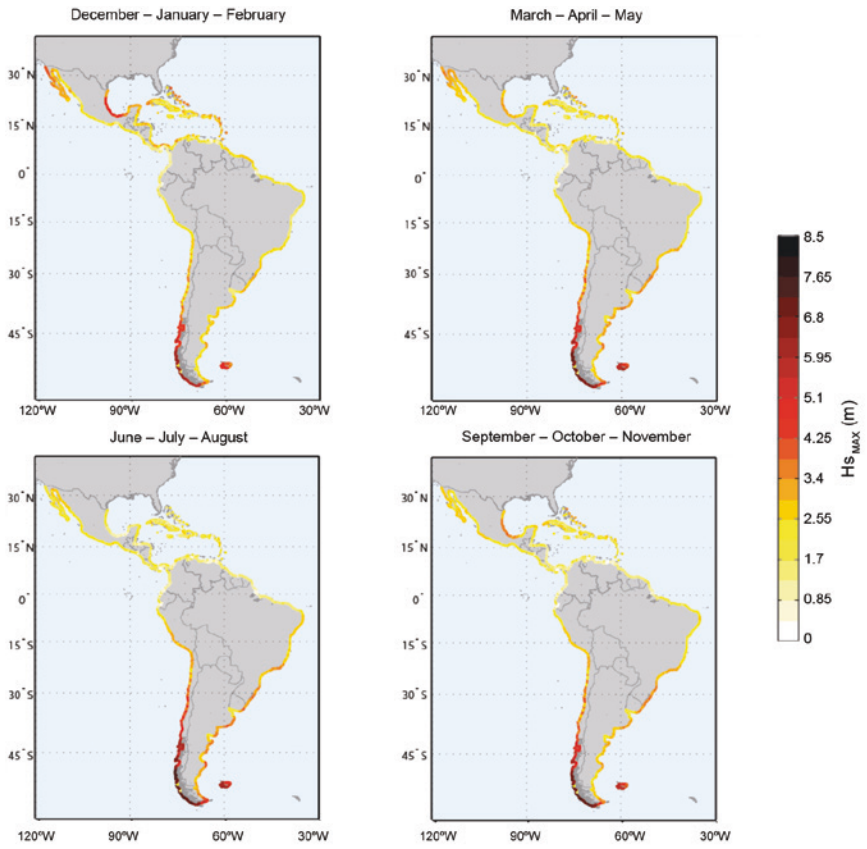

Source: Global Ocean Waves (GOW) reanalysis.

Figure 1.28 shows the predominant wave direction for each point along the coastline. The results indicate that waves generated in the Gulf of Mexico tend to move from north to south while those generated in the Caribbean Sea tend to move from east to west, which fits in with the wind patterns analysed earlier. As for the rest of the coastline, the waves generated in the low pressure areas in the South Pacific generally move in an eastward direction, while, in the northern hemisphere, waves originate in the North Atlantic.

FIGURE 1.28
MEAN WAVE DIRECTION
(Degrees north)

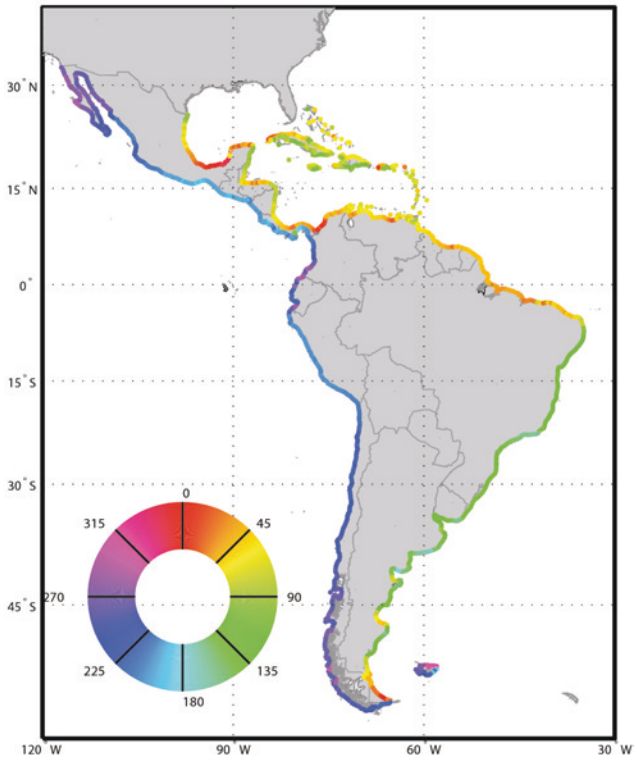

Source: Global Ocean Waves (GOW) reanalysis.

The mean significant wave height likely to be exceeded 12 hours per year exhibits the same spatial variability as the monthly peak heights, with the highest values being observed in the vicinity of Tierra de Fuego, since the swells generated in the South Pacific move through this area on their way to the South Atlantic. Hs_{12} values of from 4 m to 5 m are seen along both the Atlantic and Pacific coasts in the southern hemisphere. For other southern-hemisphere coasts, along with those of the Caribbean and Central America, the values are around 2 m to 2.5 m except in the Gulf of Mexico and along the peninsula of Baja California, where they are around 4 m to 5 m.

In the Gulf of San Matías, in Argentina, and the Plate River, the configuration of the coast is such that it is sheltered from incident waves, and conditions are therefore less severe than in the immediately surrounding areas.

FIGURE 1.29
MEAN SIGNIFICANT WAVE HEIGHT EXCEEDED 12 HOURS PER YEAR: 1948-2008
(Metres)

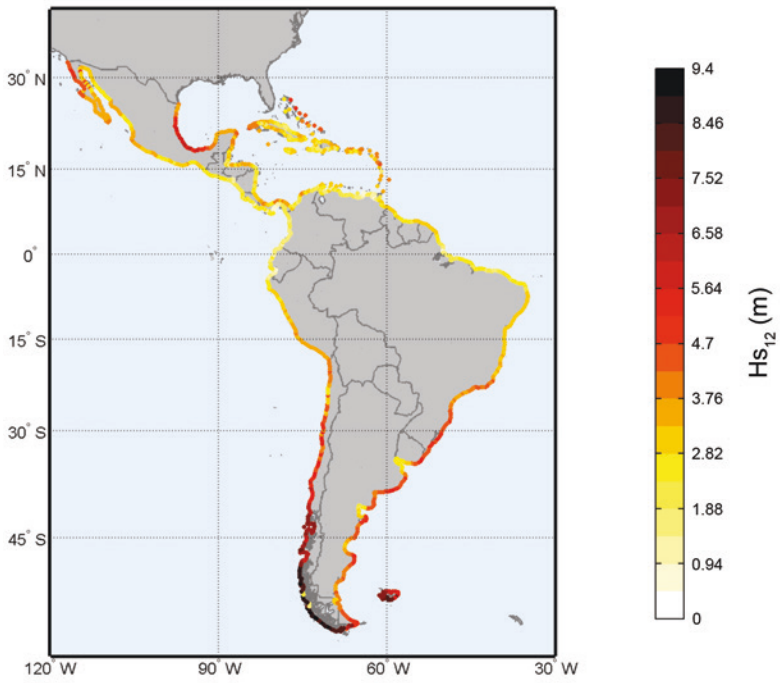

Source: Global Ocean Waves (GOW) reanalysis.

The extent of wave variability in the region is reflected in all the variables that were analysed. Given the limitations involved in depicting the results of the analysis on such a large spatial scale, it is not possible to provide a point-by-point description of the marine climate here, although an exhaustive definition of the offshore marine climate for each of the 1,132 points (at indeterminate depths) along the coasts of Latin America and the Caribbean has, in fact, been developed as part of this study. As an example, an analysis of four points along the region's coasts is presented below, together with the technical data on the marine climate at each of these points required for research and engineering applications. In addition, offshore wave conditions in the vicinity of the 100 most important ports in Latin America and the Caribbean (based on the port classification system developed by ECLAC) have been analysed, given the particular importance of having these kinds of data for these locations.

FIGURE 1.30
DESCRIPTION OF THE MARINE CLIMATE AT ONE LOCATION ON THE ARGENTINE COAST

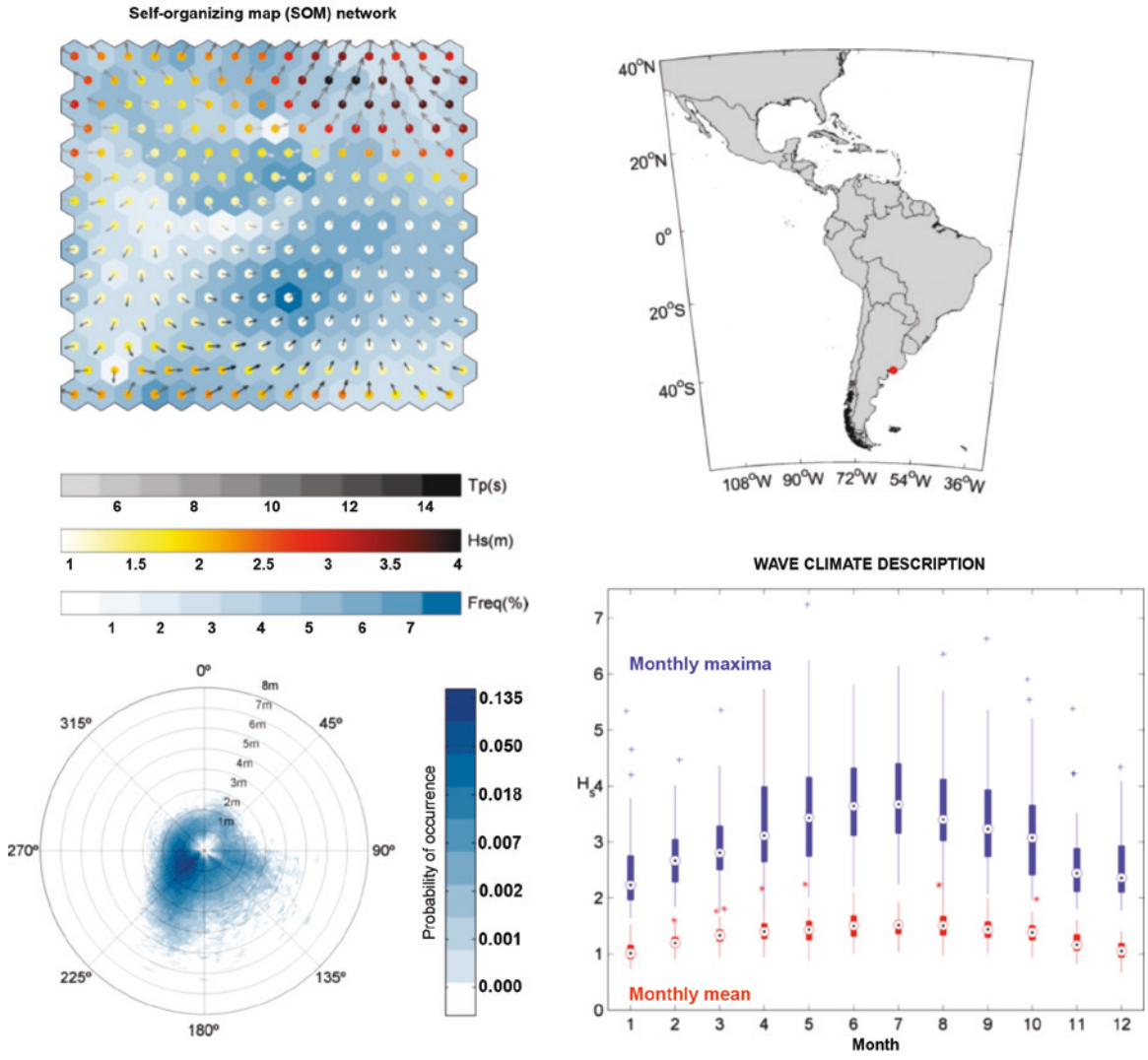

Source: Global Ocean Waves (GOW) reanalysis.
Note: Wave variables are mapped in a SOM network (upper left); the location in question is shown in the upper right quadrant; the wave rose is given in the lower left-hand graph; and the statistical distribution of the monthly mean and peak significant heights is shown in the lower right-hand graph.

FIGURE 1.31
DESCRIPTION OF THE MARINE CLIMATE AT ONE LOCATION ON THE CHILEAN COAST

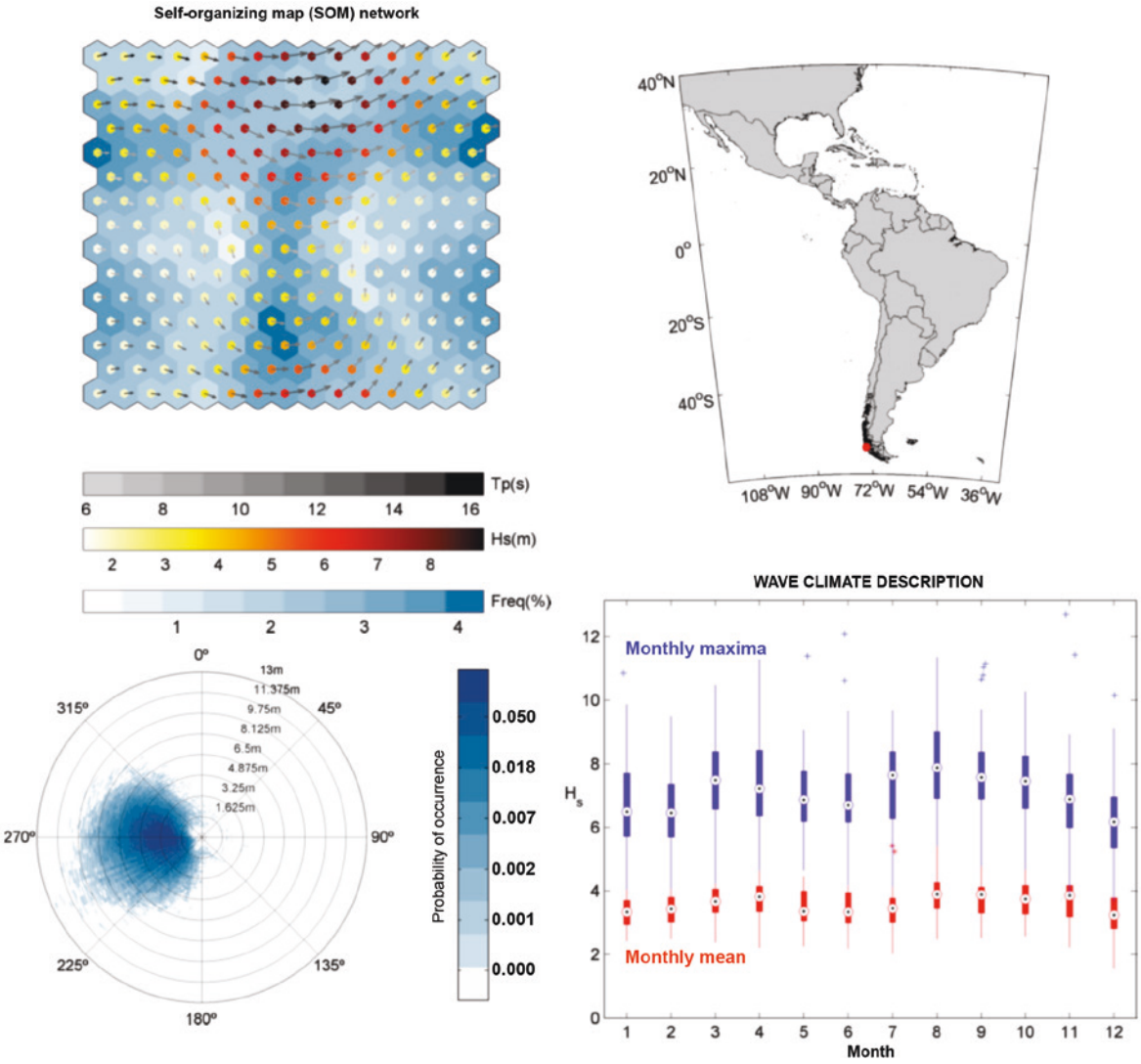

Source: Global Ocean Waves (GOW) reanalysis.
Note: Wave variables are mapped in a SOM network (upper left); the location in question is shown in the upper right quadrant; the wave rose is given in the lower left-hand graph; and the statistical distribution of the monthly mean and peak significant heights is shown in the lower right-hand graph.

FIGURE 1.32
DESCRIPTION OF THE MARINE CLIMATE AT ONE LOCATION ON THE PERUVIAN COAST

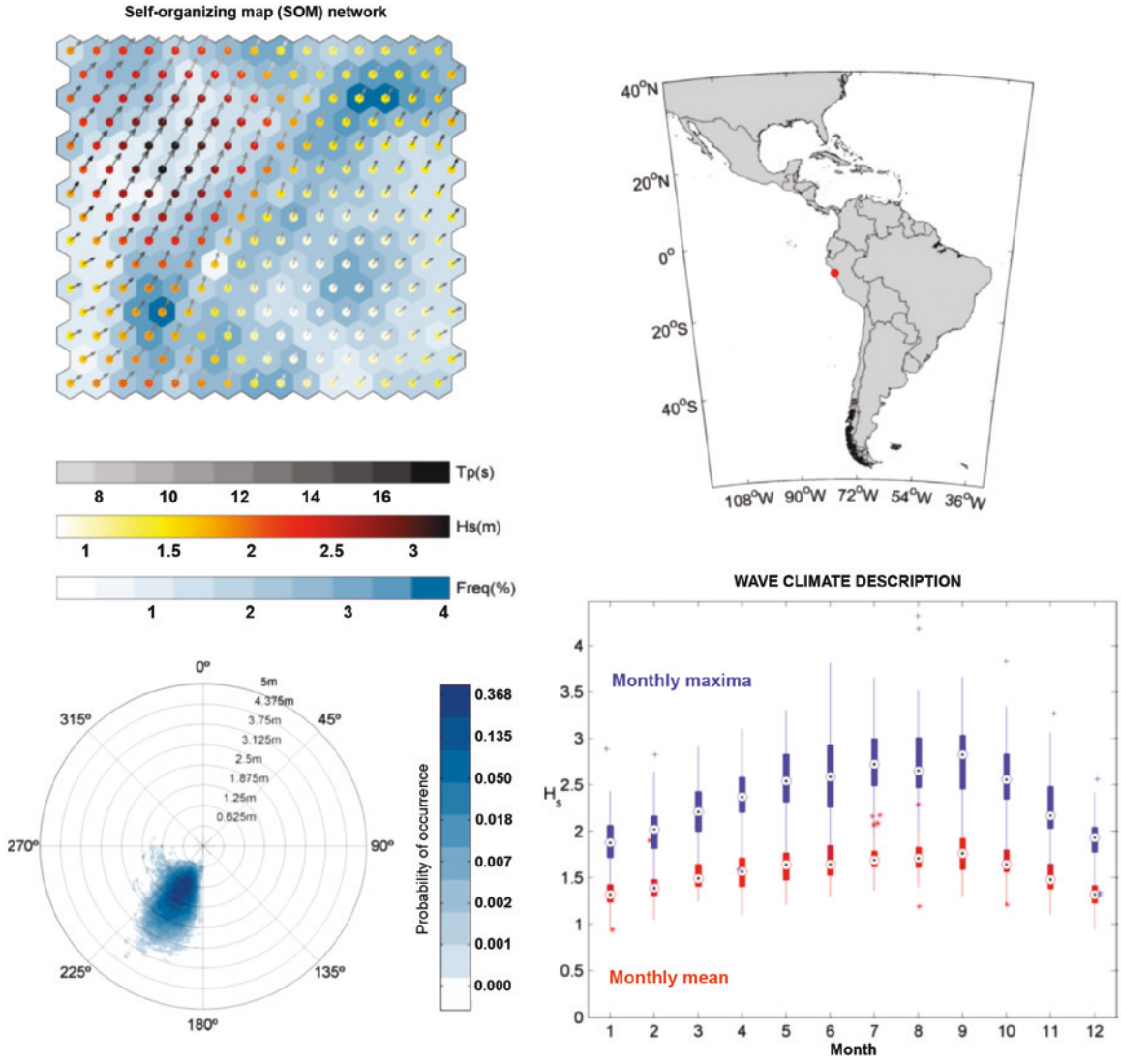

Source: Global Ocean Waves (GOW) reanalysis.
Note: Wave variables are mapped in a SOM network (upper left); the location in question is shown in the upper right quadrant; the wave rose is given in the lower left-hand graph; and the statistical distribution of the monthly mean and peak significant heights is shown in the lower right-hand graph.

FIGURE 1.33
DESCRIPTION OF THE MARINE CLIMATE AT ONE LOCATION ON THE MEXICAN COAST

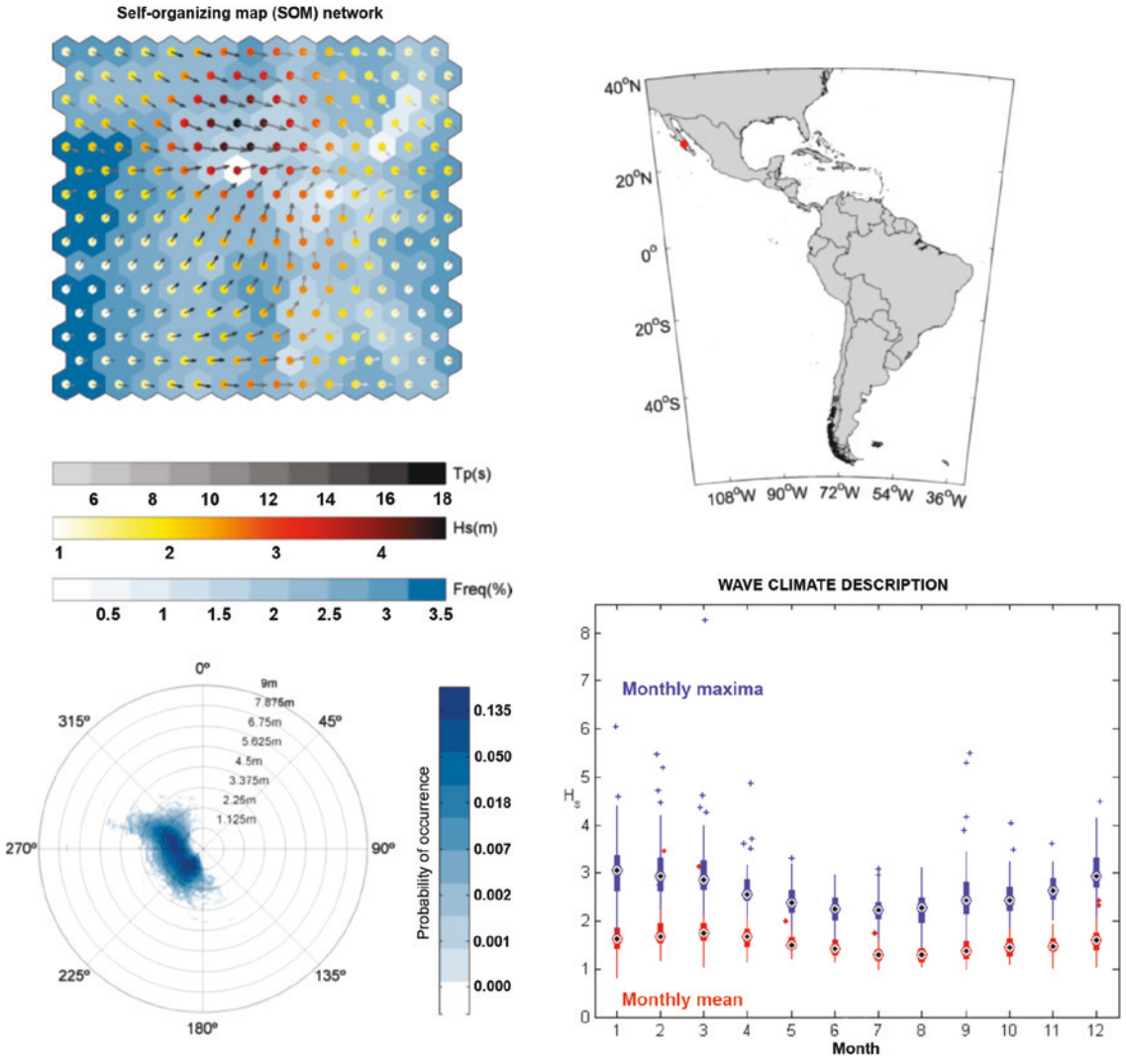

Source: Global Ocean Waves (GOW) reanalysis.
Note: Wave variables are mapped in a SOM network (upper left); the location in question is shown in the upper right quadrant; the wave rose is given in the lower left-hand graph; and the statistical distribution of the monthly mean and peak significant heights is shown in the lower right-hand graph.

The descriptions of the 1,132 offshore locations in Latin America and the Caribbean that are provided in these types of graphs are crucial inputs that add to the existing body of knowledge regarding wave patterns in the region. The results of this analysis provide data on statistical distribution (see the bar graph in the lower right-hand quadrant), the distribution of wave directions based on point of origin and intensity (see the wave rose graph in the lower left-hand quadrant), spatial and seasonal variability (right-hand map and box graphs) and the frequency of each representative sea state (SOM graph in the upper left-hand corner).

Given the usefulness of the descriptive information provided by these figures, it is important to understand how to analyse the SOM neural networks. To this end, the results for the location in Baja California given in the SOM grid in figure 1.33 will be disaggregated here.

In figure 1.34, the various patterns exhibited by the different wave variables at this same location are clear to see. The concentration of peak heights with periods of mean values is shown, as is the low representation frequency. There is a clearly bimodal pattern of wave direction, and this is also reflected in the wind rose shown in figure 1.33. It is also clear that smaller waves are more frequent than larger ones. The information provided in figure 1.34 is consolidated in the upper left-hand graph shown in 1.33.

FIGURE 1.34
REPRESENTATIVE SEA STATES IN A SOM NETWORK FOR ONE LOCATION IN MEXICO

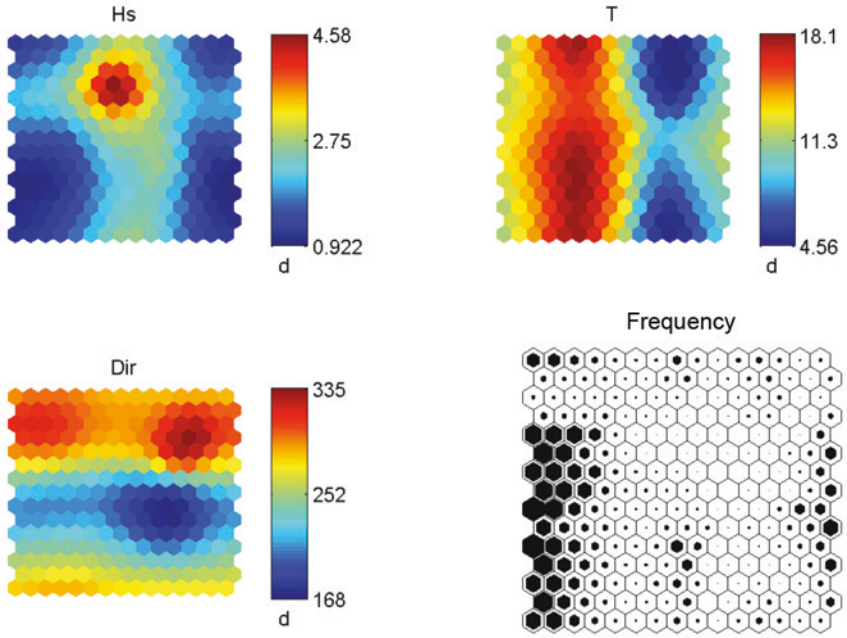

Source: Prepared by the authors.

3.2.2. Tides

The tides in Latin America and the Caribbean also exhibit a high degree of spatial variability. For purposes of analysis, the following data are provided: high tides (figure 1.35), the 0.9 quantile (figure 1.36) and the tide range (figure 1.37). The different areas in the region cover the entire spectrum, from macrotidal zones with tide ranges of over 10 m in southern Argentina to microtidal Caribbean islands where the range is less than 0.5 m.

FIGURE 1.35
HIGH TIDES: 1948-2008
(Metres)

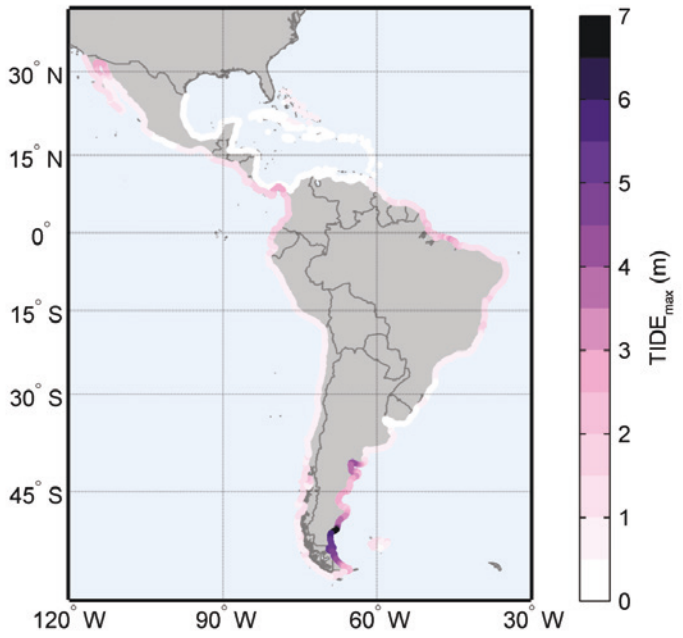

Source: Global Ocean Tides (GOT) analysis.

Two points should be made about these figures: first, there is a multiplier effect in the area of Río Negro in Argentina, where peak levels are over 5 m, relative to the rest of the nearby coastal areas, which have much lower values (around 3 m); second, there is a striking difference between the two coasts of Panama, with peaks remaining below 0.5 m along the Caribbean coast of that country but rising to around 3 m along the Pacific coast. Although this latter value is still not very high, the differential is a noteworthy feature of this territorial dividing line between two regions with radically different types of coastal dynamics.

FIGURE 1.36
0.9 TIDAL QUANTILE: 1948-2008
(Metres)

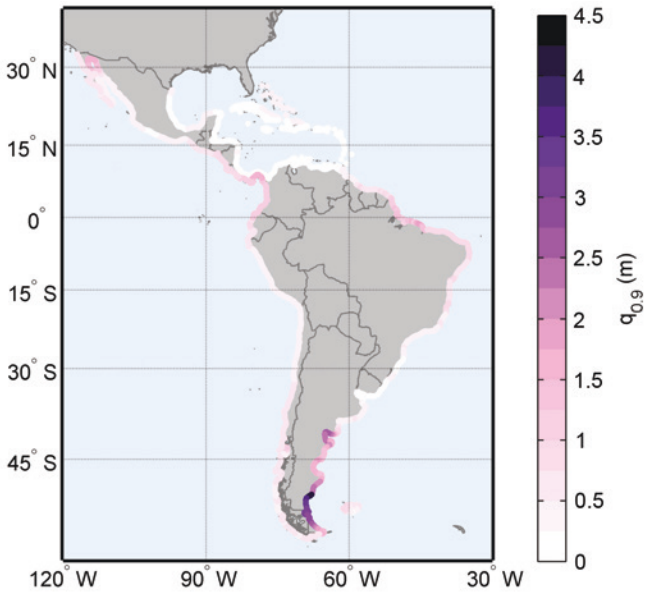

Source: Global Ocean Tides (GOT) analysis.

FIGURE 1.37
TIDE RANGE
(Metres)

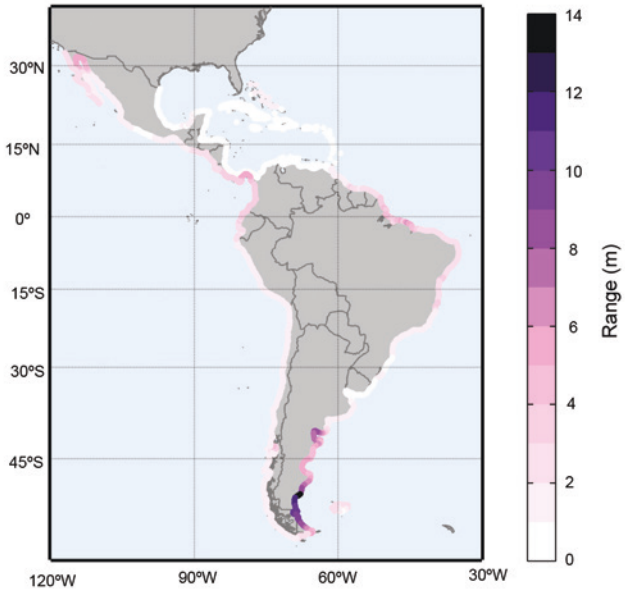

Source: Global Ocean Tides (GOT) analysis.

3.2.3. Storm surges

Numerical modelling of storm surges (Global Ocean Surges (GOS), IHC) depicts two clearly differentiated zones at both the 0.90 and 0.99 quantiles. The first of these areas has the highest values (above 1 m at the 0.99 quantile) along the entire coastline of Argentina, Uruguay and southern Brazil (vicinity of Porto Alegre). The peak values for this variable (up to 1.4 m for quantile 0.99) are recorded around the River Plate and are due to the configuration of the inlet. This is also the area in which the greatest tide ranges are seen, which means that the sea level varies even more in these coastal areas. In the rest of Latin America and the Caribbean, the values are below 0.2 m for quantile 0.99 except in the Gulf of California, where, because of its narrowness, storm surges reach approximately half a metre.

Annual seasonality for quantile 0.99 is analysed in figure 1.40. No significant changes are apparent apart from a slight increase in storm surges in the Gulf of México during the winter months. Seasonal changes do not show up in the areas with the highest surges (the coast near the mouth of the Paraná River), and the probability of values of over 1 m being recorded therefore remain constant.

FIGURE 1.38
MEAN 0.9 STORM SURGE QUANTILE: 1948-2008
(Metres)

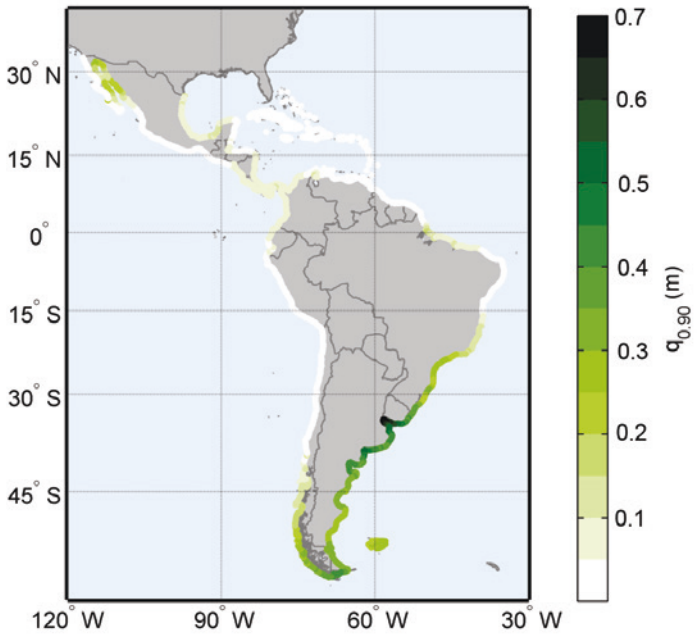

Source: Global Ocean Surge (GOS) analysis.

FIGURE 1.39
MEAN 0.99 STORM SURGE QUANTILE: 1948-2008
(Metres)

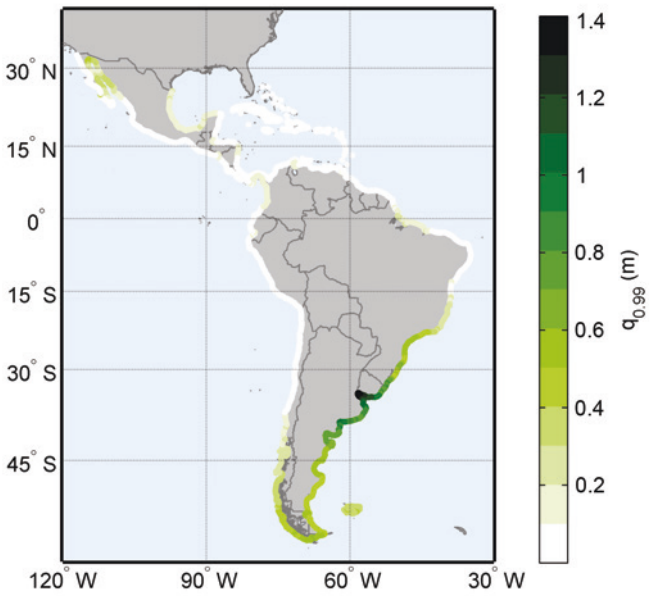

Source: Global Ocean Surge (GOS) analysis.

FIGURE 1.40
MONTHLY RANGE OF VARIATION IN STORM SURGES FOR QUANTILE 0.99 SINCE 1948
(Metres)

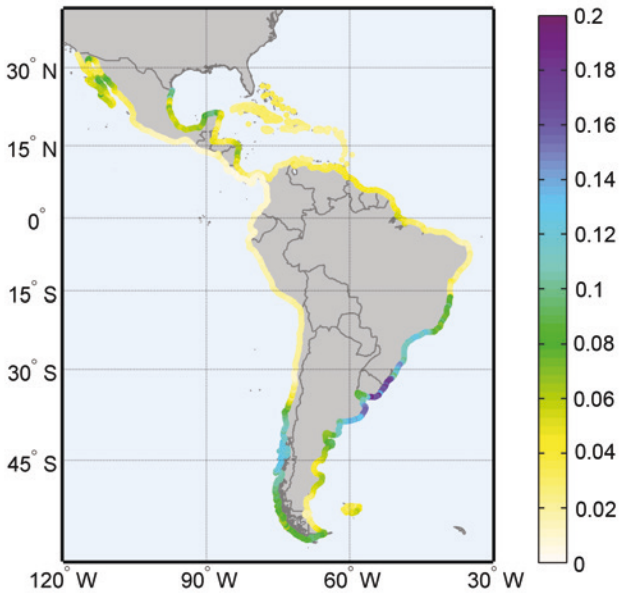

Source: Global Ocean Surge (GOS) analysis.
Note: The range runs from peak values minus the mean low values.

3.3. Extreme events

In view of the serious impacts of extreme events in the coastal areas of Latin America and the Caribbean, an analysis of the monthly peaks for significant wave heights and storm surges has been conducted in order to provide inputs for the design of maritime infrastructure. This analysis has been based on return periods of 50, 100, 250 and 500 years for both variables. For the sake of brevity, only the graphs for return periods of 50 and 500 years are shown here; the first return period represents observations for the period used in the modeled reanalysis (61 years), while the second corresponds to a standard parameter for maritime structures.

The Generalized Extreme Value (GEV) distributions for the two variables are given as the parameters. (For further information, see the references on extreme wave analysis.) This information is used to gauge the Weibull distribution if the parameter is negative, the Frechet distribution if it is positive and the Gumbel distribution if the parameter is equal to zero (see figure 1.41). Notice that a negative (Weibull) curve indicates that the extremes are bounded, whereas this is not the case with the other two distributions.

FIGURE 1.41
GENERALIZED EXTREME VALUE (GEV) DISTRIBUTIONS FOR THE DIFFERENT FORM PARAMETERS

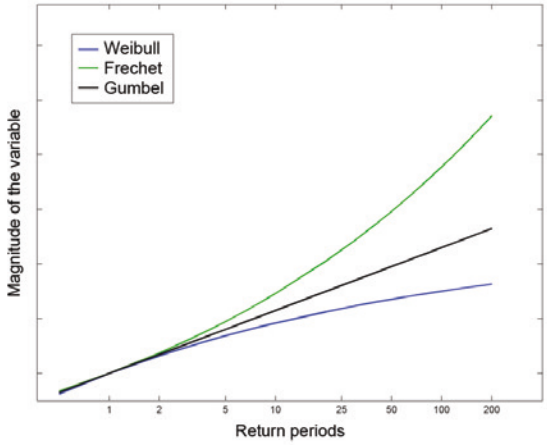

Source: Prepared by the authors.

3.3.1. Waves

As can be seen in figure 1.42 and figure 1.43, there is an enormous degree of variability in extremes, as has already been seen in the analysis of mean wave heights, monthly maximum wave heights and heights exceeded 12 hours per year (figure 1.29 and preceding figures). This spatial variability is noted for all return periods, although its scale varies across recurrence intervals (50, 100, 250 and 500 years). Thus, in the graph for a 50-year return period, the highest values (Hs above 13 m) are found in the part of South America that is exposed to South Pacific storms. High values (significant wave heights of around 10 m) are also found in the Gulf of Mexico. This is partially due to the effects of hurricanes, since, although they are not incorporated into the reanalysis of maximum wave values, they are nonetheless reflected in exceptional increases over the mean. It is noteworthy that the more sheltered areas, such as the Río Negro or River Plate, exhibit significantly lower values than those obtained for more exposed adjacent areas, as has also been seen to be the case for the results discussed in earlier sections. The

northern part of the peninsula of Baja California yields values of approximately 9 m for a mean return period of 50 years. Generally speaking, wave heights in the Caribbean Sea for a 50-year return period range from between 4 m and 5 m.

FIGURE 1.42
SIGNIFICANT WAVE HEIGHTS: 50-YEAR RETURN PERIODS BASED ON A 2010 TIME HORIZON (MEAN VALUES)
(Metres)

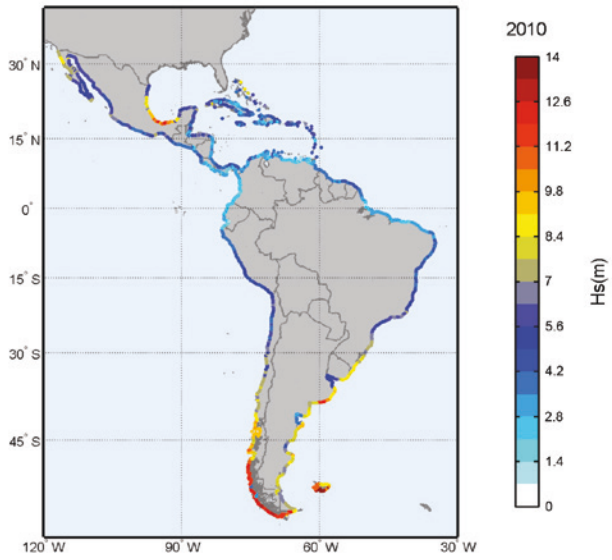

Source: Prepared by the authors.

FIGURE 1.43
SIGNIFICANT WAVE HEIGHTS: 500-YEAR RETURN PERIODS BASED ON A 2010 TIME HORIZON (MEAN VALUES)
(Metres)

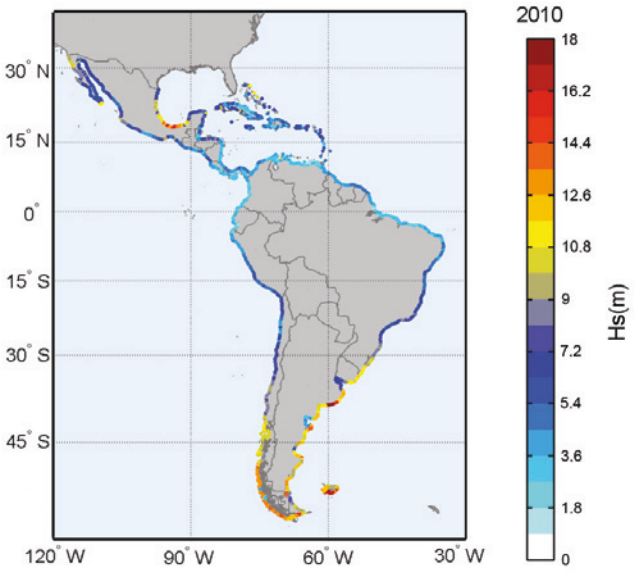

Source: Prepared by the authors.

An analysis of the parameter (see figure 1.44) used for this purpose indicates that the distribution of extreme wave heights is somewhat bounded (a Weibull distribution) everywhere except along the northern Pacific coast of Mexico and the coasts of Uruguay and Argentina, where it is more akin to a Frechet distribution. The magnitude of the parameters is generally, however, about 0.1 in both cases (negative and positive), which suggests that the fit curve is not large in any case.

FIGURE 1.44
FORM PARAMETER OBTAINED FOR EXTREME SIGNIFICANT WAVE HEIGHTS
(Adimensional)

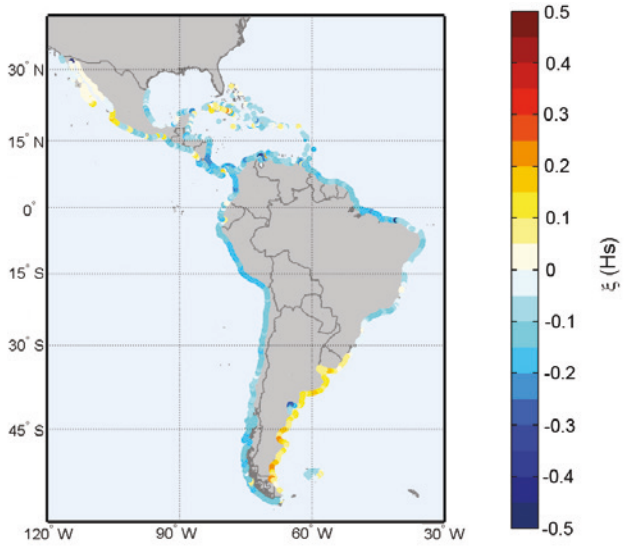

Source: Prepared by the authors.
Note: A positive value indicates that the distribution of extreme values corresponds to a Frechet distribution. A negative value signals a Weibull distribution. A Gumbel distribution is indicated if the parameter is equal to zero.

3.3.2. Storm surge

Along the same lines as the analysis of extreme wave events, an examination of extreme storm surge events has been conducted for a 50-year return period. As already discussed in section 2.2.3, there are two clearly differentiated zones in the region: the South Atlantic (below latitude 15ºS), and the rest of the region. In the first of these zones, a gradual change in values for a 50-year return period is seen within a range of from 1 m and 3 m, with peak values recorded for the area around the Rio de la Plata estuary. In the rest of the region, in contrast, the values for the same return period are under 0.5 m.

The form parameter for extreme storm surges is generally negative and hovers around a value of approximately -0.1, which means that extreme storm surge data for Latin America and the Caribbean exhibit a Weibull distribution in most cases, with the exceptions being along certain stretches of the coasts of Brazil, Peru, Colombia and Mexico, where positive values fit in more closely with a Frechet distribution. As in the case of wave activity, a high value for this parameter in entirely absent, which indicates that, whether it is bound or not, the fit curve is quite smooth in all cases.

FIGURE 1.45
STORM SURGE: 50-YEAR RETURN PERIODS AS OF 2010 (MEAN VALUES)
(Metres)

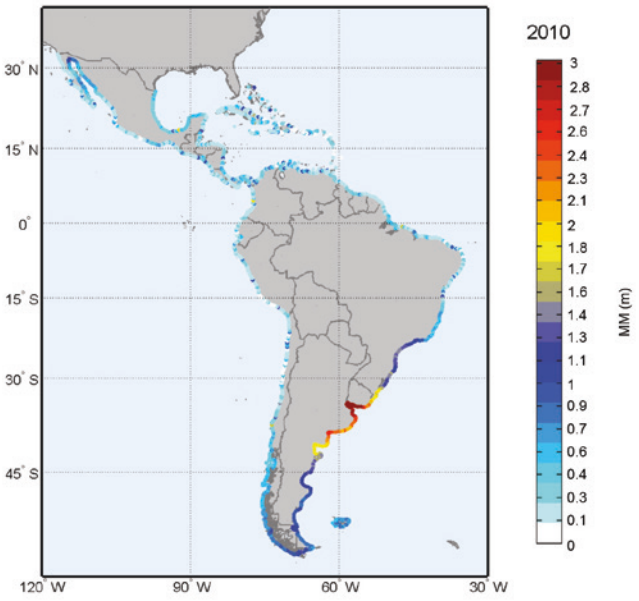

Source: Prepared by the authors.

FIGURE 1.46
FORM PARAMETER OBTAINED FOR EXTREME SIGNIFICANT WAVE HEIGHTS
(Adimensional)

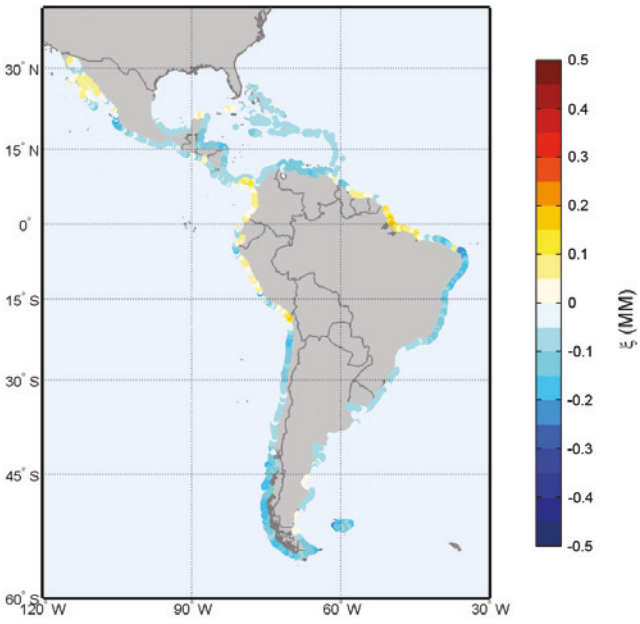

Source: Prepared by the authors.
Note: A positive value indicates that the distribution of extreme values corresponds to a Frechet distribution. A negative value signals a Weibull distribution. A Gumbel distribution is indicated if the parameter is equal to zero.

3.4. Hurricanes

Reanalyses (GOW and GOS, 1948-2008) generated using numerical models (WW3 and ROMS) that simulate the parameters associated with wave activity and variations in sea levels on the basis of atmospheric pressure and winds do not incorporate the extreme events associated with tropical storms or hurricanes because the resolution of the forcing (winds and pressure) derived from the NCEP/NCAR reanalysis is insufficient. This is depicted in figure 1.47 for the case of Hurricane Katrina (2005).

FIGURE 1.47
AIR PRESSURE AND WIND SERIES FOR FORCING USED IN THE WW3 MODEL (GOW DATABASE, TRIANGLES) AND DATA COMPILED USING THE NOAA-42001 BUOY (DOTS) ON HURRICANE KATRINA (2005)

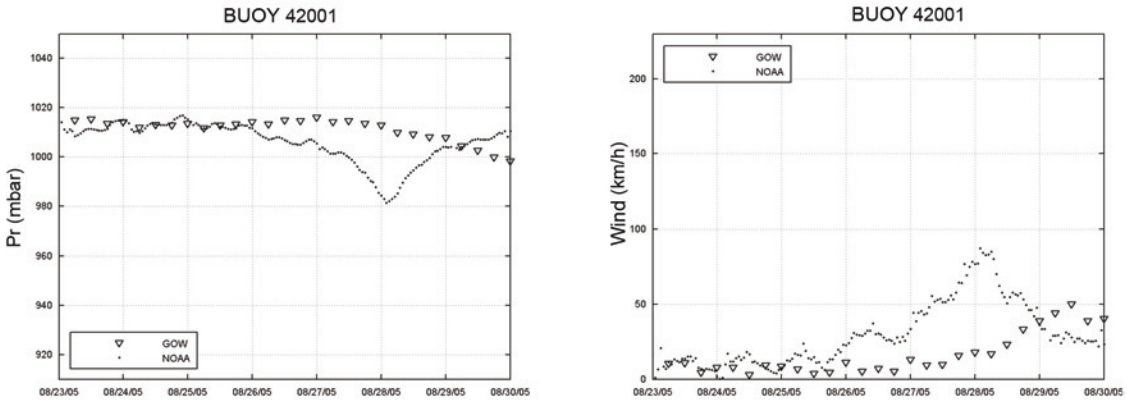

Source: Prepared by the authors.

In order to deal with this problem, air pressure and wind fields were generated using historical data on hurricanes and tropical storms based on analytical models that can be used to infer wave activity and sea levels during the 54-year period (1955-2008) for which hurricane data are available for the northern Atlantic, Caribbean, Gulf of Mexico and north-eastern Pacific (see figure 1.48). The results of this analysis are provided in annex 2, since this section is limited to describing current conditions rather than the long-term trends examined in the sections on other types of coastal dynamics.

The findings of the following analyses are detailed in annex 2:

—Evaluation and validation of **atmospheric pressure maps** of hurricanes.

—Evaluation and validation of **wind maps** of hurricanes.

—Evaluation and validation of wave maps (significant wave height *Hs* and peak period *Pp*) of hurricanes.

—Evaluation of **storm surge maps** of hurricanes.

—Development of **statistical maps** for the variables covered in the 54-year reanalysis period associated with hurricane events.

The results have been validated, on a hurricane by hurricane basis, using the data provided by various buoys in the study area (see figure 1.49).

FIGURE 1.48
POSITIONS AND INTENSITIES OF HURRICANES DURING A 54-YEAR PERIOD

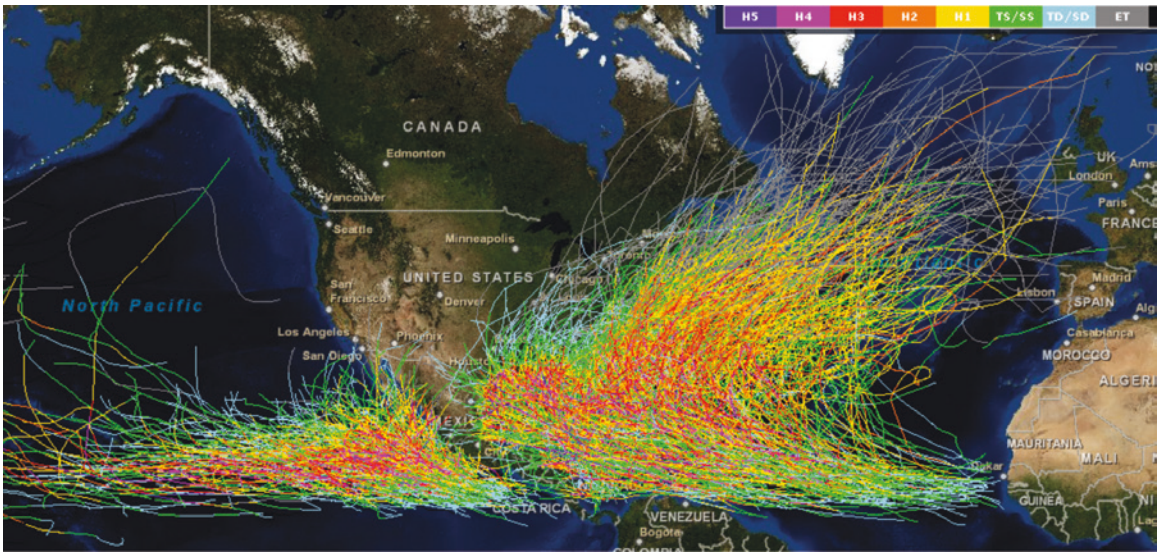

Source: Image from the National Hurricane Center, NOAA (http://www.csc.noaa.gov/beta/hurricanes/#app=2b16&3722-selectedIndex=0).

FIGURE 1.49
MAP OF THE POSITIONS AND NAMES OF THE NOAA NATIONAL DATA BUOY CENTER (NDBC) STATIONS

Source: Image from http://www.ndbc.noaa.gov/.

As can be seen from figure 1.50 and figure 1.51, the atmospheric pressure and wind fields generated using the parametric models fit the instrumental data quite well.

FIGURE 1.50

COMPARISON OF HOURLY ATMOSPHERIC PRESSURE SERIES FOR THE HURAC-HYDROMET-RANKIN VORTEX (1980) MODEL (BLUE DOTS), BUOY DATA (BLACK DOTS) AND THE NCEP/NCAR REANALYSIS (BLACK TRIANGLES) FOR HURRICANE KATRINA (2005) AT VARIOUS BUOY LOCATIONS, THE HURRICANE'S PATH AND THE SPATIAL MAP OF THE PRESSURE FIELD AT A GIVEN POINT IN TIME

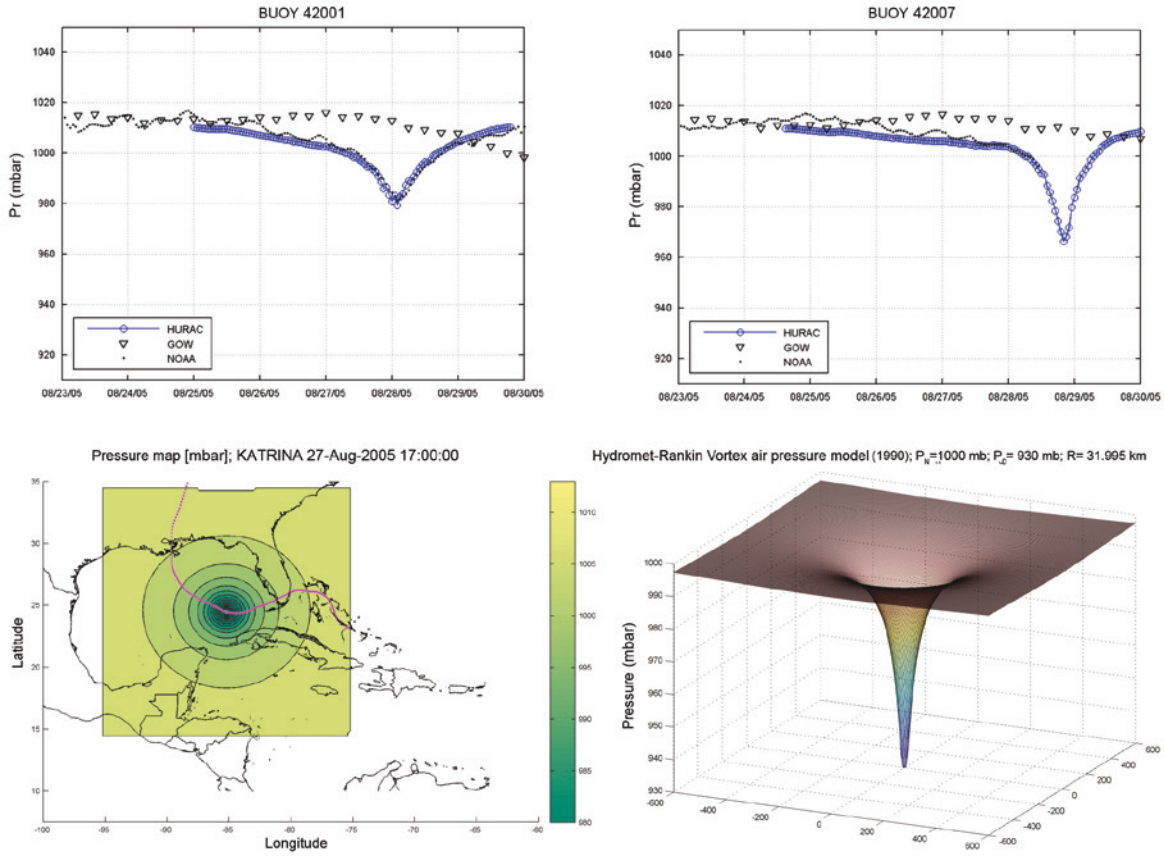

Source: Prepared by the authors.

FIGURE 1.51
COMPARISON OF HOURLY WIND SERIES FOR THE HURAC-BRETSCHNEIDER (1990) MODEL (BLUE DOTS), BUOY DATA (BLACK DOTS) AND THE NCEP/NCAR REANALYSIS (BLACK TRIANGLES) FOR HURRICANE KATRINA (2005) AT TWO BUOY LOCATIONS AND THE WIND FIELD AT A GIVEN POINT IN TIME

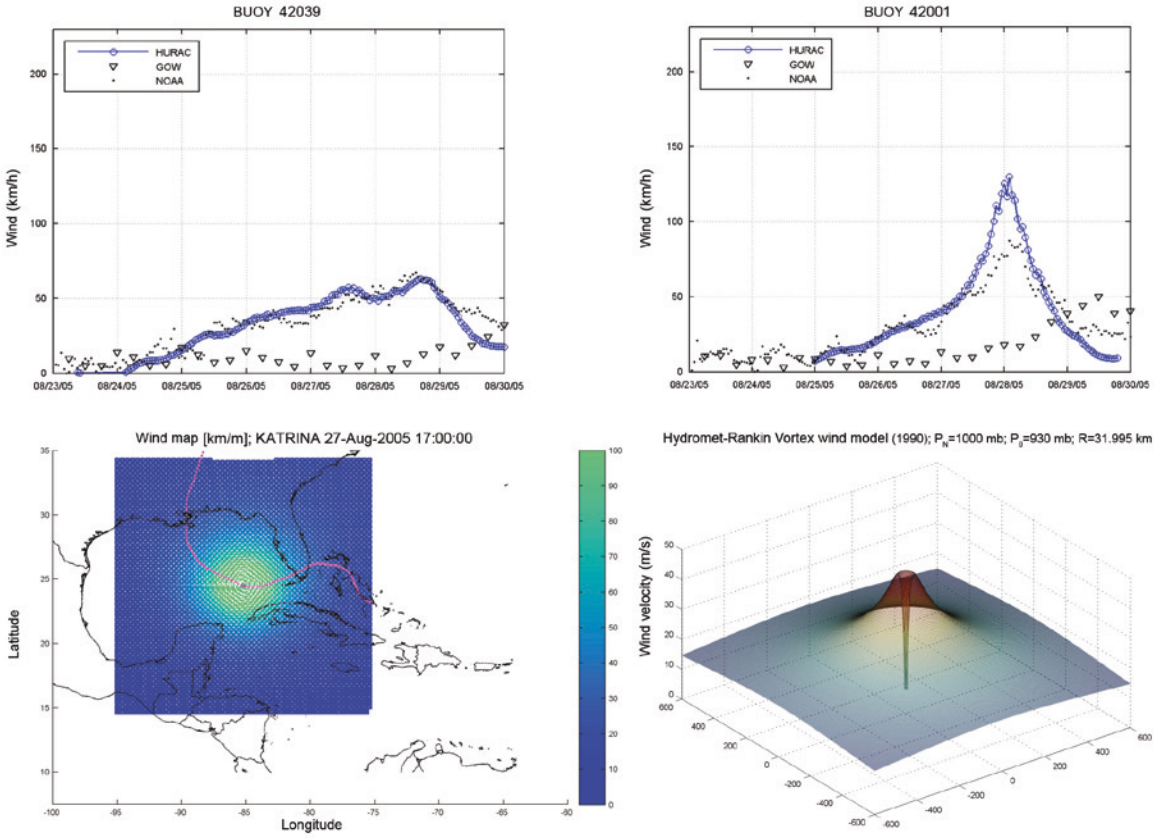

Source: Prepared by the authors.

Three different models were used to generate the wave fields. In the end, the modified Shore Protection Manual (SPM) model proved to provide the best fit with the instrumental data. Figure 1.52 shows the wave field generated by Hurricane Katrina at a given point in time according to that model.

Full information on the validation of the atmospheric pressure, wind, wave and storm surge data, together with the maps of the results for the coastal areas covered in this study, can be found in annex 2 (and are similar to those shown in 1.53 for maximum significant wave heights for the 54-year period for which hurricane data are available).

FIGURE 1.52
SIGNIFICANT WAVE HEIGHT MAP FOR HURRICANE KATRINA, MODIFIED SPM MAP (1984): 5 P.M. ON 27 AUGUST 2005
(Metres)

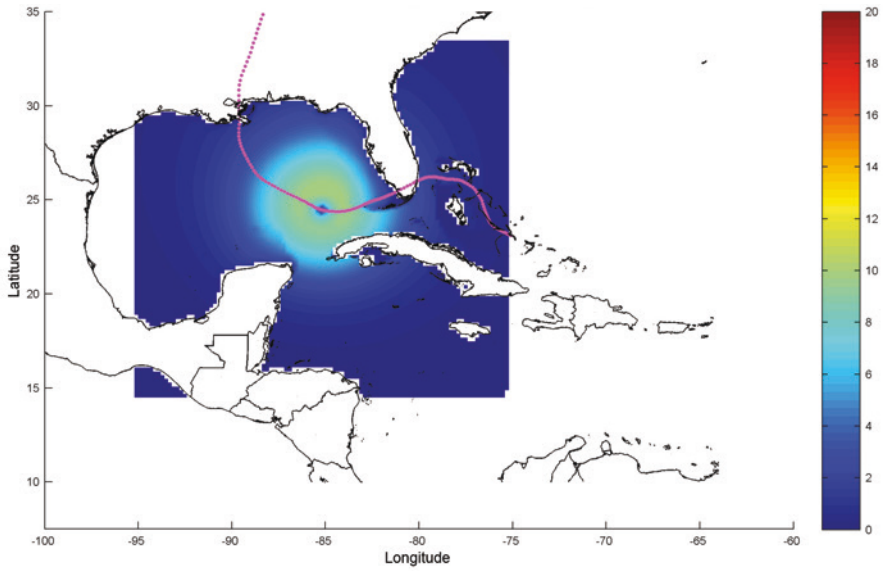

Source: Prepared by the authors.

FIGURE 1.53
MAP OF HISTORICAL MAXIMUMS (54 YEARS) FOR SIGNIFICANT WAVE HEIGHTS AT SPECIFIED CONTROL POINTS
(Metres)

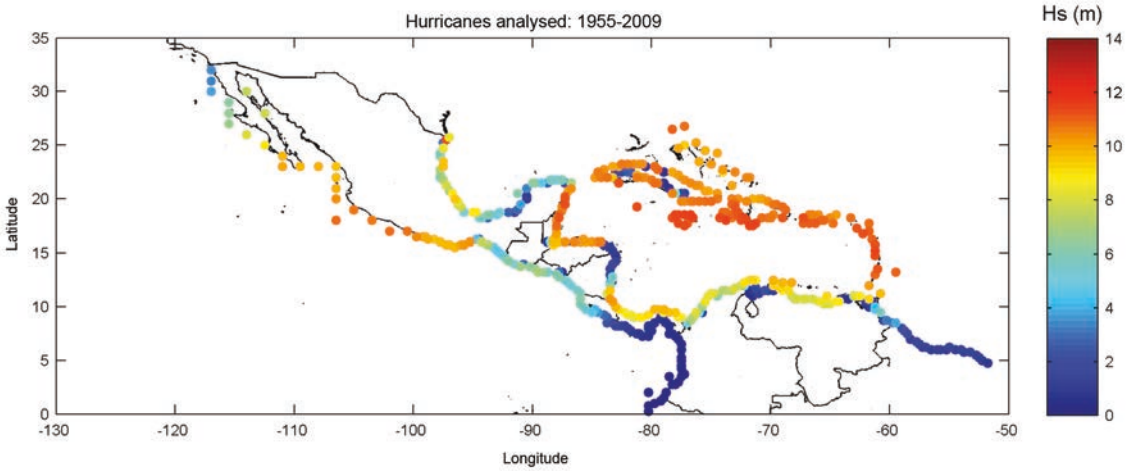

Source: Prepared by the authors.

3.5. Coastal dynamics in Latin America and the Caribbean: Conclusions

WAVES	• High degree of spatial variability associated with different latitudes and specific conditions in the Pacific Ocean, Atlantic Ocean, Caribbean Sea and the Gulf of Mexico. • Mean significant wave heights at different stations range from Hs = 0.5 m (Caribbean Sea and Ecuadorian coast) to Hs = 4 m (southern Chile). The mean seasonal maximum is as much as 8.5 m in the southern part of the continent. • Seasonal variations are much more marked in the northern hemisphere than in the southern hemisphere. • The most energetic sea states in the northern hemisphere are found in December, January and February (northern-hemisphere winter) and, in the southern hemisphere, in June, July and August (southern-hemisphere winter). • Southern Chile, with sea states amounting to more than Hs = 9, is the highest-energy zone. Other areas with Hs > 5 m include Baja California, the southern portion of the Gulf of Mexico, the Atlantic side of the Caribbean islands and some areas in southern Brazil and southern Argentina. • Mean wave direction is highly variable. The predominant direction is W-SW along the southern Pacific coast, W along Baja California, SE along the northern coast of Argentina, Uruguay and Brazil up to Recife, and NE along the northern coast of Brazil. • The sea states associated with hurricanes are covered in a supplementary annex. Peak values of around 10 m for most of the Caribbean islands have been recorded. • An analysis of extreme significant wave heights yields values of over 11 m (for a 500-year return period) for both coasts of South America and for the southern part of the Gulf of Mexico.
STORM SURGE	• The sea level rises generated by storm surges differ a great deal depending on the latitude of the location in question and on local phenomena, such as coastal areas' geometric configurations, that can amplify the surges and affect cyclone propagation speeds. • The strongest storm surges (over 1 m) have been recorded for the River Plate estuary owing to the breadth of the platform there and the funnel-shape of the estuary, which leads to higher water levels in that area during storm surges. • From latitude 45ºS down to Tierra del Fuego, the values (0.4 m) point to significant storm surges. Similar values have been recorded for southern Brazil. • The Gulf of Baja California is another site where water levels tend to rise, with increase of around 30 cm being registered. • Increases in sea levels of over 1 m in the Caribbean Sea caused by the propagation of hurricanes are covered in an annex. • Seasonal variations are quite small (differences up to 0.2 m between monthly means), which indicates that similar values and similar increases in sea levels will be found throughout the year. • A study of extreme storm surges yields values of around 3 m for the River Plate estuary for a 50-year return period.
TIDES	• There is a high degree of variability in the region, which includes micro-tidal, meso-tidal and macro-tidal zones. • The greatest tidal ranges (> 5m) are found along the southern coast of Argentina (Patagonian shelf). • This variable is a crucial element in evaluating the relative magnitude of the sea level rise in each area.
SURFACE WATER TEMPERATURE	• High degree of spatial variability associated with different latitudes, with values ranging from over 25ºC in Ecuador to under 10ºC in Tierra del Fuego. • Increased seasonality range at low latitudes.
MEAN SEA LEVEL	• The spatial pattern includes sharp regional variability. • The largest winter-summer variations in sea levels are seen between 30ºN and 30ºS. • The differentials between the monthly peaks and lows are fairly sizeable (up to 20 cm) in areas where this factor is of the same order of magnitude as tidal patterns (which are also influenced by weather patterns).
WIND	• The highest values are found in the Caribbean islands and along the Atlantic coast and the southern portion of South America. • Increased seasonality (monthly variability) is observed in the northern hemisphere. • Wind direction is generally onshore, except in Central America, where the trade winds blow from the north and north-east, and in Peru, where offshore winds predominate.

4. Methodologies for evaluating long-term trends

4.1. Methodologies for assessing or evaluating long-term variations

The scientific community has been making a determined effort in recent years to compile high-resolution time series on coastal dynamics and to run simulations using atmosphere-ocean climate models based on the IPCC scenarios. There are various ways to make use of these two types of information to assess coastal dynamics for a given time horizon throughout the twenty-first century (see figure 1.54).

A) Calculation of **long-term trends** and their extrapolation for selected time horizons: This approach is based on the assumption that the climate system is subject to an inertial constant and that emissions of greenhouse gases (GHGs) are also constant, which is clearly incorrect. The benefit offered by this approach is that it uses highly accurate long-term measured or computed data series. This is important because oceanographic experts now have the necessary scientific knowledge and databases on forcings in order to derive quantitatively reliable long (over 60 years), continuous time series on wave patterns and sea levels. The numerical modelling of these variables yields highly accurate results, which is not the case for variables such as precipitation.

B) Development of a **regression model based on time series** for which the predictor is a regional or global pattern (e.g., mean monthly SST) and the predictand is the agent of interest (statistical data on wave height, sea level, etc.). Using this type of statistical model, the values of the predictand can be calculated for the various IPCC scenarios, in which the values of the predictors are known.

C) Configuration of **climate scenarios for each time horizon** based on climate model simulations. The advantage of this approach is that it allows the GHG concentrations for each scenario to be factored in. The basic shortcoming of these climate models is the high inherent degree of uncertainty attendant on the calculated forcings for a highly non-linear system such as the atmosphere-ocean system and the inherent shortcomings of numerical models. The response to this situation has been the adoption of a mixed (multi-modal) system of analysis for use with the scientific community's existing models as a means of smoothing out the errors.

FIGURE 1.54
APPROACHES FOR CALCULATING AGENT DISTRIBUTIONS

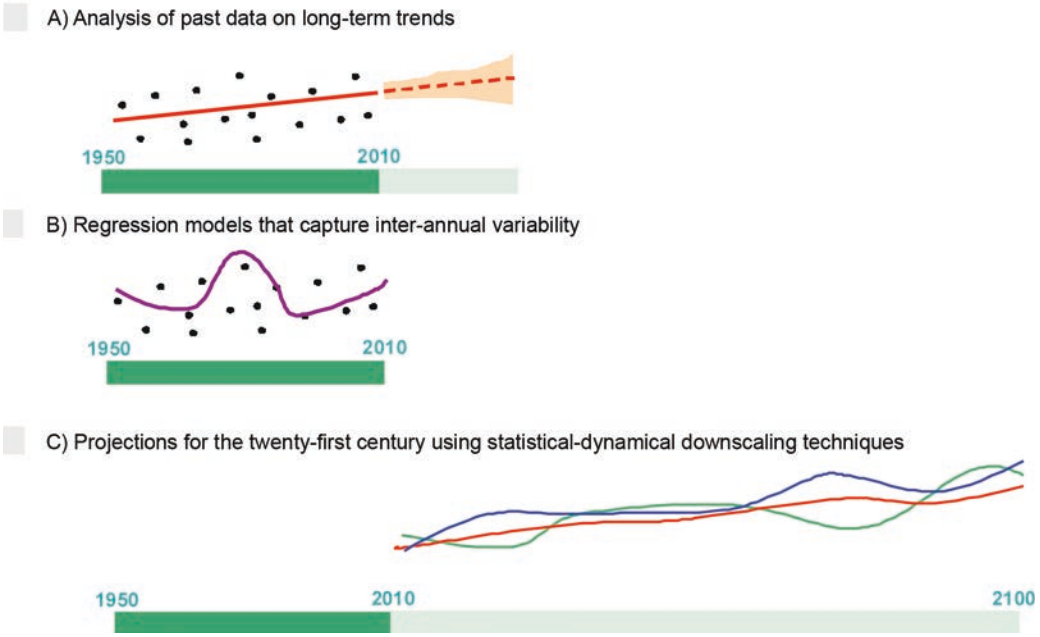

Source: Prepared by the authors.

A debate is currently going on in the scientific community about the validity of comparing the results of climate model simulations with recent trends in such variables as mean global sea levels or mean temperatures. This study has relied primarily on (A) the extrapolation of trends based on rigorous statistical models that incorporate long-term variations for each agent as well as an uncertainty factor, and (B) regression models that correlate the relevant agent with various climate indices (see figure 1.55).

FIGURE 1.55
TEMPORAL DIMENSION AND METHODOLOGIES FOR EACH TIME HORIZON

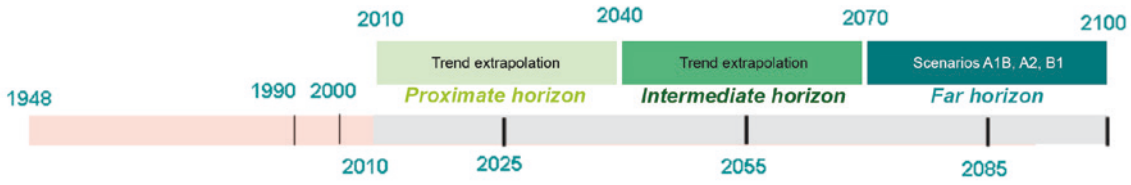

Source: Prepared by the authors.

The generally accepted view, however, is that reanalyses provide an optimum means of accurately interpolating data in terms of both time and space and of deriving dynamically consistent parameters, which makes them a suitable means of computing long-term trends. The NCEP/NCAR reanalysis is regularly updated and is therefore the best database for use in studying long-term changes and variations in the climate (Weisse and von Storch, 2010).

4.2. Techniques for the analysis of long-term trends

There are two main types of methods for deriving long-term trends from time series. One approach is to run a regression on each time series for the geophysical variable in question at each spatial location. The other is to hunt for a space-time pattern for the variable.

Traditionally, long-term trends have been calculated by making local adjustments (to the time series for a specific point) using regression models. This is the approach used in this study to obtain long-term trends for each point for the relevant variables.

This method suffers from some shortcomings, however, that make it unsuitable for working with some of the coastal variables of interest. First, the local regression model only adjusts the data temporally, which means that information on the spatial distribution of the geophysical variable is not included in the trend calculations. Second, any covariable that could influence the regression model, such as, for example, the effect of the ENSO phenomenon on sea level rise (SLR), should be taken into account a priori, since otherwise it will be reflected in the trend adjustment instead of being isolated from it. In addition, in the case of variables for which the rate of change is accelerating (or decelerating), such as sea level rise or temperature, the local regression (without subsequent processing) will not yield consistent results across the various points, and the trends are therefore not credible (the curve of the adjustments is too sharp).

In recent decades, the scientific community has devoted a huge amount of effort to extracting patterns from large gridded datasets. As explained by Hannachi (2007), various methods have been developed to find patterns of variability in the highly multi-dimensional climate system. The main objectives of these methods are twofold:

a) To reduce the dimensionality of the system by retaining a much smaller set of dominant patterns (Hannachi and O'Neill, 2001);

b) To obtain a few prominent representative patterns that are physically relevant (Wallace and Thompson, 2002).

Among these methods, empirical orthogonal functions (EOFs) have been the most widely used, but other variants have also been employed. However, EOFs are not specifically designed for trend detection, but rather for the identification of spatial patterns across time. The EOF technique can be used to find linear combinations of the different variables of a gridded spatio-temporal field that maximizes variance, subject to orthogonality constraints. The linear combinations that are thus obtained are the (uncorrelated) principal components (PCs), and the spatial (orthogonal) EOF patterns are the loadings of the PCs. Further information on the EOF method can be found in Kutzbach (1967), Preisendorfer (1988), Wilks (1995), von Storch and Zwiers (1999) and Jolliffe (2002).

Hannachi (2007) developed a variant of the traditional EOF technique that is specifically designed to detect long-term trends in spatio-temporal data fields by including the concept of **monotonicity.** The solution is obtained by means of a prior transformation of the data that provides a measure of monotonicity in the EOF analysis.

The method is based on an analysis of the eigenvalues of the covariance matrix, in much the same way as is done using the traditional EOF method, but in this case the positions in time of the data points are sorted and the data are placed in that order, rather than leaving them in their original positions. This reordering of the data is what generates their monotonicity. Maximizing the variance of a linear combination of time positions is equivalent to maximizing their monotonicity, and this makes it possible to extract the long-term trend that is hidden in the signal. One obvious benefit of this technique is that it makes it possible for inter-annual phenomena (e.g., those associated with weather variability, such as the ENSO phenomenon, the Atlantic Multidecadal Oscillation (AMO), etc.) to be isolated from the trend (see the section in this study on the analysis of weather variability in the area).

This method has been used successfully by Barbosa and Andersen (2009) to extract trend patterns in global sea surface temperatures (SST). In this study, the calculations for this variable using the Trend-EOF technique have yielded similar results to those obtained by the above-mentioned authors.

Long-term trends in dynamics and impacts have been analysed using this technique. Since the trajectories of the variables differ, some of them exhibit linear trends while the trends in others may be accelerating or decelerating. In order to address this issue, the method is used to look at a linear adjustment and a quadratic adjustment, and then the more statistically significant of the two is selected. For example, sea level rise fits a second-order quadratic model better, which indicates that the trend is accelerating, whereas the trends for wave heights have fit a linear variation more closely in recent decades.

Using both point-to-point (local) trends and those yielded by the Trend-EOF technique, long-term trends can be derived from the available time series. The statistical approach chosen for this purpose offers the added advantage of making it possible to assess the degree of uncertainty associated with the estimate so that, for each given year, a density function (see figure 1.56.) can be obtained for which the confidence interval increases as one moves along the time horizon (the x axis in the figure).

FIGURE 1.56
LONG-TERM STATISTICAL TREND

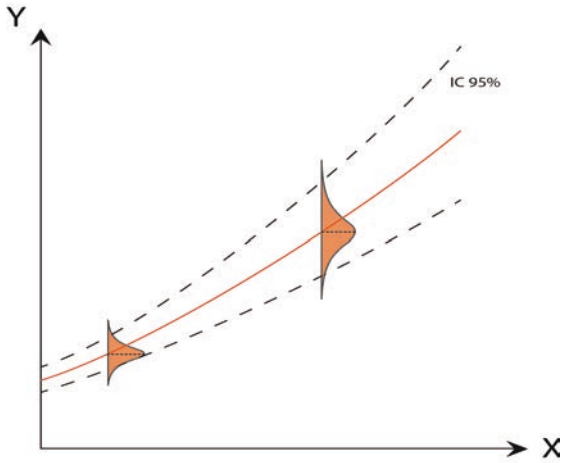

Source: Prepared by the authors.

This makes it possible to arrive at an expected value for a variable for a given year by calculating the estimated mean value based on the trend. It is also possible to obtain the probability that the variable will be greater than, or less than, a given value y_u, or even to estimate the value of the variable associated with a given probability that it will be exceeded, for example. In figure 1.57, the area shown in blue corresponds to the probability of exceeding the threshold value y_u of the random variable Y at the instant X.

FIGURE 1.57
LONG-TERM STATISTICAL TREND: PROBABILITY OF EXCEEDING A GIVEN THRESHOLD

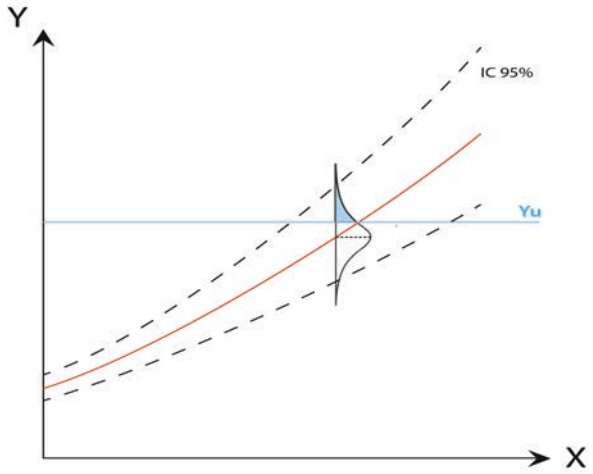

Source: Prepared by the authors.

To conclude: the method used for the calculations is mapped out in figure 1.58. Variables on three different time scales are analysed: annual series (e.g., Hs_{12}), monthly series (monthly mean Hs) and hourly series (hourly Hs). For the hourly series, the trend is analysed on the basis of monthly means, but the hourly level of resolution is taken into account in calculating the associated levels of probability and uncertainty. The original variable is deseasonalized to separate out the monthly means (for non-annual variables) and the mean is subtracted, thereby converting them into anomaly series, while introducing weights for the latitude effect in the case of Trend-EOF trends where necessary. The linear and quadratic trends for the anomaly series are analysed in order to determine which is more statistically significant (see figure 1.59). The Trend-EOF technique proves to be more suitable for working with gridded global variables for which the effects of inter-annual variability may alter the local regression. Once the long-term values for the variable have been determined for the time horizons that have been defined (2040, 2050 and 2070) and for the periods 2010-2040 and 2040-2070, the probability that a given value for the variable or anomaly, as appropriate, will be exceeded can be ascertained. The confidence intervals for these results can then be easily derived using a scale such as the one developed by IPCC.

FIGURE 1.58
CALCULATION OF TRENDS USING THE TREND-EOFS TECHNIQUE

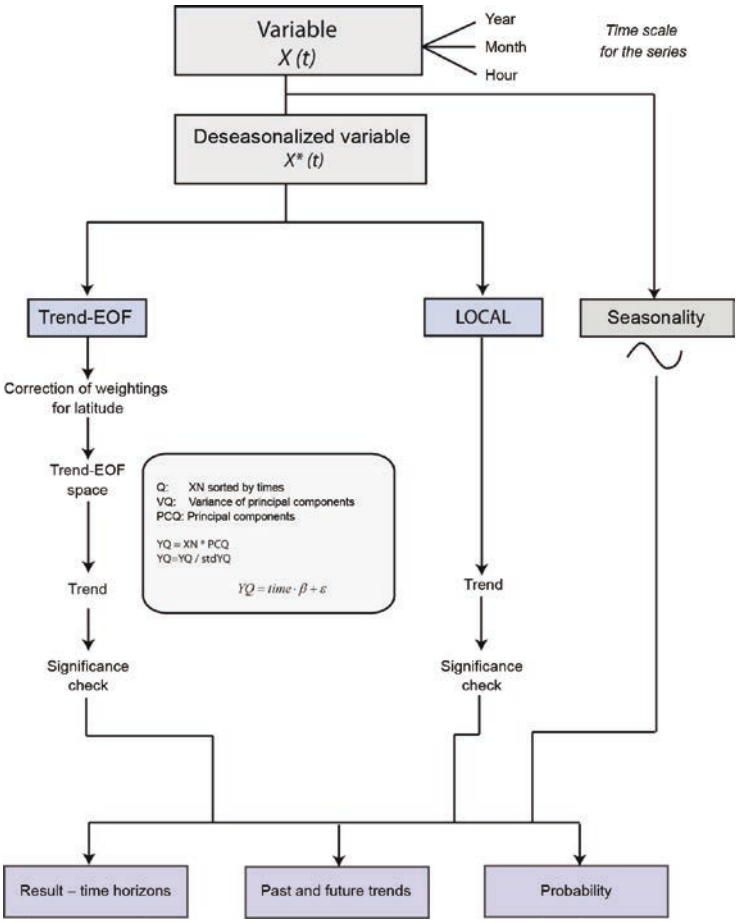

Source: Prepared by the authors.

FIGURE 1.59
STATISTICAL SIGNIFICANCE CHECK FOR TREND CALCULATIONS

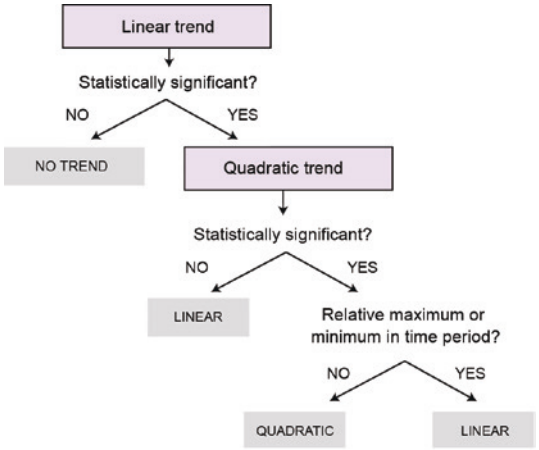

Source: Prepared by the authors.

In terms of the modification of a long-term variable, if an agent or variable *X* is defined on the basis of its probability density function *f(x)* in the first year of the defined period (shown in light green in figure 1.60.), deriving the distribution of that agent in the horizon year makes it possible to obtain the changes in the mean (upper panel) or in the dispersion (lower panel) or in both. These changes in the agents imply a change in the risk term associated with a change in a given impact in coastal areas, which may be represented, for example, by a variation in the probability that the random *X* variable will exhibit a given value.

FIGURE 1.60
CHANGES IN THE MEAN (UPPER PANEL) AND DISPERSION (LOWER PANEL) OF THE DENSITY FUNCTION OF AGENT X

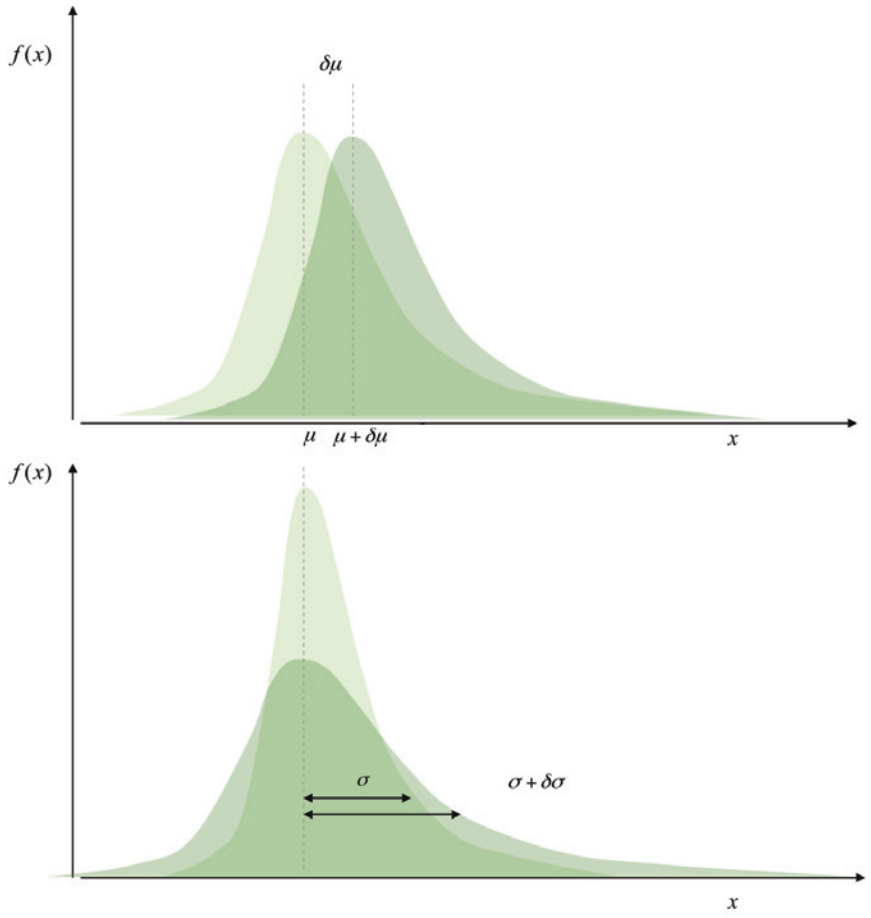

Source: Prepared by the authors.

This study will focus primarily on changes in the mean of agents' statistical distributions, since simulations using auto-regressive moving average (ARMA) models have verified that the statistical distribution does not vary significantly in the various quantiles. To demonstrate this, figure 1.61 depicts ARMA simulations of mean monthly significant wave heights which show that variations are primarily seen in the means, not the distribution.

FIGURE 1.61
ARMA SIMULATIONS OF DENSITY DISTRIBUTIONS OVER THE NEXT 35 YEARS

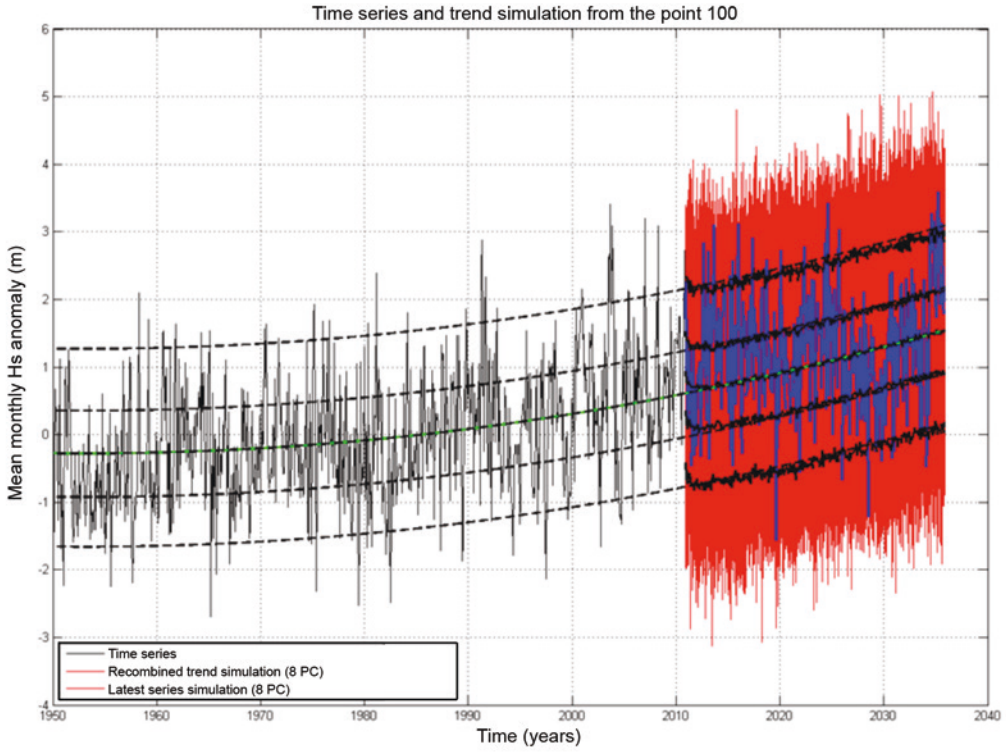

Source: Prepared by the authors.

The statistical models of extreme values encompass variations both in the means and in variance. For example, modelling of non-stationary extremes represents both temporal variations in the location parameter (mean) and in scale (variance) (see Méndez *et al.,* 2006, and Menéndez *et al.,* 2008).

The usual practise when working with statistical trend models is to assume that what varies is the mean, not the variance. Although heteroskedastic regression (variable variance) models are used today for working with trends in mean variables, in this study a homoscedastic (constant variance) has been used so that it will be possible to identify consistent spatial patterns of variation.

4.3. Approximation techniques for measuring the variation in one variable as a function of the variation in another

Variations in agents induce changes (impacts) in coastal areas. Nowadays, there are numerous coastal engineering approaches for projecting impacts on the various morphological units (beaches, estuaries, sand dunes, maritime structures, etc.) associated with the values registered for the various agents (wave dynamics and sea levels). This wide range of features of coastal morphology and terrain have to be taken into account when analysing the impacts of climate change in coastal zones.

Once the distribution of a variable has been ascertained for the starting year (2010) and a given horizon year (2040, 2050, 2070), the effects associated with climate change can be assessed. Changes in the variables of coastal dynamics (sea level, temperature, wave activity, etc.) trigger certain impacts, and those impacts (which are analysed in the third volume of the project documents) bear a functional relationship to dynamic variables (agents in terms of risk theory) or variable derived from them. There are possible approaches to assessing long-term changes in a variable (the dependent variable) as a function of variations in independent variables.

The first option is to obtain a time series for the variable y (here, coastal impacts) in relation to other variables x_i on the basis of a functional relation $y=f(x_i)$ such that the trends in the variable can be analysed using the methodology discussed above (see figure 1.58).

An alternative approach is, in simplified terms, to determine the variations in the dependent variable y and, as a function of the variations in the independent variables x_i, discounting the non-linear terms. This approach is known as the "disturbance method" because it involves "disturbing" the $y=f(x_i)$ equation in order to obtain variations of y, i.e., dy as a function of small variations in the variables x_i, dx_i.

By way of example, consider the impact in terms of beach erosion (volume of beach eroded by unit of length, defined by the random variable Y), which will depend entirely on the intensity of wave action, defined by the random variable X. Thus, there is a function, $y=f(x)$, that relates the value of the intensity of wave action *'x'* to the volume of sand that is eroded, *'y'*. The question is then: How much does the volume of sand *'y'* change as a function of changes in the intensity of wave action *'x'*? In order to answer that question, reference needs to be made to disturbance theory, which approximates the value of the function close to a given point $f(x+\delta x)$ as the sum of the value of the function at point *'x'* and the value derived from the function at point *'x'* multiplied by the variation in the value of the independent variable δx. This approach is valid only, however, if the disturbance in the independent variable is small. Otherwise, the use of the disturbance method may yield manifestly incorrect results (see figure 1.62).

FIGURE 1.62
DIAGRAM OF THE DISTURBANCE METHOD PROCEDURE

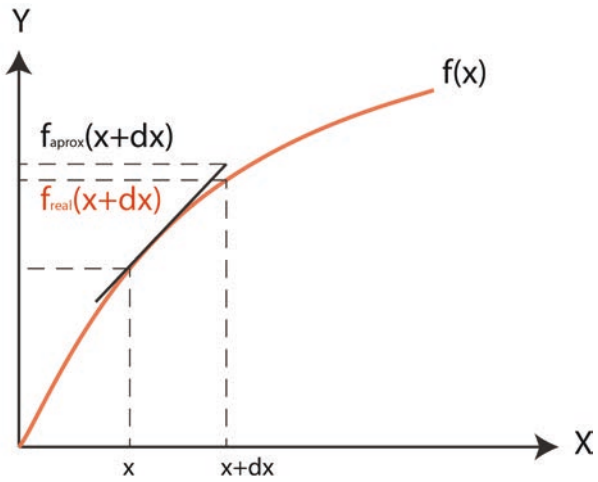

Source: Prepared by the authors.

Viewed in terms of the probabilistic method used in this study, the application of this approach is tantamount to determining the shift in the probability density function *(pdf)* of the *'y'* variable brought about by a change in the *'x'* variable (see figure 1.63.) without transforming the distribution of the *'y'* variable, since in these equations only linear relationships are considered.

Consequently, when applying this technique, it will be assumed that changes occur gradually.

This approach is a straightforward alternative to the analysis of long-term trends when it is not possible or feasible to calculate them by other means.

FIGURE 1.63
REPRESENTATION OF THE PROBABILISTIC METHOD FOR DETERMINING THE DISTRIBUTION OF A VARIABLE IN A TREND ANALYSIS

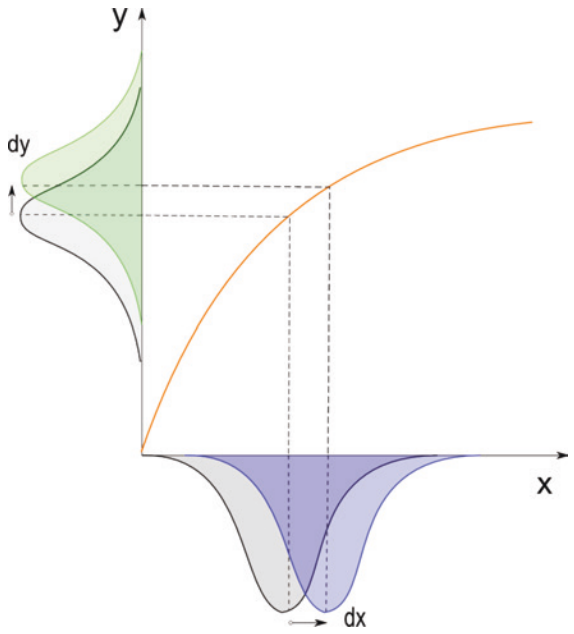

Source: Prepared by the authors.

The supplementary project document on the theoretically derived effects of climate change provides an exhaustive description of the impacts of climate change on each component of coastal areas (beaches, estuaries, dunes and coastal structures) that are associated with the different agents and the different manifestations of the relationships between current dynamics, changes in them and variations in the derived impacts.

5. Trends in coastal dynamics in Latin America and the Caribbean

5.1. Current state of knowledge about change in the Latin American and Caribbean region

The copious body of evidence gathered by the scientific community in recent years leaves no doubt about the fact that climate change is indeed happening (IPCC 2007). Figure 1.64 and figure 1.65 depict the simulations conducted using circulation models for trends that reflect both natural forcings and anthropogenic influences, all of which show that humankind is already having an observable effect on the planet's climate.

There is also evidence that sea levels have been rising gradually during the twentieth century and that they are now rising at a faster pace following a period of relative stability stretching from 0 AD to 1900 AD. Sea levels are expected to rise even further in the twenty-first century. The two main causes are thermal expansion (steric sea level rise) and the melting of the polar ice caps (IPCC, 2007).

Two core documents that provide background information on the current state of knowledge about climate change in the region are:

a) *Cambio climático y desarrollo en América Latina y el Caribe: una reseña* (ECLAC, 2009).

b) The IPCC summaries of the outputs of Working Groups Nos. 1, 2 and 3 (2007).

This study seeks to contribute to the literature on climate change in the region by computing long-term trends for all aspects of coastal dynamics covered in this analysis.

FIGURE 1.64
CLIMATOLOGICAL MODELLING OF CHANGES IN TEMPERATURE

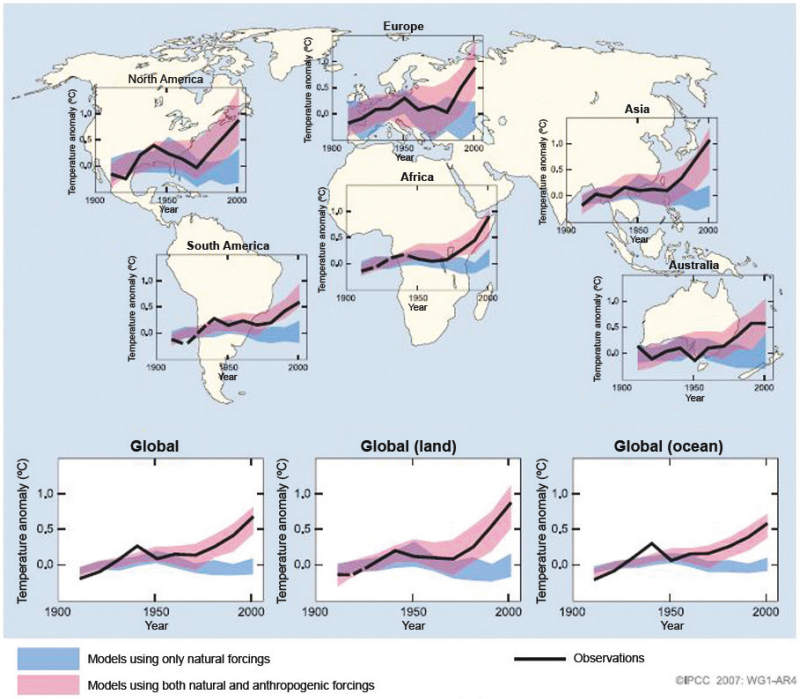

Source: IPCC, 2007.

FIGURE 1.65
OBSERVED AND SIMULATED TRENDS, BY WORLD REGIONS, OF LAND SURFACE TEMPERATURE ANOMALIES

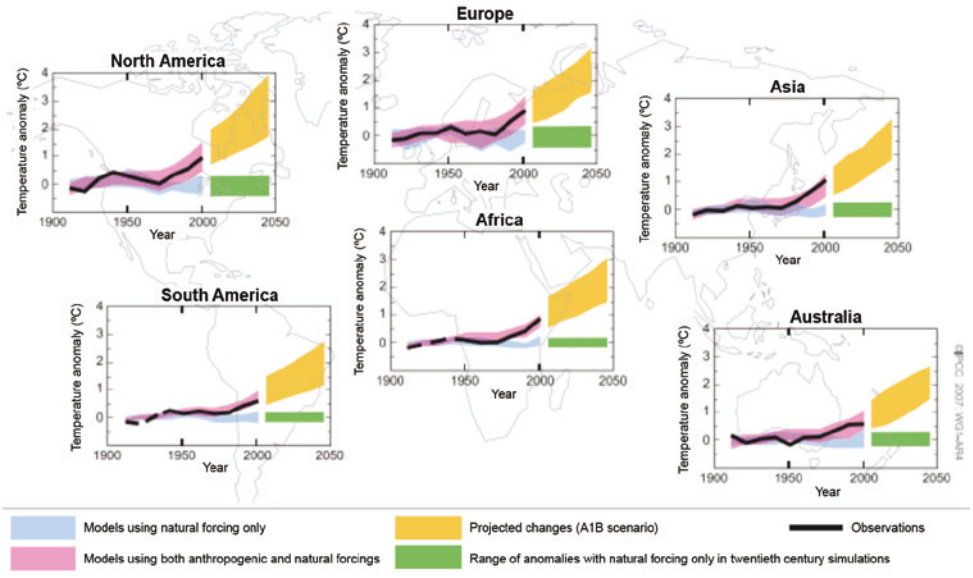

Source: IPCC, 2007.

5.2. Trends in meteo-oceanographic dynamics

5.2.1. Trends in mean sea levels (SLR)

Sea levels have been studied at the global level using both of the techniques discussed in earlier sections (Trend-EOF, or T-EOF, and local trends). Given the influence on this variable exerted by inter-annual phenomena (see the section on weather variability in Latin America and the Caribbean), the T-EOF approach appears to be more suitable in this case. In any event, the results for global patterns in the mean trends (mean variation coefficient) calculated using both of these methods at the global and regional scales are provided below. Figure 1.66 shows how the global mean has been reconstructed using the first component of the T-EOFs (which captures the global trend pattern) and the time values of the global mean from the database. The results, as may be seen, reflect a very good fit.

FIGURE 1.66
TREND AND RECONSTRUCTION FOR GLOBAL MEAN SEA LEVELS

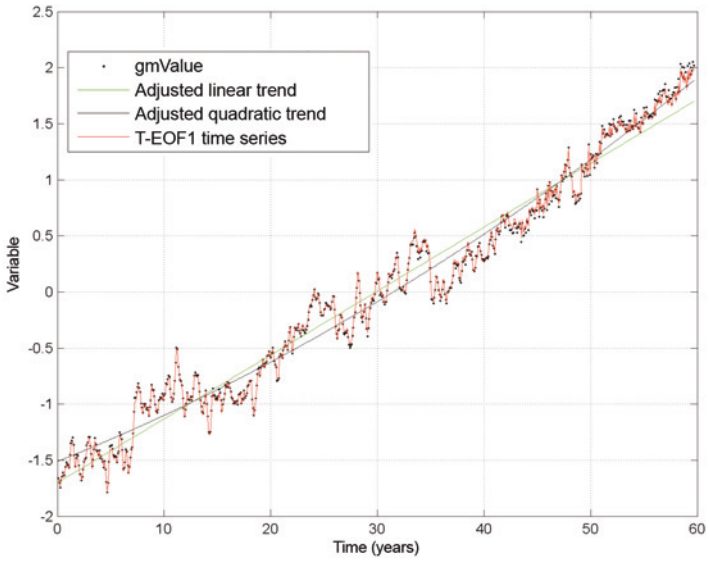

Source: Prepared by the authors.
Note: The time series for the first mode of the T-EOF is shown in red. The black (non-coincident) points represent the global mean level according to the instrumental database. The adjusted linear and quadratic trends are shown in green and black, respectively.

FIGURE 1.67
SPATIAL PATTERN OF THE MEAN (LINEAR) TREND FOR SEA LEVELS GLOBALLY AND FOR LATIN AMERICA AND THE CARIBBEAN BASED ON LOCAL TREND ADJUSTMENTS
(Mm/year)

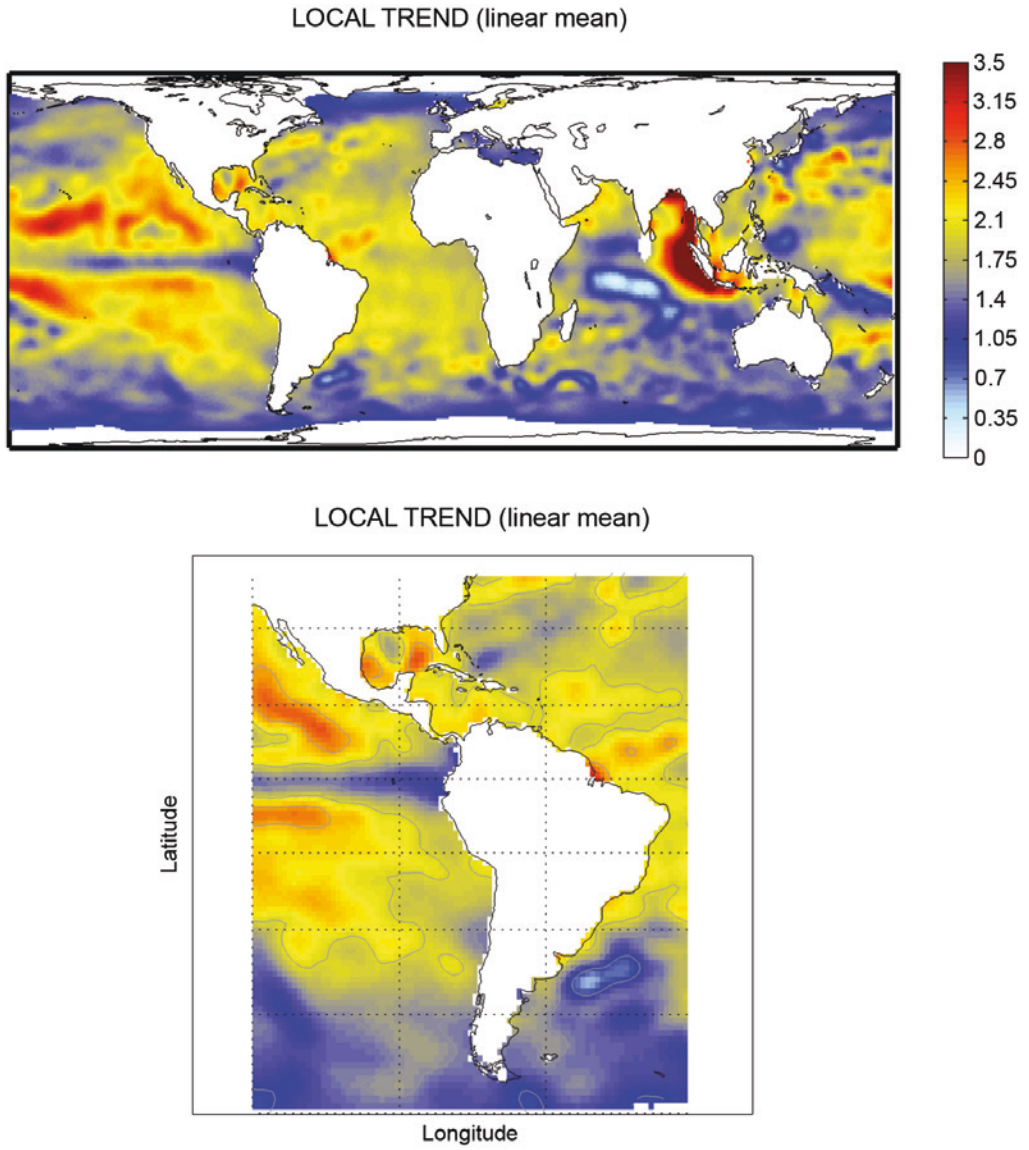

Source: Prepared by the authors.

FIGURE 1.68
TYPE OF TREND OBTAINED FROM LOCAL ADJUSTMENTS AT A GLOBAL SCALE

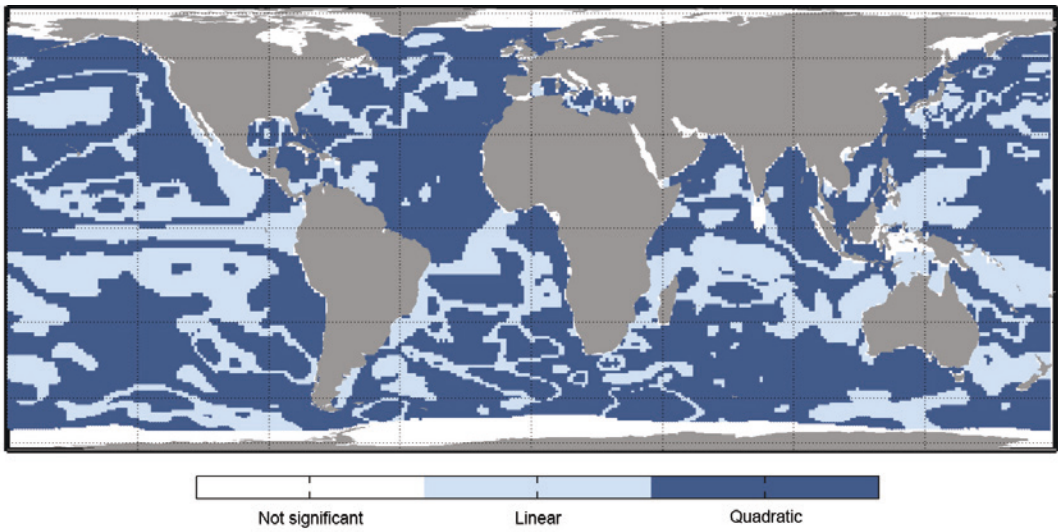

Source: Prepared by the authors.
Note: Distinctions are made between trends that are not statistically significant (no trend), linear trends and quadratic trends (the trend is accelerating or decelerating).

Figure 1.68 depicts locally adjusted trends and distinguishes between linear trends, in which the acceleration of sea level rise is not significant, and quadratic trends, in which an acceleration of sea level rise is apparent. Points where the trend is not statistically significant are not shown.

A comparison of the spatial trend patterns shown in figure 1.67 and figure 1.69 indicates that local trends are greater than those yielded by the T-EOF method for regions (the Pacific Ocean and the Indian Ocean) in which inter-annual variability is very marked.

The global trend is towards a widespread increase in sea levels resulting from thermal expansion (steric sea level rise) and the melting of the polar ice caps, among other effects of global warming (IPCC, 2007).

FIGURE 1.69
SPATIAL PATTERN OF THE MEAN (LINEAR) TREND GLOBALLY AND FOR LATIN AMERICA AND THE CARIBBEAN OF MEAN SEA LEVEL BASED ON THE ADJUSTED T-EOF TECHNIQUE
(Mm/year)

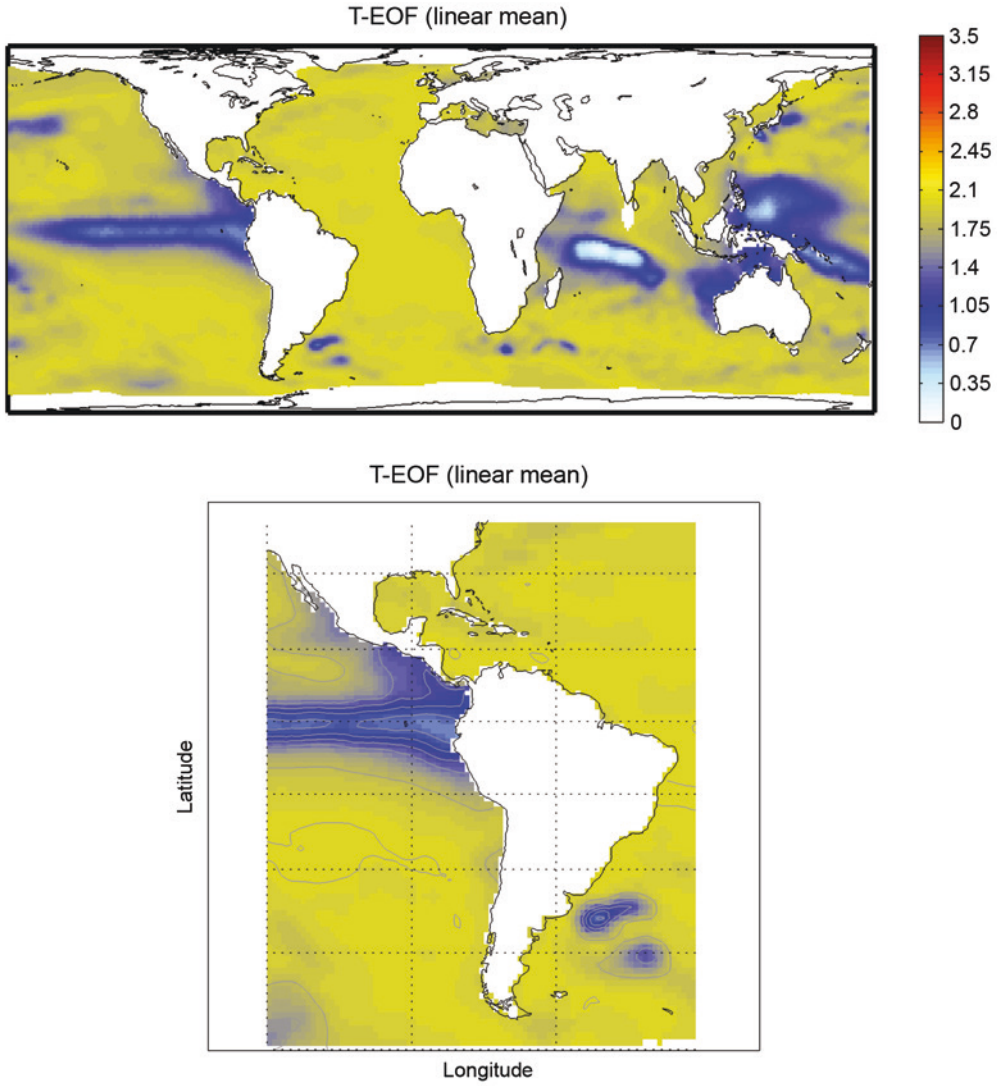

Source: Prepared by the authors.

Figure 1.70 and figure 1.71 show the trends calculated for two points using the trend methodology described earlier. In this case, the data indicate that sea level rise (SLR) will accelerate in the future. In addition, the time series reflects anomalies deriving from the ENSO phenomenon (see figure 1.70), which means that the T-EOF technique is better suited for dealing with this variable. The trend is also calculated using gridded data for global anomalies.

FIGURE 1.70
TRENDS FOR ONE LOCATION ON THE ATLANTIC COAST

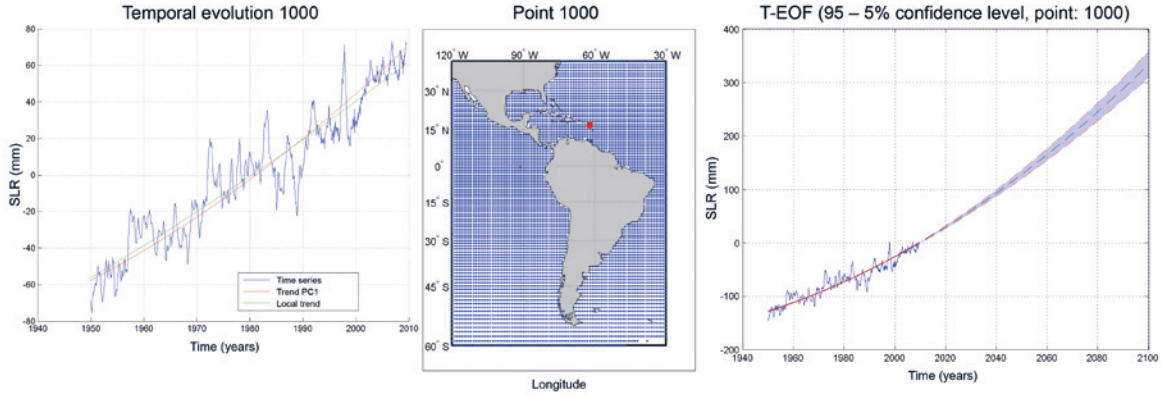

Source: Prepared by the authors.
Note: Right-hand panel: T-EOF for sea level rise (SLR). Central panel: Point location. Left-hand panel: Comparison of local and T-EOF trend calculations.

FIGURE 1.71
TRENDS FOR ONE LOCATION ON THE PACIFIC COAST

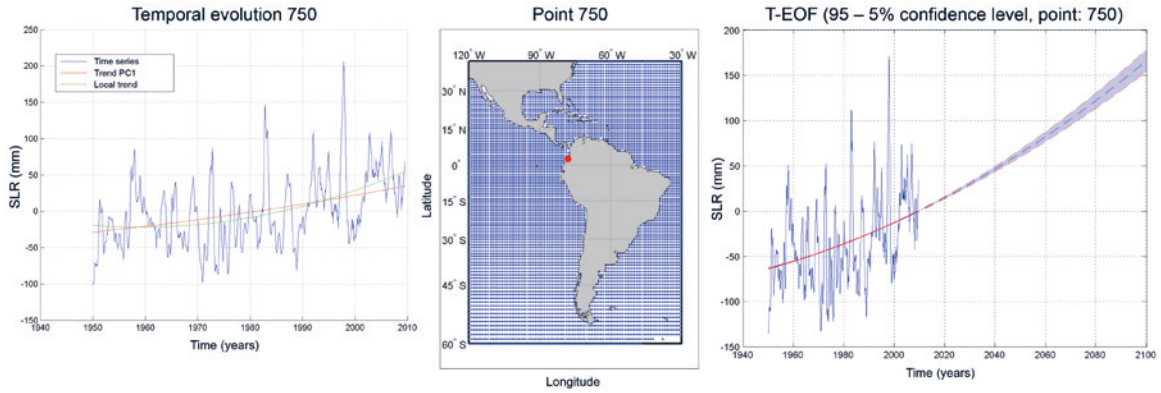

Source: Prepared by the authors.
Note: Right-hand panel: trend-EOF data for sea level rise (SLR). Central panel: point location. Left-hand panel: comparison of local trends with the T-EOF data.

Figure 1.72 shows the spatial pattern for the median trend for the two time periods of interest (2010-2040 and 2040-2070). The above graphs depict these mean trends for the specific control points in Latin America and the Caribbean that were analysed.

FIGURE 1.72
MEAN TREND IN SEA LEVELS FOR 2010-2040 (LEFT) AND 2040-2070 (RIGHT)
(Mm/year)

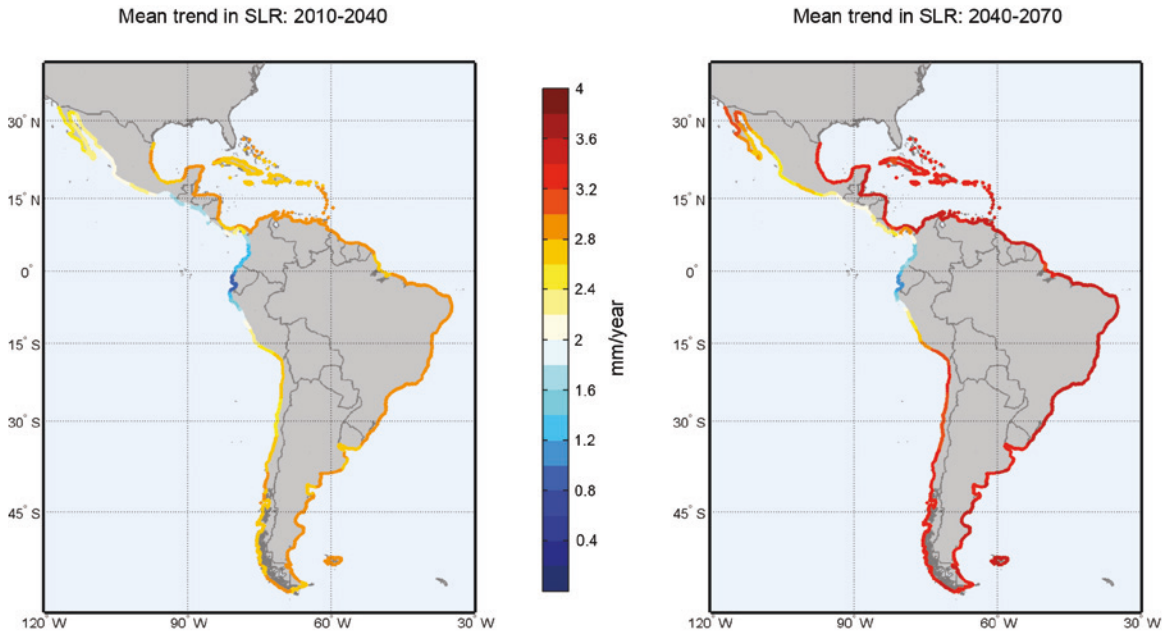

Source: Prepared by the authors.

There is no question about the fact that sea levels are trending upward at all locations in the region. The highest values for this upward trend are found along the Atlantic coast, with values of approximately 2.8 mm/year along the northern coast of South America and the Caribbean coast, while the values are lower for the Caribbean islands. In these areas, for the second part of the century, the trend rises to as much as 3.6 mm/year, on average. The equatorial zone of the Pacific has lower values (1.5 mm/year for the first period).

These linear trends represent equivalent values for 2010 and 2040 and for 2040 and 2070, respectively. figure 1.73 and figure 1.74 show the mean values and degree of uncertainty (95% confidence level) for the specific values for sea level rise that correspond to the specified horizon years, with values of up to approximately 90 mm for 2040 as a maximum and of nearly 200 mm/year for 2070 along the northern coast of South America, which is where the largest increases are expected to occur. It should be noted that the degree of uncertainty associated with these values is just 4 mm and up to 12 mm for the peak levels for 2040 and 2070, respectively.

For the sake of brevity, the values for the 2050 trends are not reported here. They can, however, be consulted using the web platform.

FIGURE 1.73
MEAN VALUES AND UNCERTAINTY BOUNDS FOR MEAN SEA LEVELS: 2040
(Millimetres)

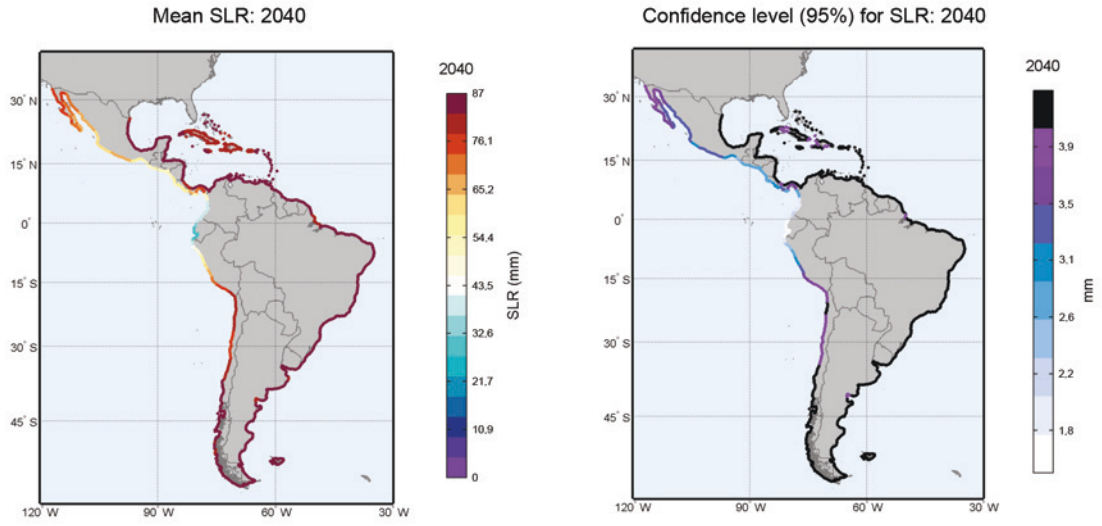

Source: Prepared by the authors.

FIGURE 1.74
MEAN VALUES AND UNCERTAINTY BOUNDS FOR MEAN SEA LEVELS: 2070
(Millimetres)

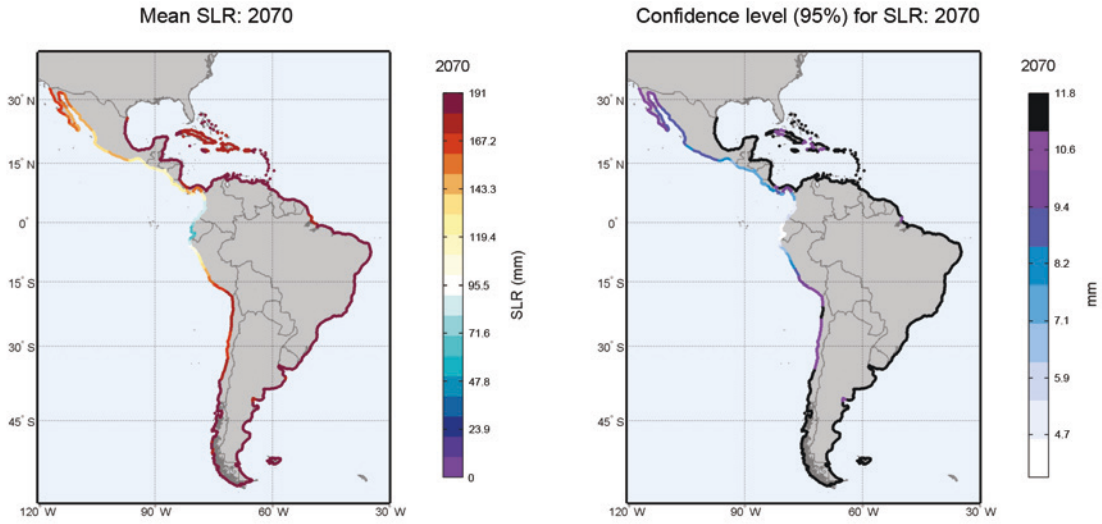

Source: Prepared by the authors.

It is worthwhile to compare the effect of climate change on mean sea levels and the expected increase if current trends continue to hold (without taking into account other hypotheses regarding extreme SLR events such as the effect of the melting of the polar ice caps). In the ENSO event of 1998 (the all-time high recorded on the NIÑO3 index), the greatest effects were seen in the equatorial zone of the Pacific (see the section on climatic/weather variability). When the calculated trend is separated out from the series on sea levels, the value for the mean sea level during that event can be determined. The upper panel in figure 1.75 shows the levels that would be reached if this event were to reoccur

(about 0.2 m, ruling out the effects of other variables such as wave activity or storm surge). The expected value yielded by these trends is far below that figure, however. Comparable values are not likely to be seen in the rest of the region until 2070.

FIGURE 1.75
COMPARISON OF EXPECTED MEAN LEVELS DUE TO SEA LEVEL RISE AND HIGHER MEAN LEVELS RECORDED DURING THE 1998 EL NIÑO EVENT
(Metres)

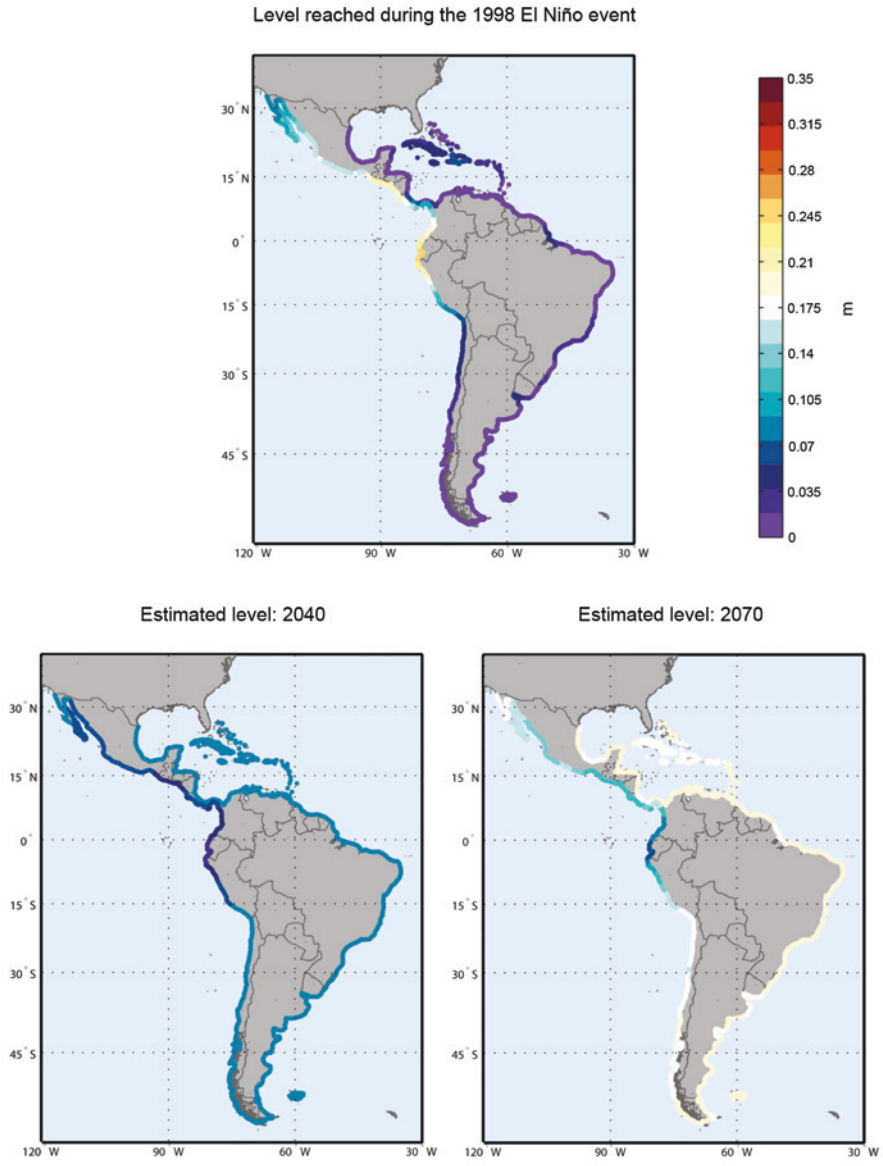

Source: Prepared by the authors.

5.2.2. Trends in relative sea level rise

The trends in mean sea level rise examined in the preceding section do not incorporate the effect of the sinking or rising land elevations associated with the glacial isostatic adjustment (GIA). The rising mean sea level resulting from land subsidence is referred to as the relative sea level rise (RSLR). Subsidence/rising elevation values have been taken from the calculations of Peltier (2000) and interpolated using the inverse distance weighting (IDW) technique to construct a grid at a resolution of 0.5 degrees. The values assigned to each segment of the coastline have been arrived at by averaging the grid values at the locations where they intersect the coastline. In the case of deltas, a change of 2 mm/year has been assumed. These data have been obtained from the DINAS Project Diva Documentation Database (DIVA).

FIGURE 1.76
MEAN SUBSIDENCE IN 2010-2070
(Mm/year)

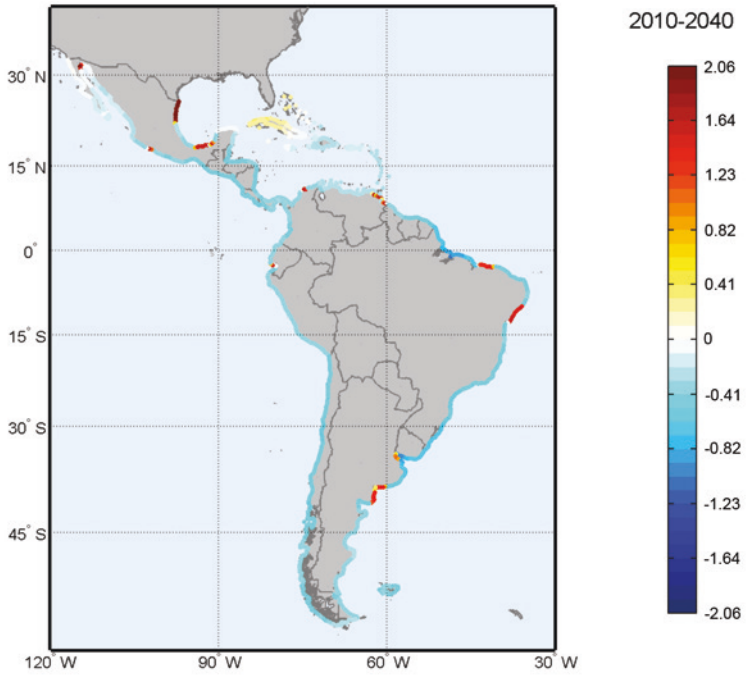

Source: DIVA Documentation Database (Peltier, 2000).

The following RSLR maps have been drawn up based on the available information on subsidence and SLR data for the entire area covered by this study.

FIGURE 1.77
MEAN RELATIVE SEA LEVEL RISE: 2010-2040 (LEFT) AND 2040-2070 (RIGHT)
(Mm/year)

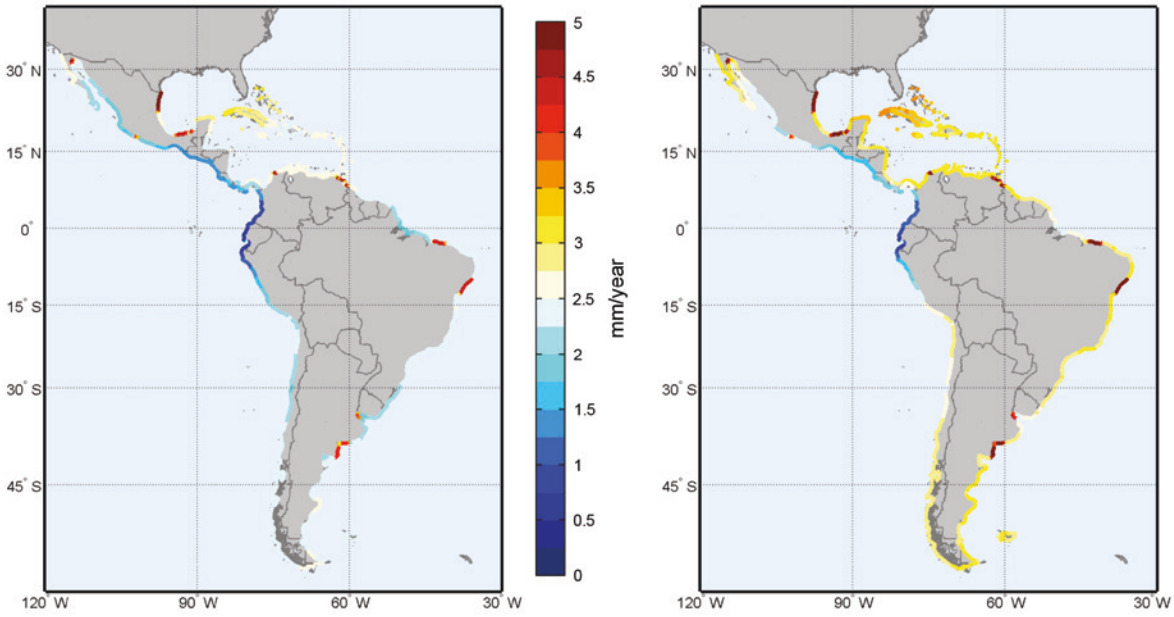

Source: Prepared by the authors.

FIGURE 1.78
MEAN RELATIVE SEA LEVEL RISE AND UNCERTAINTY BOUNDS: 2040
(Millimetres)

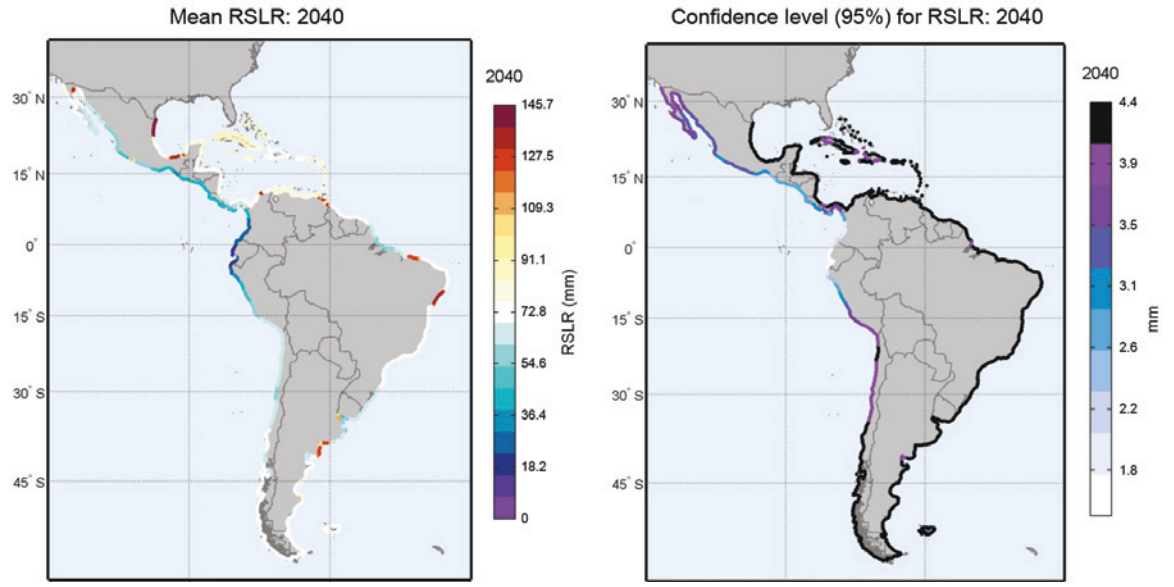

Source: Prepared by the authors.

FIGURE 1.79
MEAN VALUE AND UNCERTAINTY BOUNDS FOR RELATIVE SEA LEVEL RISE: 2070
(Millimetres)

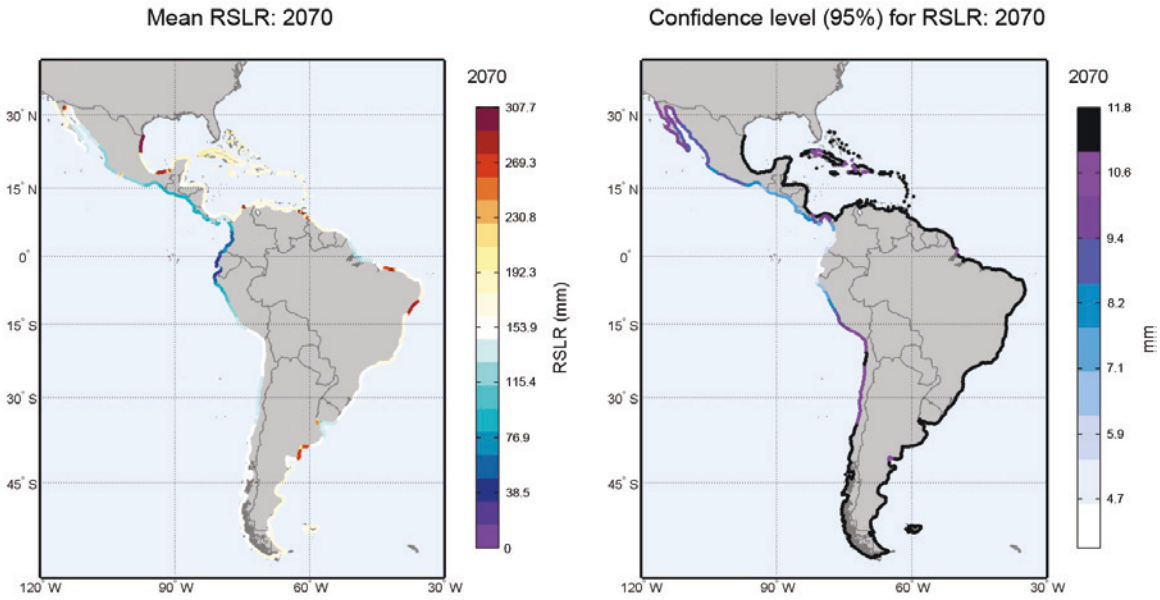

Source: Prepared by the authors.

5.2.3. Trends in salinity

Using a similar approach to the one used to study sea levels, globally gridded salinity levels have been analysed using the two techniques discussed earlier. The global mean time series does not provide a good fit with the global mean data, whereas the rest of the variables do. The reason for this may be the variability of this factor (it varies depending on the depth; a value of 5 m has been used as a standard) or the source of information (a numerical reanalysis). The analysis of this variable therefore appears to be subject to a greater degree of uncertainty than is the case for the rest of the geophysical variables included in this analysis.

Whereas the predominant trend in mean sea levels was quadratic, the linear trend seems to predominate in the case of salinity (figure 1.81.). There are also many points for which the trend is not statistically significant.

Both ways of calculating the trends (figure 1.80 and figure 1.82) yield spatially similar results, although the T-EOF technique smoothes out the trend at certain discrete points where local trends appear to exhibit isolated peaks, probably as a result of upswings in the time series for the variable.

The T-EOF technique yields null (not statistically significant) trends for the points where the results of the local analysis were not significant.

FIGURE 1.80
SPATIAL PATTERN OF THE MEAN (LINEAR) TREND FOR SALINITY (AT A DEPTH OF 5 M) GLOBALLY AND FOR LATIN AMERICA AND THE CARIBBEAN BASED ON LOCAL TREND ADJUSTMENTS
(Psu/year)

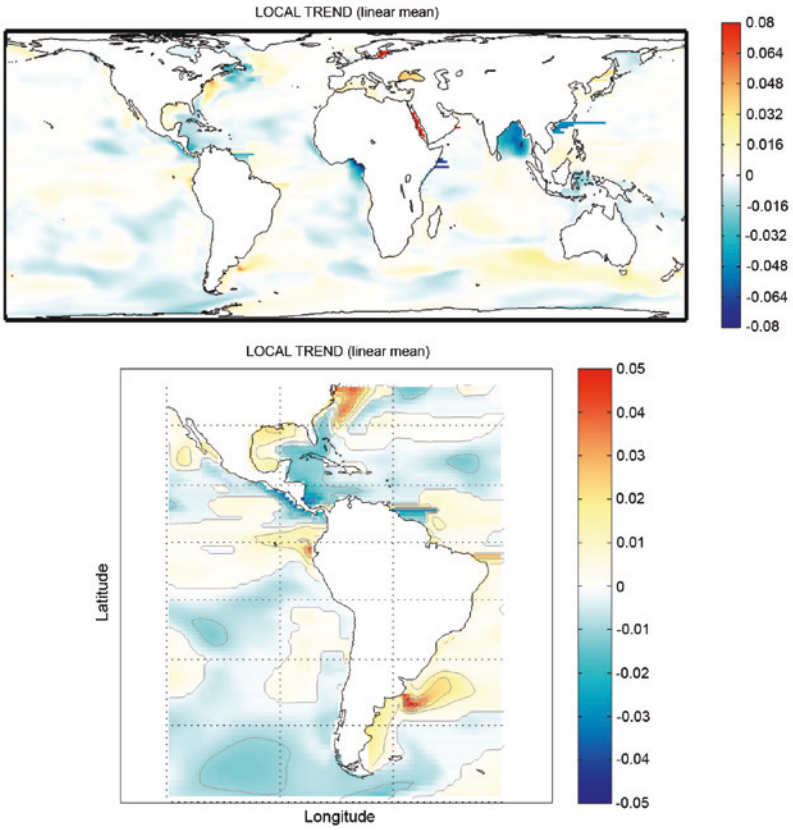

Source: Prepared by the authors.

FIGURE 1.81
TYPE OF TREND OBTAINED FROM LOAL ADJUSTMENTS OF SALINITY AT A GLOBAL SCALE

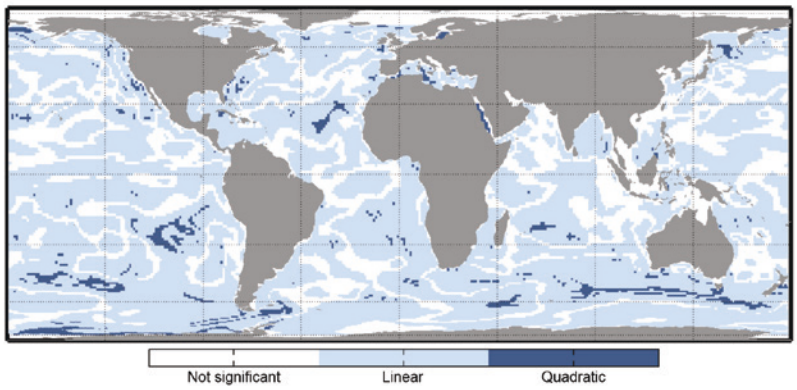

Source: Prepared by the authors.
Note: Statistically insignificant trends (no trend identified), linear trends and quadratic trends (a steepening or flattening of the trend) are differentiated.

FIGURE 1.82
SPATIAL PATTERN OF THE MEAN (LINEAR) TREND FOR SALINITY (AT A DEPTH OF 5 M) GLOBALLY AND FOR LATIN AMERICA AND THE CARIBBEAN BASED ON T-EOF ADJUSTMENTS
(Psu/year)

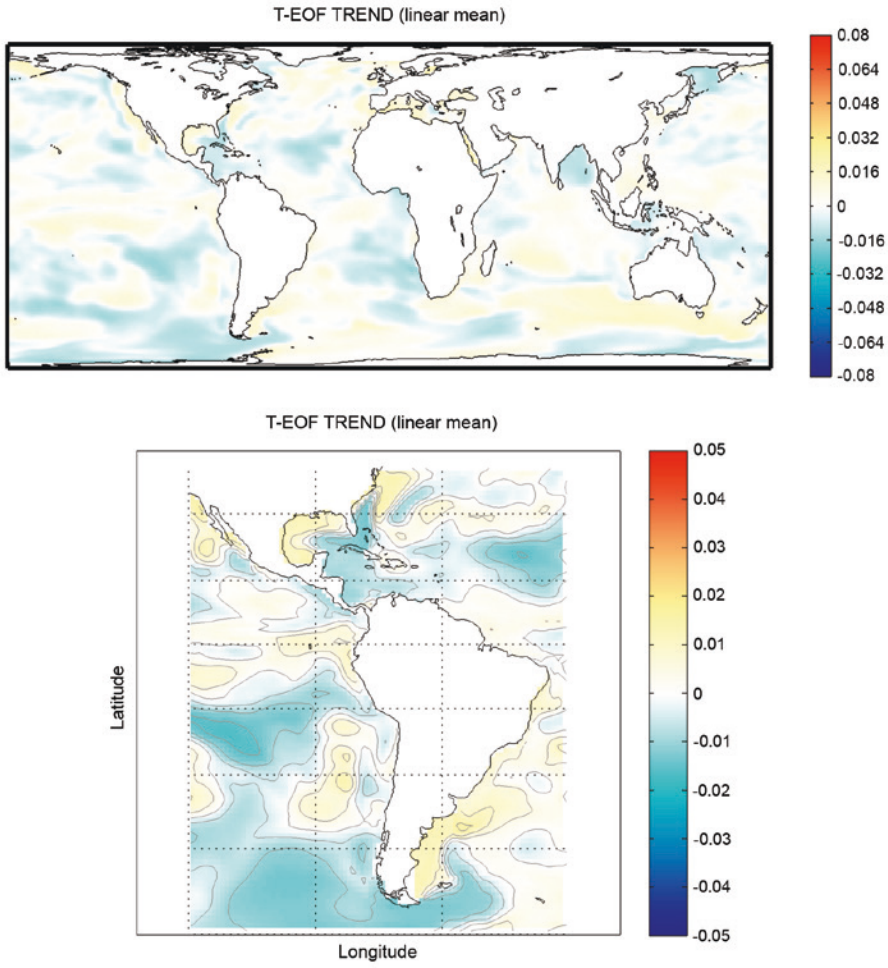

Source: Prepared by the authors.

Salinity trends have been calculated on a global scale and for each of 1,132 locations along the coasts of Latin America and the Caribbean. Figure 1.83 and figure 1.84 depict the trends for two specific locations. A comparison of the T-EOF trend and the locally adjusted trend is shown (left), along with the locations of the control points (centre) and the resulting trend (right). In both cases, the trend is declining; for the first of the points, there is a clear-cut difference between the result for the T-EOF trend and the locally adjusted trend, whereas, in the case of the second point, the results of the application of the two methods are similar. This indicates that the T-EOF method is more suitable for variables for which there is an accelerating long-term trend.

FIGURE 1.83
SALINITY TRENDS FOR ONE LOCATION ON THE COAST OF LATIN AMERICA AND THE CARIBBEAN
(Grams/kilograms)

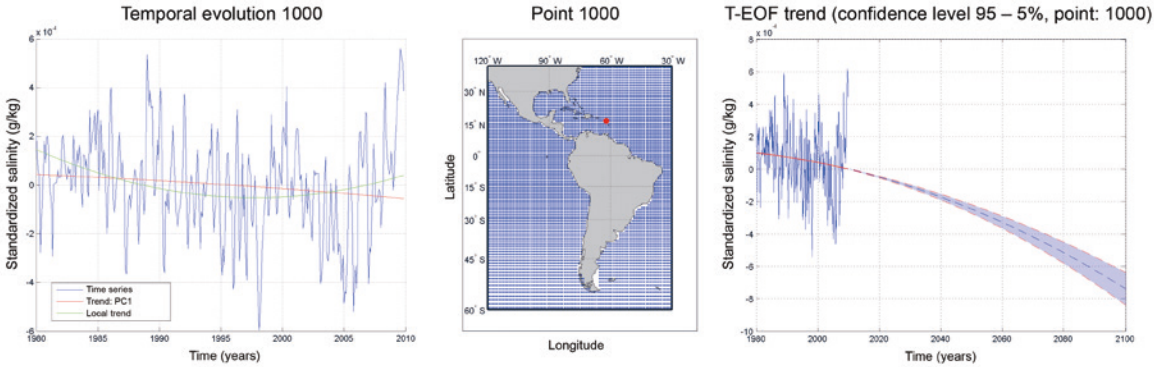

Source: Prepared by the authors.
Note: Right-hand panel: T-EOF trend. Central panel: Location of control point. Left-hand panel: Comparison of local and T-EOF trends.

FIGURE 1.84
SALINITY TRENDS FOR ONE LOCATION ON THE COAST OF LATIN AMERICA AND THE CARIBBEAN
(Grams/kilograms)

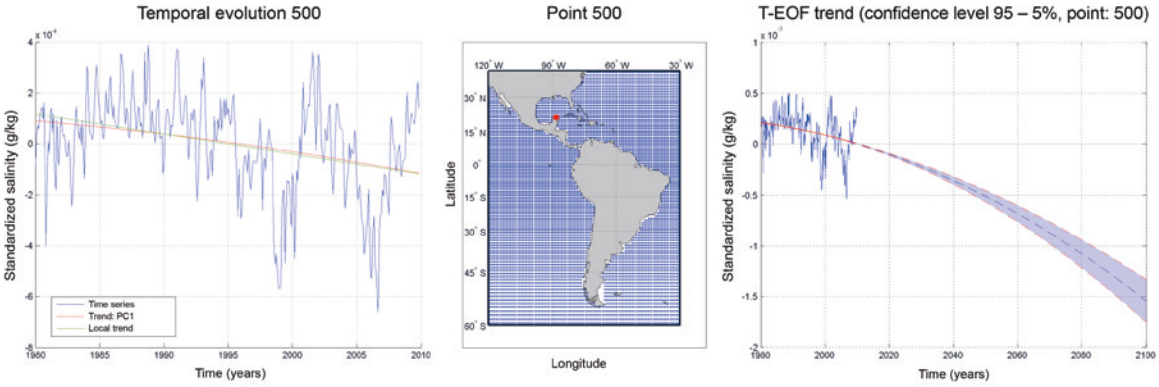

Source: Prepared by the authors.
Note: Right-hand panel: T-EOF trend. Central panel: Location of control point. Left-hand panel: Comparison of local and T-EOF trends.

Figure 1.85 shows the equivalent mean linear trend for the control points along the Latin American and Caribbean coasts for the two time periods in question calculated using the T-EOF method. While there is a declining salinity trend around 15ºN latitude, there is a rising trend along the Atlantic coast south of Ecuador, along the peninsula of Baja California and on the coast of the Gulf of Mexico. The highest trend values are obtained for the last two of these areas (mean values in 2040 and 2070 of up to 0.8 and 2 psu, respectively) (see figure 1.86 and figure 1.87). The Pacific coast of South America (Peru and Chile), which has especially abundant fishery resources thanks to intense coastal upwelling, will experience no more than very slight changes in salinity compared to the rest of the region's coasts. The greatest decreases in salinity are expected to occur along the northern Caribbean islands and the coasts of the countries in the southern portion of Central America, with values of approximately 0.7 and 1.7 psu for 2040 and 2070.

FIGURE 1.85
MEAN SALINITY TRENDS: 2010-2040 AND 2040-2070
(Psu/year)

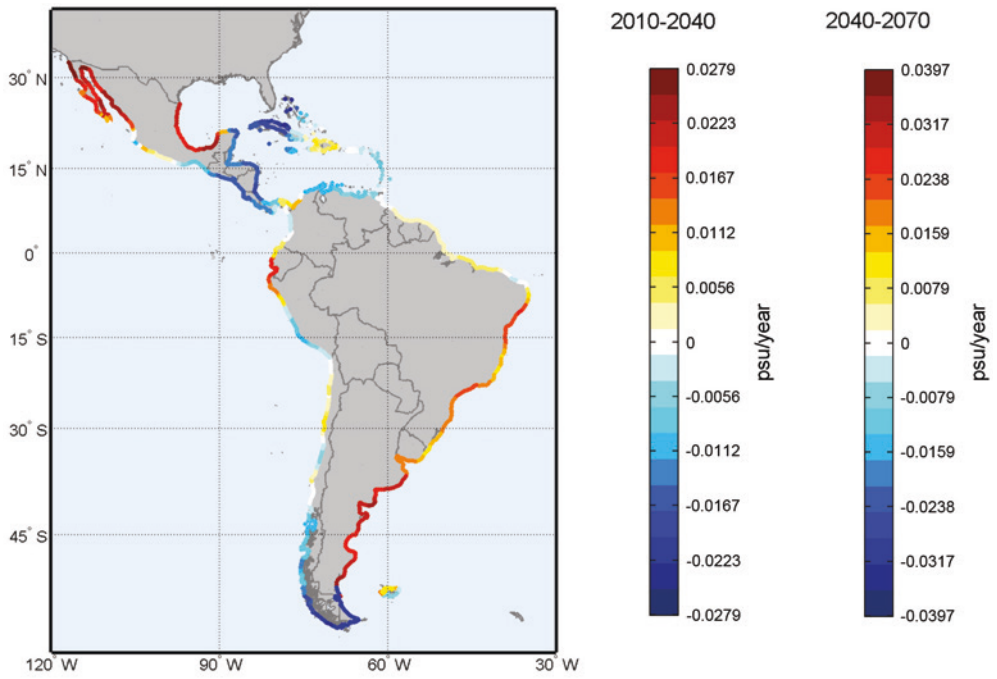

Source: Prepared by the authors.

FIGURE 1.86
MEAN VALUE AND UNCERTAINTY BOUNDS FOR SALINITY LEVELS: 2040
(Psu)

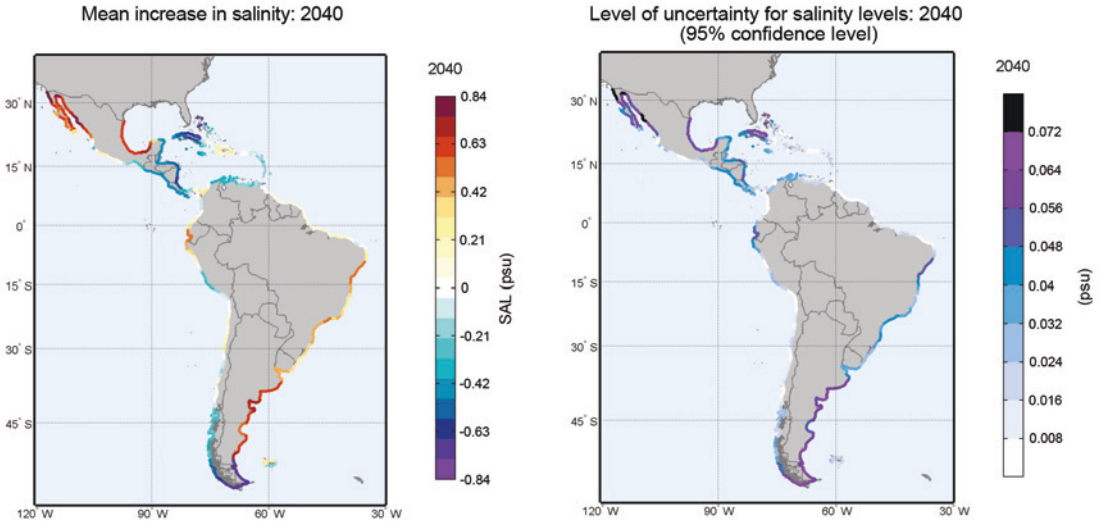

Source: Prepared by the authors.

FIGURE 1.87
MEAN VALUE AND UNCERTAINTY BOUNDS FOR SALINITY LEVELS: 2070
(Psu)

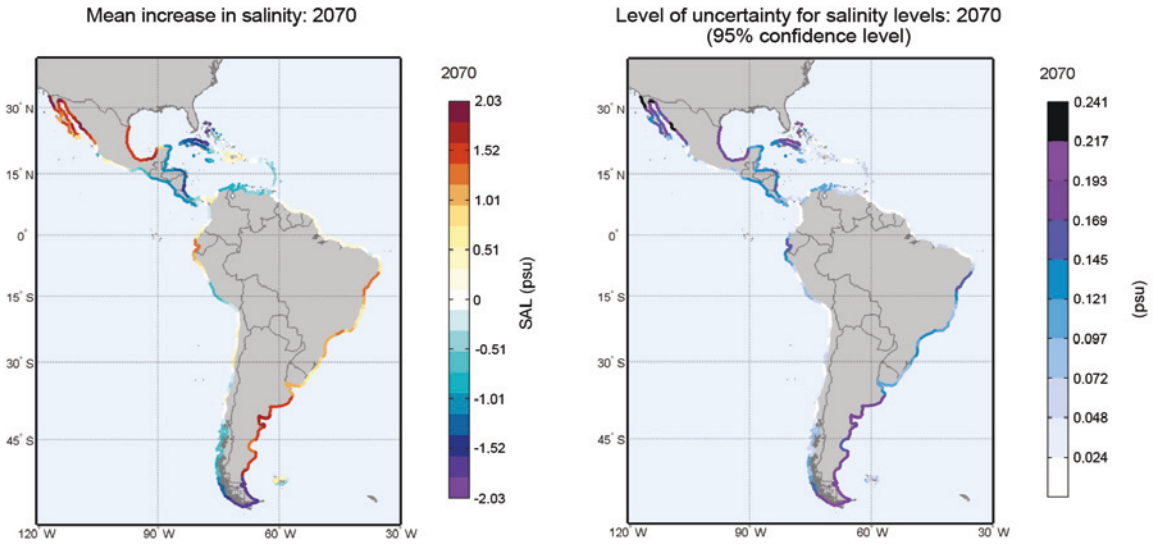

Source: Prepared by the authors.

5.2.4. Trends in sea surface temperatures

Because sea surface temperature is a variable for which the resolution of the dataset is global, both methods (local trends and T-EOF) have also been used here. Figure 1.88 shows the T-EOF time series, which picks up the global mean trend and the mean values for the time series. The level of correspondence between the two is satisfactory.

FIGURE 1.88
TREND AND RECONSTRUCTION OF THE GLOBAL SEA SURFACE TEMPERATURE ANOMALY

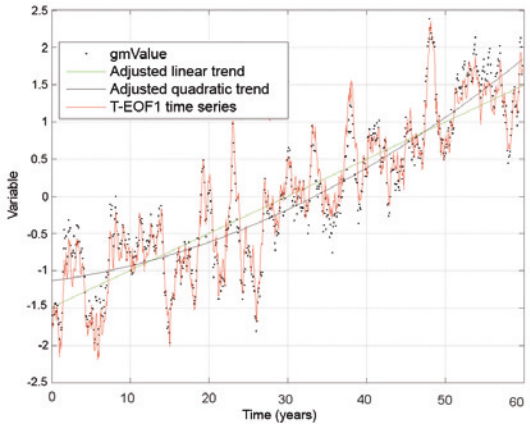

Source: Prepared by the authors.
Note: The time series for the first mode of the T-EOF is shown in red. The black (non-coincident) points represent the global mean anomaly. The adjusted linear and quadratic trends are shown in green and black, respectively.

FIGURE 1.89
SPATIAL PATTERN OF THE MEAN (LINEAR) TREND FOR SEA SURFACE TEMPERATURES GLOBALLY AND FOR LATIN AMERICA AND THE CARIBBEAN BASED ON LOCAL TREND ADJUSTMENTS
(ºC/year)

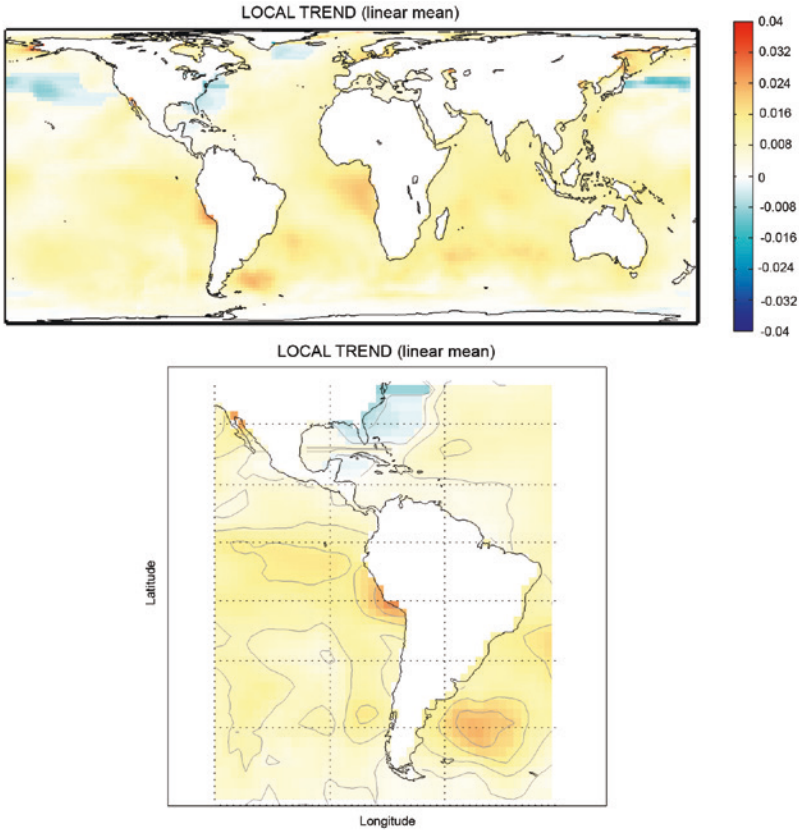

Source: Prepared by the authors.

FIGURE 1.90
TYPE OF TREND OBTAINED FOR LOCAL ADJUSTMENTS AT A GLOBAL SCALE OF SEA SURFACE TEMPERATURES

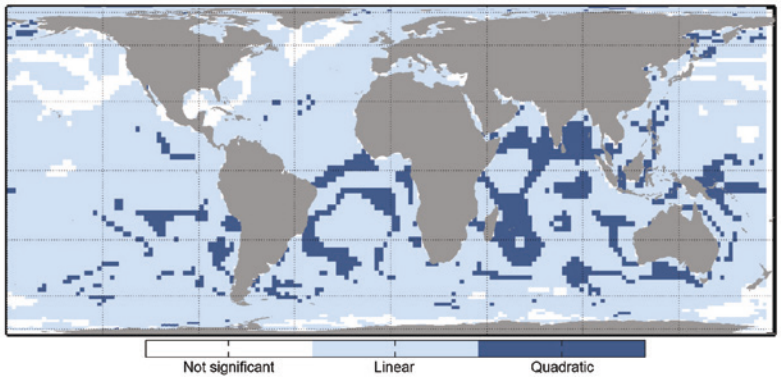

Source: Prepared by the authors.
Note: Statistically insignificant trends (no trend identified), linear trends and quadratic trends (a steepening or flattening of the trend) are differentiated.

As in the cases of sea levels and salinity, the type of local trend that is best suited to each geographical area (including the points for which no statistically significant result is obtained) is the one that has been analysed (see figure 1.90).

A comparison of the global patterns in mean trends calculated using the two methods (see figure 1.89 and figure 1.91) yields similar findings to those obtained in the cases analysed earlier. The T-EOF method appears to be more suitable for this type of global geophysical variable, since the specific trend effects associated, most probably, with year-on-year variability are reflected in peaks in the series that affect the local regression. Apart for this difference, the two spatial patterns are of a similar magnitude and are spatially similar as well.

Unlike the results for sea levels, the time series for sea surface temperatures indicates that temperatures will generally increase, except in certain areas of the ocean in the northern hemisphere where a cooling trend emerges.

FIGURE 1.91
SPATIAL PATTERN OF THE MEAN (LINEAR) TREND FOR SEA SURFACE TEMPERATURES GLOBALLY AND FOR LATIN AMERICA AND THE CARIBBEAN BASED ON T-EOF TREND ADJUSTMENTS
(ºC/year)

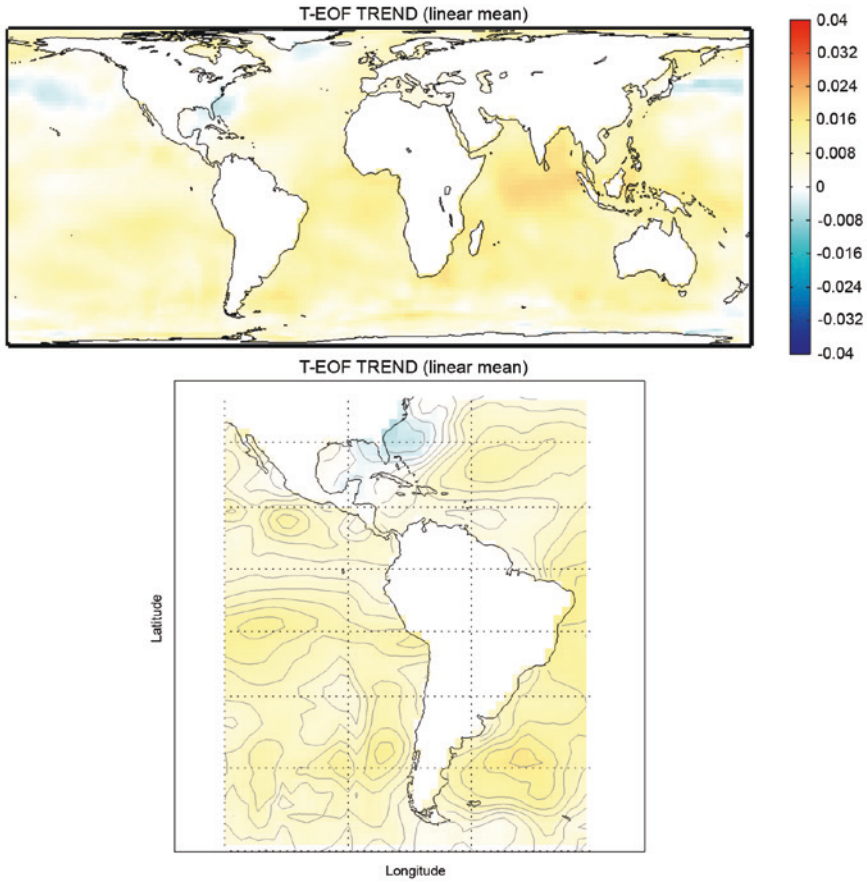

Source: Prepared by the authors.

FIGURE 1.92
SEA SURFACE TEMPERATURE TRENDS FOR A LOCATION ON THE COAST OF LATIN AMERICA AND THE CARIBBEAN
(Degrees centigrade)

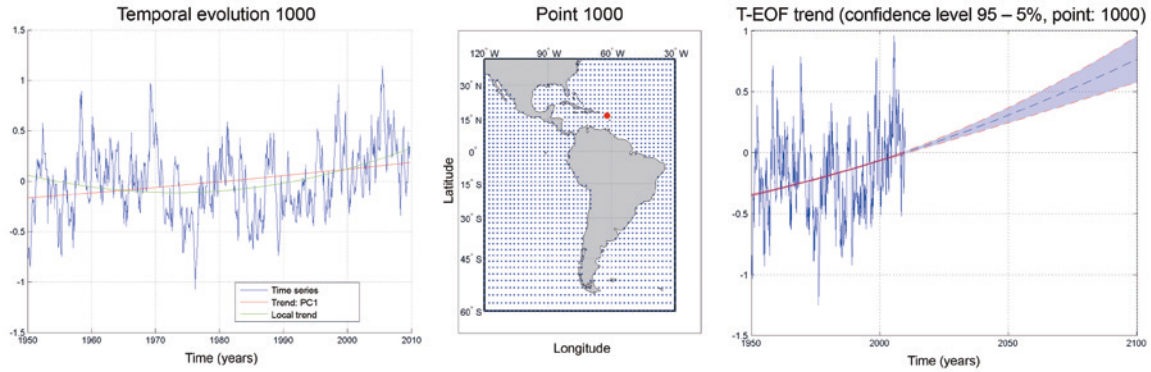

Source: Prepared by the authors.
Note: Right-hand panel: T-EOF trend. Central panel: Location of control point. Left-hand panel: Comparison of local and T-EOF trends.

FIGURE 1.93
SEA SURFACE TEMPERATURE TRENDS FOR A LOCATION ON THE COAST OF LATIN AMERICA AND THE CARIBBEAN
(Degrees centigrade)

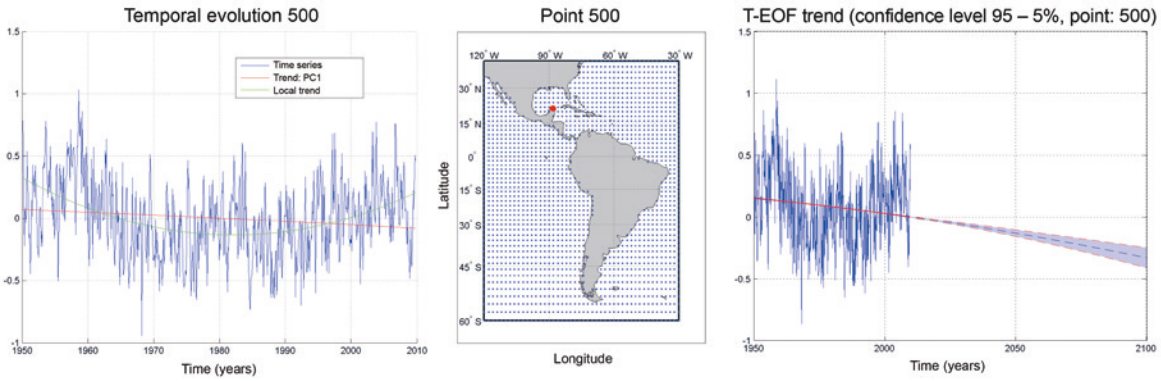

Source: Prepared by the authors.
Note: Right-hand panel: T-EOF trend. Central panel: Location of control point. Left-hand panel: Comparison of local and T-EOF trends.

The figures that show the comparisons of the different adjustments (see figure 1.92 and figure 1.93) indicate that there is a clear-cut difference between the local adjustment of the quadratic trend and the T-EOF trend. While the curve yielded by the first method is quite steep, the other method results in a smoother trend that, while not exactly linear, denotes a slight deceleration. Here again, the T-EOF method offers a better fit for this type of variable. In fact, even at the 500-point level, one is a rising trend while the other is descending.

FIGURE 1.94
MEAN SURFACE TEMPERATURE TRENDS: 2010-2040 AND 2040-2070
(Degrees centigrade/year)

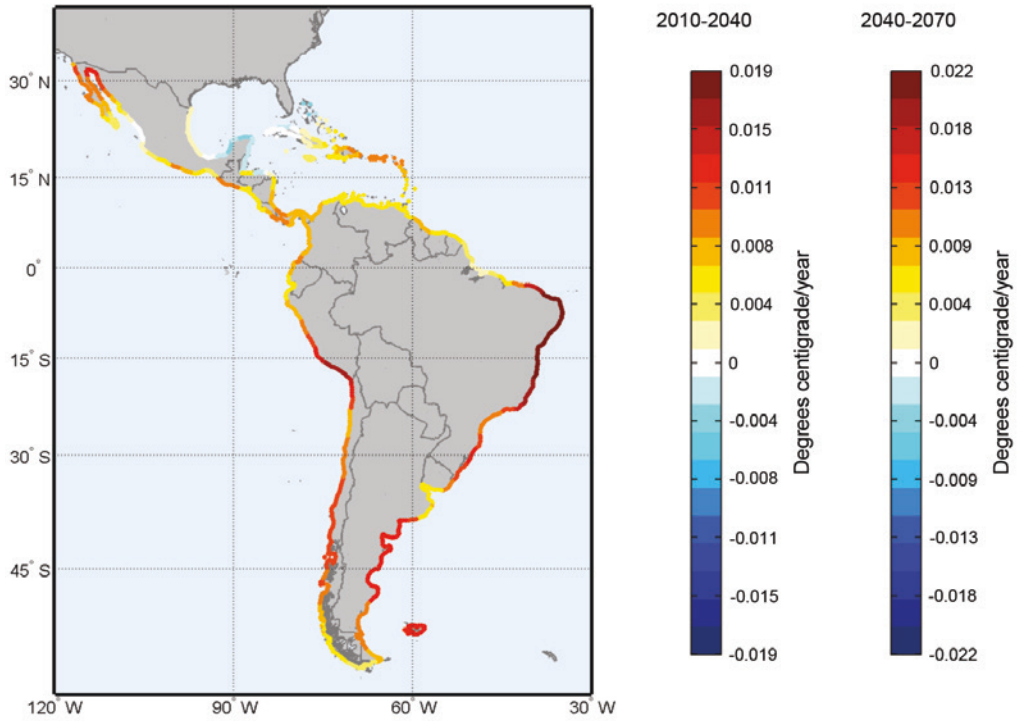

Source: Prepared by the authors.

The overall trend is towards an increase in sea temperatures, except in the northern Caribbean Sea, where the sea surface temperature is not expected to increase significantly and may even decline slightly. The sharpest increases are expected along the coast of Brazil between 0° and 15ºS (+0.57º and +1.2ºC in 2040 and 2070, with uncertainties of less than 0.1º and 0.3ºC, respectively) and the southern Peruvian and northern Chilean coasts, but in this latter area the upswing will be smaller than in Brazil. These results are, of course, subject to the quality of the underlying database.

FIGURE 1.95
MEAN VALUE AND UNCERTAINTY BOUNDS OF SEA SURFACE TEMPERATURES: 2040
(Degrees centigrade)

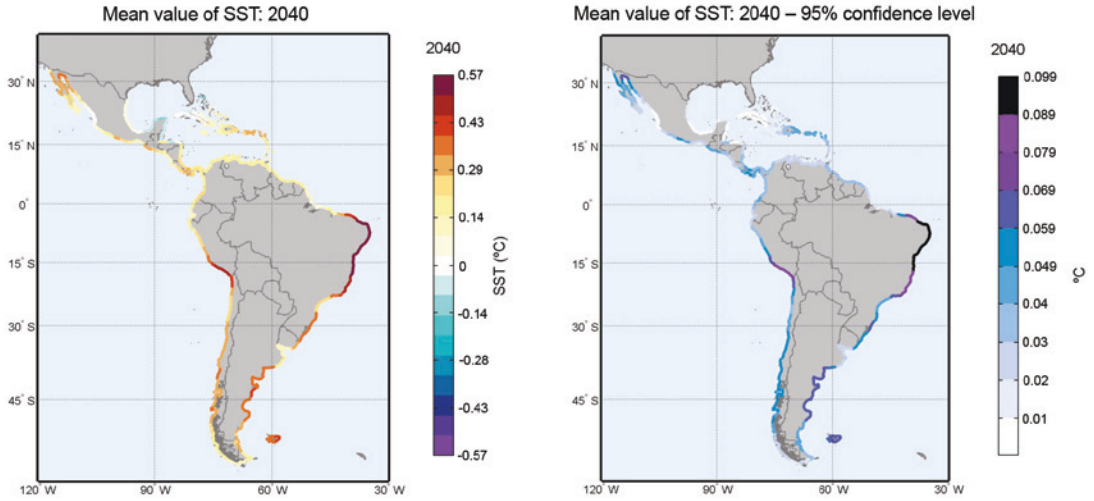

Source: Prepared by the authors.

FIGURE 1.96
MEAN VALUE AND UNCERTAINTY BOUNDS OF SEA SURFACE TEMPERATURES: 2070
(Degrees centigrade)

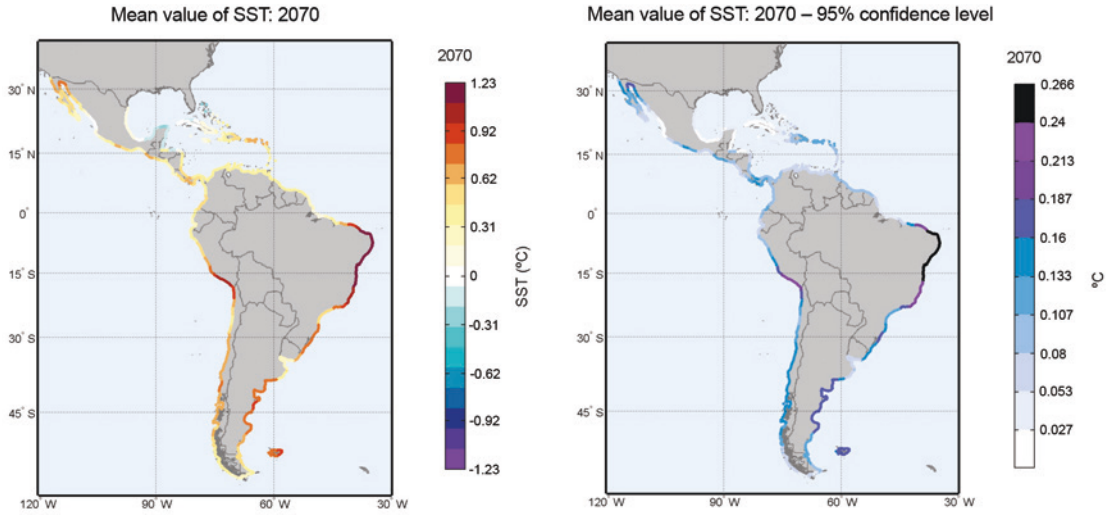

Source: Prepared by the authors.

SST is an important variable for many ecosystems, including coral reefs. Coral bleaching is analysed in the impact study (the third project document) and is one of the reasons why it is important to gauge the probability of given increases in SST for the time horizons of interest. Figure 1.97 shows the confidence levels for an increase of 1ºC in SST now and for 2040 and 2070. The degree of confidence rises significantly for the whole of the region and, for a portion of the Brazilian coast, is great enough to be classified as *likely*.

FIGURE 1.97
DEGREE OF CONFIDENCE (IPCC SCALE) REGARDING AN INCREASE IN SEA SURFACE TEMPERATURES OF 1ºC FOR DIFFERENT TIME HORIZONS

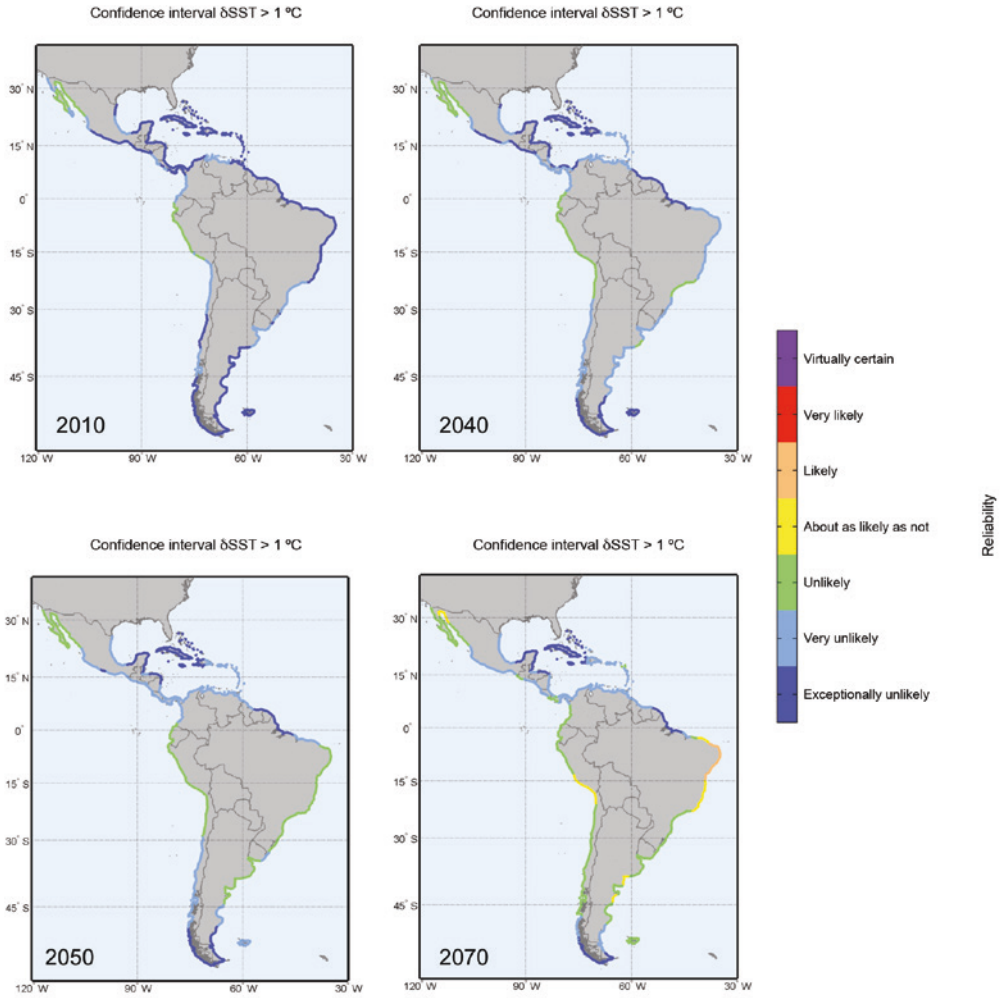

Source: Prepared by the authors.
Note: Legend of probabilities: >0.99, virtually certain; 0.9-0.99, very likely; 0.66-0.9, likely; 0.33-0.66, about as likely as not; 0.1-0.33, unlikely; 0.01-0.1, very unlikely; <0.01, exceptionally unlikely.

5.2.5. Trends in air temperatures

The last global geophysical variable for which trends have been calculating using the two methods that have been discussed here is surface air temperature. Figure 1.98 shows the global mean series based on the global mean pattern calculated using the T-EOF method and the data for the global mean anomaly, as well as the adjusted trends for the global series. Although the fit is not as good as it is in the case of sea surface temperatures (instrumental database) and much less so than in the case of mean sea levels (also instrumental), the time series does appear to fit the global data from the NCEP/NCAR reanalysis, which was chosen because of the length and spatial coverage of the series. In addition to the fact that the information source is numeric rather than instrumental, the unevenness of the land surface and the presence of such a wide range of geographical features necessarily translate into greater variability in this series.

FIGURE 1.98
TREND AND RECONSTRUCTION OF THE GLOBAL AIR SURFACE TEMPERATURE ANOMALY

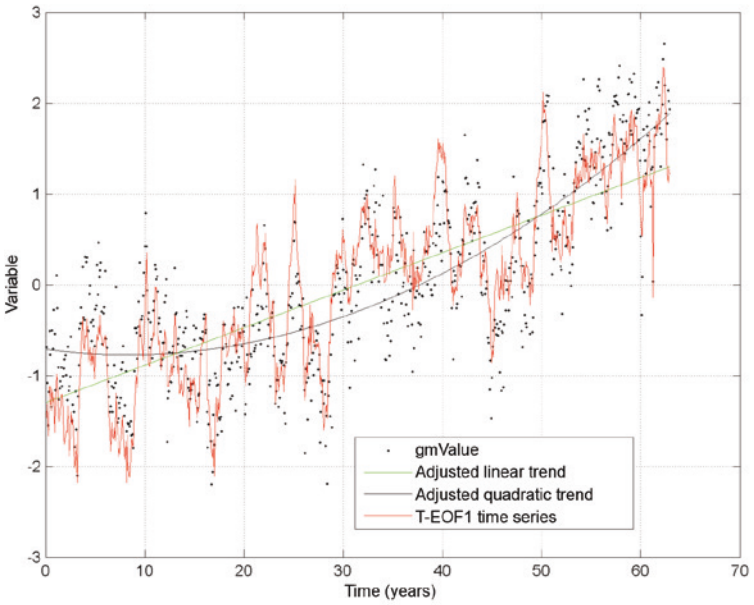

Source: Prepared by the authors.
Note: The time series for the first mode of the T-EOF is shown in red. The black (non-coincident) points represent the global anomaly. The adjusted linear and quadratic trends are shown in green and black, respectively.

FIGURE 1.99
SPATIAL PATTERN OF THE MEAN (LINEAR) TREND FOR SURFACE AIR TEMPERATURES GLOBALLY AND FOR LATIN AMERICA AND THE CARIBBEAN BASED ON LOCAL TREND ADJUSTMENTS
(Degrees centigrade/year)

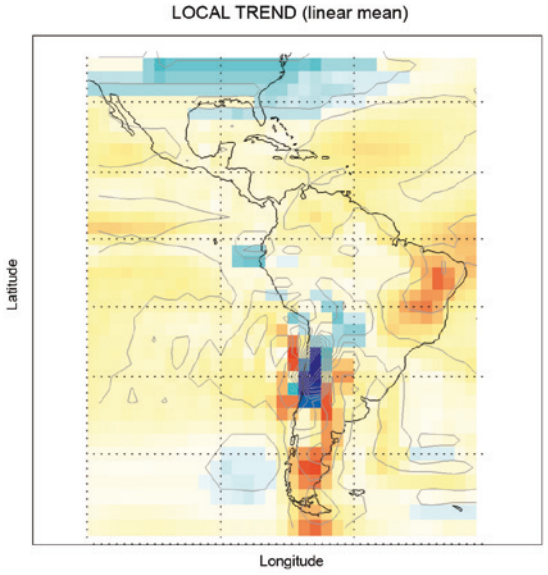

Source: Prepared by the authors.

FIGURE 1.100
TYPE OF TREND OBTAINED FOR LOCAL ADJUSTMENTS AT A GLOBAL SCALE OF AIR SURFACE TEMPERATURES

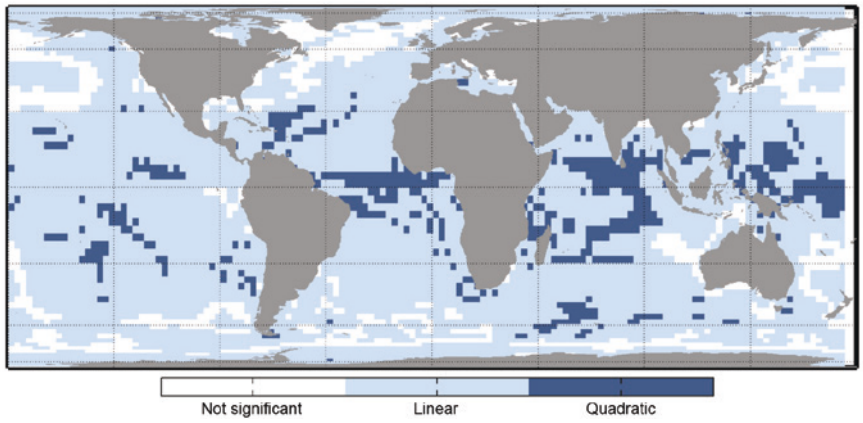

Source: Prepared by the authors.
Note: Statistically insignificant trends (no trend identified), linear trends and quadratic trends (a steepening or flattening of the trend) are differentiated.

FIGURE 1.101
SPATIAL PATTERN OF THE MEAN (LINEAR) TREND FOR SURFACE AIR TEMPERATURES GLOBALLY AND FOR LATIN AMERICA AND THE CARIBBEAN BASED ON T-EOF TREND ADJUSTMENTS
(Degrees centigrade/year)

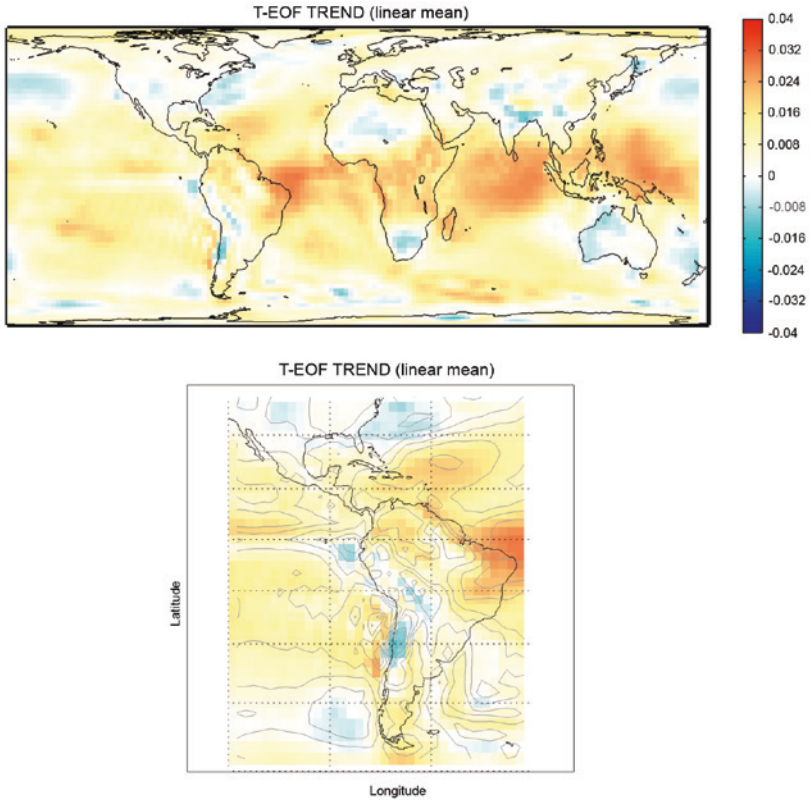

Source: Prepared by the authors.

The following figures show the different trends in air temperature for two point in the domain of interest. A comparison will show that air temperatures exhibit much greater variability for the location depicted in figure 1.102 than for the location depicted in figure 1.103. In both cases, however, there is a notable difference between the most significant local trend (in this case a linear adjustment) and the T-EOF trend.

FIGURE 1.102
TRENDS IN AIR SURFACE TEMPERATURES FOR ONE LOCATION ON THE COAST OF LATIN AMERICA AND THE CARIBBEAN
(Degrees centigrade)

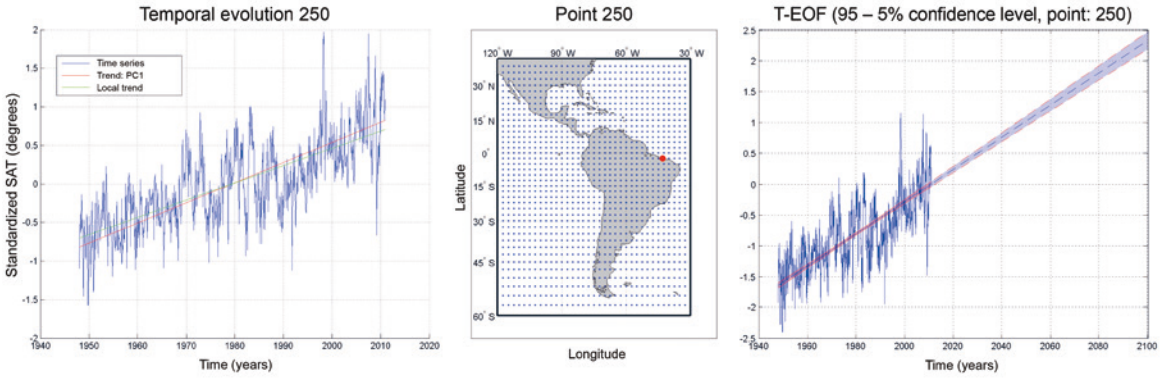

Source: Prepared by the authors.
Note: Right-hand panel: T-EOF for sea level rise (SLR). Central panel: Location of control point. Left-hand panel: Comparison of local and T-EOF trend calculations.

FIGURE 1.103
SURFACE AIR TEMPERATURE TRENDS FOR ONE LOCATION ON THE COAST OF LATIN AMERICA AND THE CARIBBEAN
(Degrees centigrade)

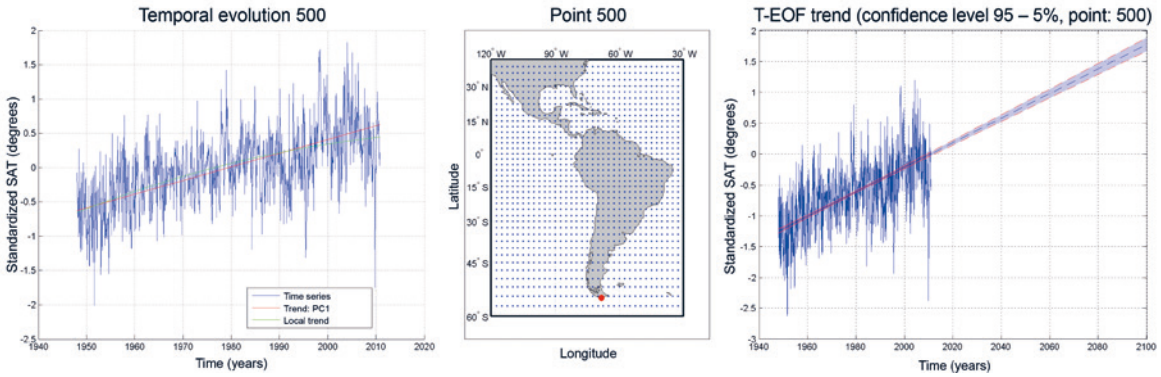

Source: Prepared by the authors.
Note: Right-hand panel: T-EOF trend. Central panel: Location of control point. Left-hand panel: Comparison of local and T-EOF trends.

Figure 1.104 depicts the equivalent mean linear trend for the two main time periods dealt with in this study. For most of the region, surface air temperatures will trend upward, with the exceptions being some areas along the Pacific coast of South America, where portions of the coastal areas of Peru, Ecuador and northern Chile exhibit null or slightly negative trends. A strong trend is observed in the Atlantic between 15ºN and 15ºS, where mean temperature increases of as much as 1.7 ºC and 3.8 ºC along the Brazilian coast are expected for 2040 and 2070, respectively, with the uncertainty bounds for a 95% confidence level amounting to 0.03ºC and 0.07ºC in the T-EOF regression (see figure 1.105 and figure 1.106).

FIGURE 1.104
EQUIVALENT MEAN LINEAR TREND IN AIR SURFACE TEMPERATURES: 2010-2040 AND 2040-2070
(Degrees centigrade/year)

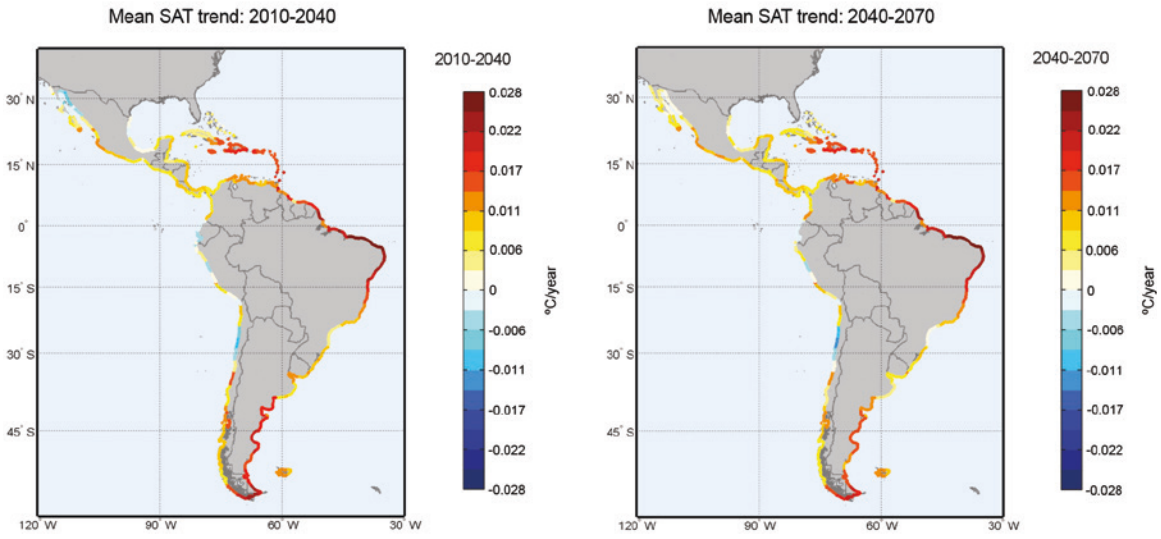

Source: Prepared by the authors.

FIGURE 1.105
VARIATION IN SURFACE AIR TEMPERATURES AND ASSOCIATED UNCERTAINTY BOUNDS: 2040
(Degrees centigrade)

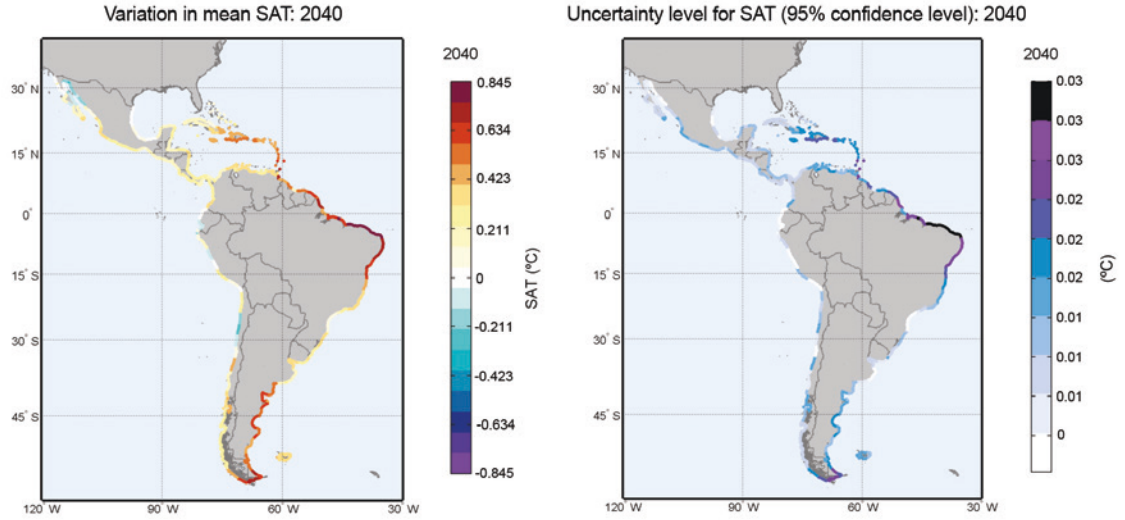

Source: Prepared by the authors.

FIGURE 1.106
VARIATION IN SURFACE AIR TEMPERATURES AND ASSOCIATED UNCERTAINTY BOUNDS: 2070
(Degrees centigrade)

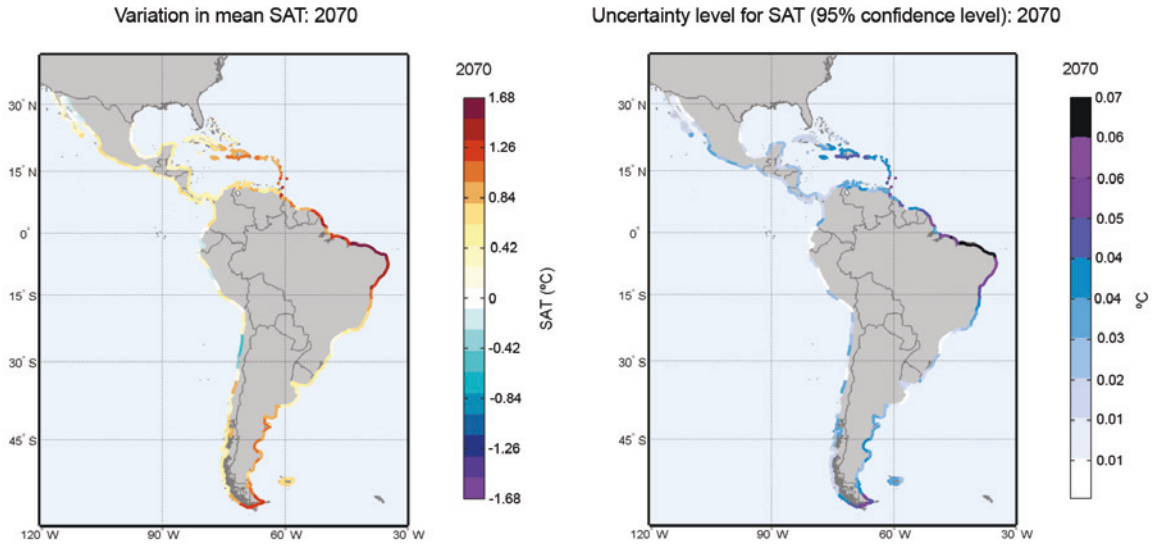

Source: Prepared by the authors.

Figure 1.107 shows the likelihood of an increase of over 1ºC in air surface temperature for the various time horizons.

FIGURE 1.107
LIKELIHOOD OF AN INCREASE IN AIR SURFACE TEMPERATURE OF 1ºC ALONG THE COASTS OF LATIN AMERICA AND THE CARIBBEAN: PRESENT, 2040, 2050 AND 2070

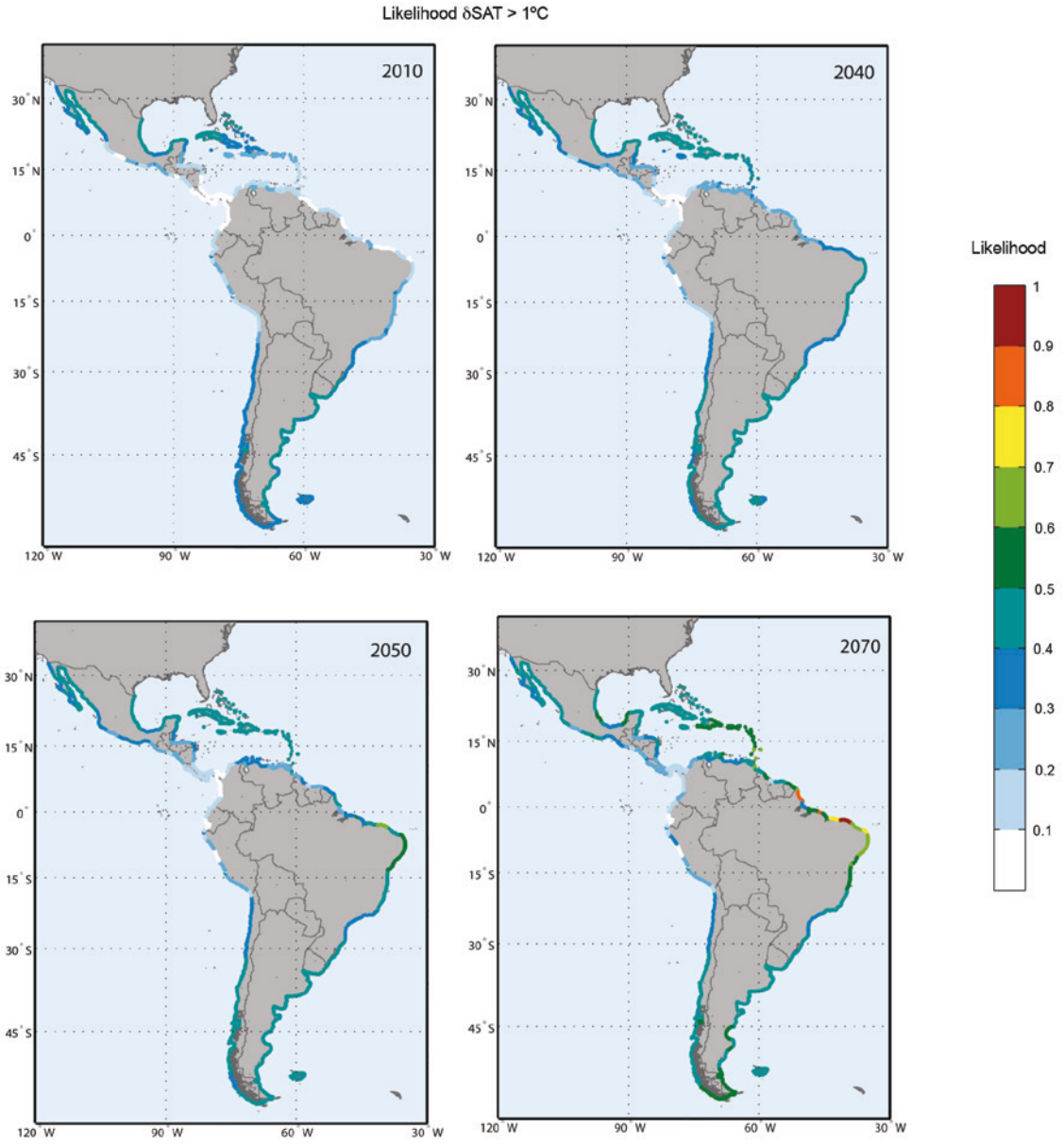

Source: Prepared by the authors.

5.2.6. Wind trends

Wind magnitude (the 0.9 quantile of wind speed at 10 m) and wind direction have both been analysed. Both wind speeds and directions have been fit to linear trends, so the local adjustment technique has been used for this analysis, since the T-EOF trend proved to be a spatially distributed linear trend.

5.2.6.1. Wind speed

The mean trend for the 0.9 quantile of wind speed at 10 m exhibits a great deal of spatial variability in the region (see figure 1.108), with upward and downward trends being registered in different locations. The largest increases are found for the southern tip of the continent, the coast of Uruguay, the Porto Alegre area in Brazil, Guatemala and El Salvador. The trend throughout northern Chile, Ecuador and northern Peru is clearly negative, however. The trend for the Atlantic coast in the southern hemisphere is, overall, positive while, for the Pacific coast, trends are stable or point to a decrease. The strongest trends are seen in two latitudinal belts: the subtropics, where the trade winds predominate, and the middle latitudes, where westerly winds flow towards polar low pressure areas.

FIGURE 1.108
MEAN TREND FOR THE 0.9 QUANTILE OF WIND SPEEDS AT 10 M: 2010-2070
(Metres/second/year)

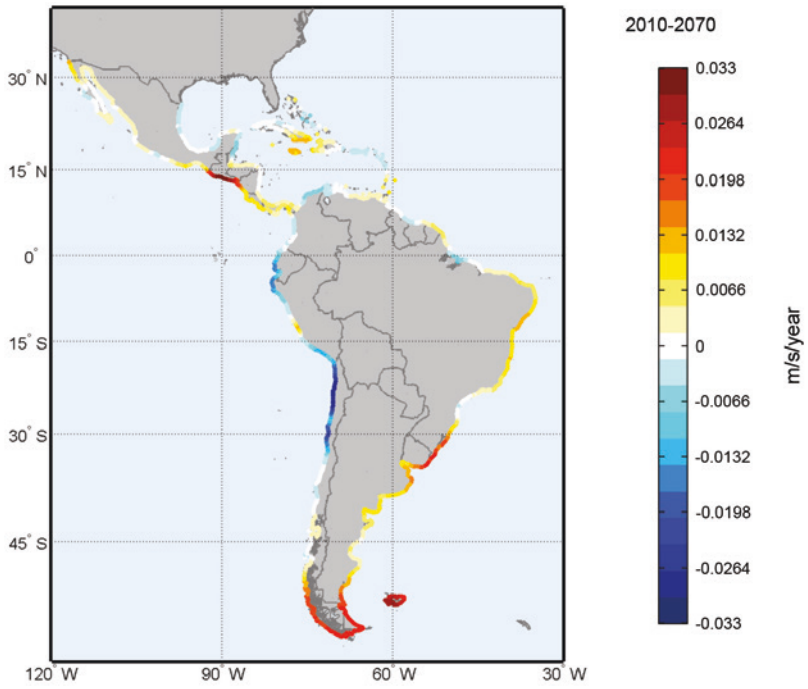

Source: Prepared by the authors.

FIGURE 1.109
VARIATION IN THE 0.9 QUANTILE OF WIND SPEEDS AT 10 M AND THE ASSOCIATED UNCERTAINTY BOUNDS: 2040
(Metres/second)

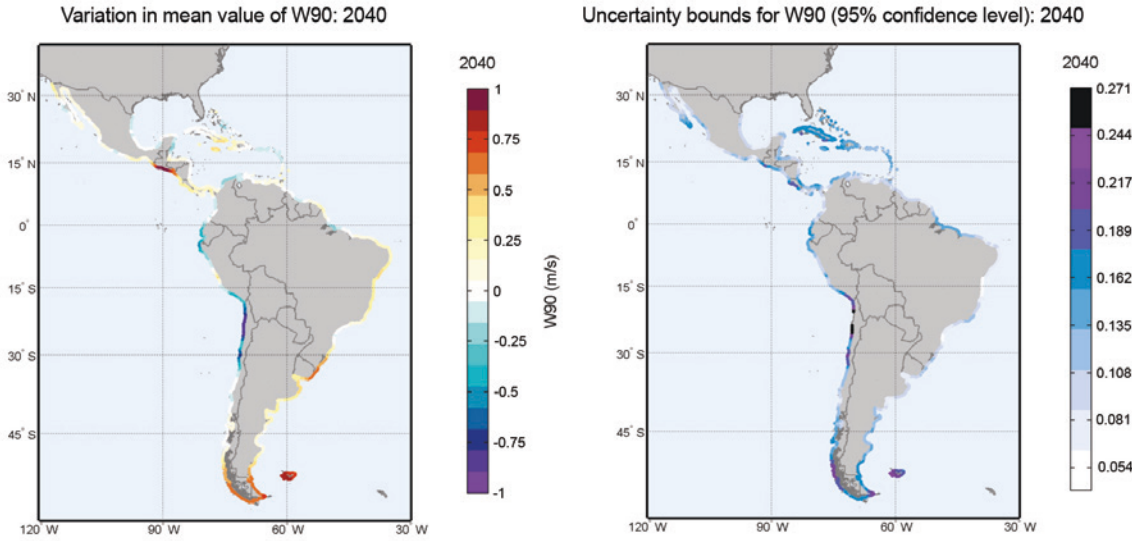

Source: Prepared by the authors.

FIGURE 1.110
VARIATION IN THE 0.9 QUANTILE OF WIND SPEEDS AT 10 M AND THE ASSOCIATED UNCERTAINTY BOUNDS: 2070
(Metres/second)

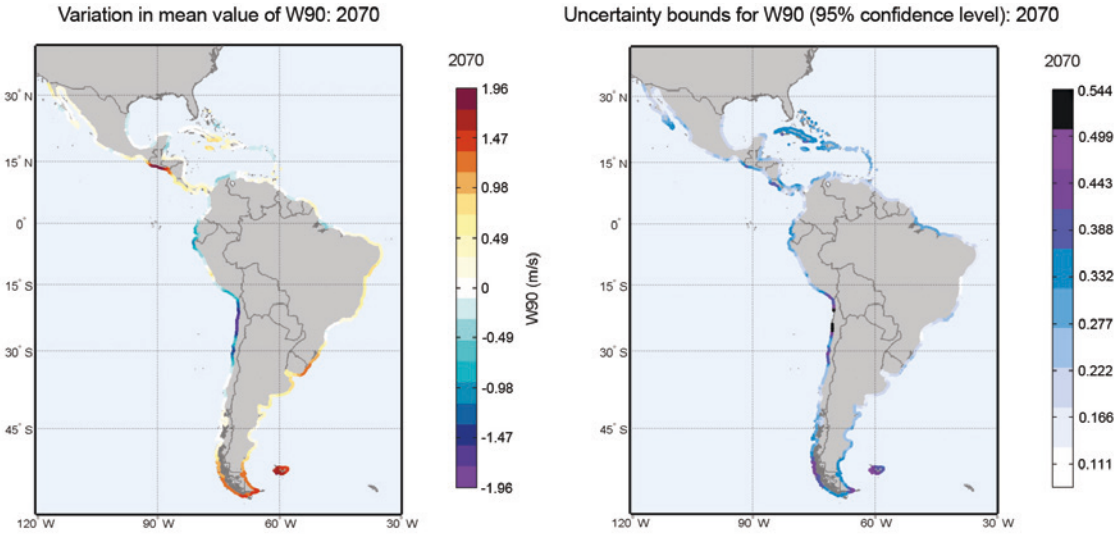

Source: Prepared by the authors.

5.2.6.2. Wind direction

Because wind directions are so highly variable, they have to be grouped into four main directional categories before any in-depth analysis is possible (see figure 1.111).

FIGURE 1.111
THE FOUR DIRECTIONAL CATEGORIES USED IN THE ANALYSIS OF WIND DIRECTION

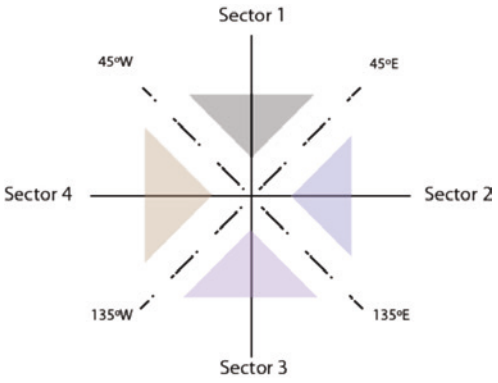

Northerly: between 45ºW and 45ºE.
Easterly: between 45ºE and 135ºE.
Southerly: between 135ºE and 135ºW.
Westerly: between 135ºW and 45ºW.

Source: Prepared by the authors.

The units of measurement are degrees, and a positive sign denotes a clockwise increase in the angle relative to the mean direction.

Figure 1.112 traces the trends calculated for the four sectors. The trend for northerly winds is generally positive (where they veer eastward) for the Pacific coast and negative (veering westward) along the Caribbean coast in the northern hemisphere, whereas there is greater variability in the southern hemisphere from one area to another. The strongest positive trends are seen along the Chilean and the northern Peruvian coasts.

The strongest trends in easterly winds are found along the Pacific coast, with offshore winds displaying a clear northward shift except in two areas: from Colombia down to Ecuador and in northern Chile. Along the Atlantic coast, the onshore winds exhibit a less definite trend. The easterlies in the vicinity of the peninsula of Baja California are veering towards the south (a positive clockwise increase).

The predominant trend in westerly winds in the southern hemisphere shows that they are veering northward, whereas, in the northern hemisphere, they are veering southward (except in the case of Cuba, where northerly winds are on the rise). The trends for the southern coasts of the Caribbean Sea are particularly strong.

Trends are not clear-cut in the case of southerly winds, with the exception of the southern Caribbean, where the winds are veering northward, and portions of the Mexican, Chilean and Cuban coasts, where they veer towards the east.

FIGURE 1.112
MEAN TREND IN CHANGES IN WIND DIRECTION IN THE NORTHERN, EASTER, SOUTHERN AND WESTERN SECTORS (POSITIVE CLOCKWISE MOVEMENT): 2010 AND 2070
(ºE/year)

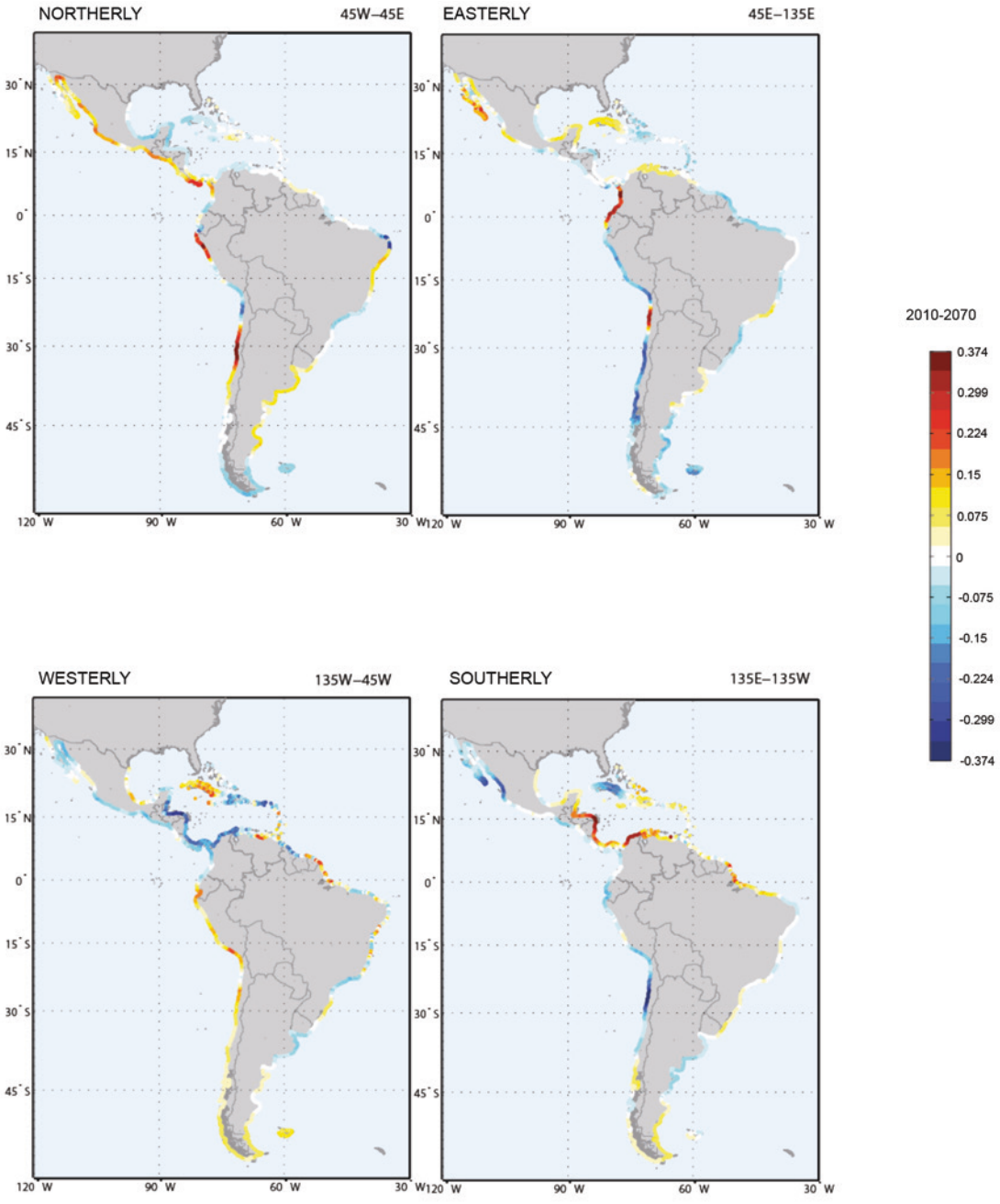

Source: Prepared by the authors.

5.3. Trends in coastal dynamics

5.3.1. Trends in wave activity

The data for wave activity have been fit to linear local trends, with a number of different variables being factored into the analysis for wave severity, wave height exceeded 12 hours per year (related to beach morphodynamics, as is explained in the chapter on impacts), mean monthly and monthly maximum significant wave heights, and wave direction (calculated as the trend associated with the mean direction of energy flow).

5.3.1.1 Trends in significant wave heights exceeded 12 hours per year

The indicator of the significant wave height exceeded during 12 hours per year (one of the indicators for annual extremes) has, for the most part, yielded upward trends (see figure 1.113), with the highest values being recorded for northern Mexico, northern Argentina, Uruguay and southern Brazil; the mean values for all those areas are around 3 cm per year. These trends indicate that Hs_{12} will have increased by as much as 0.9 m by the year 2040 and by as much as 1.8 m by the year 2070 at these locations (see fi ure 1.114 and fi ure 1.115). Areas with negative trends include the Gulf of Mexico and the Pacific coast in the southern hemisphere, while the northern coast of South America exhibits fairly flat negative and positive trends or stable trends at different locations.

FIGURE 1.113
TRENDS IN SIGNIFICANT WAVE HEIGHT EXCEEDED 12 HOURS PER YEAR (HS_{12}): 2010-2070
(Metres/year)

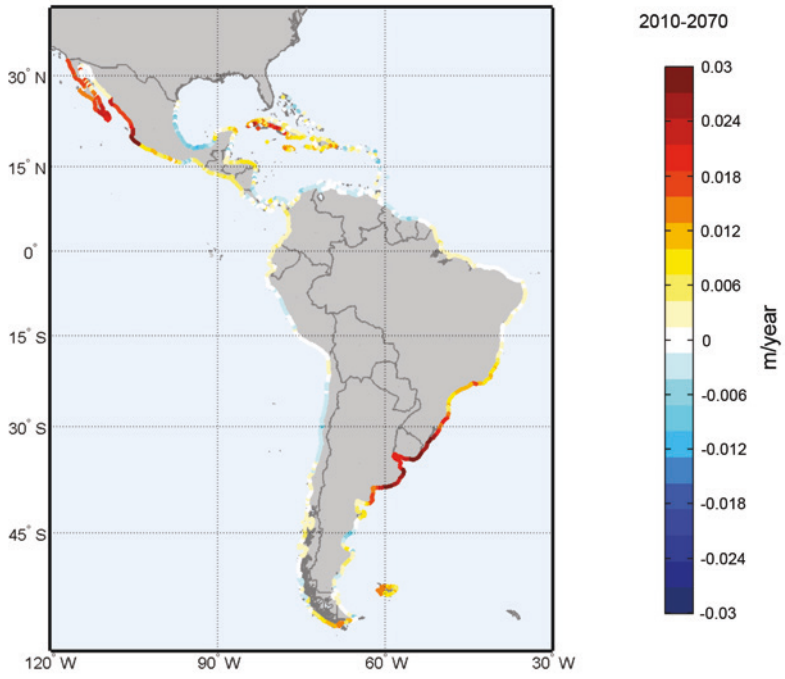

Source: Prepared by the authors.

FIGURE 1.114
VARIATION IN SIGNIFICANT WAVE HEIGHTS EXCEEDED 12 HOURS PER YEAR AND THE ASSOCIATED UNCERTAINTY BOUNDS: 2040
(Metres)

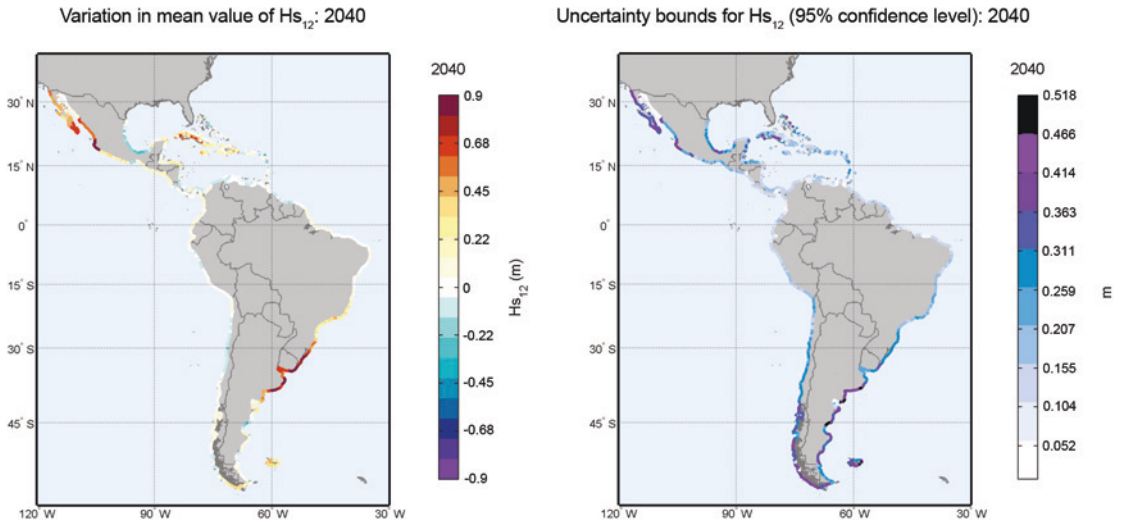

Source: Prepared by the authors.

FIGURE 1.115
VARIATION IN SIGNIFICANT WAVE HEIGHTS EXCEEDED 12 HOURS PER YEAR AND THE ASSOCIATED UNCERTAINTY BOUNDS: 2070
(Metres)

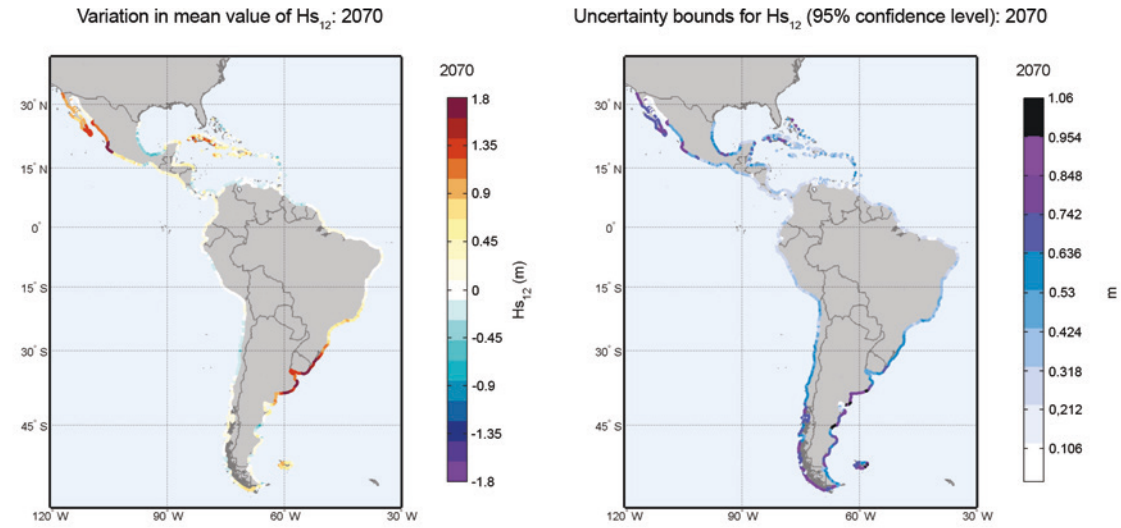

Source: Prepared by the authors.

A comparison of the effect of this variation from the mean values calculated for Hs_{12} in the section on the marine climate in Latin America and the Caribbean indicates that the areas in which the biggest increases (in magnitude) are to be expected are the same areas in which these increases represent the largest percentage rise relative to current values. This means that the impact on coastal dynamics will be even greater, since the largest increases will not be occurring in the areas with the

biggest waves but instead in areas where the waves are smaller. This, in turn, will translate into bigger impacts on the region's coasts because the beaches and maritime structures in these areas are suited to lower levels of wave activity.

In percentage terms, the greatest increases relative to current wave conditions can be expected along the coasts of the Plate River and adjacent areas and along the central Pacific coast of Mexico. Somewhat smaller increases will be seen on the coasts of the islands of Cuba, the Dominican Republic Jamaica and Haiti.

Figure 1.116 shows the probability that Hs_{12} will increase by more than 0.5 m, which is closely linked to the corresponding beach equilibrium profiles.

FIGURE 1.116
LIKELIHOOD OF AN INCREASE OF MORE THAN 0.5 M IN HS_{12}: 2010, 2040, 2050 AND 2070

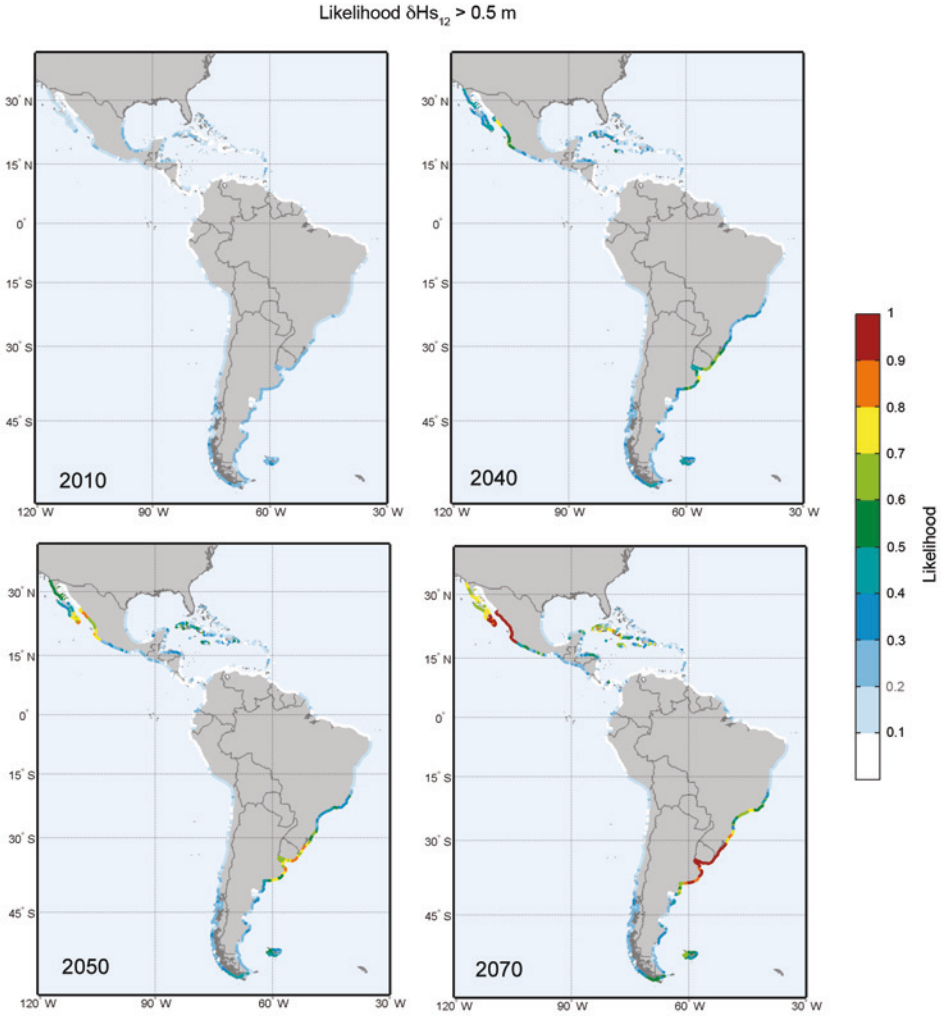

Source: Prepared by the authors.

TABLE 1.6

VARIATION IN THE LIKELIHOOD OF THE CHANGE IN HS_{12} EXCEEDING 50 CM RELATIVE TO 2010 IN THE ESTABLISHED TIME HORIZONS IN VARIOUS LOCATIONS IN THE REGION

			Variation in the likelihood of an increase in excess of 50 cm in Hs_{12} relative to 2010 levels		
Study unit	**Longitude**	**Latitude**	**2040**	**2050**	**2070**
Rio de Janeiro (BRA)	-43.23	-22.99	0.13	0.17	0.39
Santos (BRA)	-46.24	-23.93	0.18	0.30	0.50
Montevideo (URY)	-56.00	-34.86	0.31	0.45	0.73
Concepcion (CHL)	-73.09	-36.83	0.01	0.01	0.02
Valparaiso (CHL)	-71.63	-32.96	-0.01	-0.01	-0.01
Arica (CHL)	-70.45	-18.38	0.02	0.02	0.03
Chorrillos (PER)	-77.04	-12.09	-0.01	-0.01	-0.01
Talara (PER)	-81.26	-4.63	0.00	0.00	0.00
Machala (ECU)	-80.28	-3.40	0.07	0.09	0.11
La Libertad (ECU)	-80.78	-2.36	0.01	0.01	0.01
Bahía Solano (COL)	-77.38	6.05	0.00	0.01	0.03
Los Santos (PAN)	-80.26	7.34	0.01	0.01	0.02
San Jose (CRI)	-83.97	9.29	0.01	0.01	0.01
Managua (NIC)	-86.57	11.88	0.07	0.11	0.14
Acapulco (MEX)	-99.73	16.78	0.09	0.13	0.25
Ensenada (MEX)	-116.69	31.74	0.27	0.36	0.60
Cabo (MEX)	-109.85	22.98	0.57	0.65	0.78
Veracruz (MEX)	-96.02	19.05	-0.04	-0.07	-0.10
Cancun (MEX)	-86.85	21.04	0.03	0.06	0.20
P. Plata (DOM)	-70.66	19.70	0.06	0.08	0.12
Bridgetown (BRB)	-59.56	13.20	-0.09	-0.10	-0.11
Caracas (VEN)	-67.02	10.59	0.00	-0.01	-0.01
Georgetown (GUY)	-57.95	6.70	-0.02	-0.03	-0.04
Fortaleza (BRA)	-38.49	-3.81	0.00	0.00	0.00
Maceio (BRA)	-35.60	-9.52	0.00	0.01	0.01
P. Segura (BRA)	-39.00	-16.28	0.01	0.01	0.03
P. Sta Cruz (ARG)	-68.26	-50.14	-0.03	-0.04	-0.05
I. Taggart (CHL)	-75.58	-49.45	-0.01	-0.01	-0.02

Source: Prepared by the authors.

5.3.1.2. Trends in mean monthly heights

Mean monthly heights are an indicator of changes in mean wave conditions, which have an influence on various areas, including port operations.

The results (see figures 1.117, 1.118 and 1.119) point to upward trends in wave heights except along the southern coast of the Caribbean Sea and the Gulf of Mexico, where wave heights are declining at a mean rate of 2 mm/year, and the coasts of the Bolivarian Republic of Venezuela and Puerto Rico, where wave heights are virtually stable. The biggest upswings in wave heights are, once again, found along the Pacific coast of Mexico, Uruguay and southern Brazil and, in this case, also along the southern coast of Chile and, to a lesser extent, the southern coast of Peru. Expected increases amount to 0.3 m for 2040 and 0.6 m for 2070 with a margin of uncertainty of less than 0.1 m in both cases.

Interestingly, the area in which the greatest decrease for this variable is to be expected is the southern coast of the Caribbean Sea, whereas, in the case of Hs_{12}, it was the Gulf of Mexico.

FIGURE 1.117
MEAN TRENDS IN MEAN MONTHLY SIGNIFICANT WAVE HEIGHTS BETWEEN 2010 AND 2070
(Metres/year)

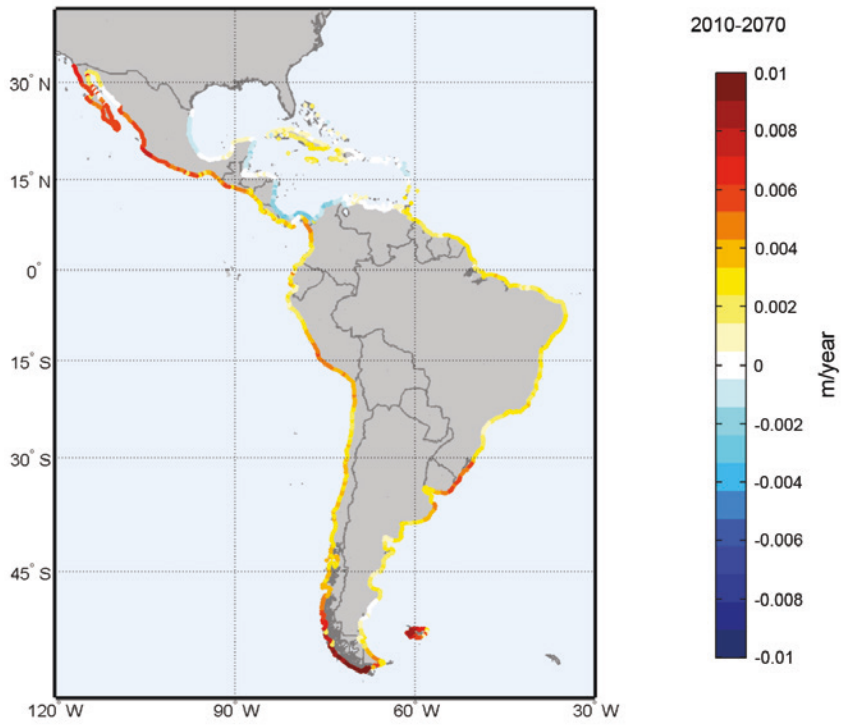

Source: Prepared by the authors.

FIGURE 1.118
VARIATION IN MEAN MONTHLY SIGNIFICANT WAVE HEIGHTS AND THE ASSOCIATED UNCERTAINTY BOUNDS: 2040
(Metres)

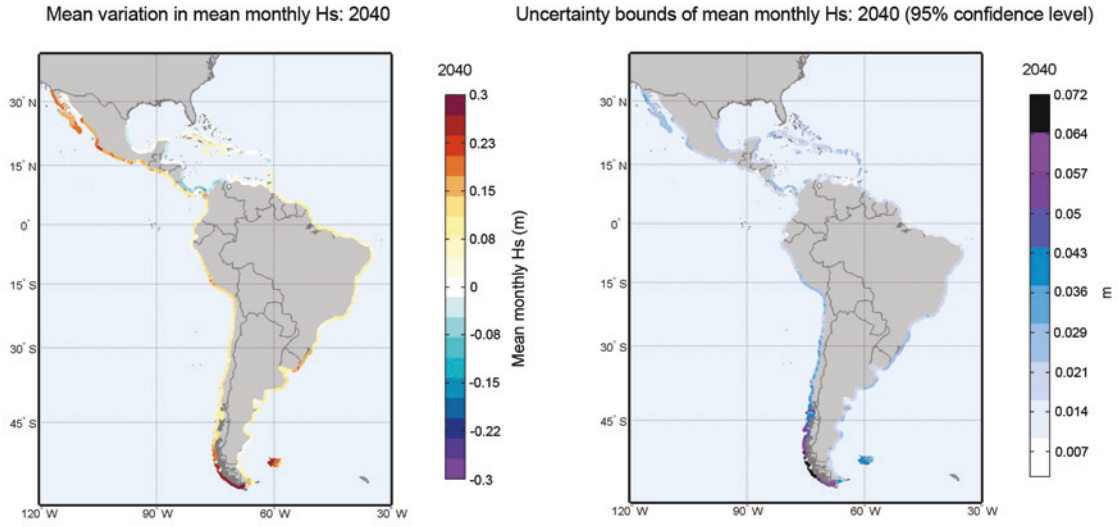

Source: Prepared by the authors.

FIGURE 1.119
VARIATION IN MEAN MONTHLY SIGNIFICANT WAVE HEIGHTS AND THE ASSOCIATED UNCERTAINTY BOUNDS: 2070
(Metres)

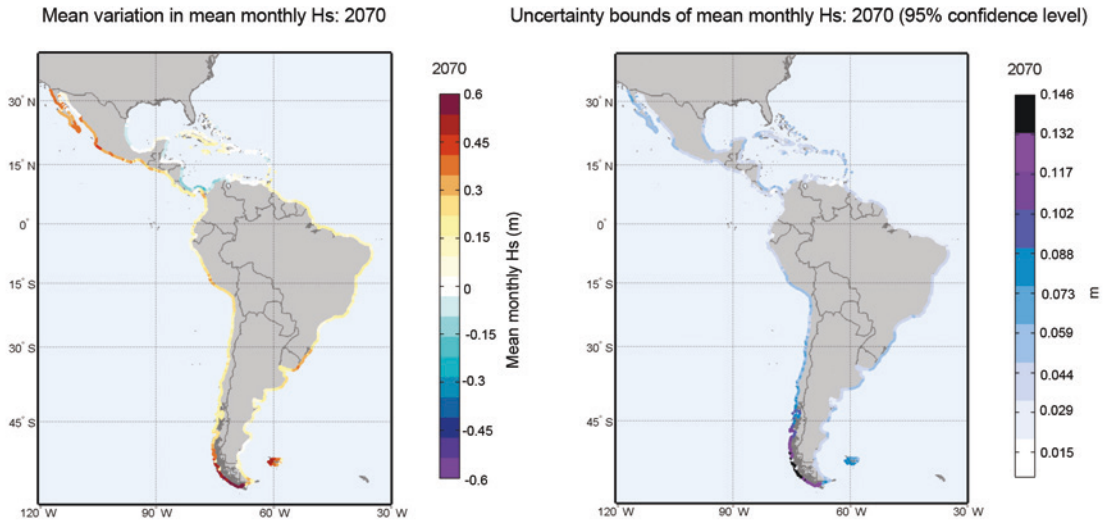

Source: Prepared by the authors.

Figure 1.120 shows the probabilities for a variation in excess of 0.2 m in mean monthly Hs in 2010 and in 2040 and 2070. A comparison of the likelihood of a variation in excess of 0.5 m in Hs_{12} (see figure 1.116) and in the mean monthly Hs indicates that, while the likelihood of this occurring along the Pacific coast of Mexico increases in both cases, for the other locations in which the future level of the Hs_{12} variable is known, for all intents and purposes, the same type of increase in mean wave conditions will not occur even in cases where mean wave heights change less.

In the northern Caribbean islands (see the information for Cuba), sizeable increases in the probabilities do not appear in the means but are, on the other hand, apparent at the high end of the wave spectrum (i.e., Hs_{12}).

In southern Brazil, an increase of 0.5 m is also more likely in Hs_{12} than in mean wave activity. However, in the southern portion of the continent (the area where the highest waves in the region are seen), considerable increases in the likelihood of mean conditions rising by more than 0.2 m are expected, whereas this is not the case for the upper strata of Hs.

FIGURE 1.120
LIKELIHOOD OF INCREASES IN EXCESS OF 0.2 M IN MEAN MONTHLY SIGNIFICANT WAVE HEIGHT: 2010, 2040, 2050 AND 2070

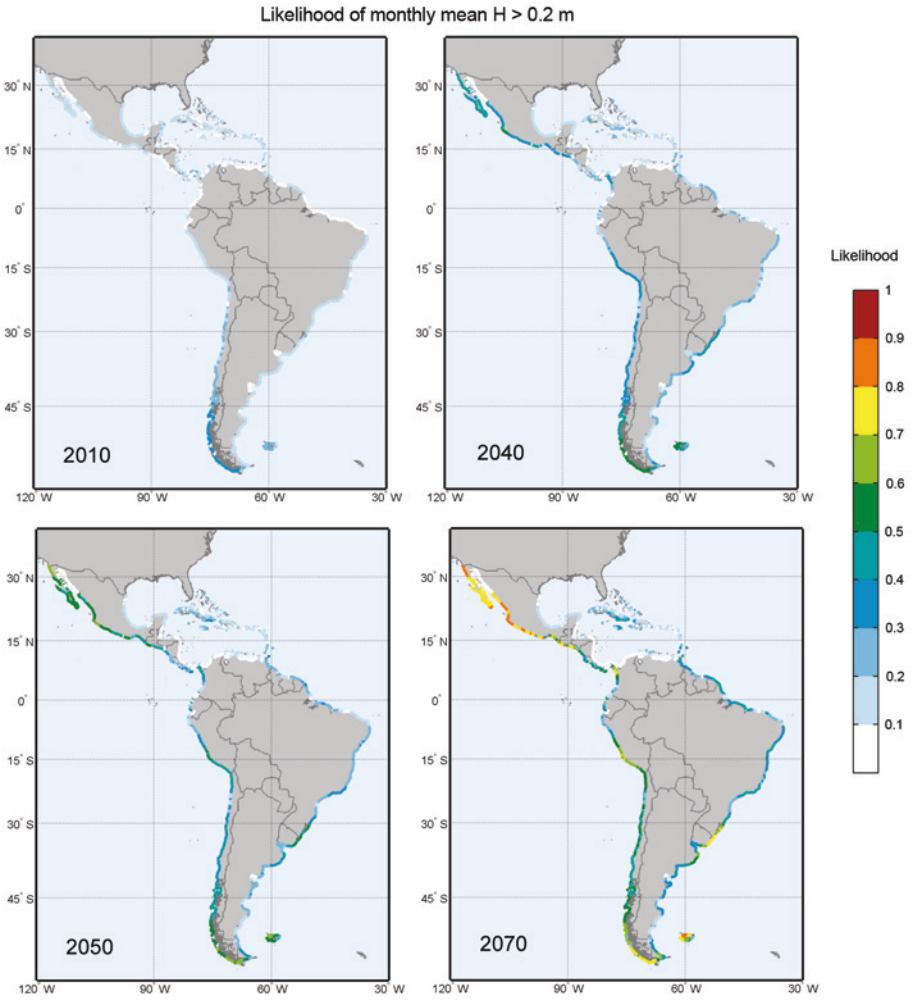

Source: Prepared by the authors.

5.3.1.3. Trends in mean directions of energy flow

An analysis of trends in mean energy flows (MEF) shows up how the directional origins of waves are shifting. This variable is closely linked to beach equilibria and configurations and to sediment transport.

The results point to a strong northward shift (a negative trend in clockwise terms) in the directional origin of waves reaching Argentina that have been generated as swells in the low-pressure areas in the southern hemisphere that then round Cape Horn. Along the rest of the Atlantic coast, on the other hand, wave origins are shifting southward (positive trend). The coasts of the Caribbean Sea are subject to quite slight or stable trends, although there is a moderate shift eastward. Along the Pacific coasts of the Central American countries, there is a general northward shift, while a southward shift is observed along the coasts of the peninsula of Baja California.

The greatest changes are expected to occur in southern Argentina and northern Mexico. While the beaches of southern Argentina are not a high-level resource because of their latitude, the beaches of northern Mexico are quite another matter. These shifts and their effect on beaches are analysed in the project document on coastal impacts and climate change as it relates to risk factors associated with the region's beaches.

FIGURE 1.121
MEAN TRENDS IN SHIFTS IN MEAN ENERGY FLOWS: 2010-2070
(ºE/year)

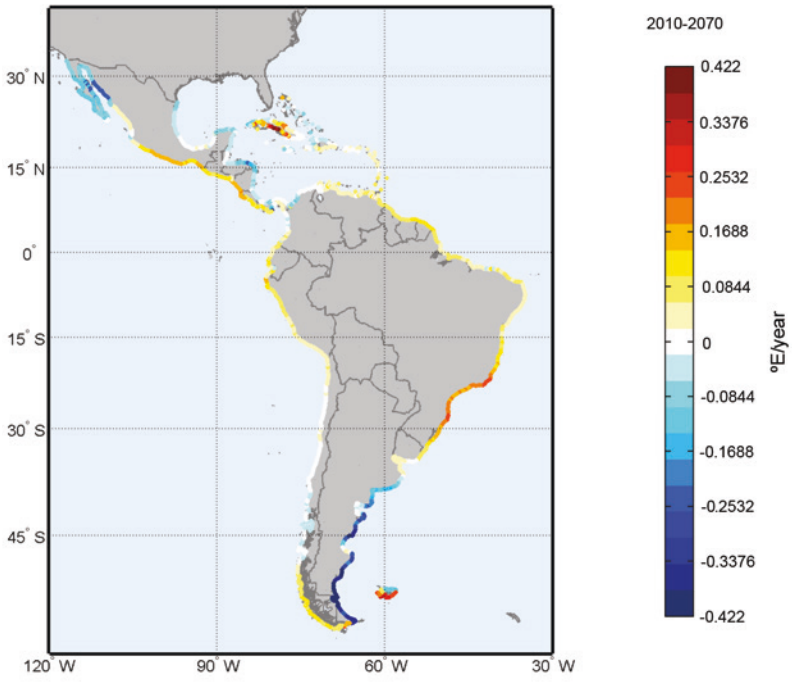

Source: Prepared by the authors.

FIGURE 1.122
VARIATION IN THE DIRECTION OF MEAN ENERGY FLOW AND THE ASSOCIATED UNCERTAINTY BOUNDS: 2040
(°E)

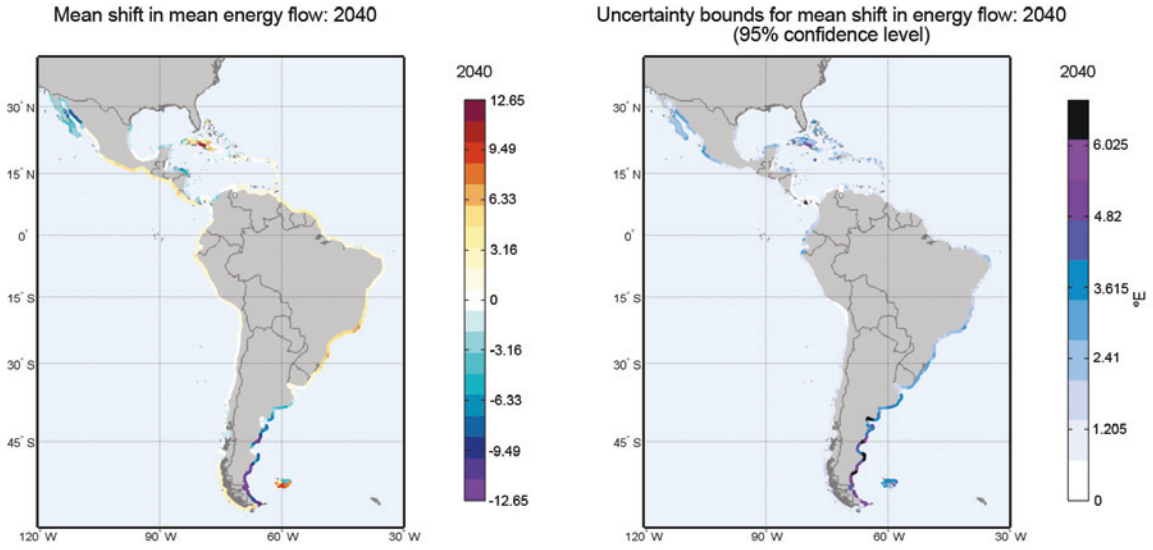

Source: Prepared by the authors.

FIGURE 1.123
VARIATION IN THE DIRECTION OF MEAN ENERGY FLOW AND THE ASSOCIATED UNCERTAINTY BOUNDS: 2070
(°E)

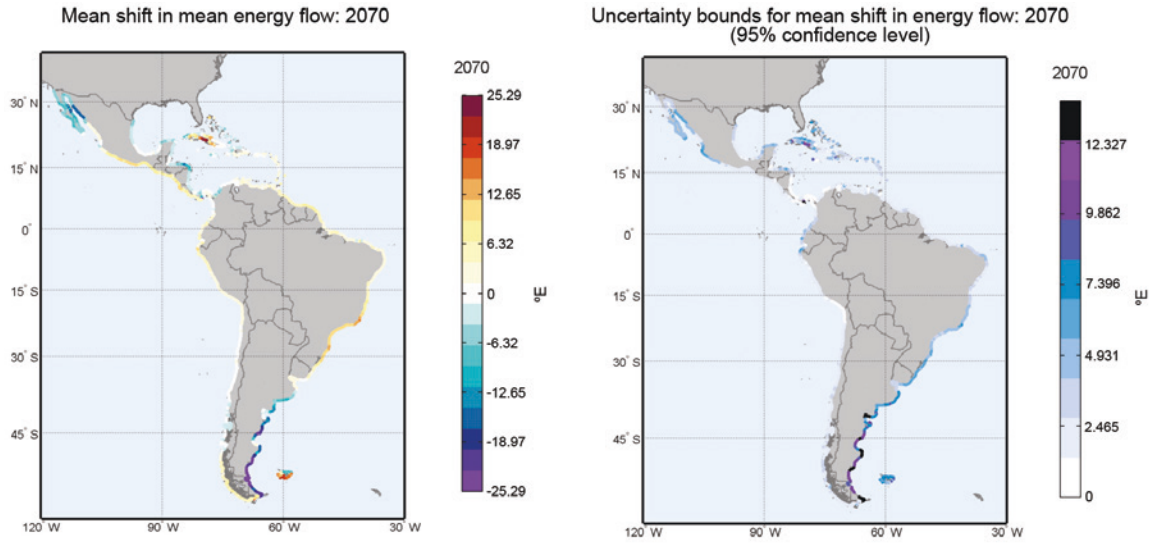

Source: Prepared by the authors.

5.4. Trends in extreme events

Extreme events are a crucial factor given the potential damage that they can cause in coastal regions. Extreme wave activity can impact ports, beaches, shipping, coral reefs and coastal erosion processes and is frequently associated with storm surges. Wave activity, storm surges and flooding are all phenomena that have to be explored as part of any analysis of climate change. In this study, the generalized extreme value (GEV) distribution is fit to non-stationary time series for this purpose, as discussed earlier, and a parameter that captures the long-term trend is introduced where the fit is significant. The variables being focused on here are the extreme values for significant wave height and storm surges. In both cases, the results for seasonal and annual trends are mapped out in spatial terms and for some of the return periods for the 2040 and 2070 time horizons, although the trends were calculated for 50-, 100-, 250- and 500-year return periods as well.

In addition, in order to take a more detailed looked at the issue of extreme events, a comparative analysis has been made of return periods at five specific locations in the region that differ a great deal from one another in terms of wave activity and storm surges.

5.4.1. Trends in extreme wave events

The results for the calculations of annual trends (see figure 1.124) are similar to the results for monthly maximum heights. The overall trend is clearly upward, with the strongest trends being seen in southern Brazil and the coasts of Uruguay, Cape Horn and the Pacific coast of Mexico, with values of between 1 and 1.7 cm/year. Trends along the northern Argentine coast are somewhat less steep. Along the southern coast of the Caribbean Sea, trends are slightly negative (lower wave heights), as is also true of some locations along the coasts of the eastern Caribbean islands. In southern Chile, where earlier calculations pointed to stable (null) or slightly negative trends, the adjustment of the extreme values does not yield any statistically significant trend.

FIGURE 1.124
LONG-TERM ANNUAL TRENDS IN EXTREME WAVE EVENTS: 2010-2040
(Cm/year)

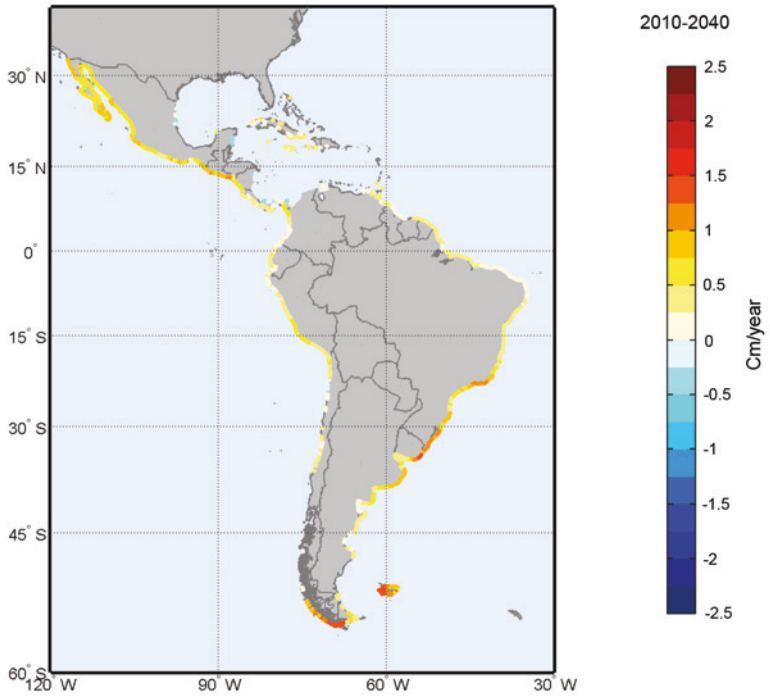

Source: Prepared by the authors.
Note: Black dots signify locations at which no statistically significant trend has been detected.

The seasonal trends (see figure 1.125) reflect a clear decline in wave heights from March to May along the southern coast of the Caribbean Sea, while seasonal trends are less marked during the rest of the year. Positive (increased wave height) trends are stronger along the Atlantic coast from March to August, however, and especially so during the spring. They are less marked during the rest of the year, although they remain positive. The strongest trends along the northern Pacific coast are seen during the winter, which is also when the strongest storms occur in that zone (see figure 1.26 and figure 1.27). Strangely enough, the lows in the stormiest areas of the continent (southern Chile and southern Argentina) occur during the summer, which is the season during which the area experiences its strongest storms.

FIGURE 1.125
LONG-TERM SEASONAL TRENDS IN EXTREME WAVE EVENTS
(Cm/year)

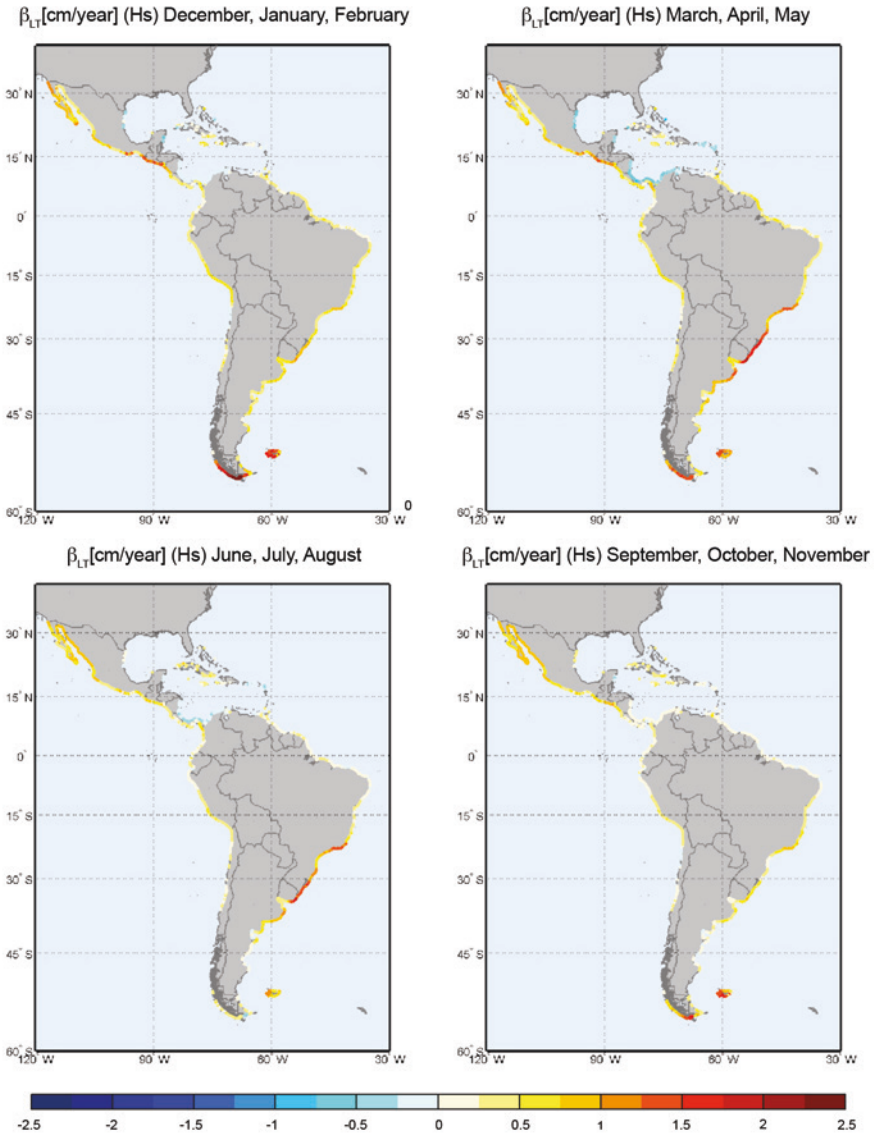

Source: Prepared by the authors.

The foreseeable trends in wave heights for the different return periods analysed in the earlier descriptive section on coastal dynamics have been calculated for significant wave heights for 50-, 100-, 250- and 500-year return periods for the two main time horizons. Figure 1.126 depicts heights for a 50-year return period for both time horizons, with the highest extremes rising by as much as 1 m between 2040 and 2070. Figure 1.127 traces the heights for a 500-year return period in 2040. As the gradation in colours shows, there is a gradual decrease in wave heights as one moves closer and closer to the equator.

FIGURE 1.126
SIGNIFICANT WAVE HEIGHTS FOR A 50-YEAR RETURN PERIOD (MEAN VALUE): 2040 AND 2070
(Metres)

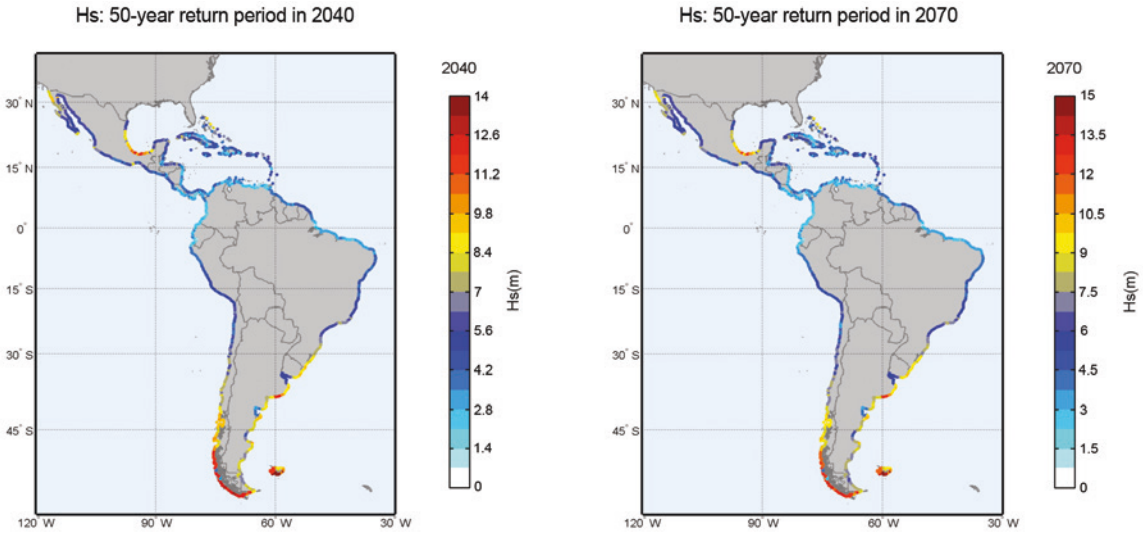

Source: Prepared by the authors.

FIGURE 1.127
SIGNIFICANT WAVE HEIGHTS FOR A 500-YEAR RETURN PERIOD (MEAN VALUE): 2040
(Metres)

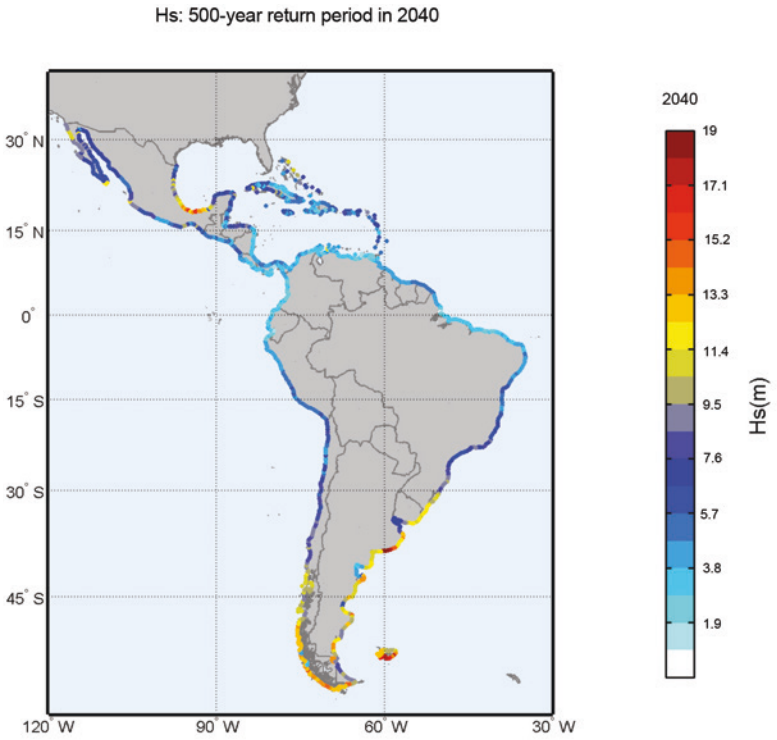

Source: Prepared by the authors.

In order to arrive at a more accurate analysis of how extreme wave heights will compare with current conditions, the best approach is to construct an index to gauge the change in wave heights between the return period calculated for 2040 and 2070 and a mean reoccurrence period of 500 years. This index (referred to as the "security index" in the chapter on impacts on ports and the associated risk factors) is calculated as follows:

$$SI=\frac{1/500}{1/N}=\frac{N}{500} \qquad (1.10)$$

Where N represents the new return period associated with the wave heights that currently have a 500-year return period.

The measurements obtained using this index are shown in figure 1.128 for the year 2040. A value of less than 1 means that the new return period is shorter than 500 years (i.e., in the case of wave heights at that location for which the probability of waves occurring in excess of that height is 1/500, the probability of waves occurring that exceed that benchmark by the horizon year will be greater or, in other words, the return period will be shorter). Values greater than 1 signify that the return period during the horizon year will be greater than 500 years, which would mean that the wave height measured on that index is more extreme because wave heights have declined in step with a downward trend.

FIGURE 1.128
FORESEEBLE VARIATION IN VALUES FOR 500-YEAR RETURN PERIODS: 2040

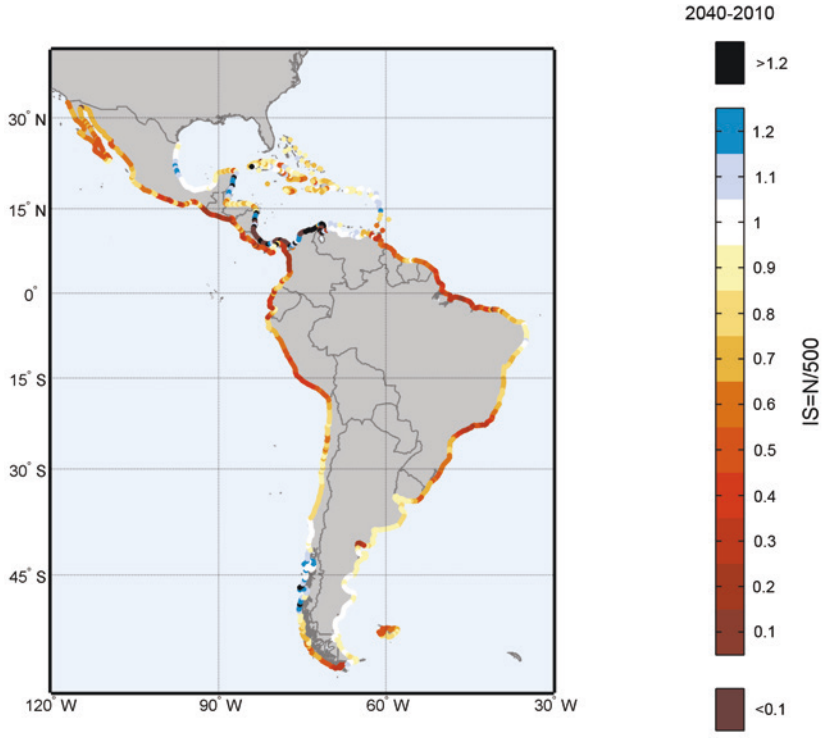

Source: Prepared by the authors.

This approach provides fresh insights regarding extreme wave events in the region. It shows that the greatest variations in return periods are not occurring in the areas with the strongest wave height trends but rather in areas where the trends are more gradual and where wave heights are currently lower. For example, the security index values registered for the northern coast of Brazil are higher than they are for that country's southern coast, even though the upward trends for the northern coast are much more gradual than they are for the southern coast (see figure 1.124). The implications of this situation for the safety ratings of maritime structures are discussed in the project documents on climate change impacts and risks for the region's ports.

In order to take a closer look at the variation in extreme wave activity and to assess it in terms of the modification of the distribution function, a comparative analysis of five different locations in the region has been conducted. The selected locations are shown in figure 1.129, while their coordinates are given in table 1.7. These are discrete areas in different countries where the coastal dynamics differ considerably.

FIGURE 1.129
A COMPARATIVE ANALYSIS OF CLIMATE-CHANGE-RELATED EXTREME WAVE EVENTS AS MEASURED BY RETURN PERIODS AND ASSOCIATED WAVE HEIGHTS AT FIVE SEPARATE LOCATIONS

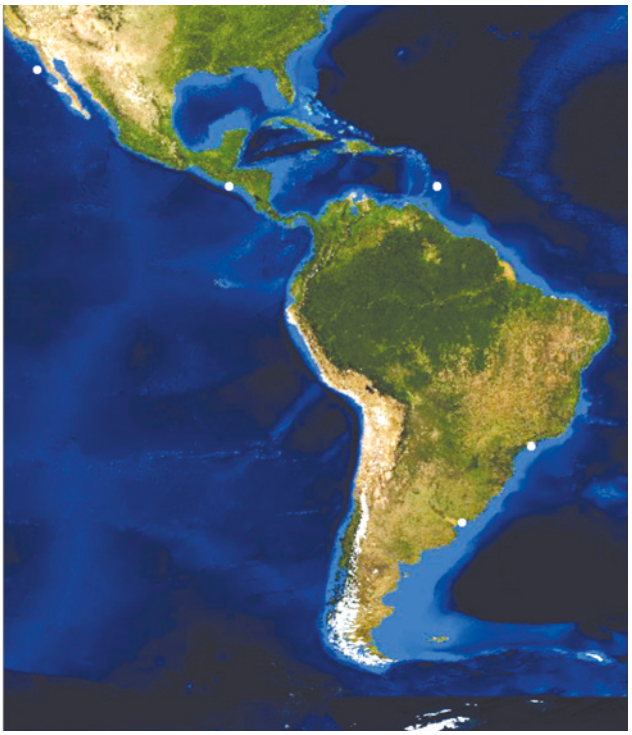

Source: Prepared by the authors.

TABLE 1.7
GEOGRAPHIC COORDINATES (REFERENCE: ELIPSOIDE WGS84) OF FIVE LOCATIONS USED IN A COMPARATIVE ANALYSIS OF EXTREME WAVE EVENTS

Location	Id point	Longitude	Latitude
Sao Paulo	332	-46.24	-23.93
Montevideo	373	-56.00	-34.86
La Libertad	709	-89.40	13.48
Baja California	859	-115.87	30.31
Barbados	900	-59.56	13.20

Source: Prepared by the authors.

While the spatial maps show the mean value for the trend obtained for each variable, the current statistical distribution and the statistical distribution for the two main time horizons (2040 y 2070) have been calculated for each location. Thus, for example, at one of the selected locations (Baja California), figure 1.130 shows how the density function for wave heights shifts relative to 2010 in the two horizon years as a result of an upward trend of approximately 1.25 cm/year (see figure 1.124).

FIGURE 1.130
PROBABILITY DENSITY FUNCTIONS FOR ONE LOCATION ON THE COAST OF THE LATIN AMERICAN AND CARIBBEAN REGION (BAJA CALIFORNIA)

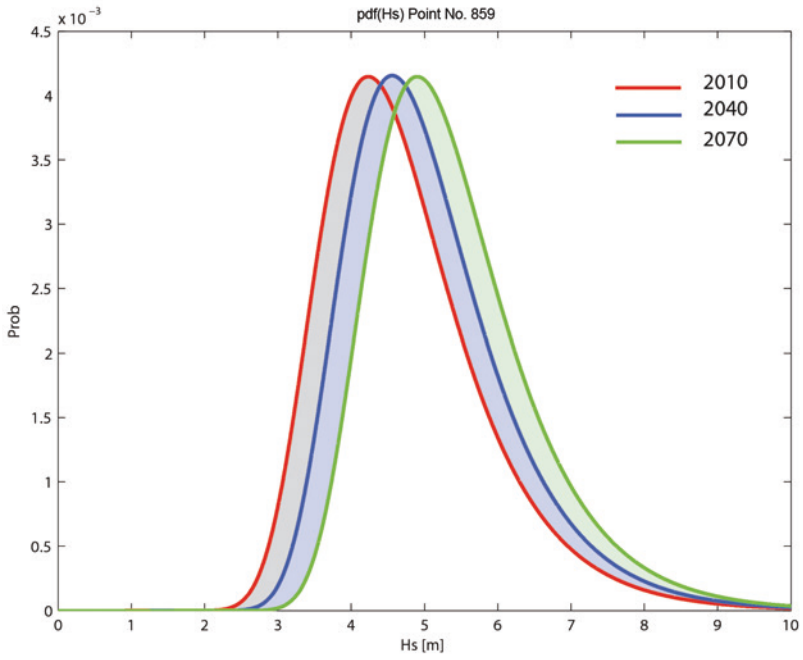

Source: Prepared by the authors.

This shift in the density function implies that the extremes (i.e., the tail of the distribution) are also shifting towards greater and greater wave heights. As shown in figure 1.131, for a significant wave threshold of 7 m, the likelihood of that threshold height being exceeded (represented by the shaded area below the distribution curve) increases year by year, rising from 0.042 to 0.087 between 2010 and 2070. This probability translates into reductions in the return period from somewhat less than 24 years at present to 17 years in 2040 and 11.5 years in 2070.

FIGURE 1.131
LIKELIHOOD THAT A 7M SIGNIFICANT WAVE HEIGHT WILL BE EXCEEDED AND THE ASSOCIATED RETURN PERIODS FOR ONE LOCATION IN LATIN AMERICA AND THE CARIBBEAN (BAJA CALIFORNIA)

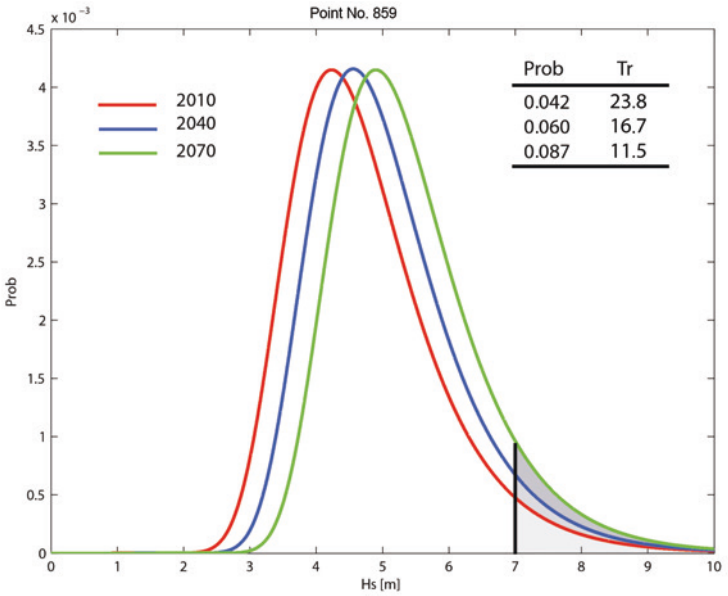

Source: Prepared by the authors.

A comparison of the 50-, 100-, 250- and 500-year return periods for the five selected locations indicates that, while there is a downward trend in wave heights for all of them, the reduction in return periods (or, inversely, the increase in the likelihood that they will be exceeded) varies significantly. Whereas at point No. 332 (São Paulo), the 50-year return period is expected to shrink to around 7 years by 2070, the return period for point No. 900 (Barbados) is expected to amount to 39 years. The wave heights for a 50-year return period at present (5 m and 4.89 m for these two locations, respectively) are projected to be 5.54 m and 4.94 m in 2070.

A comparison of point No. 373 (Montevideo) and point No. 900 (Barbados) indicates that the reductions in return periods are fairly similar (the 50-year return periods will decline to 35 years and 39 years in 2070, while the 500-year return periods will fall to 389 and 361 years, respectively). The increases in wave heights, on the other hand, for 2070 are projected to amount to 39 cm for Montevideo but just 5 cm for Barbados for a 50-year return period. This indicates that the distribution of extreme values is far more limited in the case of Barbados (see figure 1.44 for the form parameter for the extreme wave distribution) than it is for Montevideo.

TABLE 1.8
VARIATION IN RETURN PERIODS 50, 100, 250 AND 500-YEAR FOR 2040 AND 2070 AT FIVE LOCATIONS

	Tr=50			Tr=100			Tr=250			Tr=500		
Id	**2010**	**2040**	**2070**	**2010**	**2040**	**2070**	**2010**	**2040**	**2070**	**2010**	**2040**	**2070**
Sao Paulo	50	18	7	100	33	12	250	71	24	500	129	40
Montevideo	50	42	35	100	85	72	250	218	189	500	442	389
La Libertad	50	17	6	100	32	11	250	75	24	500	144	43
Baja California	50	33	22	100	67	44	250	167	111	500	333	222
Barbados	50	44	39	100	87	77	250	215	185	500	424	361

Source: Prepared by the authors.

TABLE 1.9
VARIATION IN WAVE HEIGHTS FOR 50, 100, 250 AND 500-YEAR RETURN PERIODS FOR 2040 AND 2070 AT FIVE LOCATIONS

	Hs (Tr=50)			Hs(Tr=100)			Hs(Tr=250)			Hs(Tr=500)		
Id	**2010**	**2040**	**2070**	**2010**	**2040**	**2070**	**2010**	**2040**	**2070**	**2010**	**2040**	**2070**
Sao Paulo	5.00	5.27	5.54	5.16	5.43	5.71	5.35	5.63	5.91	5.49	5.76	6.05
Montevideo	6.48	6.67	6.87	7.28	7.47	7.67	8.48	8.67	8.87	9.51	9.71	9.90
La Libertad	3.63	3.88	4.13	3.78	4.02	4.27	3.96	4.21	4.45	4.10	4.34	4.58
Baja California	9.01	9.37	9.74	9.63	10.00	10.36	10.46	10.82	11.19	11.08	11.44	11.81
Barbados	4.89	4.92	4.94	5.04	5.07	5.09	5.21	5.24	5.27	5.33	5.36	5.39

Source: Prepared by the authors.

Consequently, extreme wave heights have to be analysed both from the standpoint of probabilities and on the basis of calculated trends, since a stronger trend does not necessarily equate with a larger variation in the probability of extreme wave activity because the latter is strongly influenced by existing wave activity conditions and the distribution of extremes.

Table 1.10 shows how the 50-year return periods for significant wave heights change for the 2040 and 2070 time horizons in various locations covered in this study. These locations are used in the various project documents as a basis for evaluating levels of vulnerability and impacts.

TABLE 1.10
TRENDS IN 50-YEAR RETURN PERIODS FOR SIGNIFICANT WAVE HEIGHTS AT VARIOUS LOCATIONS

Study area	Lon (°)	Lat (°)	2010	2040	2070
Rio de Janeiro (BRA)	-43.23	-22.99	50	17.21	6.80
Santos (BRA)	-46.24	-23.93	50	17.93	7.39
Montevideo (URY)	-56.00	-34.86	50	41.85	34.73
Concepcion (CHL)	-73.09	-36.83	50	41.94	35.25
Valparaiso (CHL)	-71.63	-32.96	50	41.70	34.73
Arica (CHL)	-70.45	-18.38	50	34.29	23.86

Table 1.10 (concluded)

Study area	Lon (°)	Lat (°)	2010	2040	2070
Chorrillos (PER)	-77.04	-12.09	50	27.94	16.25
Talara (PER)	-81.26	-4.63	50	38.67	24.47
Machala (ECU)	-80.28	-3.40	50	33.87	22.92
La Libertad (ECU)	-80.78	-2.36	50	22.06	10.40
Bahía Solano (COL)	-77.38	6.05	50	16.70	6.66
Los Santos (PAN)	-80.26	7.34	50	23.82	10.69
San Jose (CRI)	-83.97	9.29	50	25.33	13.01
Managua (NIC)	-86.57	11.88	50	37.18	27.37
Acapulco (MEX)	-99.73	16.78	50	26.57	14.12
Ensenada (MEX)	-116.69	31.74	50	30.03	18.21
Cabo (MEX)	-109.85	22.98	50	40.57	32.65
Veracruz (MEX)	-96.02	19.05	50	48.60	47.20
Cancun (MEX)	-86.85	21.04	50	53.16	56.45
Puerto Plata (DOM)	-70.66	19.70	50	38.37	29.60
Bridgetown (BRB)	-59.56	13.20	50	44.24	39.16
Caracas (VEN)	-67.02	10.59	50	48.90	47.70
Georgetown (GUY)	-57.95	6.70	50	32.60	21.75
Fortaleza (BRA)	-38.49	-3.81	50	35.07	24.74
Maceio (BRA)	-35.60	-9.52	50	47.58	45.04
Porto Segura (BRA)	-39.00	-16.28	50	38.25	29.28
Puerto Santa Cruz (ARG)	-68.26	-50.14	50	50.48	50.96
Isla Taggart (CHL)	-75.58	-49.45	50	52.49	55.02

Source: Prepared by the authors.

It is important to note that, while the 100-, 250- and 500-year return periods are determined by means of statistical extrapolations from the models of extreme values, as is the usual practice in the engineering and design fields, the 50-year return periods are derived from changes in the time series even though they are drawn from the same statistical analysis. This is because the available time series cover a period of at least 60 years, and the 50-year return periods are there covered in those series.

5.4.2. Trends in extreme storm surges

Extreme storm surges have a huge impact in terms of coastal flooding, and the trends in these surges therefore warrant analysis. In order to study extreme storm surges, a generalized extreme value (GEV) distribution for monthly maximums has bee applied in order to detect any seasonal trends that turn out to be statistically significant. The 50-, 100-, 250- and 500-year return periods have been calculated for this variable in the same way as they were for wave activity. Figure 1.132 traces the values for storm surges for 50-year return periods as of the year 2040.

FIGURE 1.132
STORM SURGES FOR A 50-YEAR RETURN PERIOD AS OF 2040
(Metres)

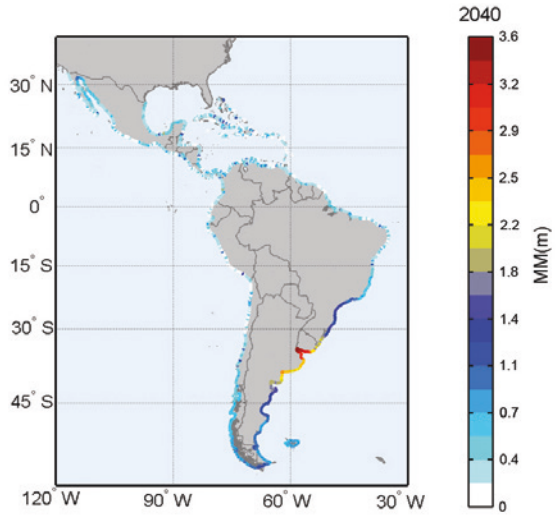

Source: Prepared by the authors.

An analysis of the annual trends in storm surges indicates that the strongest trends of all are to be found in the Plate River, where increases of as much as 5 mm/year are expected. A significant trend is also to be observed for the Gulf of California, where levels are dropping by about 4 mm/year. Along the Brazilian coast, an increase is being seen along the southern coast whereas a reduction is being recorded along the northern coast. In both cases, the variations are moderate (1.5 mm/year).

FIGURE 1.133
LONG-TERM ANNUAL TRENDS IN STORM SURGE EXTREMES: 2010-2040
(Mm/year)

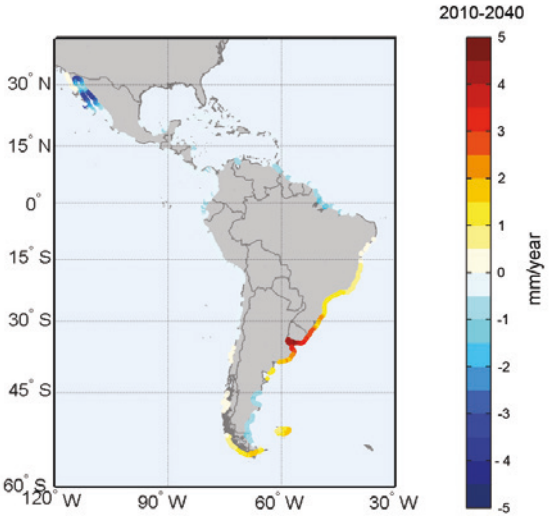

Source: Prepared by the authors.

Trends are constant throughout the year, as in the case of storm surges, with no strong seasonal variation in extremes being apparent (see figure 1.40 for the seasonality data on the 0.99 quantile for storm surges). Along the southern coast of Brazil there is a small upswing during the summer, while the trend smoothes out in the winter. This is counterbalanced by a slight downward trend during the summer in the Gulf of California.

FIGURE 1.134
LONG-TERM SEASONAL TREND IN STORM SURGES
(Mm/year)

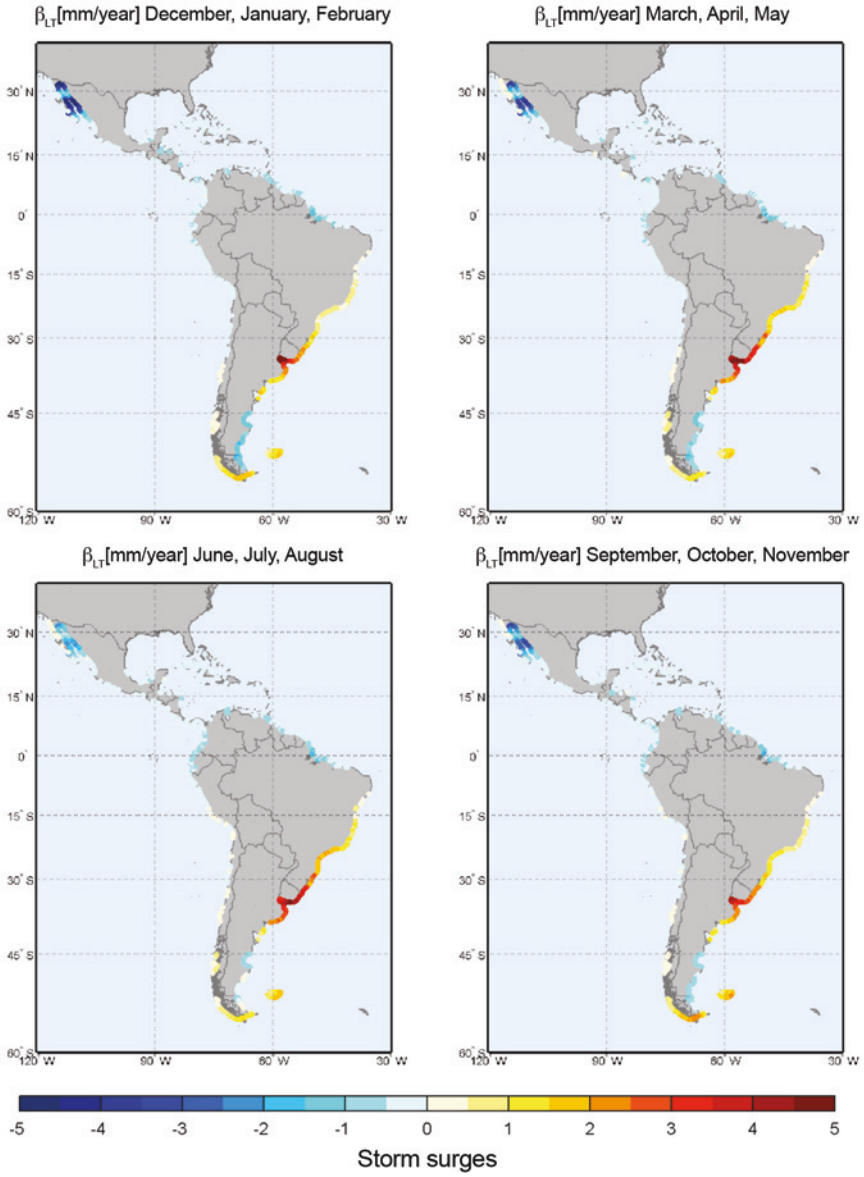

Source: Prepared by the authors.

5.5. Trends

MEAN SEA LEVEL	• There is an unmistakable upward trend in mean sea levels. Overall, the data also point to an acceleration of the trend in recent decades which can be expected to continue. • The current global mean upward trend in mean sea levels amounts to 3.3 mm/year, with a mean acceleration in the twentieth century of 0.0083 mm/year (this dovetails with the results of earlier studies). • The spatial variation within Latin America and the Caribbean ranges from lows of around 1 mm/year in Ecuador to highs of 3 mm/year in northern Brazil, the Bolivarian Republic of Venezuela and specific locations in the Caribbean. • In virtually all of the Caribbean islands, the current trend is of an increase of approximately 2.5 mm/year. • The highest rates of increase are observed in northern Brazil, the Bolivarian Republic of Venezuela and the Caribbean coast of Colombia. • The slowest rates of increase are seen in Ecuador. • A spatial analysis of the trends yields an overall upward trend of 2 mm/year. • The spatial maps indicate that a strong influence is exerted by patterns along the coasts in the equatorial zones of the Pacific, where less marked trends are also to be observed. • An extrapolation from current trends, assuming the absence of future overheating, indicates that mean sea levels will rise by around 20 cm by 2070, which is within the current seasonal range of variation. • It has been demonstrated that the values for variations in mean sea levels based on inter-annual patterns yield the same range of variation as projected trends (assuming there is no unforeseen acceleration) for the next half century. • The analysis has incorporated subsidence in some areas. The result points to a greater trend change.
SALINITY	• Increased spatial variability, with both positive and negative trends being apparent. • Significant increases along the coasts of the northern Pacific and the Atlantic coast in the southern hemisphere. • Significant negative trends in southern Chile and large parts of the Caribbean.
SEA SURFACE TEMPERATURE	• A mean increase in air temperatures along the Atlantic coast, coupled with localized decreases in some areas along the Pacific coast. • Increases of around 1ºC are to be expected along the northern coast of Brazil by mid-century.
WIND	• Upward and downward trends are found in the region, which is marked by a high degree of spatial variability. • Spatial trends in the southern part of the continent appear to be more stable, with changes of above 1 m/s expected for the second half of the century. • The prevailing wind directions are changing, with the direction of change exhibiting a high degree of spatial variability.

(concluded)

WAVE ACTIVITY	• An increase in the significant wave height exceeded 12 hours per year amounting to approximately 2.5 cm/year in southern Brazil, Uruguay and northern Argentina, as well as in Baja California, the Pacific coast of Mexico and the southern coast of Cuba. • Slight (less than 1 cm/year) or no decline in the southern coast of the Gulf of Mexico, northern Brazil and the Bolivarian Republic of Venezuela. • There is a high degree of probability that a change of more than 0.5 m in Hs_{12}, as a mean, will be registered in the second half of the century. • The largest changes in Hs_{12} during the second half of the century are expected to exceed 1 m by a large margin relative to current conditions in the locations that will experience the strongest upward trends. • The peak values for significant wave heights will rise during the southern-hemisphere summers in southern Chile (2.5 cm/year) and in the southern-hemisphere winters in Uruguay and southern Brazil (1.5 cm/year). In virtually all of the other locations, a slight (0.5 cm/year) increase is expected, with the exception of the Gulf of Mexico and the Caribbean coast of Colombia in the springtime, where decreases of about 1 cm/year are projected. • Mean wave conditions are also changing. In this case, however, the strongest trends are seen along the Pacific coast of Mexico, where the values amount to approximately 1 cm/year. • All of these trends have been calculated without taking into account the extreme waves generated by hurricanes. • Both mean and extreme conditions in the region are changing. The highest wave ranges are changing more than the mean conditions are. Along the Pacific coast in the northern hemisphere, the heights of both mean and extreme wave events are on the rise. Another area in which significant changes appear to be occurring is the zone encompassing southern Brazil, Uruguay and northern Argentina, where both mean values and extremes are also increasing. In this case, however, the upswing in mean values is smaller than it is in the northern hemisphere. • Mean wave direction exhibits marked long-term variations, with clockwise shifts in direction of up to 0.2º/year in northern Brazil, southern Ecuador and Peru, the Pacific coast of southern Mexico, Costa Rica and Panama, southern Chile (0.1º/year) and southern Brazil. In Baja California and along the Caribbean coast of Central America and Argentina, a counter-clockwise trend on the order of 0.1% has been detected.
STORM SURGE	• A slight (0.5 cm/year) upward trend in extreme values for storm surges in the area of the plate River has been detected, which is precisely where the highest values for this variable are found at the present time, and in southern Brazil. • Another focal point of change is the Gulf of California, where slight negative trends (-0.5 cm/year) emerge. • In both cases, the trends continue to be observed for all seasons, while varying in step with the slight seasonal changes seen in present conditions.

6. Analysis of inter-annual variability in the coastal dynamics of Latin America and the Caribbean

6.1. Introduction

The 2007 report of IPCC Working Group I presents evidence of long-term, large-scale changes in atmospheric circulation patterns, including shifts towards the polar regions and stronger westerly winds. It also shows that many regional climate changes can be described in terms of weather variability patterns and, consequently, may appear as changes in indices that measure the force and phase of those patterns. Fluctuations in westerly winds in the two hemispheres have recently been explained in terms of the Northern Annular Mode (NAM) and the Southern Annular Oscillation (SAM). These changes can be expressed as a shift in the circulation pattern associated with the signatures of these patterns.

Multidecadal variability is also apparent in the Atlantic ocean-atmosphere systems. For HS, changes in circulation related to the increase in SAM since the 1980s are associated with a marked warming of the Arctic Peninsula and, to a lesser extent, zones on the Antarctic continent that are cooling down. Changes in the interrelationship between the Pacific Ocean and the atmosphere in that area have also been observed. Globally, ENSO is the predominant mode of variability on inter-annual time scales, although at times this has been less apparent. The 1976–1977 climate shift associated with the phase change in the Pacific Decadal Oscillation (PDO), which has triggered a series of changes in a more El Niño-type ENSO pattern, has affected many areas, including those subject to tropical monsoons. For example, changes in North America related by means of teleconnections with ENSO and the Pacific/North American Pattern (PNA) appear to have triggered divergent changes throughout the continent, with the western portion of the continent heating up more than the eastern portion, which is also experiencing more cloud cover and greater humidity (IPCC 2007).

While there is certainty about these shifts, there is a great deal of uncertainty about how climate change will influence the ENSO phenomenon (Collins *et al.,* 2005), and no firm conclusions have been drawn as to whether the frequency and intensity of ENSO events will increase or decrease in the future (Nicholls, 2008; Collins *et al.,* 2005; Van Oldenborgh *et al.,* 2005; Cane, 2005). Because

of all these factors, it is important to incorporate the ENSO phenomenon and other climate patterns into the analysis of the dynamics occurring in Latin America and the Caribbean and in the subsequent risk assessment.

The influence that various climate indices have on the variables analysed in this study have been explored as part of this research effort. This has made it possible to arrive at a prognosis by means of a statistical downscaling exercise in which the predictor is the climate index and the predictand is the agent being examined. The climate indices are obtained on the basis of large-scale spatial/temporal patterns of sea surface temperature (SST) and sea level pressure (SLP). This approach helps us to predict how given coastal variables (e.g., sea levels) are going to behave within the context of a given value on the climate index being used.

This section of the study seeks to trace a clear-cut relationship between climate indices and the magnitude of the response to changes as measured by the indices for coastal agents. An effort is also made to analyse the time lag involved in that response. The overall objective is thus to determine how the different variables will be influenced by climate patterns.

6.2. Statistical techniques for analysing the variability of climate agents

Because macro climate patterns may be one of the major sources of spatial and temporal variability in coastal dynamics, the influence of wave activity, sea levels and storm surges has been studied using various indices: the Arctic Oscillation (AO), the Southern Annular Oscillation (SAM), the ENSO phenomenon, the Southern Oscillation Index (SOI), the Pacific/North American Index (PNA), the Western Pacific Index (WPI), the Eastern Pacific Oscillation (EPO) (which is based on East Pacific – North Pacific (EP/NP) patterns), the North Atlantic Oscillation (NAO), the East Atlantic Index (EAI), the Caribbean SST Index (CAR), the East Atlantic/Western Russia (EA/WR) pattern, the Scandinavian SCA patterns, the Dipole Mode Index (DMI), the Atlantic Multidecadal Oscillation (AMO), the Quasi-Biennial Oscillation (QBO), the Northeast Brazil Rainfall (NBR) index, the North Tropical Atlantic SST Index (NTA), the Tropical North Atlantic Index (TNA) and the Tropical Southern Atlantic Index (TSA).

Since climate patterns and the influence they exert over different variables may be coetaneous or may involve a time lag, depending on the location concerned, the time lags that may be involved in the appearance of each of these phenomena at the various locations along the coasts of Latin America and the Caribbean have been studied.

The influence on wave activity exerted by the variables captured in all the indices has been analysed, as has the influence on sea levels and the storm surge percentiles of the variables captured in the 95% most relevant indices: NIÑO3, CAR, TNA, SOI, TSA and PNA.

These results provide information about how the value of a given index (which represents a specific climate pattern) can reflect an impact on coastal dynamics. This means that projections of those values, if they can be calculated, will provide an indirect means of projecting their influence on coastal dynamics and, moreover, of projecting the point in time when those impacts will occur.

The model used to analyse the influence of the variables reflected in the different climate indices on coastal dynamics in Latin America and the Caribbean is based on a linear regression that relates each climate index to the variable of interest, discounting the trend and standardizing in order to factor out seasonality. This makes it possible to isolate the relationship between the (de-trended and deseasonalized) signal anomaly and climate variability. The regression coefficient has been determined using least squares. If the regression is statistically significant (95% p.e.), then the index is considered to have an influence on the variable in question. This linear model can be expressed as follows:

$$\frac{X(t) - \overline{X}_{month}}{\sigma_{month}} = \beta \cdot CI(t) \qquad (1.11)$$

Where $X(t)$ is the trend signal; X_{month} and σmonth are the mean and the monthly deviation, respectively, for the corresponding month for all years in the time series, while β represents the coefficient of the linear correlation and IC is the time series of the climate index in question (which is also standardized).

In order to ascertain what portion of the variance in each dynamic is accounted for by the variables reflected in the climate indices, a "coefficient of determination" has been introduced. This coefficient represents the relationship between the variance of the residual of the model and the variance of the original signal. This indicator reflects the percentage of the variation in the dependent variable that is accounted for by the model and is calculated as follows:

$$R^2 = \frac{VE}{VT} = 1 - \frac{VNE}{VT} \qquad (1.12)$$

Where VE represents the variation in the dependent variable that is explained by the model, VNE represents the variation in the dependent variable that is not explained by the model, and VT is the total variation in the dependent variable.

The following figures depict the coefficient of correlation obtained for the time series on the different variables and the series for climate indices (both standardized by deducting the mean and dividing by the standard deviation). The results show how the variables reflected in the different indices influence the variables being analysed. In other words, they show whether or not the variables underlying a given index do or do not have an influence on a specified coastal variable (and, if they do, how much they influence it).

However, in order to determine the scale of the effect of a given value on a climate index for the variables of interest, the product of the following calculation has to be obtained:

$$X_i = \sigma_{month} \cdot \beta_{CI} \cdot CI_i + X_{month} \qquad (1.13)$$

Where CI_i represents a given value on the climate index that can be obtained using the meteorological data provided by various agencies (such as NOAA). In order to make that information available in this study, the results for the term $\sigma_{month} \cdot \beta_{CI}$ and x_{month}, are mapped out spatially so that, by multiplying the index value by the first term and adding the second, the impact on variable X can be obtained. Note that, for variables for which there is a monthly time resolution, 12 read-outs (one for each month) will be obtained. For ease of use, these results have been consolidated into a single figure for each index and variable by using the mean of standard deviations and mean monthly values for the 12-month period.

6.3. Description of climate indices

A number of climate indices have been analysed, and descriptions and results are provided below for those that have been demonstrated to have the strongest influence on wave activity, the direction of mean energy flow, mean sea levels and storm surges.

AO (Arctic Oscillation) and SAM (Southern Hemisphere Annular Mode)

The Arctic Oscillation (AO) and the Southern Hemisphere Annular Mode (SAM) are the two climate patterns that are exerting the greatest influence in the northern and southern hemispheres, respectively. The AO index measures atmospheric circulation over the Arctic. It is the predominant pattern in non-seasonal variations in sea level pressure at latitudes to the south of 20ºN and is characterized by pressure anomalies of one sign in the Arctic and anomalies of the opposite sign around 37º-45ºN (Thompson y Wallace, 1998). The positive phase is associated with below-normal pressure in the polar region, which causes low-pressure areas to shift to the north, generating more humid conditions over Scotland and Scandinavia and drier conditions in areas such as the Iberian Peninsula and the countries to the east.

FIGURE 1.135
TIME SERIES FOR THE AO CLIMATE INDEX

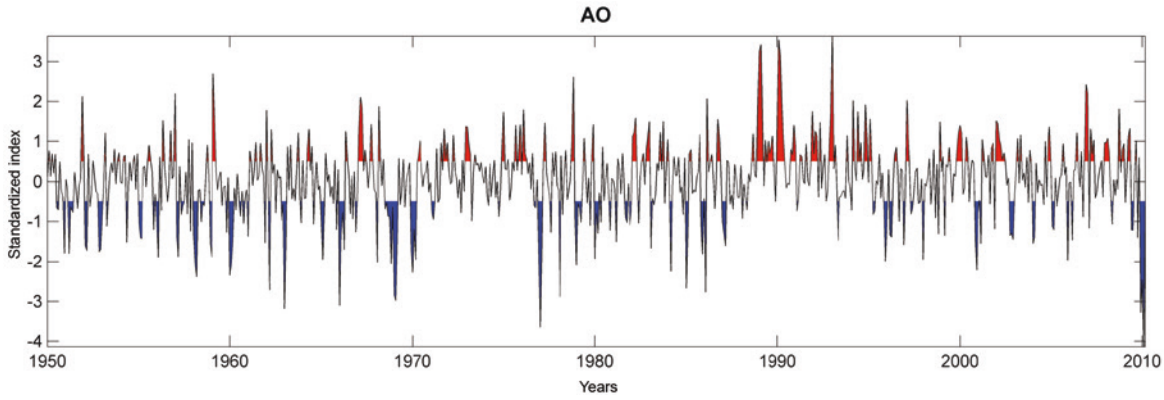

Source: Prepared by the authors.

In the southern hemisphere, SAM is the equivalent of the AO index for latitudes above 20ºS. It typically reflects pressure anomalies of one sign around Antarctica and anomalies of the opposite sign for areas above latitudes 40º-50ºS (Thompson and Wallace, 2000).

FIGURE 1.136
SAM CLIMATE INDEX TIME SERIES

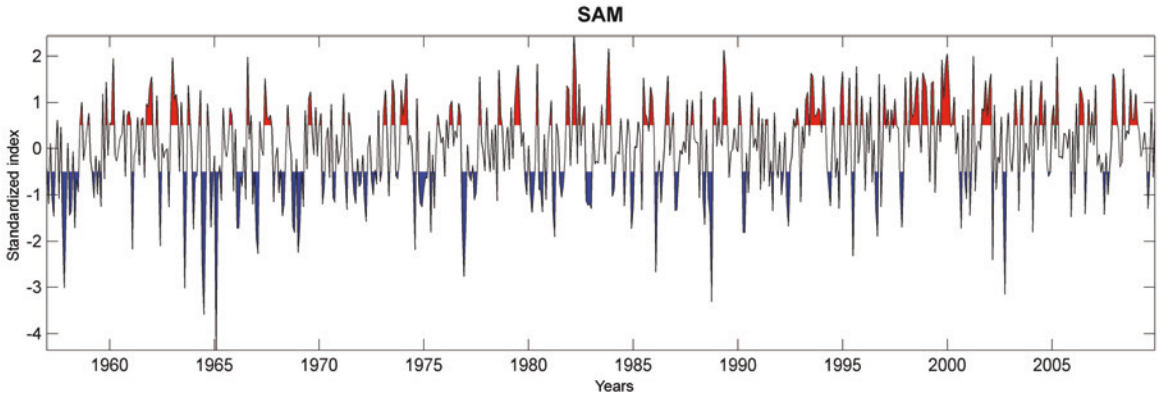

Source: Prepared by the authors.

ENSO (El Niño Southern Oscillation)

The phenomenon known as the El Niño Southern Oscillation (ENSO) is apparently the strongest and most predictable of all the main systems that influence climate variability. This phenomenon, which is a combination of oceanic and atmospheric forces, is known to have a bearing on floods, droughts and other changes in different regions of the world, especially in South America, Indonesia and Australia (Rasmusson y Carpenter, 1983). It is a quasi-regular phenomenon that appears in a variable timeline of from 2 to 6-7 years. ENSO is composed of an oceanic component ("El Niño" or "La Niña", depending on the phase) marked by the heating or cooling of surface waters in the eastern tropical zone of the Pacific Ocean, and by an atmospheric component, the Southern Oscillation, which is characterized by changes in surface pressure in the western tropics of the Pacific Ocean. The two components are linked: when the El Niño is present, pressures rise in the western Pacific, while, during the La Niña phase, the cooling of surface waters is reflected in the presence of lower pressure centres in the eastern Pacific.

FIGURE 1.137
PRESSURE ANOMALIES IN THE PACIFIC IN THE PRESENCE OF EL NIÑO AND LA NIÑA

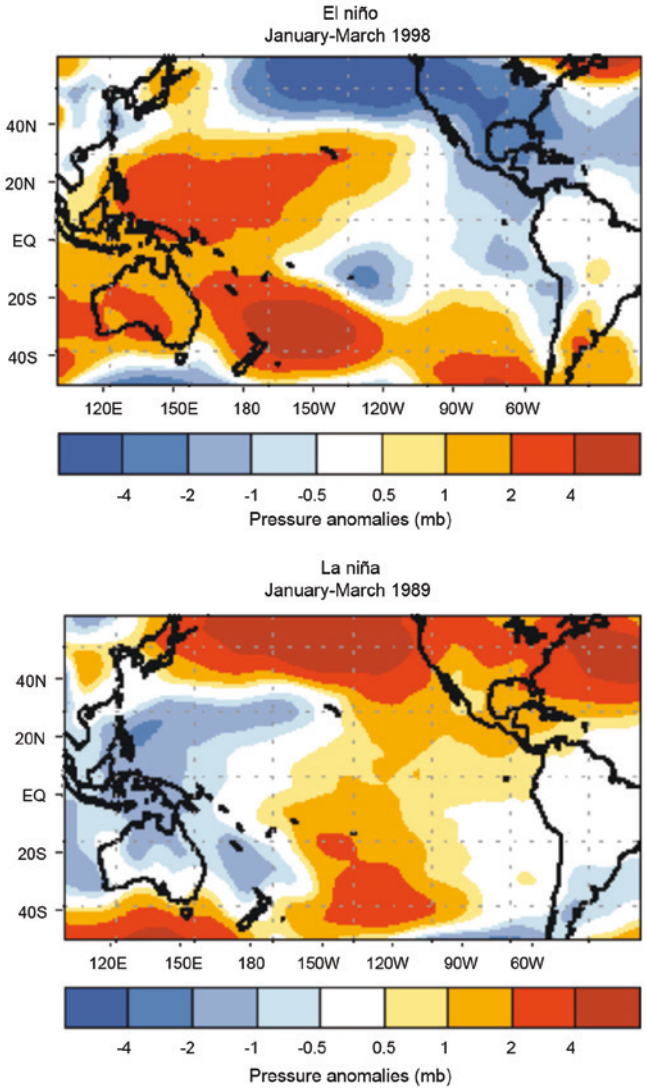

Source: NOAA (http://www.cpc.ncep.noaa.gov/products/analysis_monitoring/ensocycle/soilink.shtml).

Under normal conditions, the trade winds move the warm surface waters of the Pacific Ocean toward the west, which is why sea levels are approximately half a metre higher along the coasts of Indonesia than they are along the coasts of Peru and Ecuador and why the surface water temperatures in these two zones differ by some 8ºC. As a result, in the presence of strong winds, the central eastern area of the Pacific tends to be colder around the equator than in adjacent northern and southern locations. Consequently, the thermocline shifts towards the surface along the coasts of South America and goes deeper along the coasts of the South-East Asia. This causes cold, nutrient-rich water from the deeps of the ocean to ascend in the east, which creates zones rich in fishery resources along the coast of South America. These upwellings give rise to the "Pacific cold tongue", which stretches from the southern coast of South America westward for thousands of kilometres all along the coast of Ecuador.

FIGURE 1.138
SCHEMATA OF WINDS AND OCEANIC STRUCTURE UNDER NORMAL ENSO CONDITIONS FROM DECEMBER TO FEBRUARY

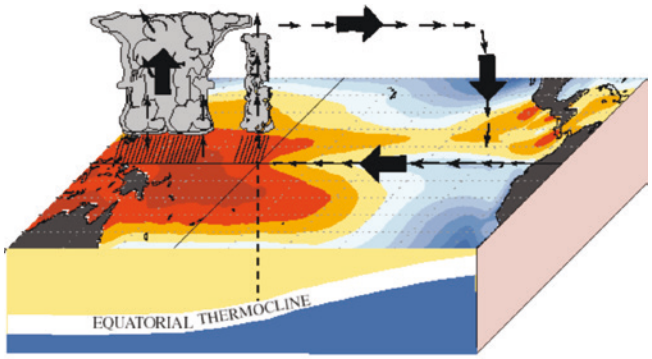

Source: NOAA (http://www.cpc.ncep.noaa.gov/products/analysis_monitoring/ensocyclemeanrain.shtml).

During the upward phase, the trade winds weaken and the cold tongue declines, which gives way to an intrusion of warmer water from the western Pacific. Under these conditions, the thermocline moves deeper in the eastern Pacific and ceases to trigger the upwellings of cold, nutrient-rich water. The result is a downturn in the productivity of South American Pacific fisheries. The strongest effects associated with this anomaly occur between December and February and are referred to as "El Niño"; they tend to last for several months.

The downward phase of ENSO is referred to as "La Niña" and represents the flip side of the El Niño phenomenon. During this phase, the trade winds shift the surface waters of the Pacific towards the west, which gives rise to warm, humid conditions in this area and causes the Pacific cold tongue to rise and shift in the eastern Pacific. The climate impacts of La Niña events tend to be the opposite of those of El Niño but to be less intense.

FIGURE 1.139
SCHEMATA OF WINDS AND OCEAN STRUCTURE DURING EL NIÑO AND LA NIÑA

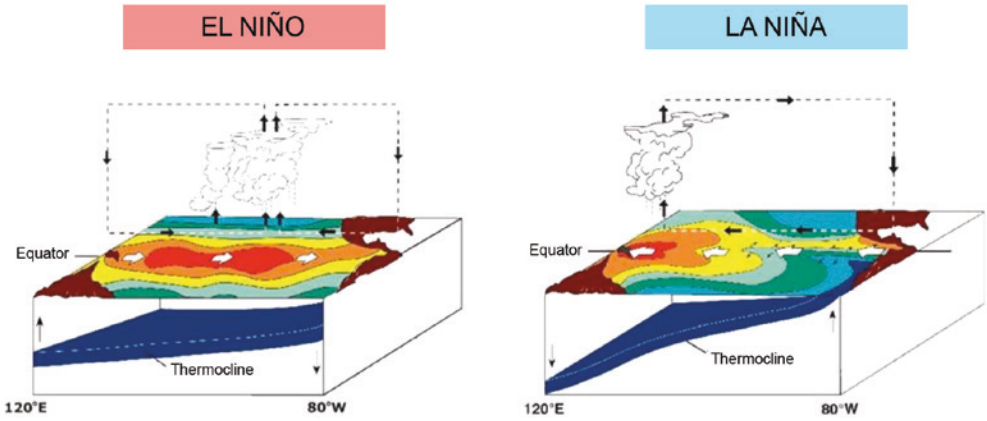

Source: Wikipedia (http://en.wikipedia.org/wiki/El_Niño-Southern_Oscillation).

The ENSO phenomenon is monitored with the help of sea surface temperature (SST) indices, Niño indices, pressure indices and the Southern Oscillation Index (SOI). There are SST indices for four regions along the equator that are used to measure temperature differences in these zones: NIÑO1 (80º-90ºW, 5º-10ºS), NIÑO2 (80º-90ºW, 0º-5ºS), NIÑO3 (90º-150ºW, 5ºN-5ºS) and NIÑO4 (150º-160ºW, 5ºN-5ºS). These regions were defined in the early 1980s, but their configuration has been modified various times since then, so what were once regions NIÑO1 and NIÑO2 are now region NIÑO 1+2; there is also a new region called NIÑO 3.4 (120º-150ºW, 5ºN-5ºS), which is the one that is used the most to gauge the ENSO phenomenon because it correlates very well with the SOI. In this study, however, the NIÑO3 index has been used because it is a closer fit for the area under study than the NIÑO 3.4 region is.

FIGURE 1.140
NIÑO INDEX REGIONS

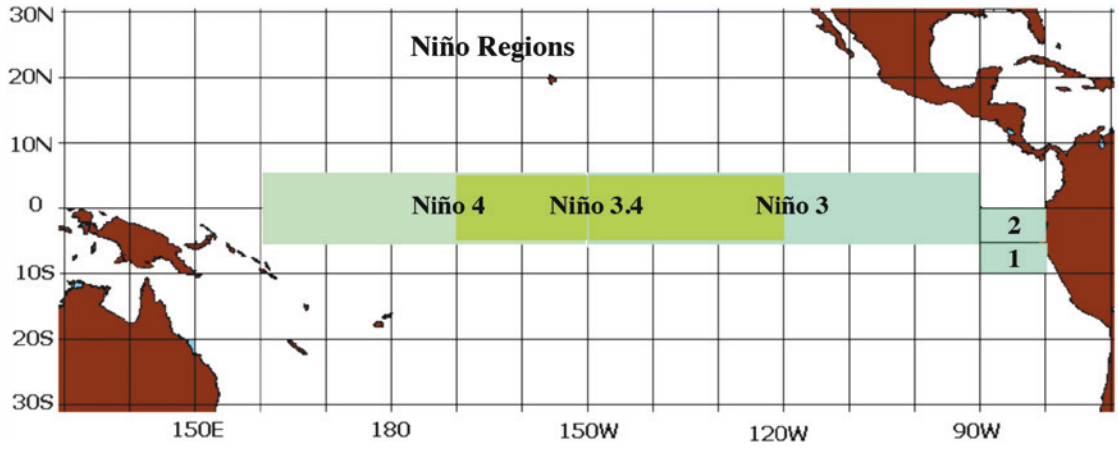

Source: NOAA (http://www.srh.noaa.gov/jetstream//tropics/enso.htm).

The SOI represents the atmospheric component of the phenomenon and is based on the difference between standardized sea level pressure levels between Tahiti in the central Pacific and Darwin in Australia. During the upward SOI phase, barometric pressure in Tahiti is greater than it is in Darwin (the La Niña phase), while in the downward phase, pressure increases in the west and falls in the east as the trade winds grow weaker (the El Niño phase).

The two indices are correlated, as can be seen from figures 1.141 and 1.142. The upper panel depicts changes in the SOI over time, while the lower panel shows the results for NIÑO3 for the same time period. When pressure is lower in Tahiti than in Darwin, the temperature anomaly in NIÑO3 is positive (shown in red in the figure), which is associated with the warm phase of ENSO and El Niño events. On the other hand, when pressure in Tahiti is greater than in Darwin, temperatures in NIÑO 3 are below normal and La Niña occurs (the cold phase of the ENSO is shown in blue).

FIGURE 1.141
TIME SERIES FOR THE SOUTHERN OSCILLATION INDEX (SOI)

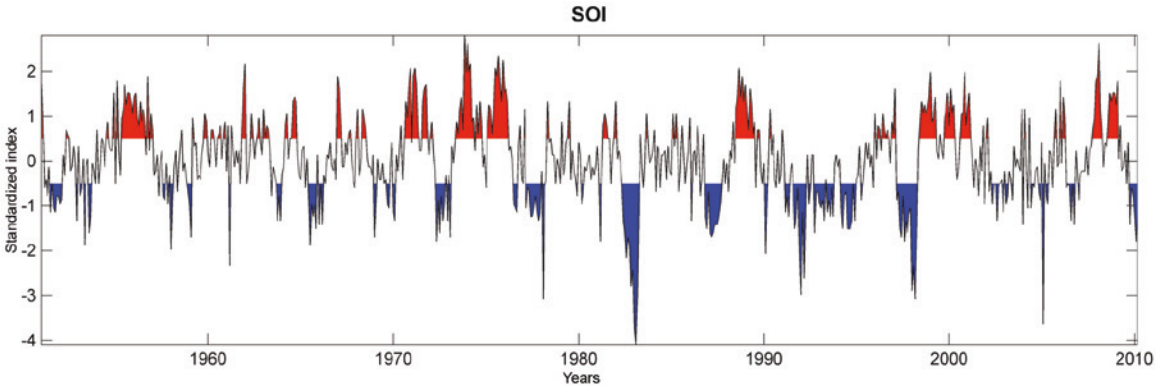

Source: Prepared by the authors.

FIGURE 1.142
TIME SERIES FOR THE NIÑO3 INDEX

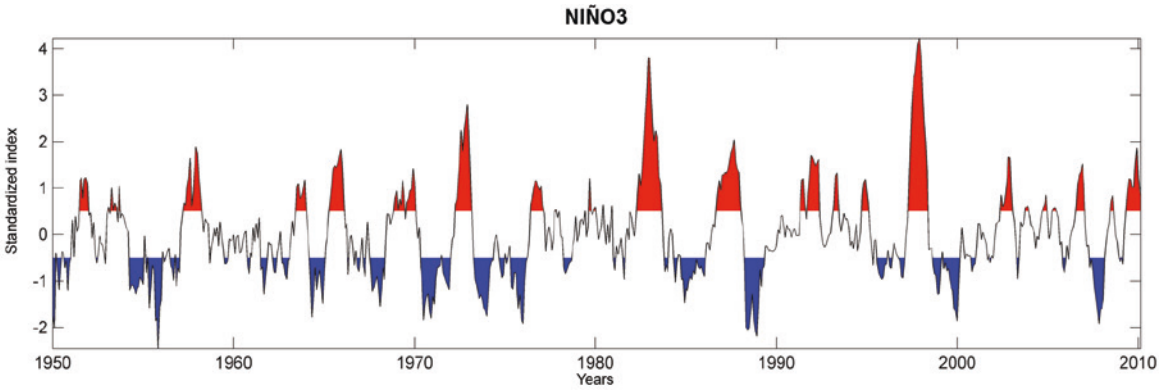

Source: Prepared by the authors.

Atlantic Multidecadal Oscillation (AMO)

The Atlantic Multidecadal Oscillation (AMO) is a mode of variability occurring in the northern Atlantic Ocean that has its principal expression in the sea surface temperature (SST) field. There is evidence of the presence of this mode in time series observations and models, but there is some controversy regarding its extent and, in particular, its influence on surface sea temperatures in the hurricane-breeding areas of the tropics in the Atlantic Ocean.

FIGURE 1.143
TIME SERIES FOR THE ATLANTIC MULTIDECADAL OSCILLATION (AMO) INDEX

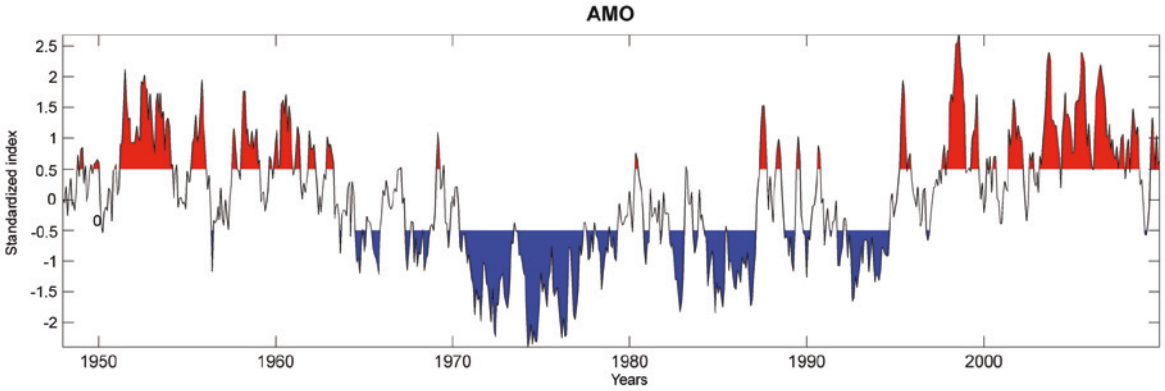

Source: Prepared by the authors.

The AMO index correlates with air temperature and precipitation in much of the northern hemisphere (particularly North America and Europe) and north-eastern Brazil, as well as with precipitation in the Sahel in Africa and summer weather in North America and Europe. It is also associated with changes in the frequency of droughts in North America and major hurricanes in the Atlantic.

Recent research findings suggest that the AMO is related to the occurrence of major droughts in the midwest and south-east of the United States. When the AMO index registers a warming or positive phase, droughts in these areas tend to be more frequent and to last longer. When the AMO index registers a cooling or negative phase, just the opposite is observed. Two of the worst droughts in the twentieth century took place during warming phases in the AMO (1925 and 1965), which triggered the dust bowl in the 1930s and the drought of the 1950s. In Florida and the Pacific North-West, the positive phase of the index seems to be correlated with the opposite effect causing heavier precipitations.

Climate models seem to indicate that the warming phase of the AMO is associated with increased precipitation in the summer in India and the Sahel and with cyclonic activity in the northern Atlantic. Paleoclimatic studies confirm that this pattern (increased precipitation during warming phases and decreased precipitation in cooling phases) has persisted in the Sahel for the last 3,000 years.

The frequency of major Atlantic hurricanes does not correlate closely with the AMO. During warming phases on the index, the number of weaker hurricanes (categories 1 and 2) increases slightly, however. The index of hurricane activity does correlate closely with the AMO, on the other hand. If hurricane activity is increasing as a result of climate change, it is being masked by the quasi-periodic AMO cycle. Judging from the typical duration of negative and positive AMO phases, the current warm phase is expected to persist at least until 2015 and may continue up to 2035. Enfield and Cid-Serrano (2010) project a peak level at around 2020. The implications of the present cycle in terms of wave activity in Latin America and the Caribbean can be analysed on the basis of the information and findings presented in the annex on this subject.

North Tropical Atlantic (NTA) SST Index

The NTA index is calculated on the basis of average SST anomalies for 60W-20W, 6N-18N, 20W-10W and 6N-10N. The information has been drawn from the COADS database for 1951-1991 and obtained from the National Centers for Environmental Prediction (NCEP) for the years since then.

The anomalies have been calculated using climate data for 1951-2000, which has been smoothed using a three-month moving average, and have been projected for 20 EOF patterns.

FIGURE 1.144
TIME SERIES FOR THE NORTH TROPICAL ATLANTIC (NTA) CLIMATE INDEX

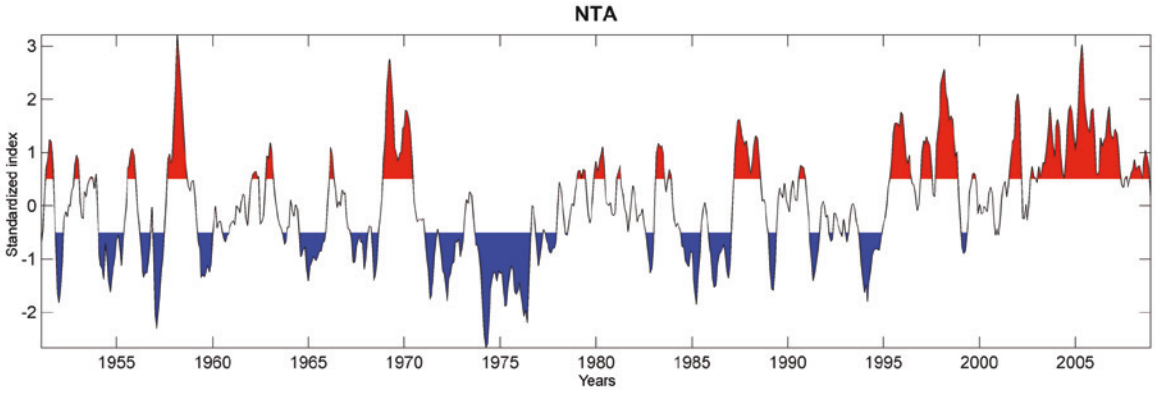

Source: Prepared by the authors.

FIGURE 1.145
GEOGRAPHICAL ZONES OF THE CARIBBEAN (CAR), NORTH TROPICAL ATLANTIC (NTA) AND TROPICAL SOUTHERN ATLANTIC (TSA) CLIMATE INDICES

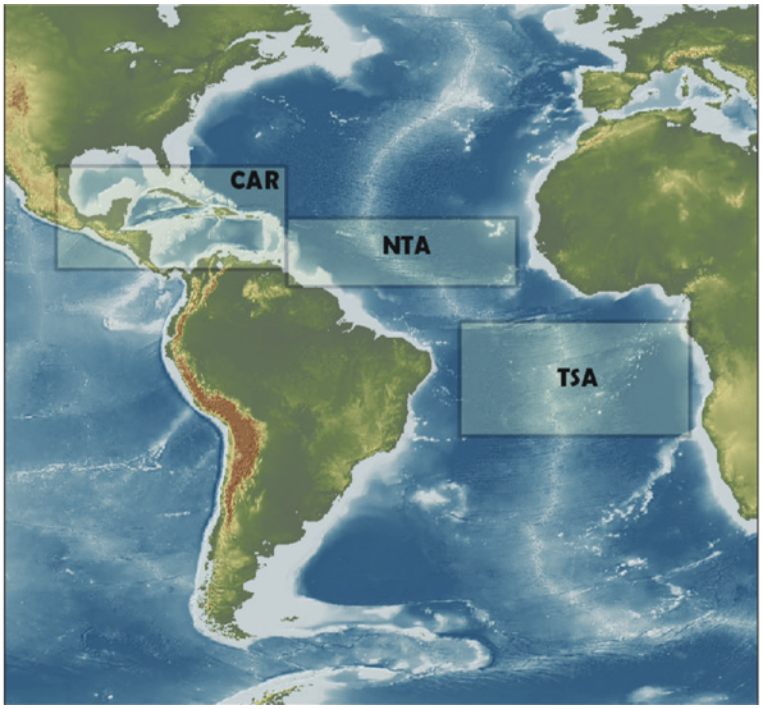

Source: Prepared by the authors.

Tropical Southern Atlantic (TSA) Index

The TSA index gauges the mean monthly SST anomaly in the area between Ecuador and 20ºS and between 10ºE and 30ºW. The information was drawn from the Geographic Information Science and Technology (GIST) and NOAA optimum interpolation (OI) databases for 1x1º grids.

FIGURE 1.146
TIME SERIES FOR THE TROPICAL SOUTHERN ATLANTIC (TSA) CLIMATE INDEX

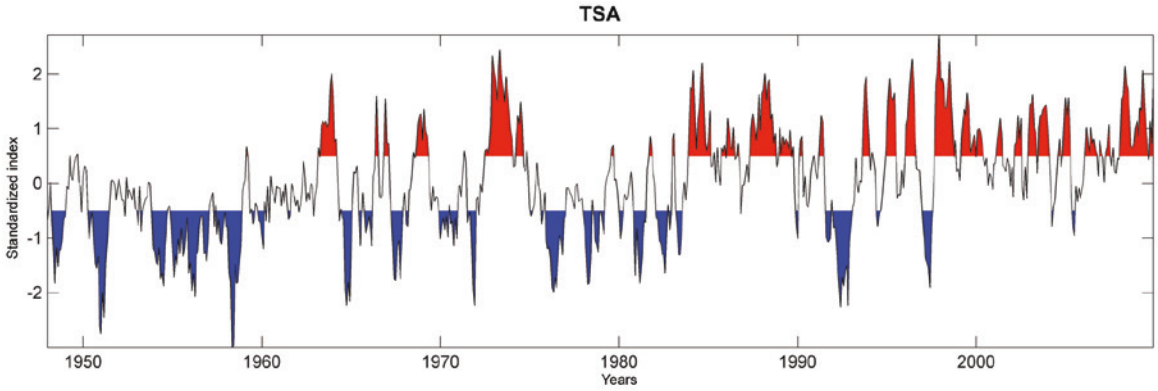

Source: Prepared by the authors.

Caribbean (CAR) SST Index

This index reflects the averaged SST anomalies in the Caribbean Sea. The information has been drawn from the COADS database for 1951-1991 and from the NCEP database for the years since then. The anomalies have been calculated on the basis of climate information for 1951-2000 that was smoothed using a three-month moving average and have been projected for 20 EOF patterns. Further information on the index projections can be obtained from NOAA.

FIGURE 1.147
CAR CLIMATE INDEX TIME SERIES

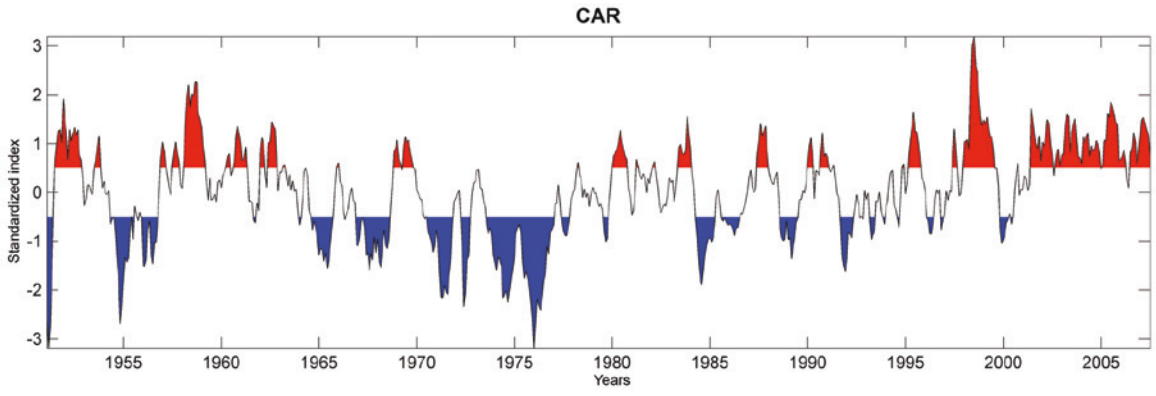

Source: Prepared by the authors.

6.4. Results

The influence reflected in these climate indices has been analysed on the basis of three statistics for wave height (95th percentile, monthly mean and monthly maximum), the direction of mean energy flow, (untrended) anomalies in mean sea levels and the 95th percentile for storm surges.

In addition to the influence exerted in terms of the correlation of each index with each variable, an atlas is provided of the values of the coefficients of correlation, multiplied by the mean of the typical monthly deviations for the variable and another of the mean value of the variable in order to determine the mean contribution for that variable of a given climate index value.

In addition to analysing the influence exerted by the factors underlying each index on coastal dynamics, a time-lagged analysis was conducted of the occurrence on the climate index and the peak level of influence on the various coastal dynamics.

6.4.1. Results for the correlation of contemporary climate indices

This section will present only a sampling of the more significant results for the correlation of the above-mentioned climate indices with the variables of wave activity, sea levels and storm surges. The full results for the correlations between each of the variables and all of the indices are given in an annex to this document.

The following figures show the correlation coefficient *(β)* for the climate index with a standardized variable (equation 1.2). The cases in which the correlation was not significant are not shown.

6.4.1.1. Results for wave activity

(a) Results for monthly 95th percentiles for Hs

Figure 1.148 shows the results for the correlation of monthly figures for the 95th percentile of significant wave heights (standardized ahead of time by deducting the mean and dividing by the typical deviation of the monthly series). There is a high positive correlation between the two indices, with a value of approximately 0.3 for the SOI index along the Pacific coasts of Central America and southern Peru. This indicates that, for a unit value of the climate index, 0.4 units of the standardized sign for the variable are accounted for by the influence exerted by the index in those areas. This positive correlation is found along the Pacific coast below 18ºN for the SOI index and throughout for the NTA index.

FIGURE 1.148
CORRELATION OF THE 95TH PERCENTILE OF SIGNIFICANT WAVE HEIGHT WITH VARIOUS CLIMATE INDICES

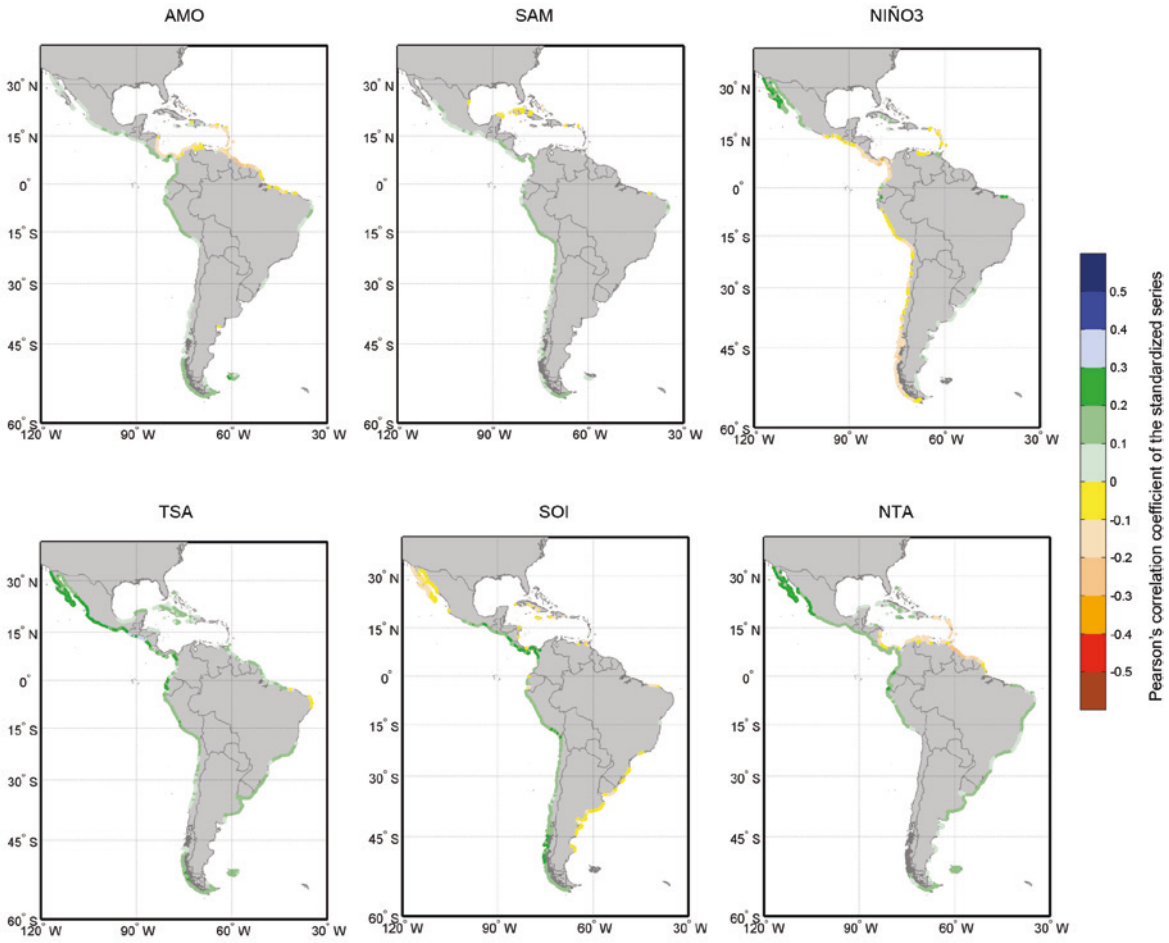

Source: Prepared by the authors.

There is a negative correlation for the SOI index along portions of the Atlantic coast and the California peninsula, however, which suggests that opposing effects are occurring along these two coastlines. Along the Pacific coast, wave activity increases when the SOI index is positive, whereas it declines along the Atlantic coast in such cases.

The correlation with the NTA index is positive everywhere except along the coast between 0º and 15ºN in the Atlantic and the Caribbean Sea.

(b) Results for monthly mean significant wave heights

FIGURE 1.149
CORRELATION FOR MONTHLY MEAN SIGNIFICANT WAVE HEIGHTS: SOI (UPPER LEFT), CAR (LOWER LEFT) AND NTA (RIGHT) INDICES

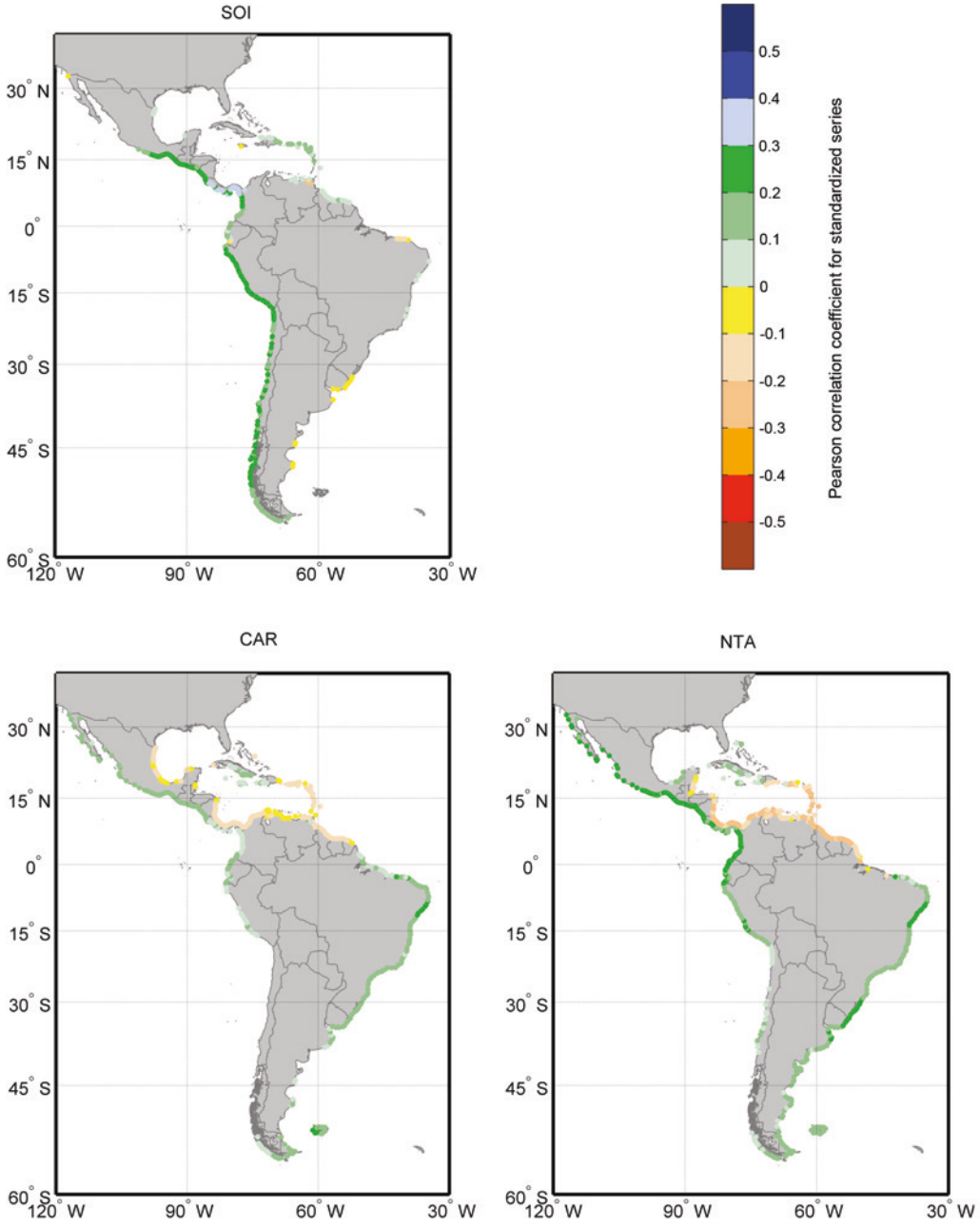

Source: Prepared by the authors.

There is a clear positive correlation between monthly mean significant wave heights and the SOI index along the Pacific coast, while almost no indication of any significant influence is seen along the Atlantic coast. The CAR index reflects a stronger influence in the Caribbean and along the Pacific coast of Central America, with wave activity diminishing in the Caribbean Sea when the index registers positive readings. The influence of the NTA index is seen throughout the region, with wave activity increasing, except in the southern Caribbean Sea and the Atlantic coast in the tropics, where the opposite effect is observed when the index registers positive values.

(c) Results for monthly maximum significant wave heights

The results for monthly maximum significant wave heights include the TSA index's positive correlation for the Pacific coast up to northern Chile and a portion of the southern Atlantic coast. The results for the SOI and NTA indices are similar to those obtained for monthly mean heights, although the areas for which negative correlations with the NTA arise are fewer in these cases, whereas negative or weak correlations for the SOI index are found along longer stretches of the Atlantic coast.

FIGURE 1.150
CORRELATION OF MONTHLY MAXIMUM SIGNIFICANT WAVE HEIGHTS WITH THE SOI (UPPER LEFT), TSA (LOWER LEFT) AND NTA (RIGHT) INDICES

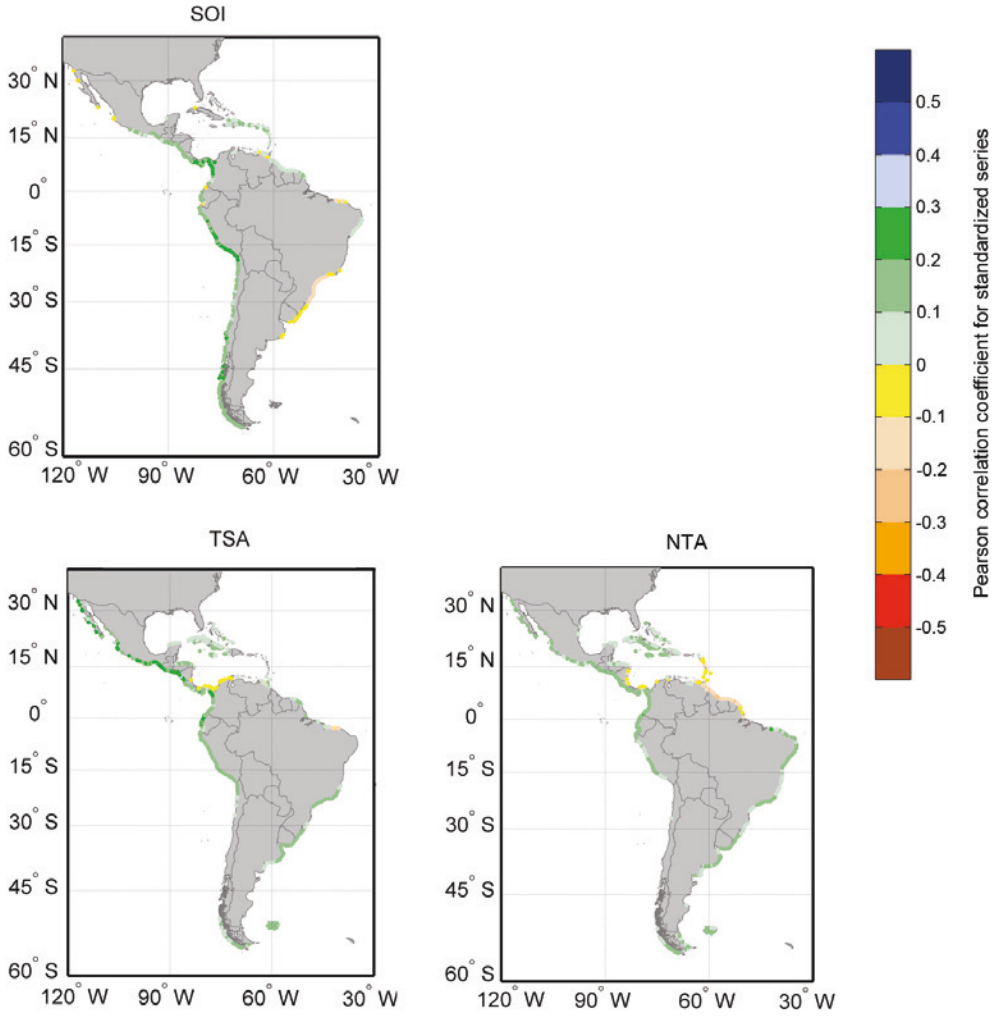

Source: Prepared by the authors.

6.4.1.2. Correlation between climate indices and the direction of mean energy flow

The direction of mean energy flow for wave activity is strongly correlated with the NIÑO3, SAM, TSA and NTA climate indices. In the case of the NIÑO3 index, the positive correlation is especially strong along the coasts of Chile, Ecuador and north-western Mexico. This indicates that the predominant wave direction is shifting towards the north (clockwise) when this index is positive. In the Caribbean islands, a high positive correlation is also obtained for this index, but in this case the shift is towards the east and occurs during positive phases of NIÑO3.

FIGURE 1.151
CORRELATION OF THE DIRECTION OF THE MEAN ENERGY FLOW OF WAVE ACTIVITY WITH THE NIÑO3 (UPPER LEFT), TSA (LOWER LEFT), SAM (UPPER RIGHT) AND NTA (LOWER RIGHT) INDICES

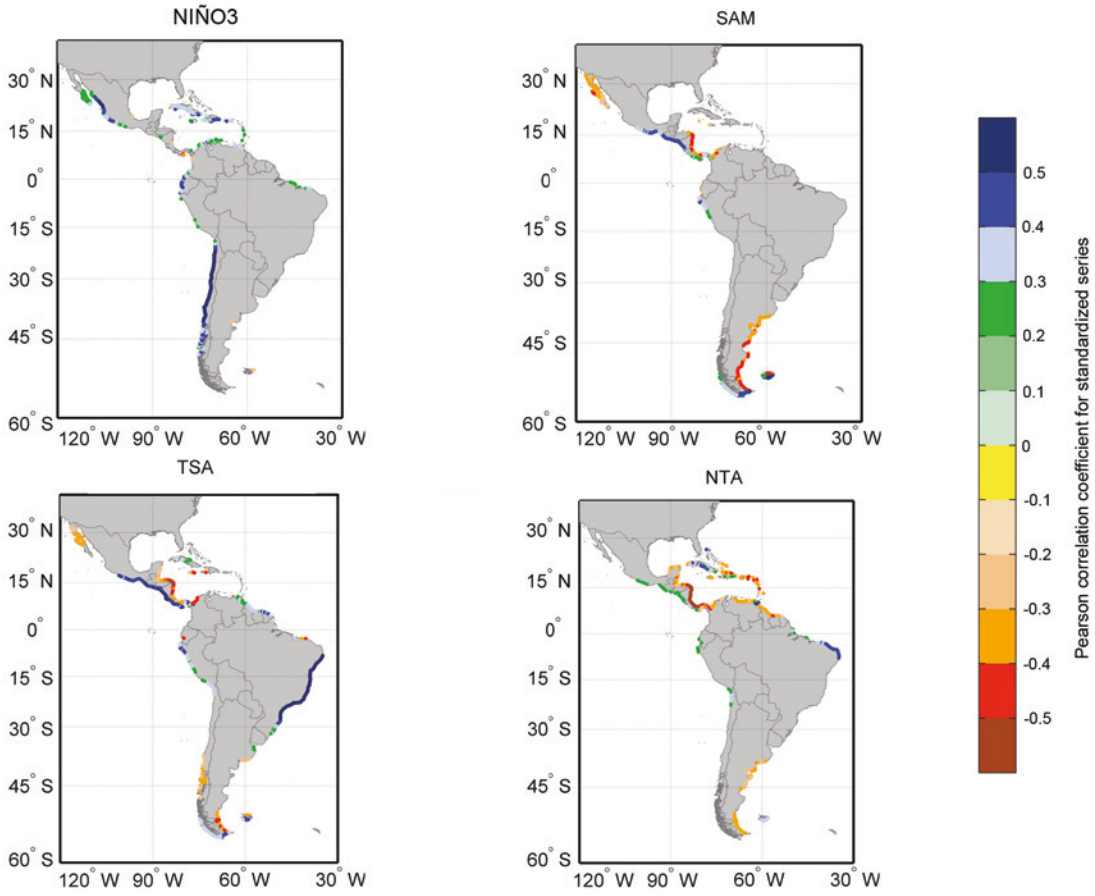

Source: Prepared by the authors.

For the SAM index, the strongest correlations are a positive one for the Central American coast between 10ºN and 15ºN and a negative one for the Caribbean coast of Nicaragua, Argentina and the Baja California peninsula.

The TSA index appears to be most influential for positive phases along the southern coast of Brazil and the Pacific coast of Central America, while it displays a negative correlation for the Caribbean coat of Central America and the far south of Argentina and southern Chile.

For the NTA index, a negative correlation is widespread for the southern coasts of the Caribbean Sea down to Guyana. A positive correlation is found for limited areas along the Brazilian coast (between Fortaleza and Recife) and along the northern coast of Cuba.

FIGURE 1.152
CORRELATION BY STANDARD DEVIATION (POSITIVE DEGREES IN A CLOCKWISE DIRECTION) FOR THE DIRECTION OF MONTHLY MEAN ENERGY FLOW OF WAVE ACTIVITY AND THE NIÑO3 (UPPER LEFT), TSA (LOWER LEFT), SAM (UPPER RIGHT) AND NTA (LOWER RIGHT) INDICES

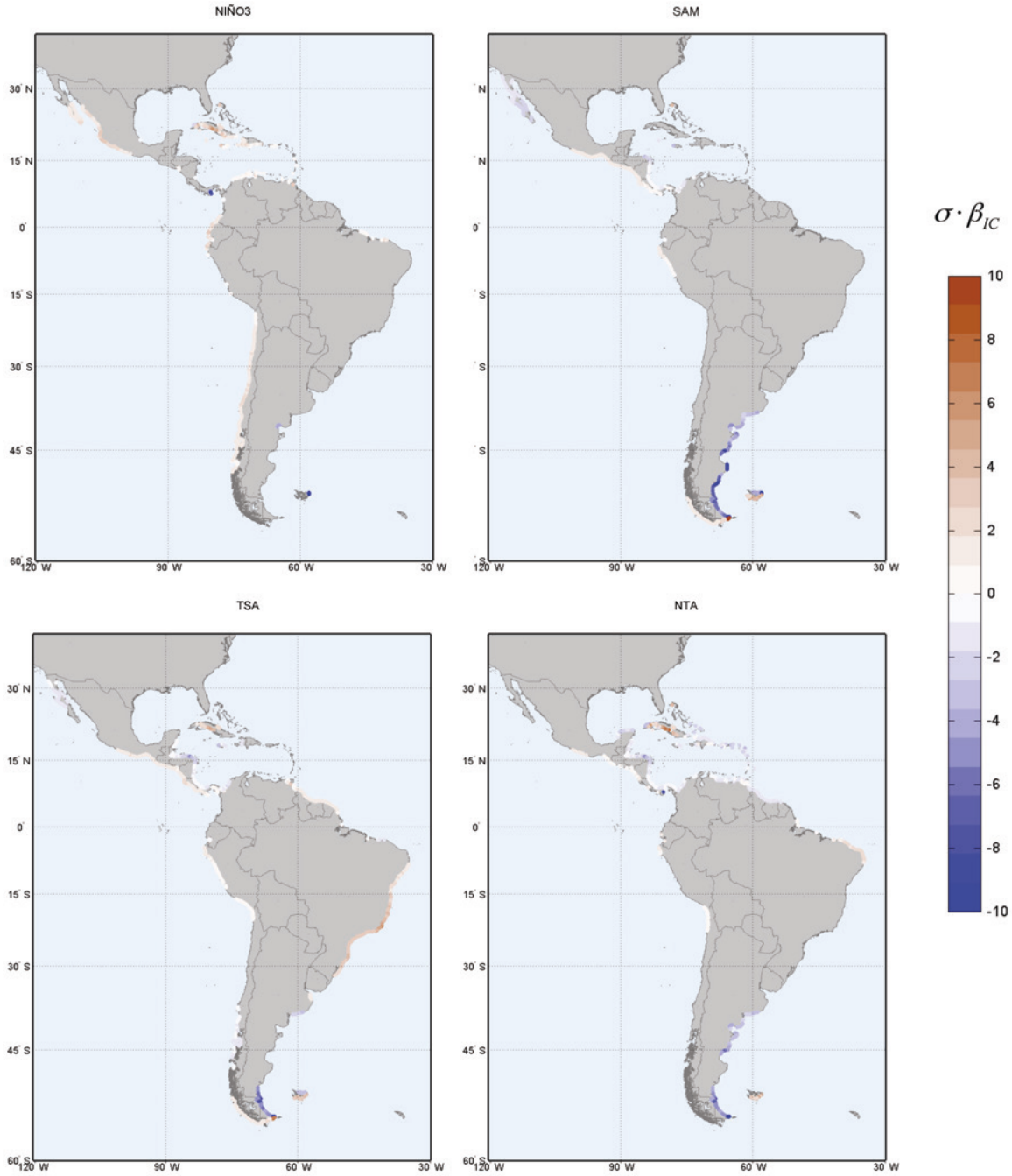

Source: Prepared by the authors.

6.4.1.3. Correlation of climate indices with mean sea levels

FIGURE 1.153
CORRELATION OF SEA LEVELS AND THE NIÑO3 (UPPER LEFT), CAR (UPPER CENTRE), AMO (UPPER RIGHT), TSA (LOWER LEFT), SOI (LOWER CENTRE) AND NTA (LOWER RIGHT) INDICES

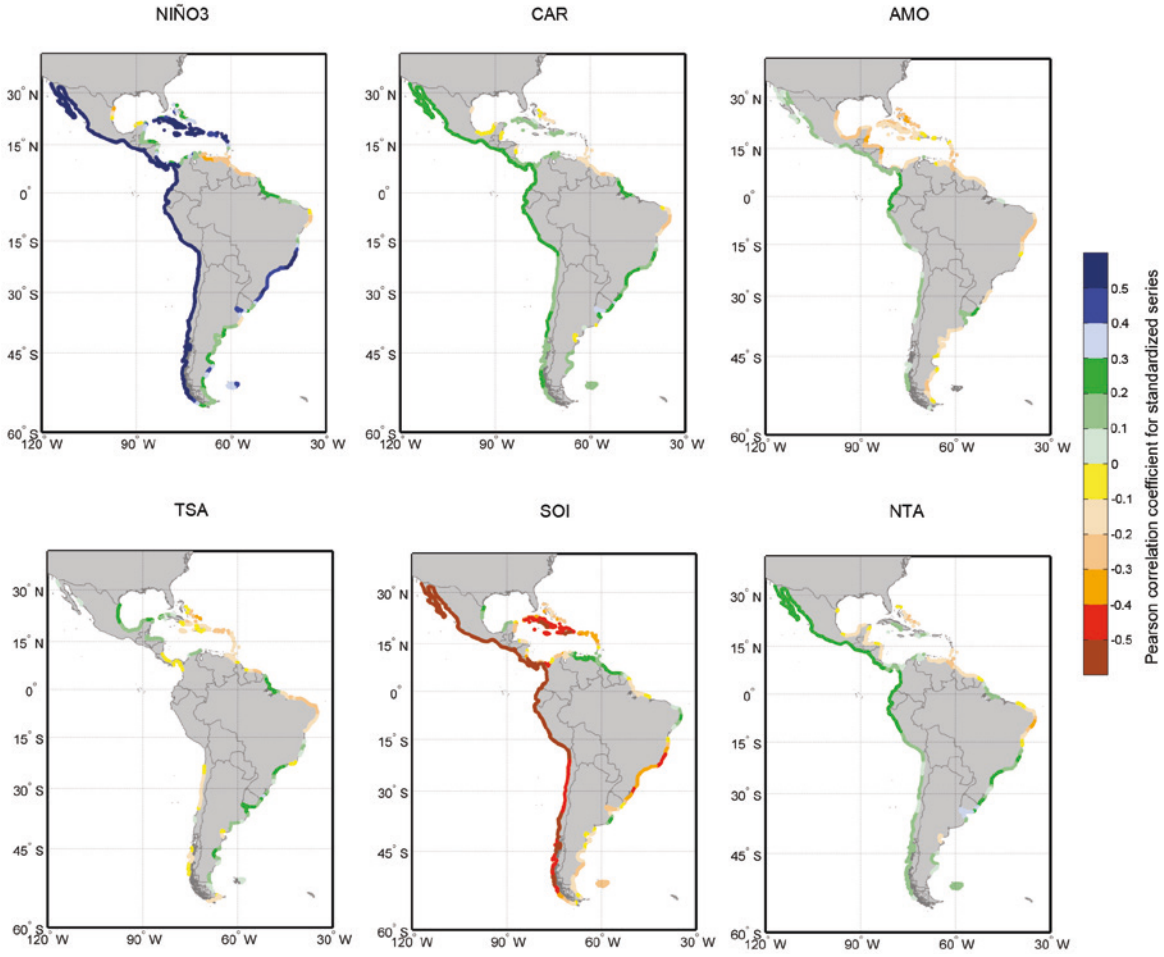

Source: Prepared by the authors.

There is a very strong correlation between sea levels and many of the indices and especially with the NIÑO3, SOI, CAR, AMO and NTA indices.

The NIÑO3 index exhibits a high correlation (above 0.5) with a standardized anomaly for sea levels in the area stretching from Ecuador on the Atlantic coast to 15ºS on the Pacific coast. In more southerly latitudes, the correlation is still positive but less marked. Thus, the NIÑO3 index depicts a widespread rise in sea levels throughout the domain and particularly up to the 15ºS parallel. The correlation is much weaker for the Gulf of Mexico, however.

The SOI index yields results that are just the opposite of those of the NIÑO3 index. Although they are not as widespread, there are high negative correlations with the positive phase of the index, which indicates that the positive values on the index correspond to a reduction in seal levels in the area up to 15ºS latitude.

The CAR index also yields a positive (0.2-0.3) correlation with sea level anomalies in the subtropics, as does the NTA index, although the size of the latter's effect in terms of latitudes is more limited.

The AMO index displays a marked negative correlation, with the North Atlantic oscillation being associated with a slight negative correlation on the Atlantic face of the Caribbean islands, the Gulf of Mexico, the peninsula of Baja California and northern Chile. There is a positive correlation along the Central American coast below 15ºN and along the Atlantic coast of South America down to northern Brazil, with the correlation becoming negative below 5ºS, approximately.

FIGURE 1.154
CORRELATION OF STANDARD DEVIATION IN SEA LEVELS WITH THE NIÑO3 INDEX (UPPER LEFT), CAR INDEX (UPPER MIDDLE), AMO INDEX (UPPER RIGHT), TSA INDEX (LOWER LEFT), SOI INDEX (LOWER MIDDLE) AND NTA INDEX (LOWER RIGHT)

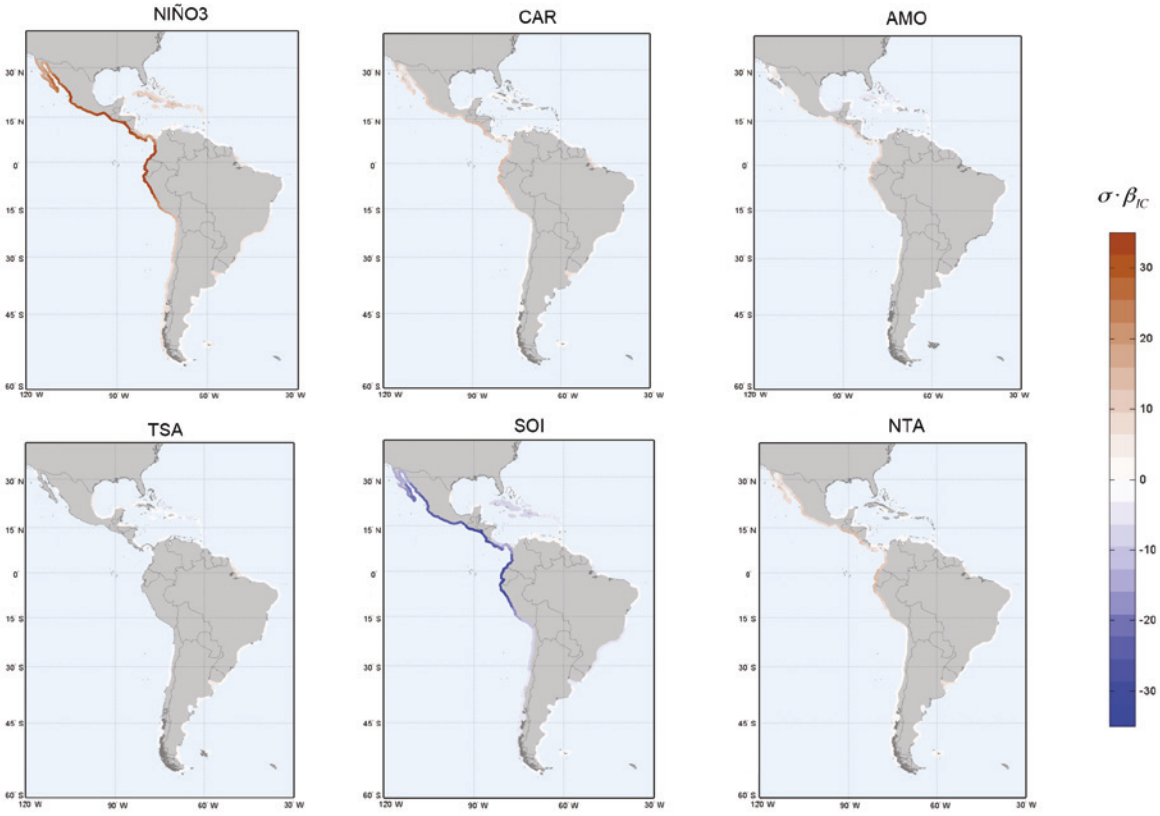

Source: Prepared by the authors.

For the mean sea levels, since there are a series of anomalies in annual mean values, the term in this case is null.

6.4.1.4. Correlation of climate indices at the 95th quantile for storm surges

The positive correlation with the NIÑO3 index of around 0.25 for storm surges in the area of the Plate River is located precisely in the part of the Latin American and Caribbean region where storm surges are the highest (see figure 1.38 and figure 1.39). Positive values on this index are related with widespread occurrences of extreme highs in storm surges along the Atlantic face of the continent, including the Caribbean islands, up to the Gulf of Mexico, where the correlation turns negative. The trends along the Pacific coast are much more mixed, with positive correlations to the west of the Baja California Peninsula, negative ones in the Gulf of California, positive correlations along the coast of Mexico, slightly negative correlations along Central America, moderate positive ones for Ecuador and slightly negative ones for most of Chile.

The SAM index traces storm surges for the most part up to approximately 5ºS and for more southerly locations along the South Atlantic coast as well. Most of its correlations are negative, with the exception of those for Cuba, the eastern portion of the Gulf of Mexico and to the south of the peninsula of Baja California.

The NTA shows a high correlation for the peninsula of Baja California, the coast of the southern Atlantic and the Caribbean islands, especially in the case of Barbados. This index yields a negative correlation, however, along both coasts of the mainland between 15ºN latitude and Ecuador.

FIGURE 1.155
CORRELATION AT THE 95TH QUANTILE FOR STORM SURGES FOR THE AMO INDEX (UPPER LEFT), NTA INDEX (UPPER MIDDLE), SOI INDEX (UPPER RIGHT), NIÑO3 INDEX (UPPER LEFT) AND CAR INDEX (LOWER MIDDLE)

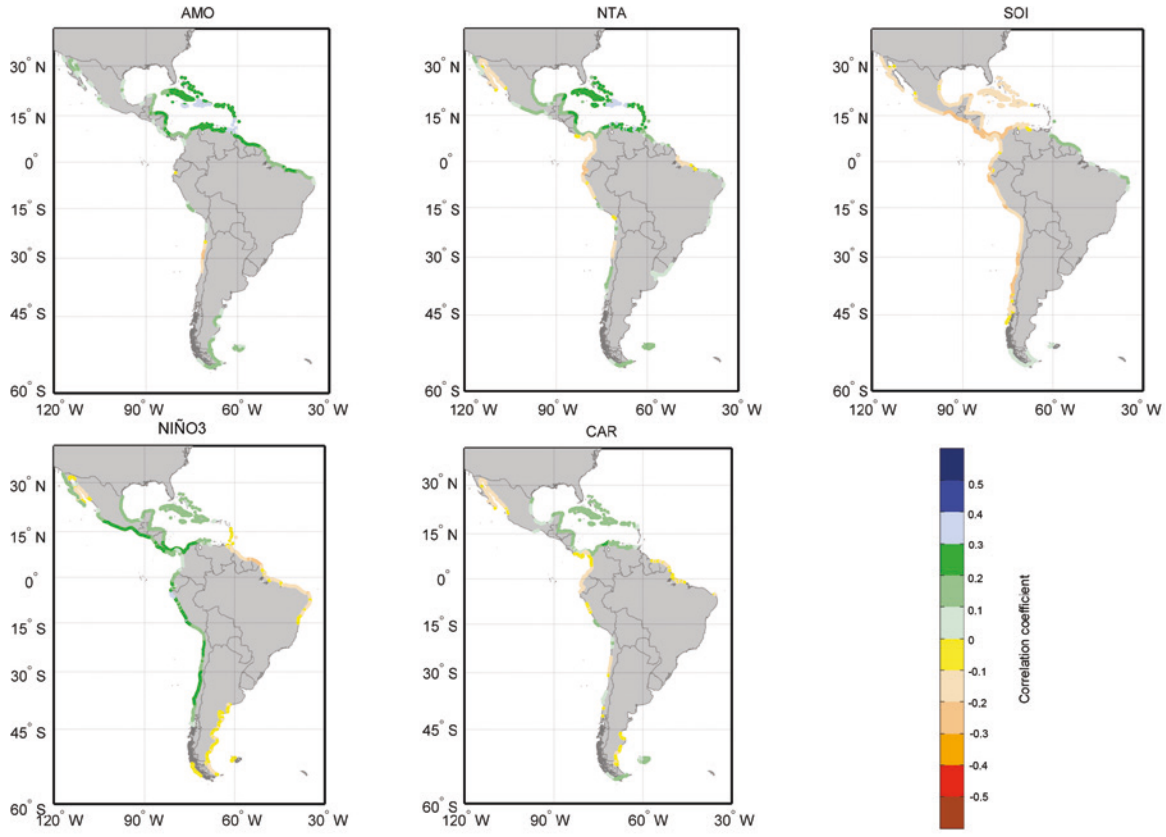

Source: Prepared by the authors.

6.4.2. Time lag analysis (cross-correlation)

The above results measure the correlation between contemporaneous series on coastal dynamics and climate indices. The resulting picture is a "snapshot" of what would happen if the response to each weather phenomenon were to occur in the same month as the phenomenon itself. There is no reason why the response of coastal dynamics to the weather conditions described by the indices would make itself evident immediately, however. Depending on the type of phenomenon concerned (temperature, pressure, wave activity, etc.), the response will have a different origin and will thus arise at different times and will display a different degree of momentum. In order to assess the time lag in these responses, the various indices are analysed using cross-correlations to determine the maximum lag and to find out whether it is statistically significant or not.

By way of example, two of the calculated cross-correlations are shown below to illustrate the maximum correlations at t=0 (left) and t=tb (right).

FIGURE 1.156
ANALYSIS OF THE CROSS-CORRELATIONS FOR ONE OF THE VARIABLES WITH THE NIÑO3 INDEX – POINT 363 (LEFT) AND THE SOI INDEX – POINT 450 (RIGHT)

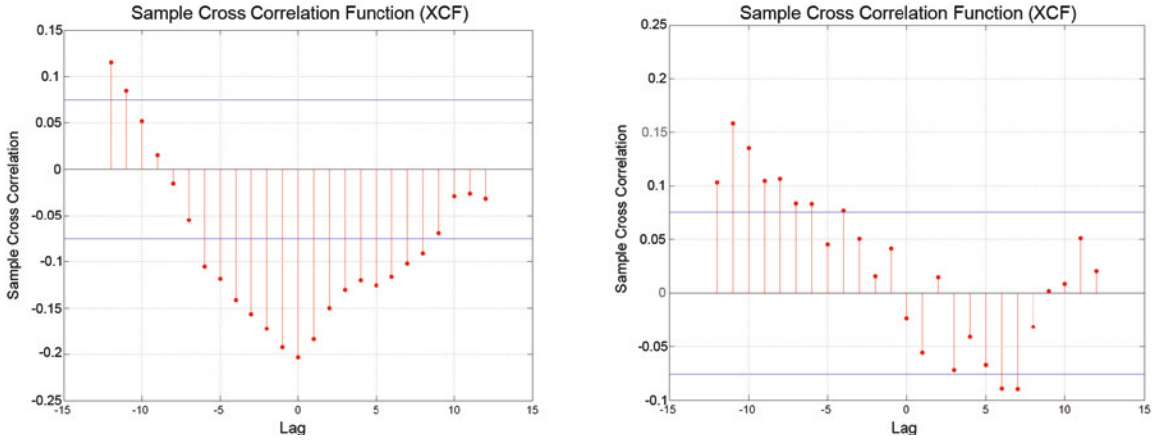

Source: Prepared by the authors.

6.4.2.1. Results for wave activity

(a) Results for the 95th percentile of Hs

An analysis of figure 1.157 shows that effects on wave activity exhibit both a substantial forward and backward lag (between 1 and 3 months) for most of the indices, with the exceptions being the SAM and AMO indices, where the effects are contemporaneous for most of the domain.

6.4.2.2. Time lag for climate indices for mean direction of energy flow

Unlike the situation with respect to the severity of wave activity, the mean direction of energy flow is clearly an outcome of the presence of the meteorological conditions that are mirrored in weather indices, since, as is shown in most of the graphs in figure 1.158, the time lag is less than one month. An exception is the direction along the Pacific coast of Central America, where, as measured by the TSA index, the effect appears from two to three months after the maximum value of this index is recorded.

FIGURE 1.157
TIME LAGS FOR THE MAXIMUM CORRELATION FOR THE 95TH PERCENTILE FOR SIGNIFICANT WAVE HEIGHT WITH THE VARIOUS CLIMATE INDICES

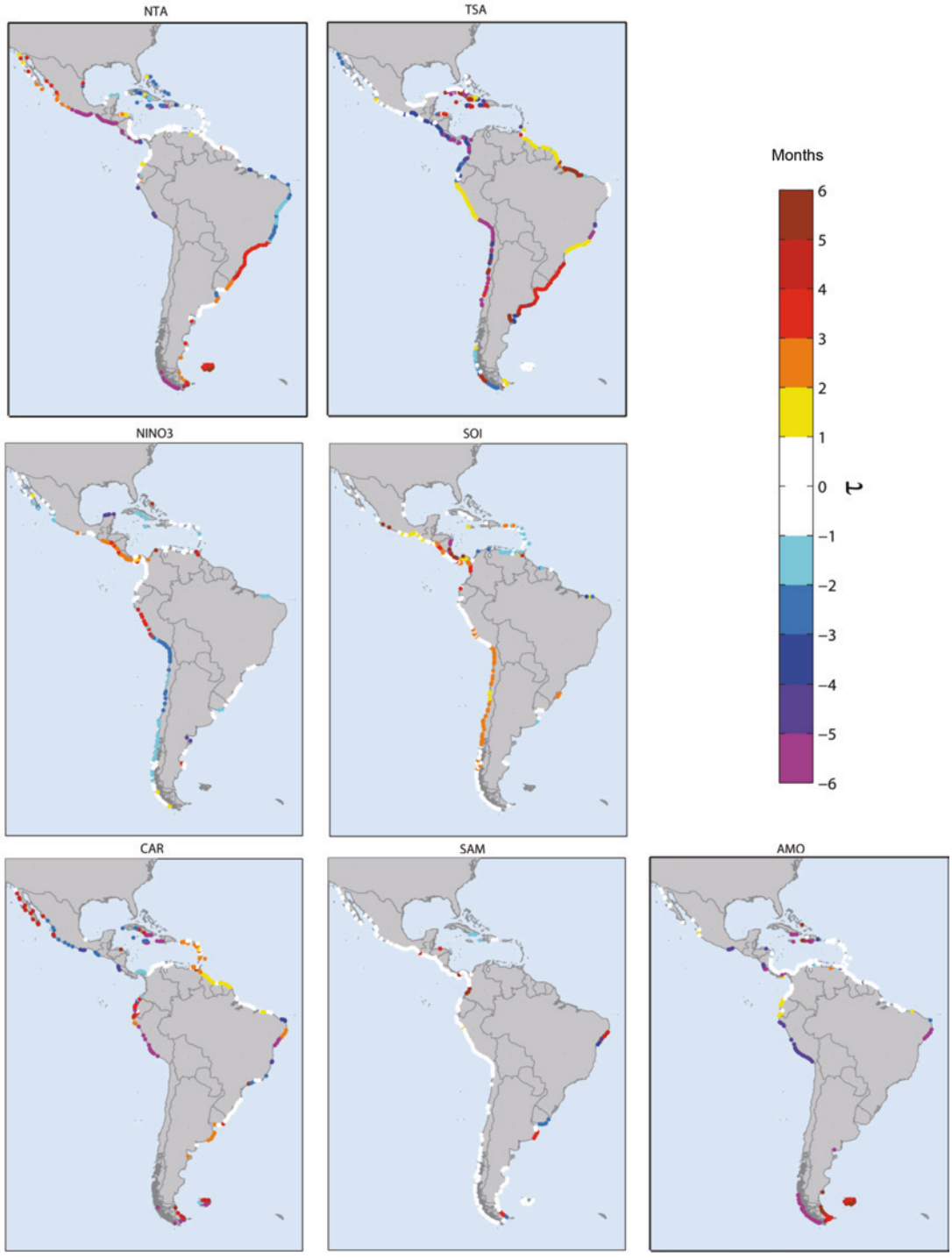

Source: Prepared by the authors.

FIGURE 1.158
TIME LAGS IN THE CORRELATION FOR THE MEAN DIRECTION OF FLOW OF WAVE ACTIVITY WITH THE VARIOUS CLIMATE INDICES

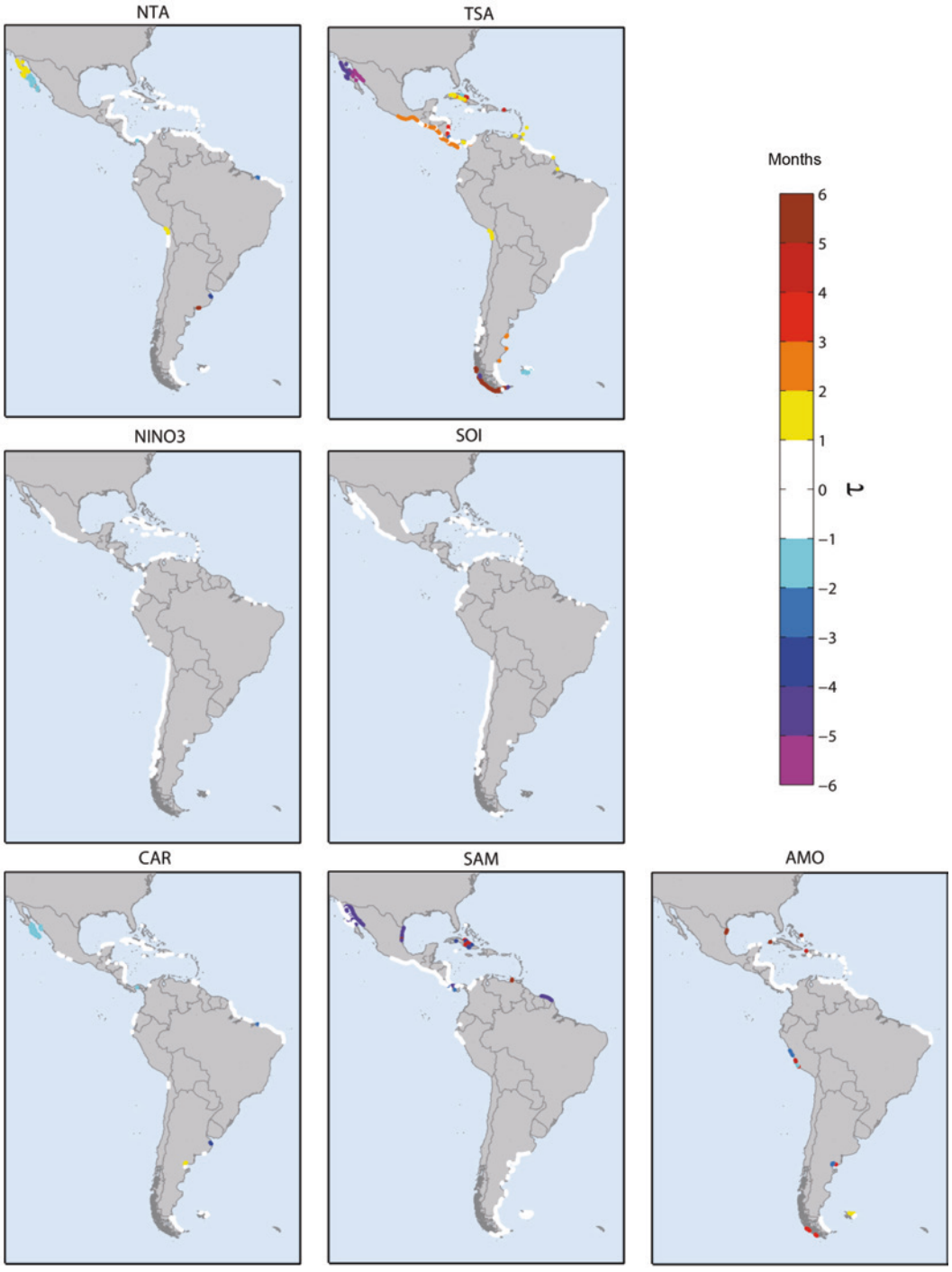

Source: Prepared by the authors.

6.4.2.3. Time lag in climate indices for mean sea levels

A reading of figure 1.159 leads to two clear-cut conclusions. First, the indices for which the highest correlations with sea levels are obtained (NIÑO3 and SOI) register those effects in the month following the one in which the highest value of the index is registered. Second, an observable time lag is seen in both the TSA and CAR indices. In the TSA index, the effect is seen five months before, while, in the case of the CAR index, the measurement is seen five months after the value was registered on the climate index.

FIGURE 1.159
TIME LAGS IN THE CORRELATION FOR MEAN SEA LEVELS WITH THE VARIOUS CLIMATE INDICES
(Months)

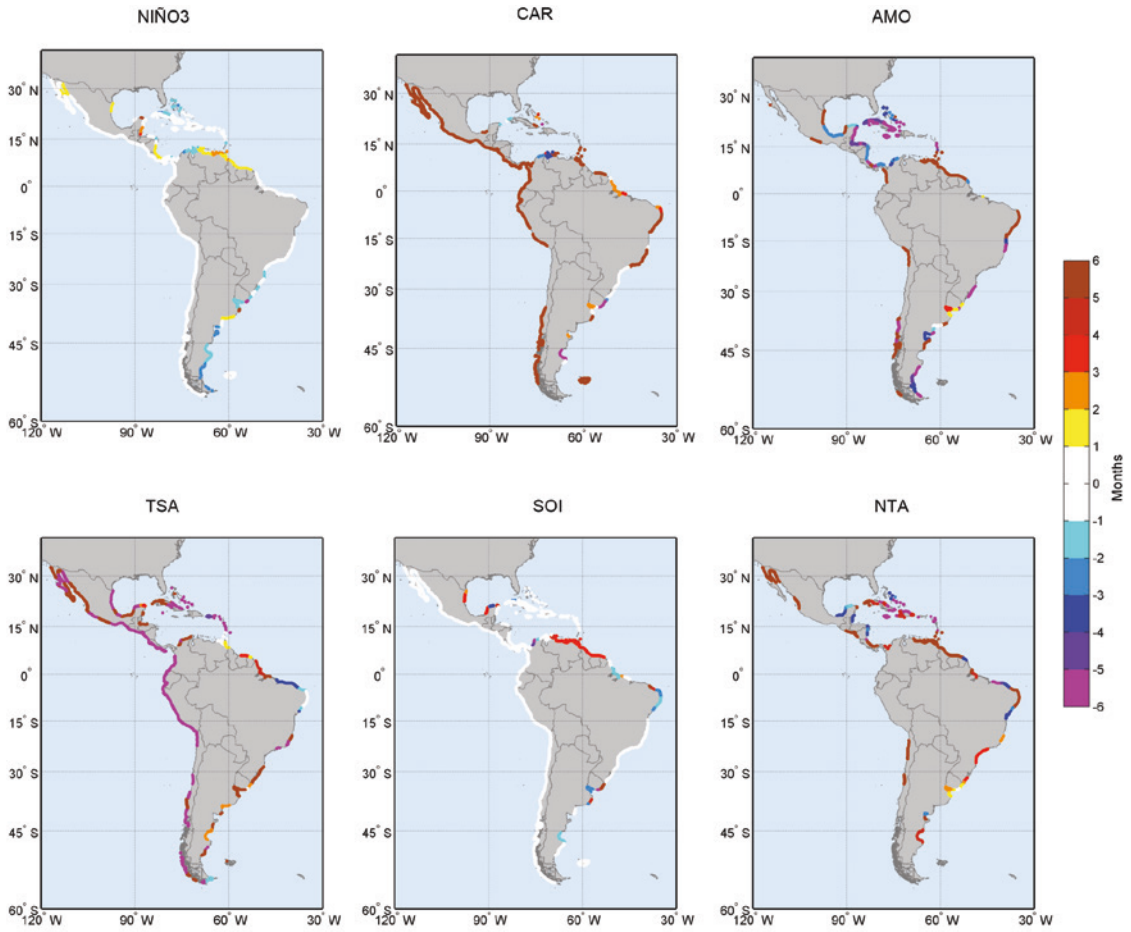

Source: Prepared by the authors.

6.4.2.4. Time lags for the 95th percentile for storm surges for the various climate indices

As in the case of wave activity, the time lags involved in the effects of storm surges vary widely. The SAM index, which is one of the most important ones for measurements of this variable, exhibits a coetaneous effect with those measured by climate indices.

FIGURE 1.160
TIME LAG FOR THE 95TH PERCENTILE FOR CORRELATIONS WITH STORM SURGES FOR THE VARIOUS CLIMATE INDICES
(Months)

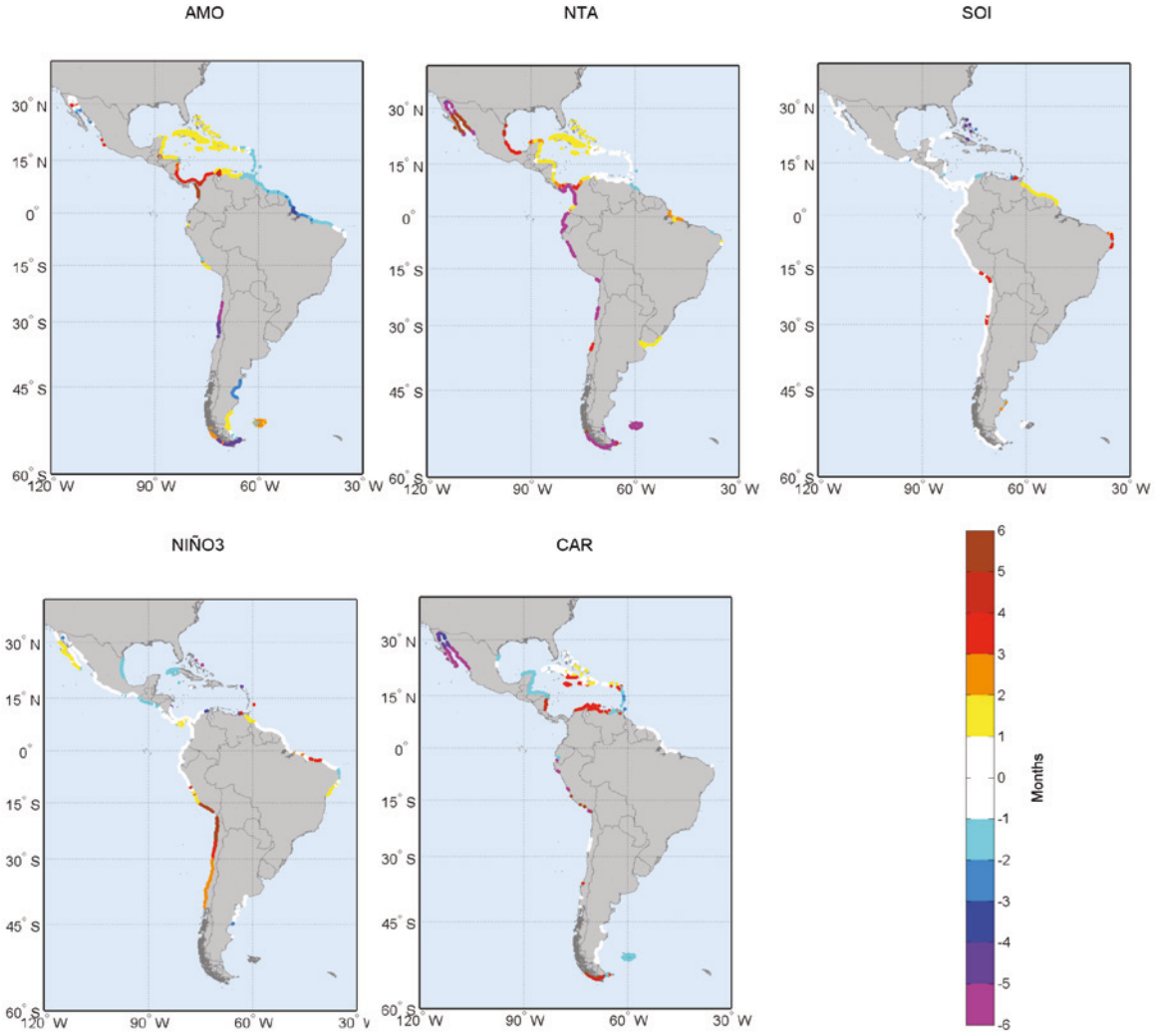

Source: Prepared by the authors.

All of these results for year-on-year changes attest to the importance of using this time scale and to the need to take these findings into account when analysing climate change in coastal areas. While it is true that it is highly questionable whether today's climate change projections based on global climate models (GCMs) faithfully reflect actual climate patterns, the ability to quantify the influence that each pattern exerts, as measured by the corresponding index, on the coastal variables under study here is of crucial importance.

6.5. Overview of inter-annual variability in coastal dynamics

Since macro-patterns can be one of the most important drivers of spatial and temporal variability in coastal dynamics, attention has been devoted to the influence of wave activity, sea levels and storm surges as measured by the AO, SAM, SOI, PNA, WP, EP/NP, NAO, EA, CAR, EA/WR, SCA, DMI, AMO, QBO, NBR, NTA, TNA and TSA climate indices.

CLIMATE VARIABILITY	• The strongest influence in the higher range of wave heights is found in the NTA for northern Brazil and the southern Caribbean islands and in NIÑO3 for northern Mexico (Pacific coast). In the mid-range, slight positive correlations (around 0.2) are exhibited by the SOI for the Pacific coast, while negative correlations are registered on the CAR and NTA indices for the southern Atlantic and the Caribbean and positives ones on the NTA index for the Pacific and Atlantic coasts in the southern hemisphere. • The mean direction of energy flow (predominant wave direction) is closely correlated with a number of the indices (above 0.5) for various parts of the coastlines covered in this study. There is a positive correlation with the NIÑO3 in Chile and western Mexico and with the SAM in Central America and the southern and northern extremes of the study domain. Correlations with the TSA for the Brazilian and Central American coasts are apparent as well, as is a negative correlation on the NTA for the Caribbean. • The NIÑO3 index reflects a strong influence on mean sea levels along the entire Pacific coast and along the southern Brazilian coast (a Pearson correlation coefficient of over 0.5 for standardized data). There is also a slightly positive correlation (around 0.2) for sea levels on the CAR index for the Pacific coast. Along the northern Pacific coast, the correlation with the NTA index is striking. The AMO index reflects a strong influence on sea levels in the Caribbean Sea (with a negative sign). • Storm surges correlate with the NTA and AMO indices in the Caribbean, while the influence of the factors captured by the SOI and NIÑO3 indices is more apparent in the Pacific (and the northern Caribbean islands).

The overall conclusion to be drawn from the analysis of variability in weather patterns is that this is one of the factors that needs to be studied in order to account for much of the year-on-year variability for some variables in the long-term trends. The two time scales used for the two factors should not be confused, as both are necessary in order to arrive at an understanding of weather variability in the recent past as a basis for extrapolating possible future trends.

7. General conclusions

This is the first of the project documents to be prepared as part of the regional study on the effects of climate change on the coasts of Latin America and the Caribbean (Project C3A) being conducted by the Environmental Hydraulics Institute of Cantabria and ECLAC.

The first section of this document presented a study of current conditions in terms of the coastal dynamics of the region. It maps out the results of a spatial and temporal assessment of such variables as mean sea levels, sea surface temperatures, salinity, wave activity, tides and storm surges. This description of current physical conditions lays the groundwork for a study designed to determine how the different variables have changed and what impacts future variations may have on the region's coastlines.

A second section of this document has been devoted to an analysis of changing trends in the different variables and extrapolations of those changes for the years 2040, 2050 and 2070 at a given level of statistical certainty. This section provides a frame of reference for the analysis of the implications of these changes, which are dealt with in the third project document (coastal impacts). The second project document focuses on the region's position in terms of its coastal regions' vulnerability and exposure to various sorts of risks.

Given the importance of climate variability in terms of its influence on many of the variables examined in this study, however, a simple correlation analysis has been used to determine what influence the various patterns (represented by climate indices) have on the relevant variables as they apply to the coasts of the study domain. The influential nature of these indices of natural variability has been incontrovertibly demonstrated.

Bibliography

Ardalan, A.A. and H. Hashemi-Farahani (2007), "A harmonic approach to global ocean tide analysis based on TOPEX/POSEIDON satellite", *Marine Geophysical Research,* vol. 28, No. 3, Springer.

Barbosa, S. and B. Andersen (2009), "Trend patterns in global sea surface temperature", *International Journal of Climatology,* vol. 29, No. 14, Wiley.

Barnston, A.G. and R.E. Livezey (1987), "Classification, seasonality and persistence of low- frequency atmospheric circulation patterns", *Monthly Weather Review,* vol. 115, No. 6, American Meteorological Society.

Behringer, D.W. and Y. Xue (2004), "Evaluation of the global ocean data assimilation system at NCEP: the Pacific Ocean", Eighth Symposium on Integrated Observing and Assimilation System for Atmosphere, Ocean, and Land Surface, AMS 84th Annual Meeting, Washington State Convention and Trade Center, Seattle, Washington.

Bird, E.C.F. (1985), *Coastline Changes,* Nueva York, Wiley & Sons.

Booij, N., R.C. and L.H. Holthuijsen (1999), "A third-generation wave model for coastal regions, Part I: Model description and validation", *Journal of Geophysical Research,* vol. 104, No. C4.

Budgell, W.P. (2005), "Numerical simulation of ice-ocean variability in the Barents Sea region", *Ocean Dynamics,* vol. 55, No. 3-4, Springer.

Camus, P. and others (2007), "A methodology to evaluate wave energy resources in shallow waters", paper presented at the 7th European Wave and Tidal Energy Conference (EWTEC).

Cane, M. (2005), "The evolution of El Niño, past and future", *Earth and Planetary Science Letters,* vol. 230, No. 3-4, Amsterdam, Elsevier.

Cavazos, T. (1997), "Downscaling large-scale circulation to local winter rainfall in north-eastern Mexico", *International Journal of Climatology,* vol. 17.

Church, J.A. and others (2004), "Estimates of the regional distribution of sea level rise over the 1950 to 2000 period", *Journal of Climate,* vol. 17, American Meteorological Society.

Chylek, P. and G. Lesins (2008), "Multidecadal variability of Atlantic hurricane activity: 1851–2007", *Journal of Geophysical Research,* vol. 113.

CIESIN (Center for International Earth Science Information Network) (2002a), "Country-level Population and Downscaled Projections based on the B2 Scenario, 1990-2100", Columbia University [online] http://www.sedac.ciesin.columbia.edu/mva/downscaling/ciesin.html.

_____ (2002b), "Country-level GDP and Downscaled Projections based on the A1, A2, B1, and B2 Marker Scenarios, 1990-2100", Columbia University [online] http://www.sedac.ciesin.columbia.edu/mva/downscaling/ciesin.html.

_____ (2005), "Gridded Population of the World and the Global Rural-Urban Mapping Project", Columbia University [online] http://www.sedac.ciesin.columbia.edu/gpw.

Collins, M. and others (2005), "El Niño- or La Niña-like climate change", *Climate Dynamics,* vol. 24, No. 1, Springer.

Curry, J.A. (2008), "Potential increased hurricane activity in a greenhouse warmed world", *Sudden and Disruptive Climate Change,* M. MacCracken (ed.), London, Earthscan.

ECLAC (Economic Commission for Latin America and the Caribbean) (2010), "Ranking 2010 de actividad portuaria de contenedores en América Latina y el Caribe", Santiago, Chile.

Egbert, G.D., A.F. Bennett and M.G.G. Foreman (1994), "TOPEX/POSEIDON tides estimated using a global inverse model", *Journal of Geophysical Research,* vol. 99, No. C12.

Egbert, G.D. and S.Y. Erofeeva (2002), "Efficient inverse modeling of barotropic ocean tides", *Journal of Atmospheric and Oceanic Technology,* vol. 19, No. 2, American Meteorological Society.

Emanuel, K., R.A. Sundararajan and J. Williams (2008), "Hurricanes and global warming", *Bulletin of the American Meteorological Society,* vol. 89, No. 3, American Meteorological Society.

Enfield, D.B. and L. Cid-Serrano (2010), "Secular and multidecadal warmings in the North Atlantic and their relationships with major hurricane activity", *International Journal of Climatology,* vol. 30, No. 2, Wiley.

Enfield, D.B. and others (1999), "How ubiquitous is the dipole relationship in tropical Atlantic sea surface temperatures?", *Journal of Geophysical Research,* vol. 104, No. C4.

Forema, MGG. (1977), "Manual for tidal heights analysis and prediction", *Pacific Marine Sciences Report,* Sidney, Institute of Ocean Sciences.

GEBCO (General Bathymetric Chart of the Oceans) [online] http://www.gebco.net/.

Goldenberg, S.B. and others (2001), "The recent increase in Atlantic hurricane activity: causes and implications", *Science,* vol. 293, No. 5529, American Association for the Advancement of Science.

Goodess, C.M. and others (2007), "An intercomparison of statistical downscaling methods for Europe and European regions - assessing their performance with respect to extreme temperature and precipitation events", *Climatic Change*.

Grinsted, A., J.C. Moore and S. Jefrejeva (2010), "Reconstructing sea level from paleo and projected temperatures 200 to 2100 AD", *Climate Dynamics,* vol. 34, No. 4, Springer.

Gutiérrez, J.M. and others (2004), "Clustering methods for statistical downscaling in short-range weather forecast", *Monthly Weather Review,* vol. 132, No. 9, American Meteorological Society.

____ (2002), "Probabilistic networks for statistical downscaling and spationalization of meteorological data", *Geophysical Research Abstracts,* vol. 4.

Hannachi, A. (2007), "Pattern hunting in climate: a new method for finding trends in gridded climate data", *International Journal of Climatology,* vol. 27, No. 1.

Hannachi, A. and A. O'Neill (2001), "Atmospheric multiple equilibria and non-Gaussian behaviour in model simulations", *Quarterly Journal of the Royal Meteorological Society,* vol. 127, No. 573, Wiley.

Hewitson, B.C. and R.G. Crane (2006), "Consensus between GCM climate change projections with empirical downscaling: precipitation downscaling over South Africa", *International Journal of Climatology,* vol. 26, No. 10, Wiley.

Hong, H.P. (1998), "An efficient point estimate method for probabilistic analysis", *Reliability Engineering and System Safety,* vol. 59, No. 3, Amsterdam, Elsevier.

Horton, R. and others (2008), "Sea-level rise projections for current generation CGCMs based on the semiempirical method", *Geophysical Research Letters,* vol. 35, No. 2.

Huebener, H. and M. Kerschgens (2007), "Downscaling of current and future rainfall climatologies for southern Morocco. Part I: Downscaling method and current climatology", *International Journal of Climatology,* vol. 27, No. 13, Wiley.

Hunter, J. (2010), "Estimating sea-level extremes under conditions of uncertain sea-level rise", *Climatic Change,* vol. 99, No. 3-4, Springer.

IPCC (Intergovernmental Panel on Climate Change) (2007), *Contribution of Working Group 1 to the Fourth Assessment Report of the Intergovernmental Panel on Climate Change,* S. Solomon and others (eds.), Cambridge, Cambridge University Press.

Izaguirre, C. and others (2010), "Extreme wave climate variability in southern Europe using satellite data", *Journal of Geophysical Research,* vol. 115, No. C4.

Jolliffe, I.T. (2002), *Principal Component Analysis,* New York, Springer.

Komen, G.J. and others (1994), *Dynamics and Modelling of Ocean Waves,* Cambridge University Press.

Kohonen, T. (2001), "Self-organizing maps", *Springer Series Information Sciences,* vol. 30, New York, Springer.

Kutzbach, J.E. (1967), "Empirical eigenvectors of sea-level pressure, surface temperature and precipitation complexes over North America", *Journal of Applied Meteorology,* vol. 6, No. 5, American Meteorological Society.

Luceño, A., M. Menéndez and F.J. Méndez (2006), "The effect of temporal dependence on the estimation of the frequency of extreme ocean climate events", *Proceedings of the Royal Society-A,* vol. 462, The Royal Society.

Méndez, F.J. and others (2006), "Estimation of the long-term variability of extreme significant wave height using a time-dependent POT model", *Journal of Geophysical Research,* vol. 111.

_____ (2007), "Analyzing monthly extreme sea levels with a time-dependent GEV model", *Journal of Atmospheric and Oceanic Technology,* vol. 24, No. 5, American Meteorological Society.

Menéndez, M. and others (2008a), "The influence of seasonality on estimating return values of significant wave height", *Coastal Engineering,* vol. 56, No. 3, Amsterdam, Elsevier.

_____ (2008b), "Variability of extreme wave heights in the northeast Pacific ocean based on buoy measurements", *Geophysical Research Letters,* vol. 35, No. 22, Wiley.

Morales, J.M. and others (2010), "Probabilistic power flow with correlated loads and wind sources", *IET Generation, Transmission & Distribution,* vol. 4, No. 5.

Nakicenovic, N. and others (2000), *Special Report on Emissions Scenarios: A Special Report of Working Group III of the Intergovernmental Panel on Climate Change,* Cambridge, Cambridge University Press.

Nicholls, N. (2008), "Recent trends in the seasonal and temporal behaviour of the El Niño-Southern Oscillation", *Geophysical Research Letters,* vol. 35, No. 19.

Nicholls, R.J. and A. Cazenave (2010), "Sea-level rise and its impact on coastal zone", *Science,* vol. 328 [online] http://www.ncbi.nlm.nih.gov/pubmed/20558707.

Nicholls, R., F. Hoozemans and M. Marchand (1999), "Increasing flood risk and wetland losses due to global sea-level rise: regional and global analyses", *Global Environmental Change,* vol. 9 [online] http://linkinghub.elsevier.com/retrieve/pii/S0959378099000199.

Ortiz-Royero, J.C. and A. Mercado-Irizarry (2008), "An intercomparison of SWAN and WAVEWATCH III models with data from NDBC-NOAA buoys at oceanic scales", *Coastal Engineering Journal,* vol. 50, No. 1, World Scientific Publishing.

Pawlowicz, R., B. Beardsley and S. Lentz (2002), "Classical tidal harmonic analysis including error estimates in MATLAB using T_TIDE", *Computers and Geosciences,* vol. 28, No. 8, Amsterdam, Elsevier.

Peltier, W.R. (2001), "Glacial isostatic adjustment corrections", *Sea Level Rise: History and Consequences,* B.C. Douglas, M.S. Kearney and S.P. Leatherman (eds.), Academic Press.

_____ (2000), "Earth Physics and Global Glacial Isostasy: From Paleo-Geodesy to Space-Geodesy", *International Association of Geodesy Symposia,* vol. 123, Springer.

Penland, C. and L. Matrosova (1998), "Prediction of tropical Atlantic sea surface temperatures using linear inverse modeling", *Journal of Climate,* vol. 11, No. 3, American Meteorological Society.

Preisendorfer, R.W. (1988), *Principal Component Analysis in Meteorology and Oceanography,* Amsterdam, Elsevier.

Prudhomme, C., D. Jakob and C. Svensson (2003), "Uncertainty and climate change impact on the flood regime of small UK catchments", *Journal of Hydrology,* vol. 277, No. 1-2, Amsterdam, Elsevier.

Rahmstorf, S. and others (2007), "Recent climate observations compared to projections", *Science,* vol. 316, American Association for the Advancement of Science.

Rasmusson, E.M. and T.H. Carpenter (1983), "The relationship between eastern equatorial Pacific sea surface temperatures and rainfall over India and Sri Lanka", *Monthly Weather Review,* vol. 111, No. 3, American Meteorological Society.

Saha, S. and others (2006), "The NCEP climate forecast system", *Journal of Climate,* vol. 19, No. 15.

Salathé, E.P. (2005), "Downscaling simulations of future global climate with application to hydrologic modeling", *International Journal of Climatology,* vol. 25, No. 4, Wiley.

Schmidli, J., C. Frei and P.L. Vidale (2006), "Downscaling from GCM precipitation: A benchmark for dynamical and statistical downscaling methods", *International Journal of Climatology,* vol. 26, No. 5, Wiley.

Schwartz, M.L. (ed.) (2005), *Encyclopedia of Coastal Science,* Springer.

Shanahan, T.M. and others (2009), "Atlantic forcing of persistent drought in West Africa", *Science,* vol. 324, No. 5925, American Association for the Advancement of Science.

Snarey, M. and others (1997), "Comparison of algorithms for dissimilarity-based compound selection", *Journal of Molecular Graphics and Modelling,* vol. 15, No. 6, Amsterdam, Elsevier.

The WAMDIG Group (1988), "The WAM model - A third generation ocean wave prediction model", *Journal of Physical Oceanography,* vol. 18, No. 12.

Thompson, D.W.J. and J.M Wallace (2000), "Annular modes in the extratropical circulation. Part I: Month-to-month variability", *Journal of Climate,* vol. 13, No. 5, American Meteorological Society.

_____ (1998), "The Arctic oscillation signature in the wintertime geopotential height and temperature fi lds", *Geophysical Research Letters,* vol. 25, No. 9, Wiley.

Tolman, H.L. (2003), "Treatment of unresolved islands and ice in wind wave models", *Ocean Modelling,* vol. 5, No. 3, Amsterdam, Elsevier.

_____ (2002), "Limiters in third-generation wind wave models", *Journal of Atmospheric and Ocean Science,* vol. 8, No. 1, Taylor & Francis.

_____ (1999), "User manual and system documentation of WAVEWATCH-III version 1.18", *Technical Note,* No. 166.

_____ (1997), "User manual and system documentation of WAVEWATCH-III version 1.15", *Technical Note,* No. 151.

_____ (1989), "The numerical model WAVEWATCH: a third generation model for the hindcasting of wind waves on tides in shelf seas", *Communications on Hydraulic and Geotechnical Engineering,* Delft University of Technology.

Tomas, A., F.J. Mendez and I.J. Losada (2008), "A method for spatial calibration of wave hindcast data bases", *Continental Shelf Research,* vol. 28, No. 3, Amsterdam, Elsevier.

United States Army Corps of Engineers (1984), *Shore Protection Manual,* Coastal Engineering Research Center.

Van Dorn, W.C. (1953), "Wind stress on an artificial pond", *Journal of Marine Research,* vol. 12.

Van Oldenborgh, G.J., S.Y. Philip and M. Collins (2005), "El Niño in a changing climate: a multi-model study", *Ocean Science,* vol. 1.

Van Vuuren, D.P., P.L. Lucas and H.B.M. Hilderink (2006), "Downscaling drivers of global environmental change Enabling use of global SRES scenarios at the national and grid levels", Netherlands Environmental Assessment Agency [online] http://www.pbl.nl/en/publications/2006/DownscalingDriversOfGlobalEnvironmentalChangeScenarios.

Vermeer, M. and S. Rahmstorf (2009), "Global sea level linked to global temperature", *Proceedings of the National Academy of Sciences,* vol. 106, No. 51.

Von Storch, H. and F.W. Zwiers (1999), *Statistical Analysis in Climate Research,* Cambridge, Cambridge University Press.

Wallace, J.M. and D.W.J. Thompson (2002), "The Pacific Center of Action of the Northern Hemisphere annular mode: real or artifact?", *Journal of Climate,* vol. 15, No. 14, American Meteorological Society.

Wallace, J.M. and D.S. Gutzler (1981), "Teleconnections in the geopotential height field during the Northern hemisphere winter", *Monthly Weather Review,* vol. 109, No. 4, American Meteorological Society.

Weisse, R. and H. von Storch (2010), *Marine Climate and Climate Change. Storms, Wind Waves and Storm Surges,* New York, Springer.

Wilby, R.L. and I. Harris (2006), "A framework for assessing uncertainties in climate change impacts: low flow scenarios for the River Thames", *Water Resources Research,* vol. 42, No. 2, Wiley.

Wilks, D.S. (1995), *Statistical Methods in the Atmospheric Sciences,* San Diego, Academic Press.

Xue, Y., T.M. Smith and R.W. Reynolds (2003), "Interdecadal changes of 30-yr SST normals during 1871-2000", *Journal of Climate,* vol. 16, No. 10, American Meteorological Society.

Zhang, K., B.C. Douglas and S.P. Leatherman (2004), "Global warming and coastal erosion", *Climatic Change,* vol. 64, No. 1-2, Springer.

Zorita, E. and H. Von Storch (1999), "The analog method as a simple statistical downscaling technique: comparison with more complicated methods", *Journal of Climate,* vol. 12, No. 8, American Meteorological Society.

Annex 1

Description, calibration and validation of databases on waves, storm surges and tides compiled by IHC

A1. 1. Methodologies and techniques for constructing high space and time resolution numerical databases of past and future maritime climate

Owing to the lack of information on waves, not only in Latin America and the Caribbean, but in the Southern hemisphere more generally, a methodology was developed to obtain 61-year series of wave parameters for the area under study, with fine space and time resolution. The numerical model is described below, along with the features of the database generated, and its validation and calibration using satellite and buoy data.

A1.1.1. Description of the numerical model

The numerical model used to generate the wave series was the WaveWatch III (Tolman 1997, 1999), a third generation model developed by NOAA/NCEP, similar to WAM (WAMDIG 1988, Komen and others 1994). WWIII is the latest development of the initial WWI model developed by the University of Delft (Tolman, 1989) and later refined by NASA in the WWII model.

The WWIII model differs from its predecessors in many significant ways, including in aspects of structure, numerical resolution method and physical parameterizations. WWIII solves the spectral action density balance equation. The implicit assumption of these equations is that the medium (depth and current) as well as the wave field vary on time and space scales that are much larger than the corresponding scales of a single wave.

Accordingly, one of the model's limitations is that it cannot simulate the effect of wave propagation at smaller depths as effectively as other models. For this reason, the results of simulations performed using WWIII are usually used as starting points for simulations with the SWAN wave propagation model. The SWAN (Simulating Waves Nearshore, Booij and others, 1999) model is also

based on wave action conservation, but has been found more effective for solving phenomena affecting shallower swell. The SWAN propagation model is widely accepted and used in coastal engineering worldwide. The model's official website is available at www.swan.tudelft.nl. A complete list of references and some applications can be found at: http://vlm089.citg.tudelft.nl/swan/references/references.htm.

The wage propagation model uses 10 m winds as forcing, with a temporal resolution of 6 hours and a spatial sampling based on a global Gaussian T62 grid, with 192 longitude and 94 latitude grid points (1.875º in longitude and 1.9041º in average longitude), from the United States NCEP/NCAR atmospheric reanalysis system. These winds have the advantage of covering the period 1948-2008 fully and evenly, and are updated monthly.

A1.1.2. Characteristics of the GOW reanalysis: configuration and forcing

The IHC GOW (Global Ocean Wave) reanalysis is organized on different spatial scales. First, wind-waves were obtained on a global grid (see figure 1.161), which gives waves on a global scale with grid point resolution of 1.5º longitude and 1º latitude. New grids were then added to this global grid in order to study certain areas in detail with finer resolution. Three detail grids were used: one each for the Pacific and Atlantic coasts of South America, both with a resolution of 0.5ºx0.5º, and one for the Caribbean, with a finer resolution of 0.25ºx0.25º to allow for the characteristics of the islands and the Caribbean Sea, following recommendations arising from NOAA experiences with its operational model in the area (see figures 1.161 and 1.162).

FIGURE 1.161
GLOBAL GRID FOR GOW REANALYSIS

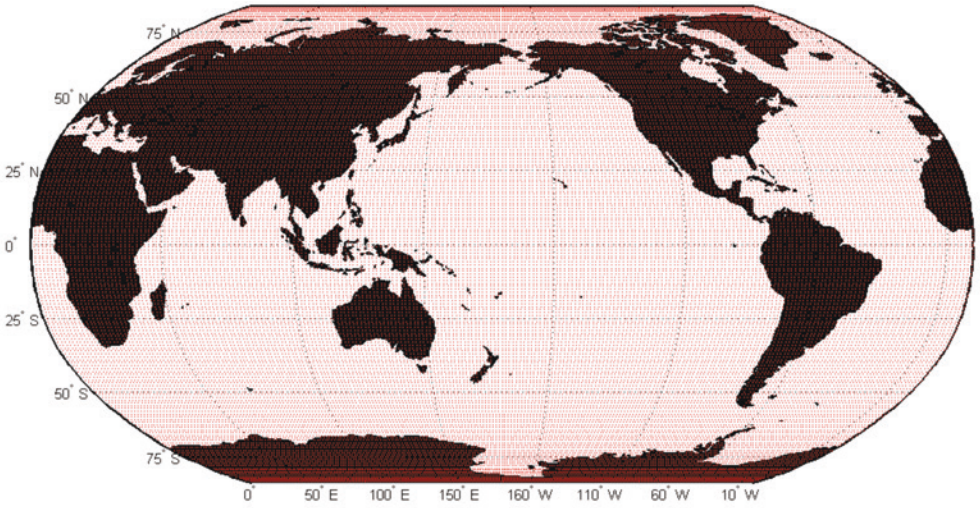

Source: Prepared by the authors.

The time range for GOW analysis is from 1948 to 2010, with 1-hourly resolution. Although the study uses the time series up to 2008 only, the reanalysis is updated regularly as NCEP winds are published.

The results obtained for the Latin American and Caribbean coasts are as follows: (1) statistical wave parameters with hourly temporal resolution and spatial resolution equal to that of the detail grids, and (2) wave energy spectra with 3-hourly temporal resolution and spatial resolution of approximately 1º.

FIGURE 1.162
DETAIL GRIDS FOR WAVE REANALYSIS IN LATIN AMERICA AND THE CARIBBEAN AND THEIR SPATIAL RESOLUTION

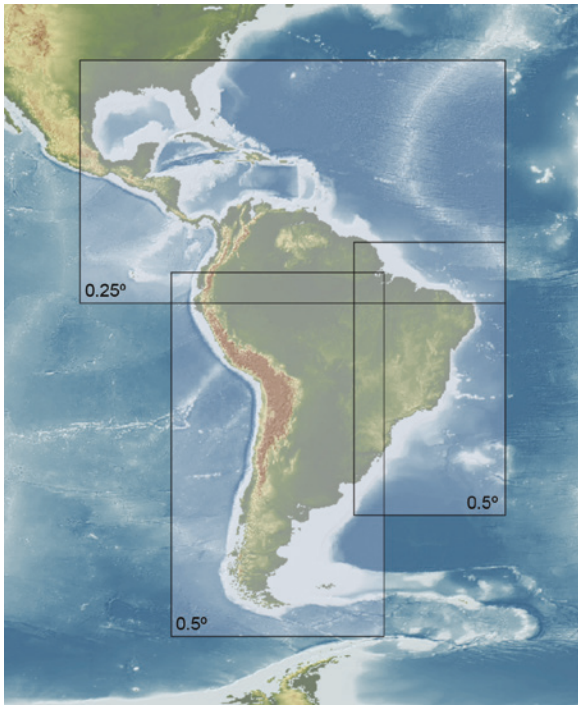

Source: Prepared by the authors.

The atmospheric forcing data used are 10 m wind fields and NCEP-NCAR sea ice schemes, with 6-hourly time resolution and spatial resolution of 1.9º latitude and 1.875º longitude. These data have global coverage and a time range of 1948-present.

Accurate wave data and measurement of their trends over time in this part of the world require taking into account the effect of tropical cyclones, which are known as hurricanes in the Atlantic and North-East Pacific. However, the NCEP/NCAR data time and space resolution do not support accurate representation of the increase in wave height caused by hurricanes, which are, moreover, very common in this region. Figure 1.163 shows the historical trajectories of hurricanes in the Atlantic (1851-2009) and the North-East Pacific (1949-2009).

FIGURE 1.163
HISTORICAL TRAJECTORIES OF HURRICANES IN THE ATLANTIC (A) AND NORTH-EAST PACIFIC (B)

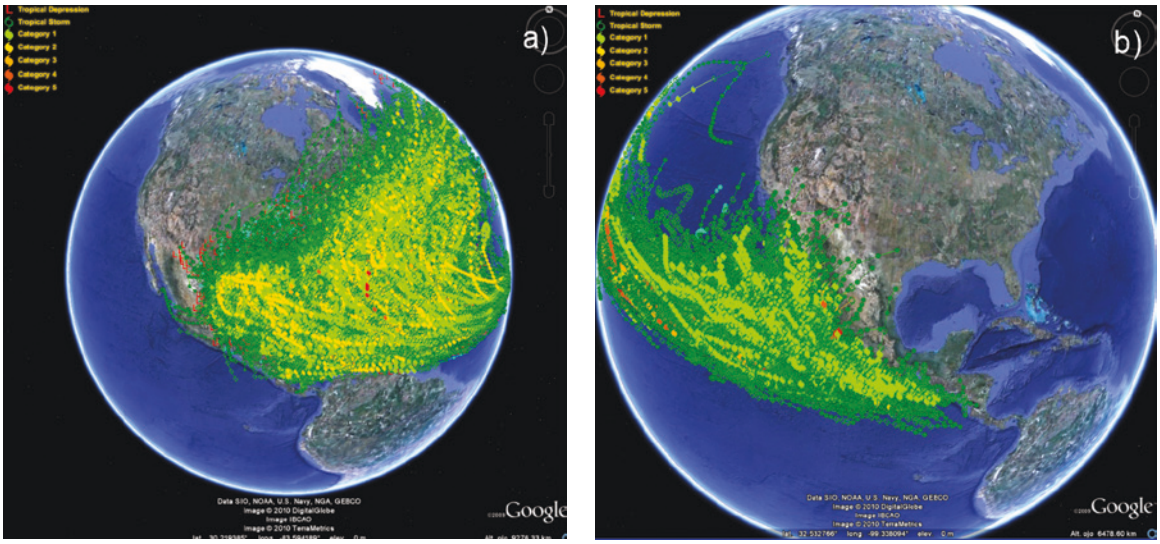

Source: University of Illinois. Department of Atmospheric Sciences. http://www.atmos.uiuc.edu/index.html.

Accordingly, the study of waves in this study area must be carried out in two stages:

Stage I: Generation of 61-year wave reanalysis (1948-2008) for the whole of the study area, using NCEP/NCAR forcing (6 h; 2º approx.).

Stage II: Hurricane-generated wind waves occurring in the period 1948-2008. To obtain the forcing produced during these events, a hurricane generation model was built using the NOAA HURDAT database (United States). HURDAT captures the trajectories and intensities of tropical cyclones estimated by a posteriori analysis of all the data available (see annex on hurricanes).

So far in this study, stage I has been completed, and a preliminary analysis using empirical formulas has been conducted of the effect of hurricanes on swell and storm surge on the coasts of the Caribbean and Central America.

A1.1.3. Validation of GOW reanalysis

The results of the global reanalysis were validated using buoy and satellite data. The buoys used were the outer network of OPPE buoys on the Spanish coast and NOAA buoys in the rest of the world, covering regions with very varied wave conditions. Figure 1.164 shows the exact locations for which the reanalysis was validated using buoys across the world.

FIGURE 1.164
WAVE BUOYS USED TO VALIDATE THE GOW REANALYSIS GLOBAL GRID

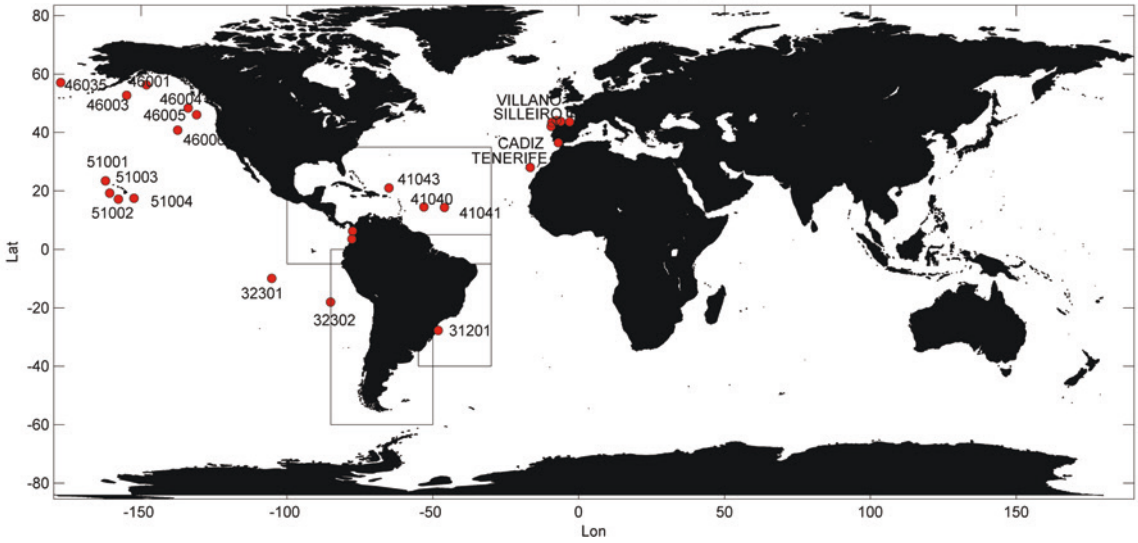

Source: Prepared by the authors.

Figures 1.165 through 1.168 show examples of validation carried out for some of the buoys used to corroborate the numerical results obtained from the global grid. The series are for 2006, and the correlation parameters were calculated for the full register for each buoy.

FIGURE 1.165
VALIDATION FOR NOAA BUOY 46003. REGION: NORTH PACIFIC. GLOBAL GRID

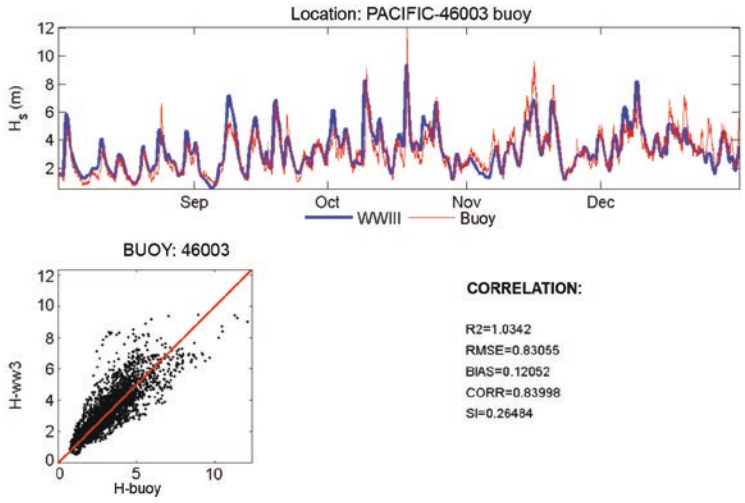

Source: Prepared by the authors.
Note: Bisector (R2), Root mean square error (RMSE), Bias (BIAS), Correlation coefficient (CORR), Scatter index (SI).

FIGURE 1.166
VALIDATION FOR NOAA BUOY 46005. REGION: NORTH PACIFIC. GLOBAL GRID

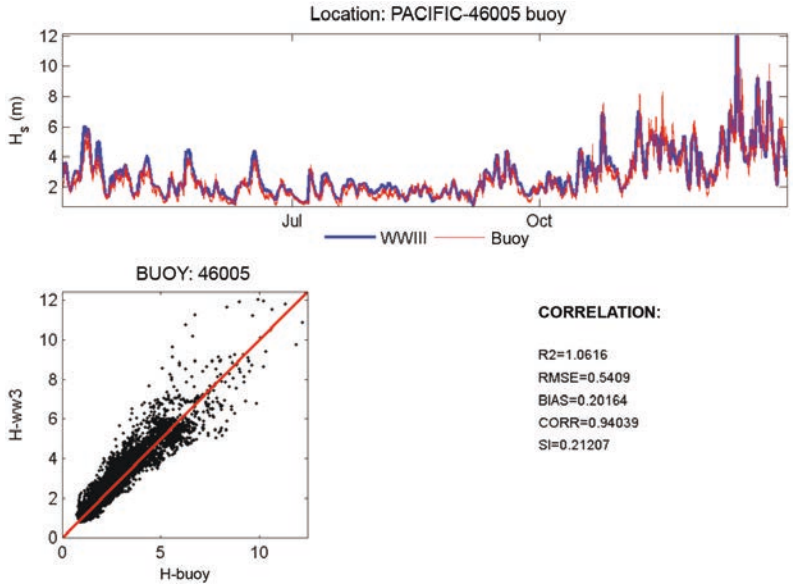

Source: Prepared by the authors.
Note: Bisector (R2), Root mean square error (RMSE), Bias (BIAS), Correlation coefficient (CORR), Scatter index (SI).

FIGURE 1.167
VALIDATION FOR SILLEIRO BUOY-UNDEFINED DEPTHS (OPPE). REGION: NORTH ATLANTIC. GLOBAL GRID

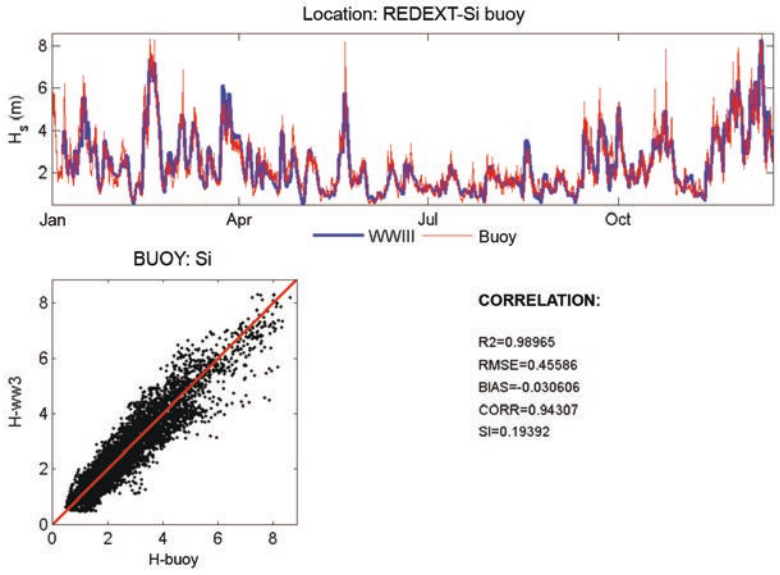

Source: Prepared by the authors.
Note: Bisector (R2), Root mean square error (RMSE), Bias (BIAS), Correlation coefficient (CORR), Scatter index (SI).

FIGURE 1.168
VALIDATION FOR BILBAO BUOY- DEEP WATER (OPPE). REGION: NORTH ATLANTIC. GLOBAL GRID

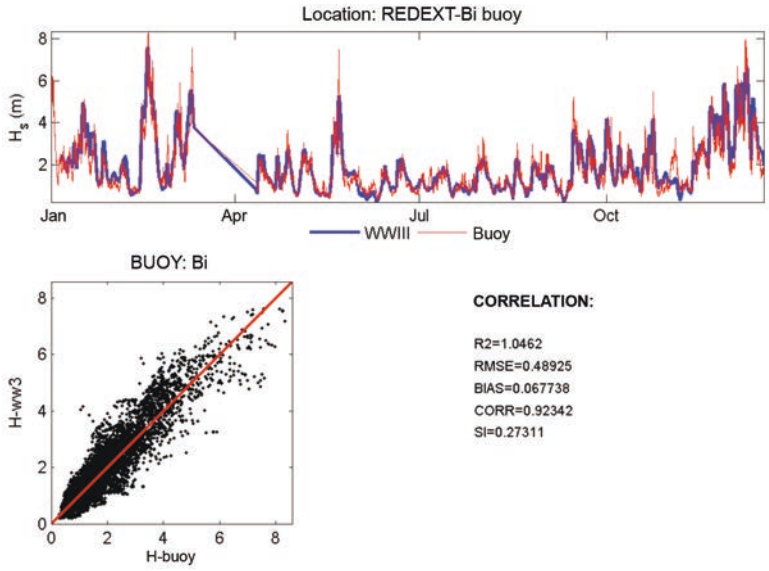

Source: Prepared by the authors.
Note: Bisector (R2), Root mean square error (RMSE), Bias (BIAS), Correlation coefficient (CORR), Scatter index (SI).

Validation of heights and peak periods in the Caribbean is represented in figure 1.169 below, which shows the time series for 2007 and 2008 for NOAA buoy 41043, to the north of Puerto Rico.

FIGURE 1.169
WAVE HEIGHT TIME SERIES AND PEAK PERIODS FOR NOAA BUOY 41043, TO THE NORTH OF PUERTO RICO

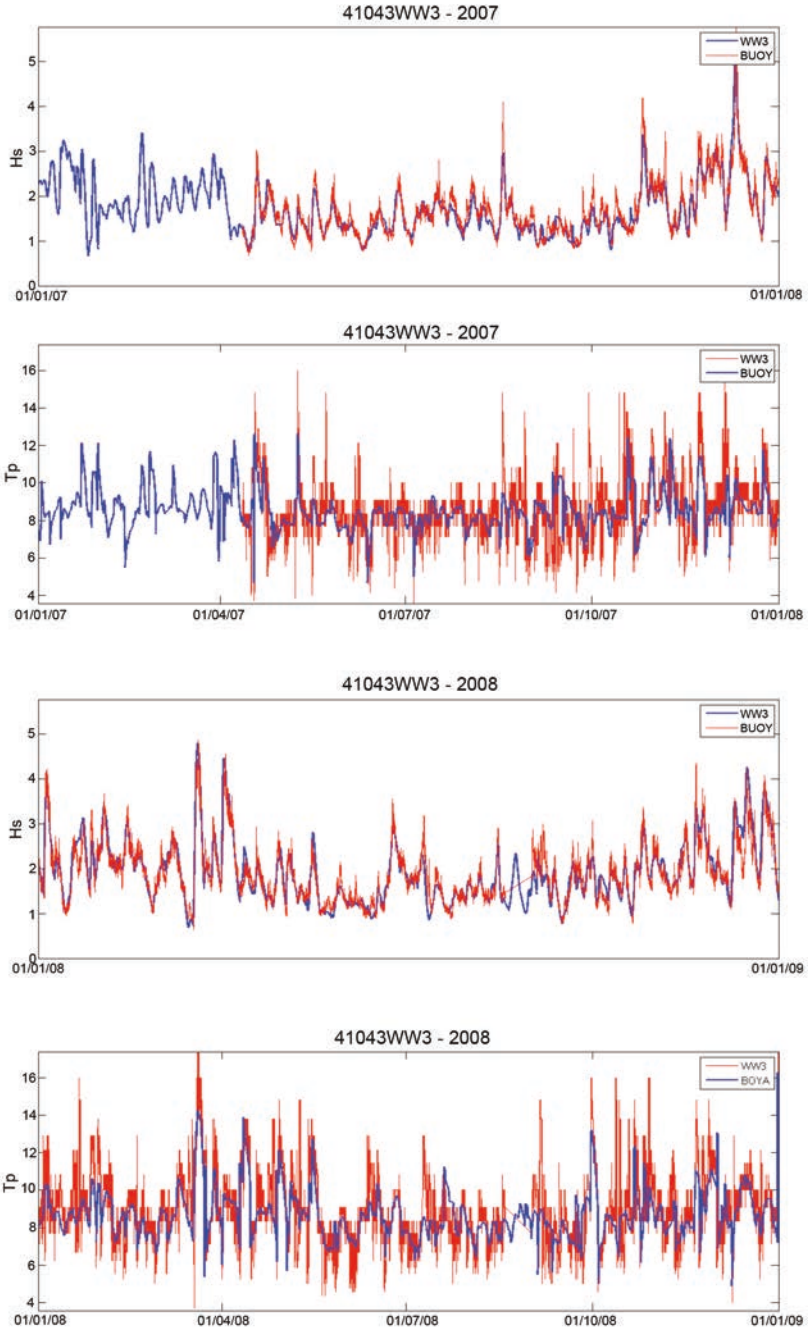

Source: Prepared by the authors.

Figure 1.170 below compares quantiles for buoys 41043, 32302 and 41040, in order to illustrate the differing behaviour from one area to another, especially at the extremes. Buoy 41040 records a hurricane which is not modelled in the reanalysis, because NCEP global winds do not properly capture winds caused by cyclones or hurricanes. For that reason, it was considered necessary to model hurricane winds using historical data to model waves in the tropical area during the period these storms occur.

FIGURE 1.170
SCATTER PLOTS AND QUANTILES FOR BUOYS 41043, 32302 AND 41040

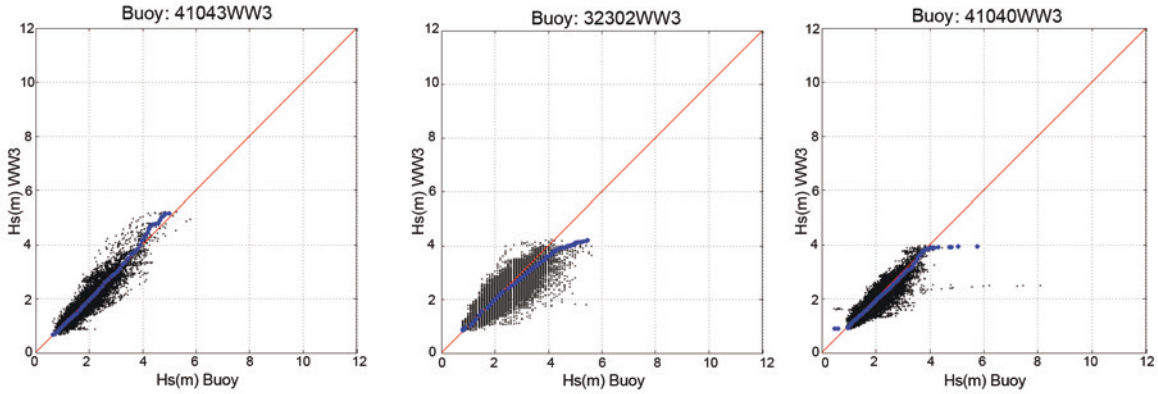

Source: Prepared by the authors.
Note: A hurricane may be observed in the record for buoy 41040 (right-hand chart).

Moreover, as is evident in the chart for buoy 32302, the numerical results of the model show some divergence from the instrumental measurements, especially in the extreme quantiles. Accordingly, the numerical results must be calibrated spatially to lessen the dispersion and improve the concordance between the numerical results and the instrumental records throughout the study area.

The results of the GOW reanalysis were also compared with satellite measurements. The correlation efficient (figure 1.171), root mean square error, scatter index and bias in the significant wave height data were calculated for 1992-2008.

FIGURE 1.171
ROOT MEAN SQUARE ERROR BETWEEN GOW REANALYSIS AND SATELLITE DATA, MARCH-MAY 2000

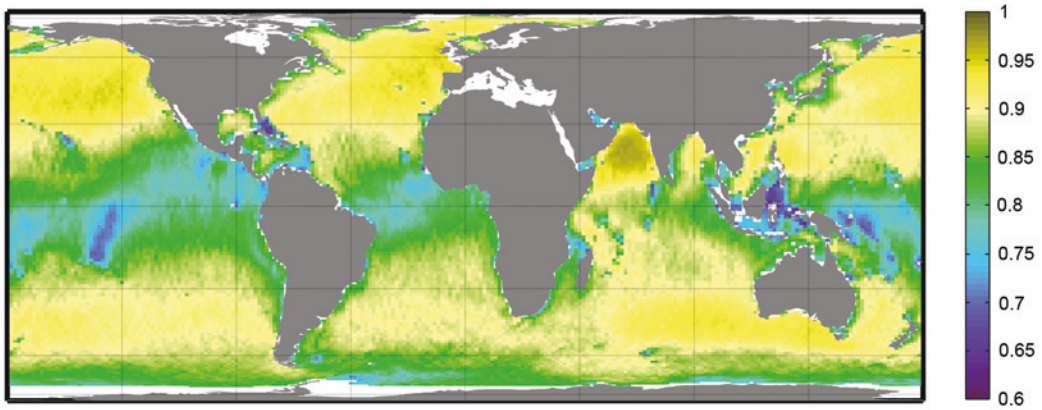

Source: Prepared by the authors.

A1.1.4. Calibration of GOW reanalysis

A wave calibration model is needed to correct the numerical wave data in certain locations to match the instrumental measurements. The parametric model proposed takes into account wave direction and is represented by the equation (Minguez and others, 2010):

$$H_c = \alpha(\theta) \cdot H_{sc}^{b(\theta)} \quad \text{(A1.1)}$$

Where H_{sc} is uncalibrated wave height and H_c is calibrated wave height.

The characteristics of the calibration model proposed are as follows.

The satellite data used were those acquired by the Cantabria Environmental Hydraulics Institute for the project (explained in section 2 on information sources), as shown in figure 1.172. The data taken for each point are at a distance of around 1.5º and perpendicular to the coast. In the case of islands, leeward side data are not selected, since the wave height and direction are different on each side (see figure 1.173).

The satellite database was purchased from the firm AQUATICA, which ran comprehensive quality controls on the database to support its use. The databases come from the AVISO network: http://www.aviso.oceanobs.com/.

FIGURE 1.172
SATELLITE DATA ACQUIRED FOR THE STUDY

Source: Prepared by the authors.

FIGURE 1.173
SELECTION OF SATELLITE DATA AROUND A POINT ON THE PACIFIC COAST OF MEXICO, USING ANGLE-TO-LAND CRITERION

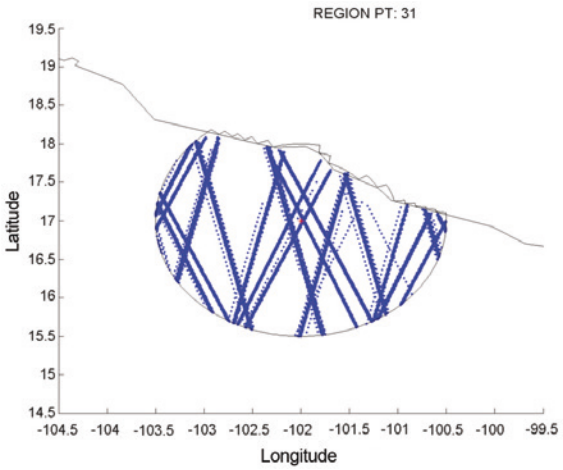

Source: Prepared by the authors.

In order to avoid the outliers caused by hurricanes that distort the calibration in tropical areas, those points were eliminated on the basis of standardized residuals analysis. Figure 1.174 shows a scatter chart for the area to the north of Colombia, where the blue points represent data admitted in the calibration, whereas the red points represent discarded outliers.

FIGURE 1.174
IDENTIFICATION OF OUTLIERS IN WAVE CALIBRATION
(Metres)

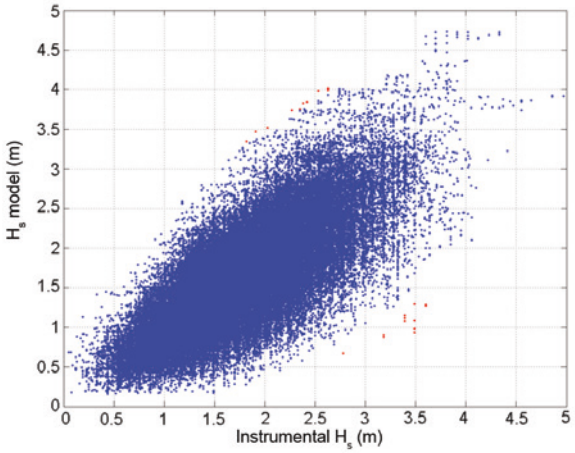

Source: Prepared by the authors.
Note: On the horizontal scale are plotted the significant wave height values from instrumental records; on the vertical scale the results of the numerical model. The red dots represent data identified as outliers.

The model parameters (a and b in eq. (1.4)) are adjusted to splines which take wave direction into account, so that the transformation of wave heights varies depending on the direction. This directional effect is reflected in the calibration roses for each point, as shown in the example in figure 1.175.

FIGURE 1.175
CALIBRATION ROSE AS A FUNCTION OF WAVE DIRECTION, WITH A 95% CONFIDENCE INTERVAL

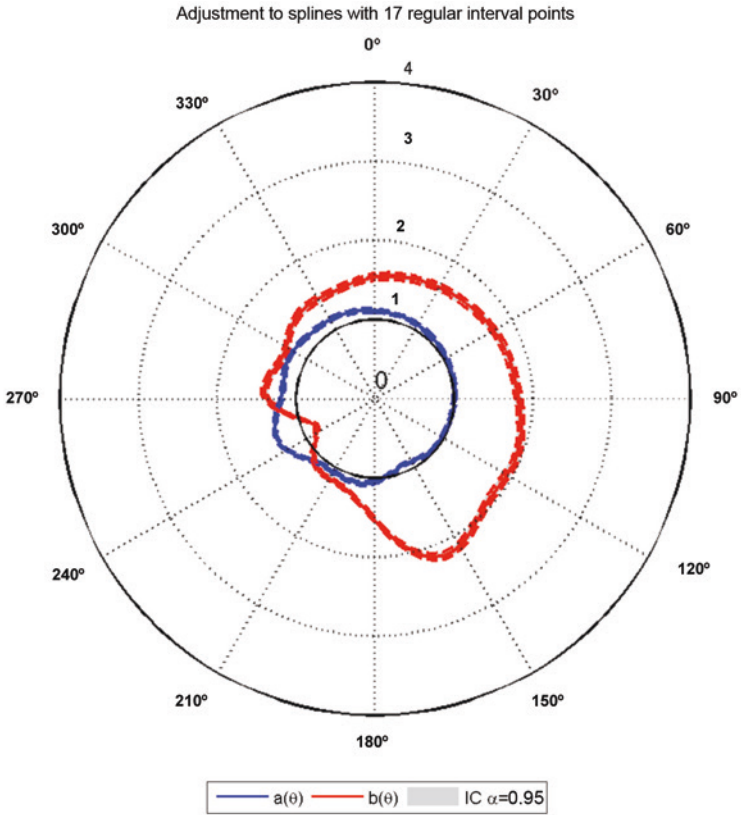

Source: Prepared by the authors.

The model parameters are adjusted by calibrating the data population quantiles, rather than hourly data. As a result, the extremes, which are less frequent and therefore fewer in number in the records —but more intense— are weighted in the calibration method (see figure 1.176).

FIGURE 1.176
CHART OF WAVE REANALYSIS QUANTILES (LEFT) AND SATELLITE DATA (RIGHT)

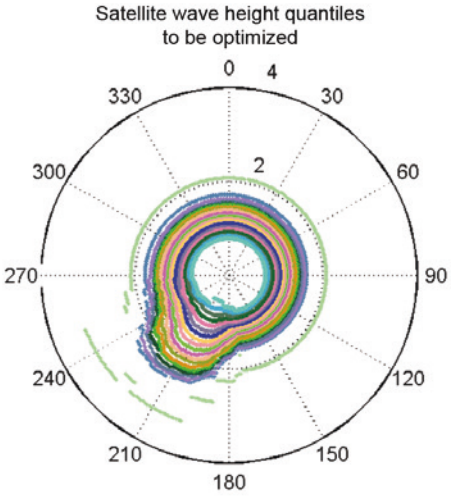

Source: Prepared by the authors.

Once the model parameters have been obtained, the transformation given by the calibration equation is applied to the hourly wave series. The effect of the calibration is shown in figure 1.177 and figure 1.178.

FIGURE 1.177
EXAMPLES OF CALIBRATION ON WAVE HEIGHT QUANTILES

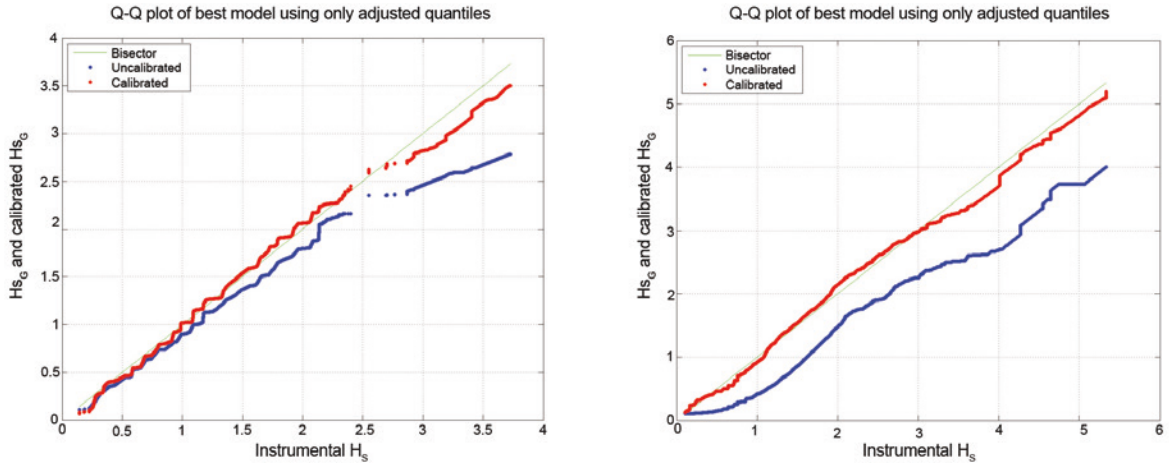

Source: Prepared by the authors.
Note: On the left, the calibration affects the extremes to a greater degree, whereas on the right the effect is equally evident on small and large heights.

FIGURE 1.178
SPATIAL EFFECT OF CALIBRATION. VALUES OF ROOT MEAN SQUARE ERROR (RMSE) (A AND B) AND SCATTER INDEX (C AND D) ON GLOBAL WAVE HEIGHT, BEFORE (A AND C) AND AFTER CORRECTION (B AND D)

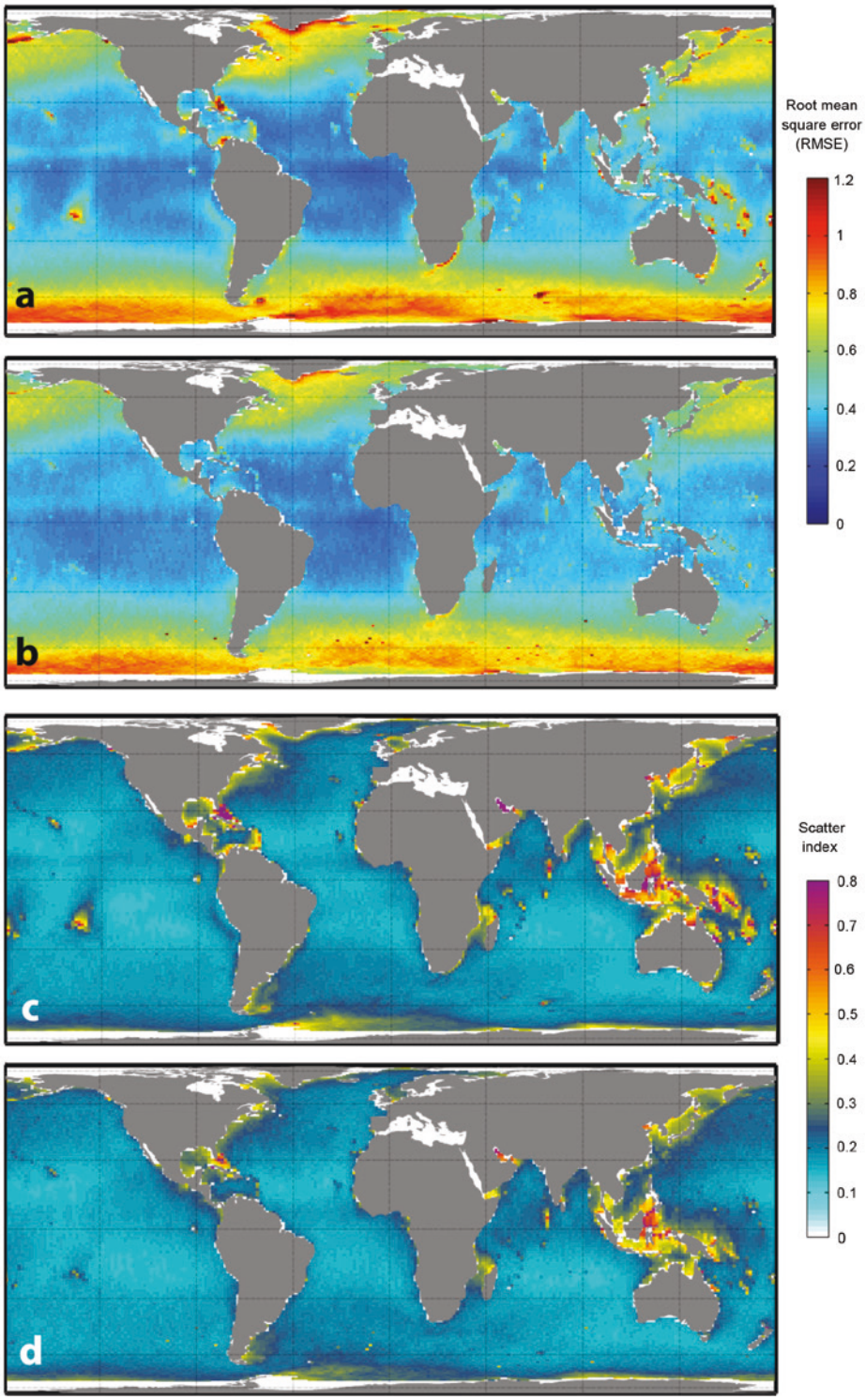

Source: Prepared by the authors.

Wave calibration is conducted only for wave height, because the only information that is available uniformly for Latin America and the Caribbean is for significant wave height, from satellite data. Neither period nor direction can be calibrated, because of the lack of data, much less of spectral form. It is possible that part of the error observed in wave height could be caused by direction error, but since there is no significant lag between the buoy series and the reanalysis, the wave height variable at one point is an indirect indicator of the direction of propagation and the direction can thus be considered accurate. Moreover, the validation performed using buoy data showed adequate correlation with the direction registered by these instruments.

A1.2. Methodologies and techniques for constructing high space and time resolution numerical databases for storm surges

Storm surge refers to the rise in sea level occurring because of tangential wind pressure on a body of water together with the effect of atmospheric pressure. This abnormal rise is one of the components used in determined total sea level and its importance relative to tides and other factors depends on the geographical area analysed. To gauge the risk of flooding on Latin American and Caribbean coasts, it is thus necessary to analyse the magnitude of storm surge, as one of the components of flooding level and total sea level.

In this study a methodology was developed to obtain 61-year hourly series for 1948-2008 for storm surge for the entire area under study. The numerical model and data used are described below, along with the features of the database generated and its validation.

A1.2.1. Description of the numerical model

The model used to calculate storm surge was the Regional Ocean Modeling System (ROMS) three-dimensional circulation model developed by the Rutgers Ocean Modeling Group. Since the model includes highly efficient and precise physical and numerical algorithms, it is widely used today by the scientific community for diverse applications (Haidvogel and others, 2000; Marchesiello and others, 2003; Peliz and others, 2003; Di Lorenzo, 2003; Dinniman and others, 2003; Budgell, 2005; Warner and others, 2005a, b; Wilkin and others, 2005).

The ROM model numerically solves equations known as primitive equations, in which pressure is considered to follow a hydrostatic law. Primitive equations comprise the equation representing the conversation of mass, the equation for the transport of different substances and temperature and salinity, and the equation of state for calculating water density. This study uses the 2D version of the model, given the bathymetric nature of the problem at hand.

A1.2.2. Data and methodology

Bathymetry

The bathymetry used comes from the database of the 2-Minute Gridded Global Elevation Data, ETOPO2. This database contains ocean bathymetry on a global scale, taken from altimetry (satellite) data (see chapter 3).

This bathymetry was used to construct a grid covering the calculation area, with a resolution of 1/4º. Figure 1.179 shows the bathymetry configuration after interpolation of the grid for the calculation area.

FIGURE 1.179
BATHYMETRY USED FOR STORM SURGE REANALYSIS IN THE STUDY AREA, GRID 1 (RESOLUTION: 1/4º)

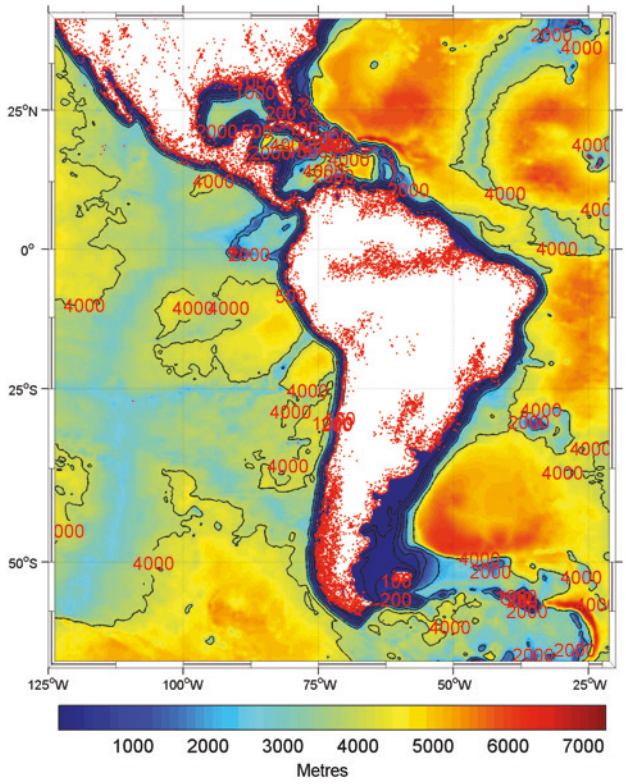

Source: Prepared by the authors.

Atmospheric forcing

The forcing used in the circulation model is 10 m winds and sea-level pressure (SLP) with 6-hourly time resolution and space resolution of 1.9041º latitude and 1.875º longitude, from the NCEP/NCAR Center in the United States. These data cover the period 1948-2008 fully and evenly, and are updated monthly.

Accurate measurement of sea level and its trend in this area requires taking into account the effect of tropical cyclones, which are known as hurricanes in the Atlantic and North-East Pacific. However, the NCEP/NCAR data time and space resolution do not support accurate representation of the increase in wave height caused by hurricanes, which are, moreover, very common in this region. Figure 1.163 shows the historical trajectories of hurricanes in the Atlantic (1851-2009) and the North-East Pacific (1949-2009).

Accordingly, the study of storm surge in this study area must be carried out in two stages:

Stage I: Generation of 61-year reanalysis (1948-2008) of storm surge for the whole of the study area, using 1/4º resolution (grid 1, see figure 4.26.), using NCEP/NCAR forcing(6 h; 2º approx.).

Stage II: Hurricane-generated storm surge occurring in the period 1948-2008. To obtain the forcing produced during these events, a hurricane generation model was built using the NOAA HURDAT database (United States). HURDAT captures the trajectories and intensities of tropical cyclones estimated by a posteriori analysis of all the data available (see annex on hurricanes).

As in the case of waves, so far in this study, stage I has been completed, as well as a simplified version of a more detailed study of hurricanes, using empirical formulas.

Start-up of the model and boundary conditions

The numerical simulation begins in January 1948. Since this is the first month for which NCEP/NCAR forcings exist, the model must start up "cold". That is, there are no initial free surface or current speed conditions. Accordingly, there is a "warm-up" period for which the results are not valid. In this configuration, this period is found to last 15 days. The rest of the months take as initial conditions the values of the variables obtained at the last moment of the immediately previous month. As a result, in the 61-year series, only the first 15 days of January 1948 are disregarded.

Boundary conditions are calculated using inverse bathymetry based on NCEP/NCAR pressure values.

A1.2.3. Characteristics of Global Ocean Surge (GOS) in Latin America and the Caribbean

The database obtained, which will be referred to as IHC Global Ocean Surge (GOS) reanalysis, has a 1-hourly resolution and covers from 1948 to 2008. The results obtained are the rise in sea level caused by storm surge for the coast of Latin America and the Caribbean (represented in figure 1.180.) with spatial resolution of 1/4º. Figures 1.180 and 1.181 show two examples of results with respect to free-surface rise in different areas for a particular date.

FIGURE 1.180
RESULTS OF GOS REANALYSIS OF FREE-SURFACE RISE CAUSED BY STORM SURGE ON 17/12/1992. GULF OF MEXICO AND THE CARIBBEAN

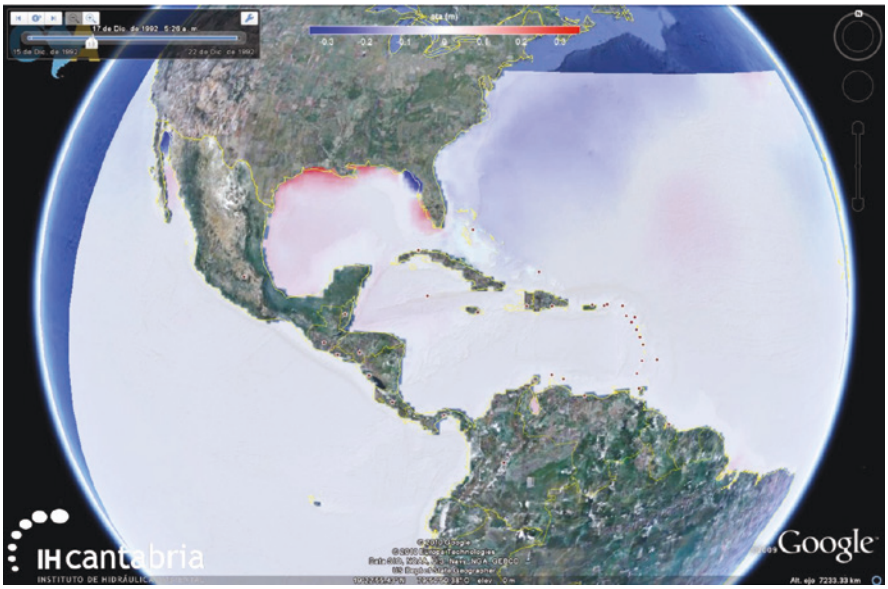

Source: Prepared by the authors.

FIGURE 1.181
RESULTS OF GOS REANALYSIS OF FREE-SURFACE RISE CAUSED BY STORM SURGE ON 17/12/1992. SOUTH AMERICA

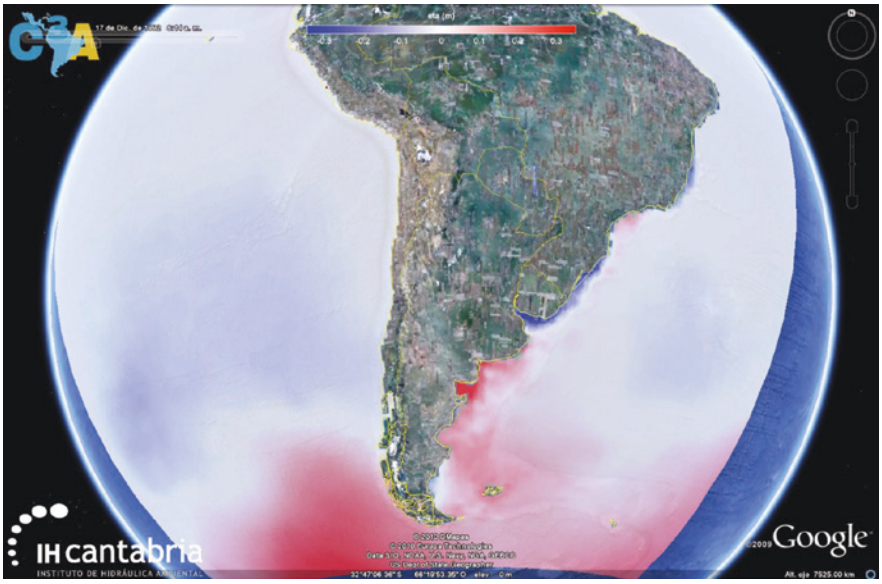

Source: Prepared by the authors.

A1.2.4. Validation of GOS reanalysis in Latin America and the Caribbean

The results of GOS reanalysis were validated using tide gauge data obtained from the University of Hawaii Sea Level Center (UHSLC), described in chapter 3. The validation performed at different points of the Atlantic and the Pacific coasts to verify the results of the analysis is described below.

Figure 1.182 shows the location and name of the tide gauges used to verify those points. Figures 1.183 through 1.188 portray the comparison of the storm surge series recorded by tide gauges and those obtained from reanalysis, over a one-year period. The upper charts show the measured series in red and the numerical series in blue. The lower charts show the scatter plots of the tide gauge data vis-à-vis the model and the quantile-quantile comparison. The bisector (R2), bias (BIAS), correlation coefficient (CORR) and root mean square error (RMSE) are also shown. The correlation parameters were calculated for the entire register of each tide gauge. As may be observed, the tide gauge series are a good fit with the numerical series, with RMSE varying between 5 cm and 10 cm. The bias remains close to 0 and the correlation varies among the positions analysed. For the points situated around Northern Mexico, the reanalysis reflects smaller results than the tide gauges. This is because of maximums related to tropical storms and hurricanes that are not adequately captured in the NCEP wind forcings. Tide gauges around South America correlated more with the numerical series, owing to better quality pressure and wind fields in the NCEP/NCAR atmospheric reanalysis.

FIGURE 1.182
LOCATIONS AND NAMES OF TIDE GAUGES

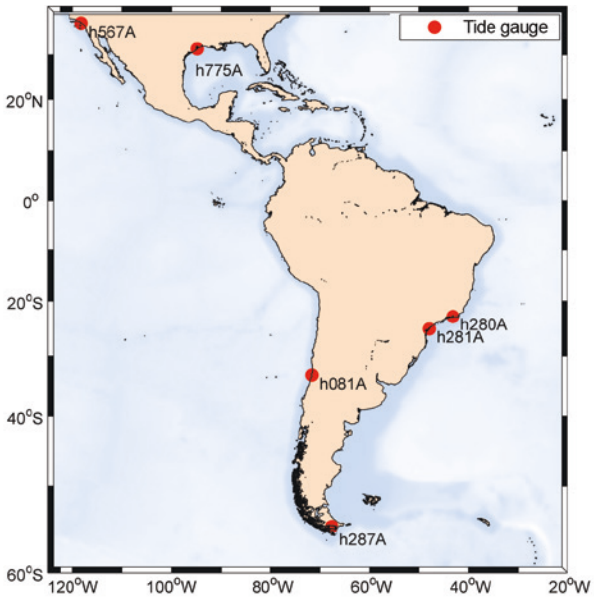

Source: Prepared by the authors.

FIGURE 1.183
COMPARISON OF THE STORM SURGE SERIES GIVEN BY GOS REANALYSIS AND TIDE GAUGE H775A LOCATED IN THE GULF OF MEXICO

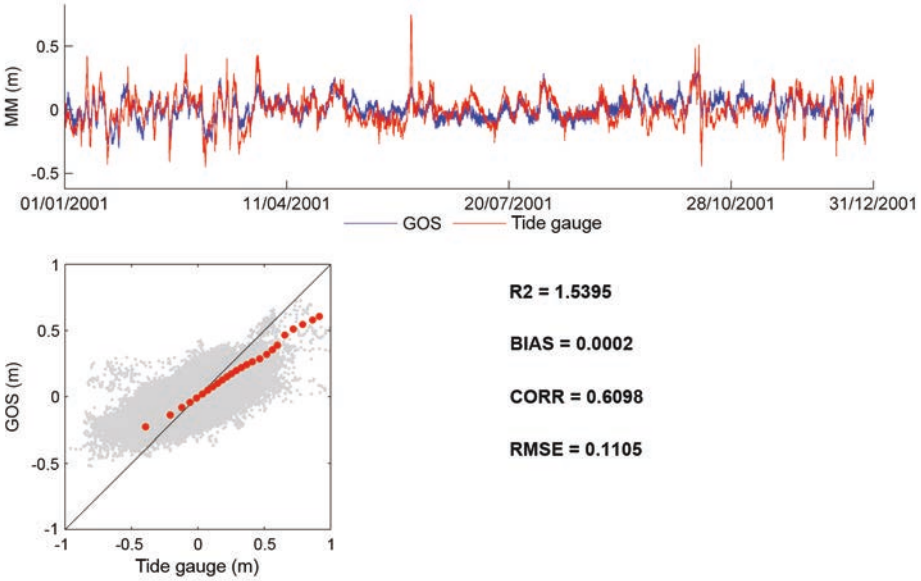

Source: Prepared by the authors.
Note: Bisector (R2), Bias (BIAS), Correlation coefficient (CORR), Root mean square error (RMSE).

FIGURE 1.184
COMPARISON OF THE STORM SURGE SERIES GIVEN BY GOS REANALYSIS AND TIDE GAUGE H280A LOCATED ON THE ATLANTIC COAST

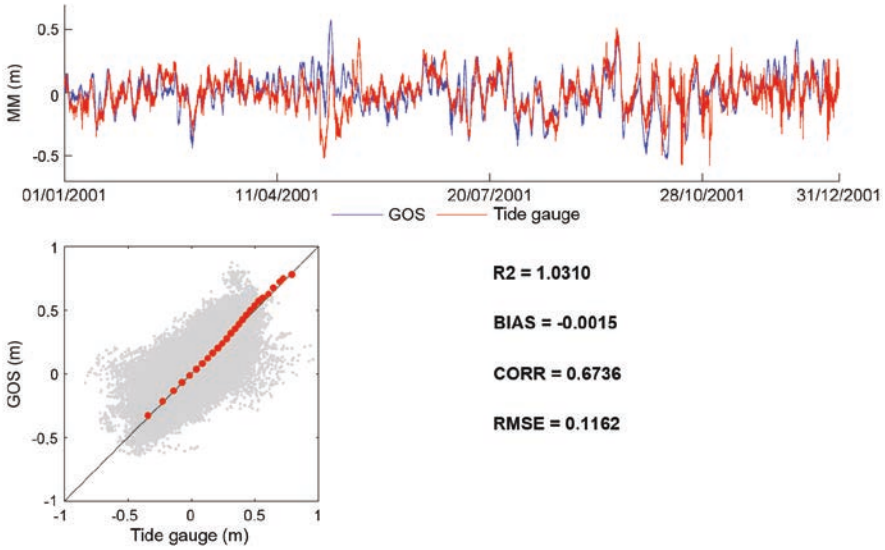

Source: Prepared by the authors.
Note: Bisector (R2), Bias (BIAS), Correlation coefficient (CORR), Root mean square error (RMSE).

FIGURE 1.185
COMPARISON OF THE STORM SURGE SERIES GIVEN BY GOS REANALYSIS AND TIDE GAUGE H281A LOCATED ON THE ATLANTIC COAST

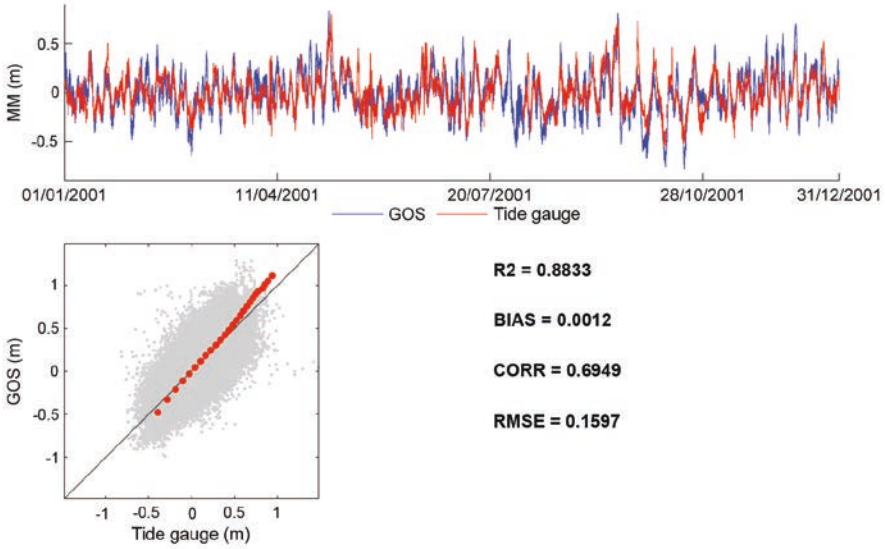

Source: Prepared by the authors.
Note: Bisector (R2), Bias (BIAS), Correlation coefficient (CORR), Root mean square error (RMSE).

FIGURE 1.186
COMPARISON OF THE STORM SURGE SERIES GIVEN BY GOS REANALYSIS AND TIDE GAUGE H567A LOCATED ON THE PACIFIC COAST

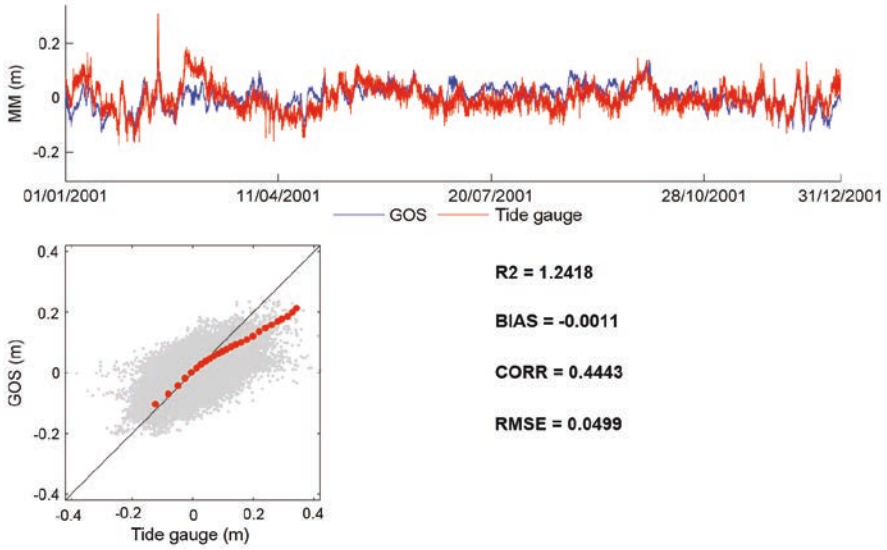

Source: Prepared by the authors.
Note: Bisector (R2), Bias (BIAS), Correlation coefficient (CORR), Root mean square error (RMSE).

FIGURE 1.187
COMPARISON OF THE STORM SURGE SERIES GIVEN BY GOS REANALYSIS AND TIDE GAUGE H081A LOCATED ON THE PACIFIC COAST

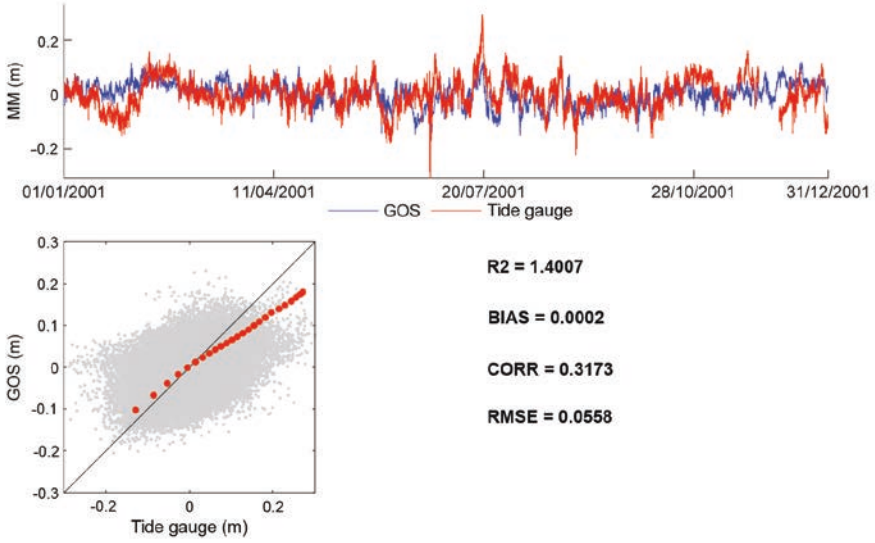

Source: Prepared by the authors.
Note: Bisector (R2), Bias (BIAS), Correlation coefficient (CORR), Root mean square error (RMSE).

FIGURE 1.188
COMPARISON OF THE STORM SURGE SERIES GIVEN BY GOS REANALYSIS AND TIDE GAUGE H287A LOCATED IN THE SOUTH OF CHILE

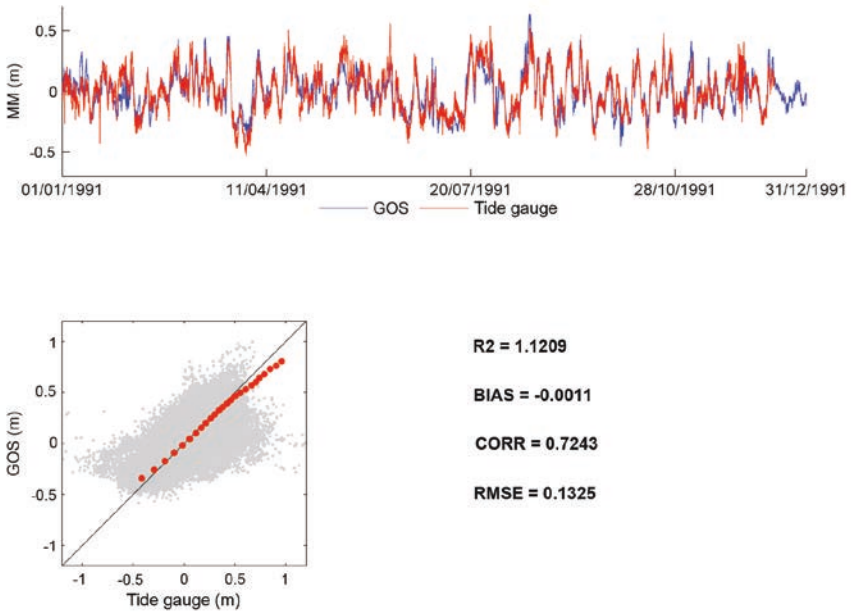

Source: Prepared by the authors.
Note: Bisector (R2), Bias (BIAS), Correlation coefficient (CORR), Root mean square error (RMSE).

A1.3. Methodologies and techniques for generating hourly astronomical tide series

A1.3.1. Description of the databases

As mentioned in section 2 of this document, the IHC Global Ocean Tides (GOT) database was obtained using data from the TPXO global tides model developed by the University of Oregon (Egbert and others, 1994; Egbert and Erofeeva, 2002). TPXO is an inverse tide model that assimilates information on sea level from observations by the TOPEX/Poseidon sensor. That model represents a best fit (in terms of minimum squares) to the Laplace tide equation with satellite data from the TOPEX/Poseidon mission. TPXO is one of the most accurate global storm surge models today.

The TPXO database resulting from the model provides four semidiurnal (M2, S2, N2, K2), four diurnal (K1, O1, P1, Q1) and two long-period (Mf and Mm) harmonic constituents. The data are provided on a 1440 x 721 point, 0.25º resolution full global grid. The TPXO database, as well as a more detailed description of the numerical model, is available at: http://volkov.oce.orst.edu/tides/global.html.

A1.3.2. Application of the TPXO database in GOT reanalysis

The TPXO database was used to calculate tides on the coasts of Latin America and the Caribbean. Specifically, the tide was calculated at the points on the coast shown in figure 1.189.

FIGURE 1.189
LOCATION ON THE COAST OF LATIN AMERICA AND THE CARIBBEAN AT WHICH THE TIDE HAS BEEN CALCULATED

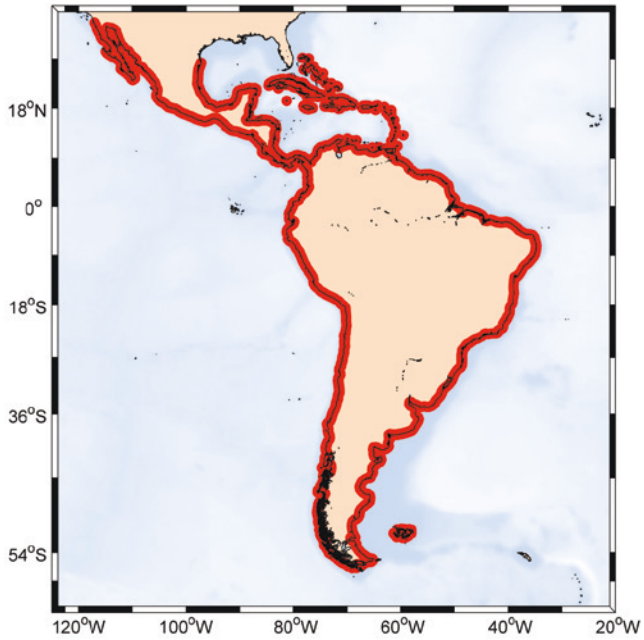

Source: Prepared by the authors.

The harmonic components were extracted from the TPXO database for each point on the Latin American and Caribbean coast (see figure 1.189). These were used to calculate the tide for each point for the period, 1948-2100, with 1-hourly time resolution. In order to obtain the variation in tide modulation at each point, the prediction was made year to year.

The tide was calculated using the data processing tools developed by the *Institut de Recherche pour le Developpement* of France (http://roms.mpl.ird.fr/) and the T_Tide harmonic analysis model (Paulowicz and others, 2002), which is widely used by scientists.

The results obtained for the coast of Latin America and the Caribbean were: (1) hourly tide series for the period 1984-2100, and (2) characterization of the tide, by means of analysis of parameters such as maximum tidal amplitude, statistical characterization of tide range and the variation in annual highs.

A1.3.3. Validation of GOT reanalysis in Latin America and the Caribbean

The results of the tide GOT reanalysis were validated using tide gauge data from the University of Hawaii Sea Level Center (UHSLC) (http://ilikai.soest.hawaii.edu/uhslc/rqds.html). The data series used have 1-hourly time resolution, and registers vary between 1940 and 2007, depending on the season.

Figure 1.190 shows the location of tide gauges used to validate the results of tide reanalysis in the Latin American and Caribbean region.

FIGURE 1.190
LOCATION OF TIDE GAUGES

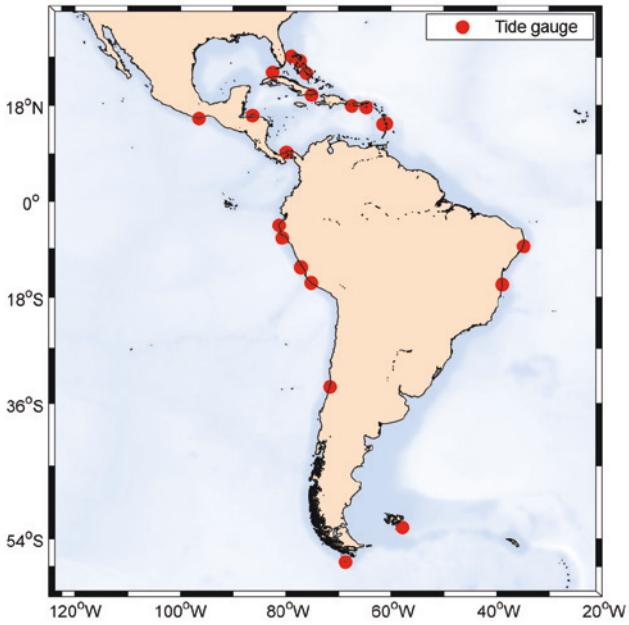

Source: Prepared by the authors on the basis of data from tide gauges of the University of Hawaii Sea Level Center (UHSLC).

To validate the results obtained, the tide calculated using the procedure described above was compared with the data obtained from tide gauges. The validation procedure followed for each tide gauge may be summarized as follows:

a) Prediction of tide using the harmonic constants from the TPXO database, at a point on the Latin American and Caribbean coast termed target point.

b) Selection of a tide gauge close to the target point.

c) Harmonic analysis of the tide gauge sea level series. The harmonic analysis of sea level was obtained by applying the technique developed by Foreman (1977) implemented in the T_Tide model (Paulowicz and others, 2002).

d) Prediction of tide using the harmonic constants obtained in step 3.

e) Comparison of the tide calculated using the constants from the TPXO database and that resulting from analysis of tide gauge data.

f) Estimation of the differences observed by calculating statistical parameters, such as the root mean square error (RMSE) and the correlation coefficient.

Figures 1.191 through 1.194 show the validation carried out for some of the tide gauges. The figures show the comparison between the tide series calculated using TPXO data at the target point and those calculated using tide gauge data, for different points located on the Atlantic and Pacific coasts. The period analysed is 2002. The map (upper left chart) shows the position of the target point in red and the location of the nearest tide gauge in green. The middle and lower charts show, respectively, the tide prediction during 2002 and an enlargement of the period 5/01/2000 - 21/01/2000. The upper right chart shows the RMSE throughout the year, with boundary values of 0.1 m shown in red. The results show a good fit between the tide prediction obtained from the tide gauge and that obtained using the TPXO database, with errors generally in the order of 0.1 m.

FIGURE 1.191
VALIDATION AT A POINT ON THE LATIN AMERICAN AND CARIBBEAN COAST LOCATED IN THE CARIBBEAN

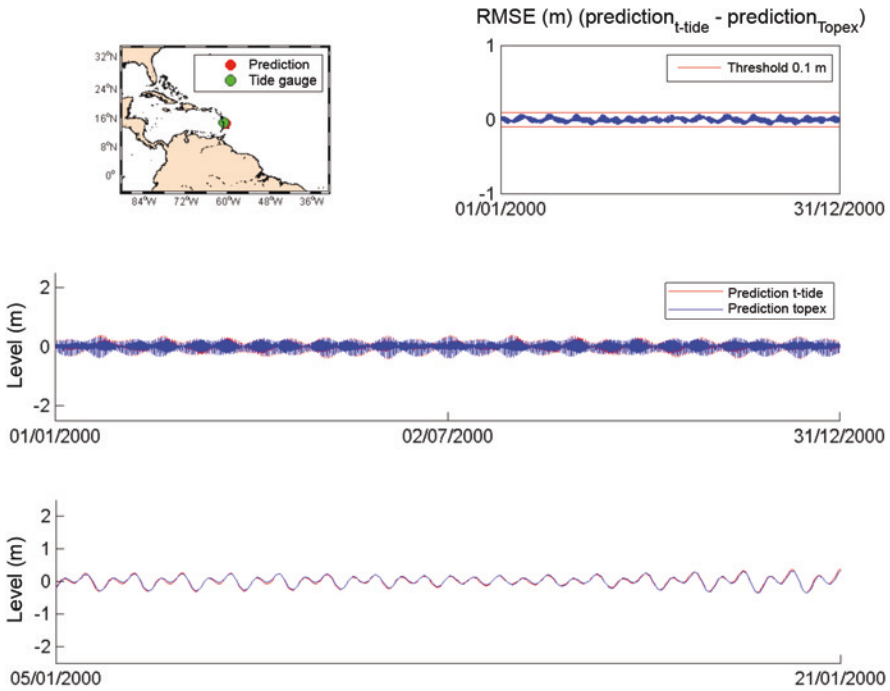

Source: Prepared by the authors.

FIGURE 1.192
VALIDATION AT A POINT ON THE LATIN AMERICAN AND CARIBBEAN COAST LOCATED IN CENTRAL AMERICA

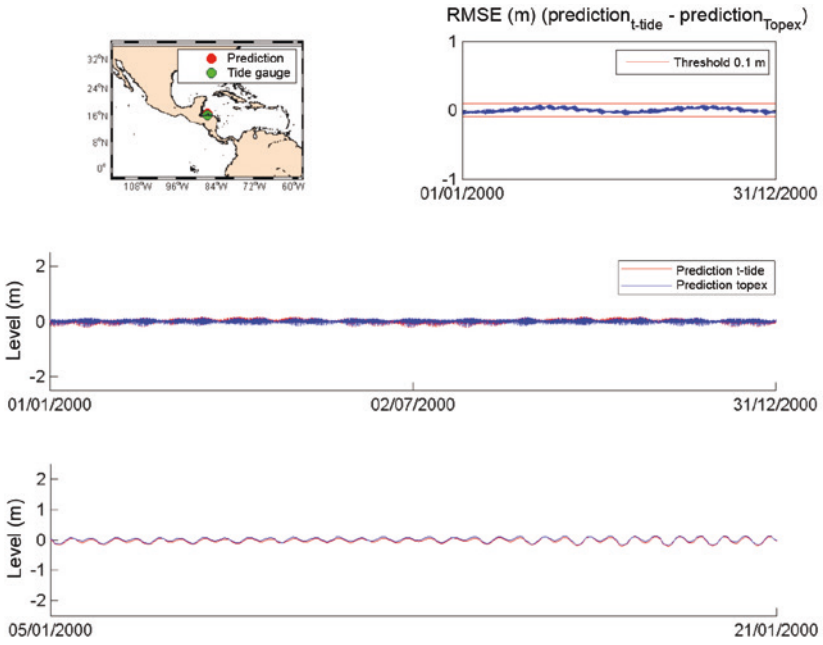

Source: Prepared by the authors.

FIGURE 1.193
VALIDATION AT A POINT ON THE LATIN AMERICAN AND CARIBBEAN COAST LOCATED ON THE PACIFIC COAST

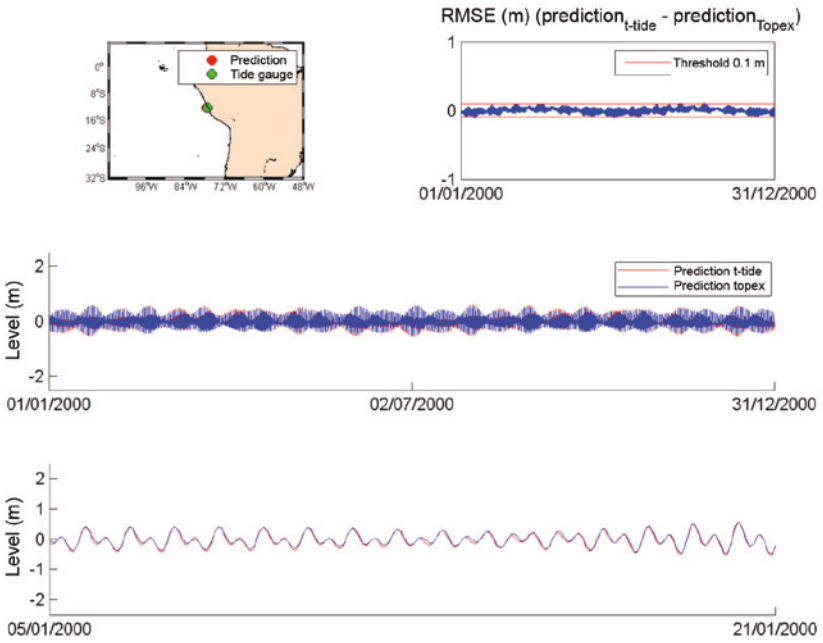

Source: Prepared by the authors.

FIGURE 1.194
VALIDATION AT A POINT ON THE LATIN AMERICAN AND CARIBBEAN COAST LOCATED ON THE ATLANTIC COAST

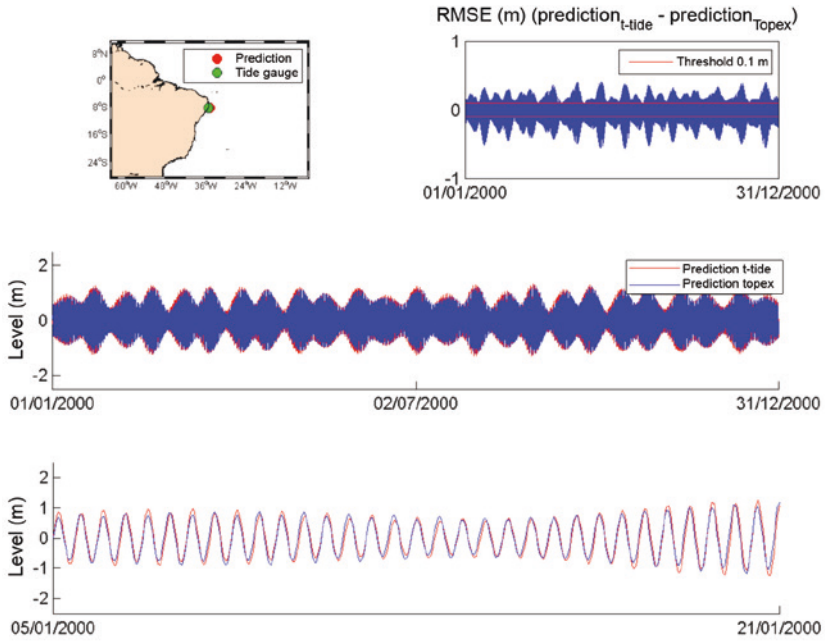

Source: Prepared by the authors.

With a view to obtaining a representative error value, the mean value of RMSE was calculated for each point and represented spatially. Figure 1.195 shows that, in general, only small differences are observed between the two series. Specifically, the minimum and maximum values of RMSE are 0.02 m and 0.16 m, respectively.

FIGURE 1.195
ROOT MEAN SQUARE ERROR OF RESIDUALS
(Metres)

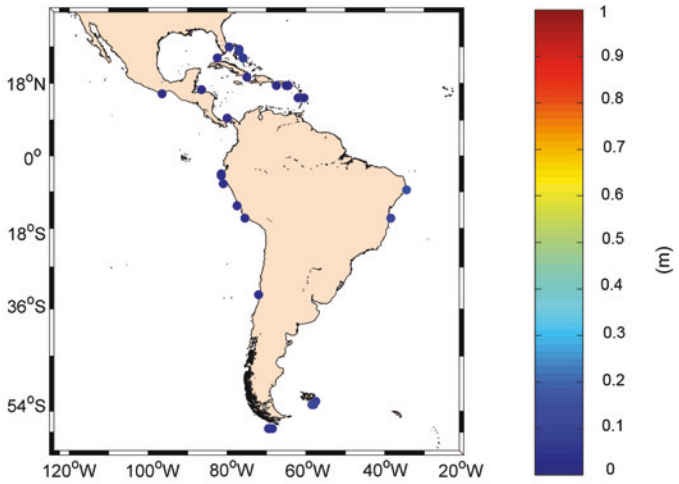

Source: Prepared by the authors.

A scatter plot and correlation coefficient were used to represent the combined behaviour of the two tide series. Figures 1.196 through 1.199 show scatter plots for the tide series shown in the preceding figures. In each case, the map on the left shows the location of the tide gauge. The graph on the right shows the respective scatter plot and correlation coefficient. In all cases there is a good fit between the two series, with correlation coefficient higher than 0.8 for all points.

Figure 1.200 shows the spatial variation of the correlation coefficient (R^2) obtained for each point. The results show that R^2 is close to 1 for most of the points.

FIGURE 1.196
SCATTER PLOT FOR A POINT ON THE LATIN AMERICAN AND CARIBBEAN COAST LOCATED IN THE CARIBBEAN

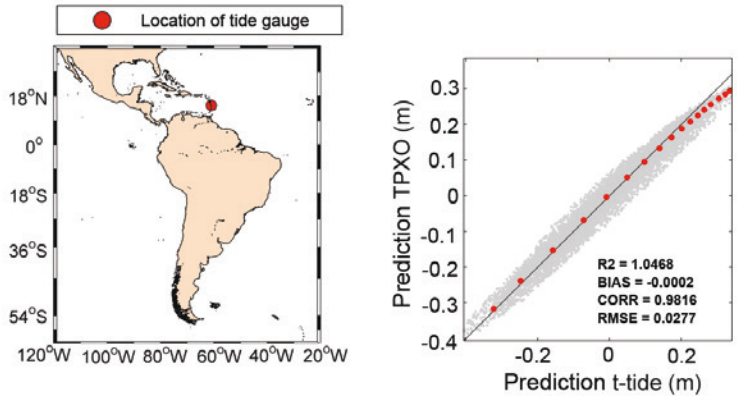

Source: Prepared by the authors.
Note: The right chart also shows the quantile-quantile comparison, the correlation coefficient for bisector (R2), bias (BIAS), correlation coefficient (CORR) and root mean square error (RMSE).

FIGURE 1.197
SCATTER PLOT FOR A POINT ON THE LATIN AMERICAN AND CARIBBEAN COAST LOCATED IN CENTRAL AMERICA

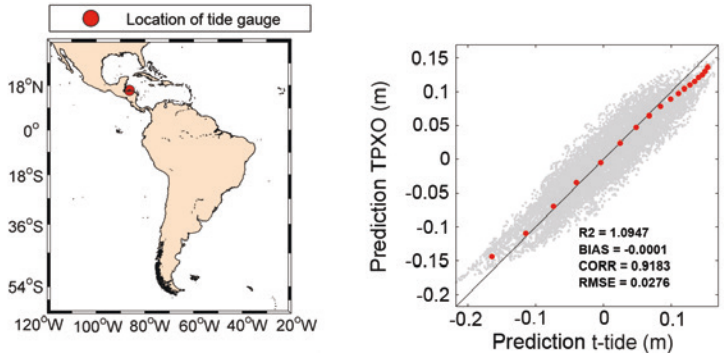

Source: Prepared by the authors.
Note: The right chart also shows the quantile-quantile comparison, the correlation coefficient for bisector (R2), bias (BIAS), correlation coefficient (CORR) and root mean square error (RMSE).

FIGURE 1.198
SCATTER PLOT FOR A POINT ON THE LATIN AMERICAN AND CARIBBEAN COAST LOCATED ON THE PACIFIC COAST

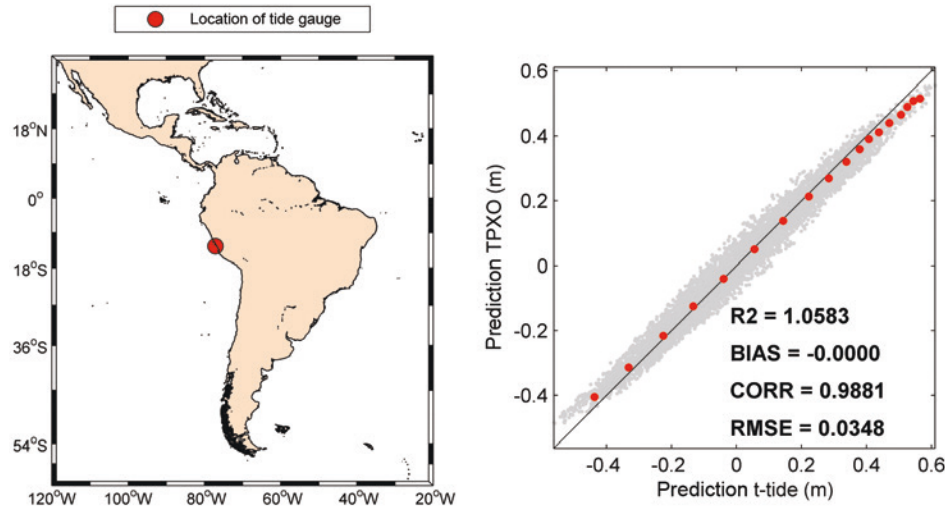

Source: Prepared by the authors.
Note: The right chart also shows the quantile-quantile comparison, the correlation coefficient for bisector (R2), bias (BIAS), correlation coefficient (CORR) and root mean square error (RMSE).

FIGURE 1.199
SCATTER PLOT FOR A POINT ON THE LATIN AMERICAN AND CARIBBEAN COAST LOCATED ON THE ATLANTIC COAST

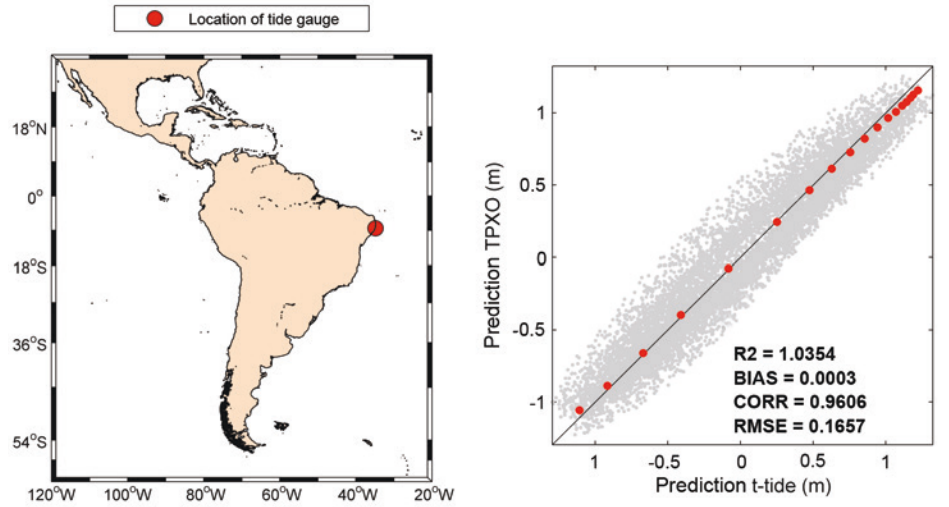

Source: Prepared by the authors.
Note: The right chart also shows the quantile-quantile comparison, the correlation coefficient for bisector (R2), bias (BIAS), correlation coefficient (CORR) and root mean square error (RMSE).

FIGURE 1.200
VALUE OF CORRELATION COEFFICIENT R^2

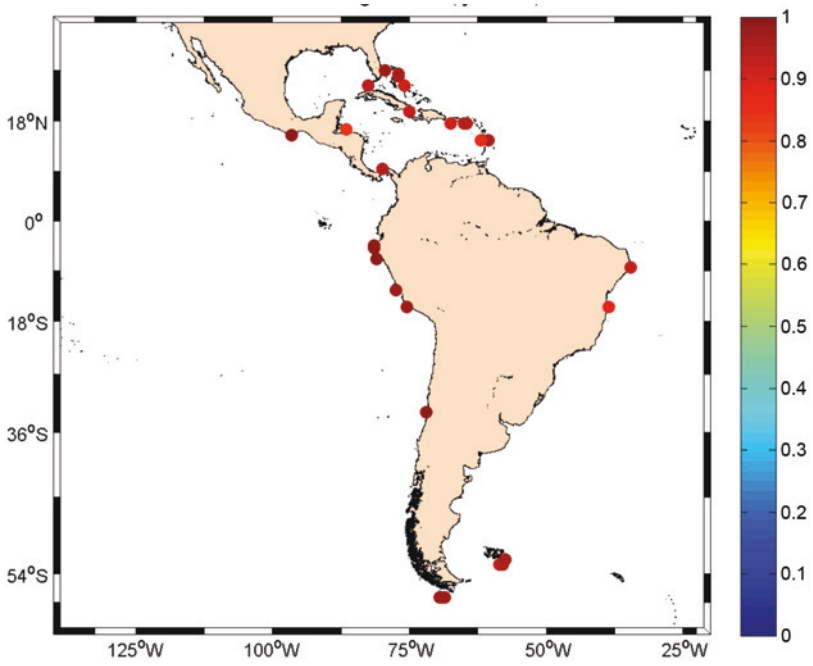

Source: Prepared by the authors.

A1.3.4. Characterization of the tide

One the database for the GOT tide series had been validated, this information was used to characterize the tide in Latin America and the Caribbean.

For each point, the following information was calculated: (1) maximum tidal amplitude (historical high tide level), (2) tide range time series (CM), (3) tide range exceeded in 50%, 10%, 5% and 1% of cases, (4) tide range for each year, and (5) standard deviation of annual high tide range.

By way of example, figures 1.201, 1.202 and 1.203 show the GTO (tide in the period 1948-2100), at three points on the Caribbean, Pacific and Atlantic coasts, respectively.

FIGURE 1.201
TIDE AT A POINT LOCATED ON THE CARIBBEAN COAST, 1948-2100
(Metres)

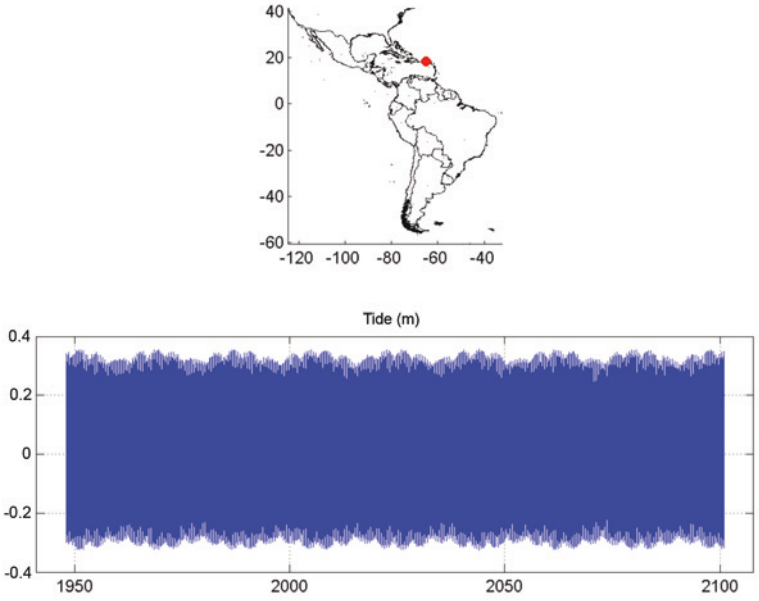

Source: Prepared by the authors.

FIGURE 1.202
TIDE AT A POINT LOCATED ON THE PACIFIC COAST, 1948-2100
(Metres)

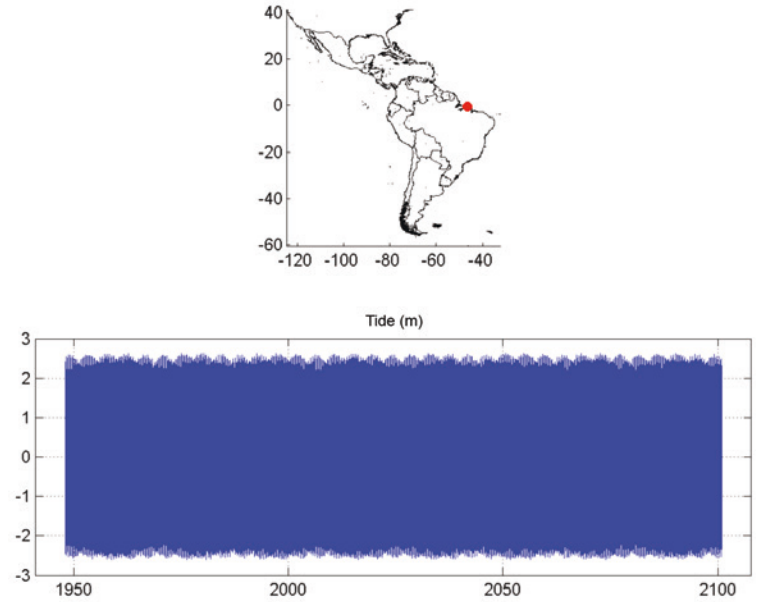

Source: Prepared by the authors.

FIGURE 1.203
TIDE AT A POINT LOCATED ON THE ATLANTIC COAST, 1948-2100
(Metres)

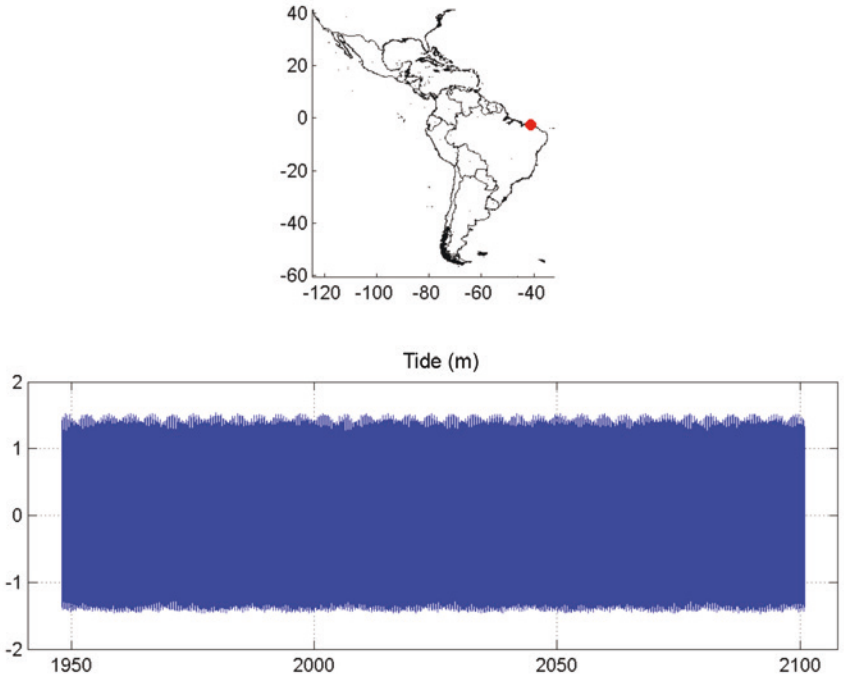

Source: Prepared by the authors.

Figure 1.204 shows the maximum tide amplitude along the length of the Latin American and Caribbean coast. The smallest values are observed in the Caribbean area, of around 0.5-0.6 m, and the largest are on the coast of Argentina, with tide amplitudes of 6-7m.

FIGURE 1.204
MAXIMUM TIDE AMPLITUDE, 1948-2100
(Metres)

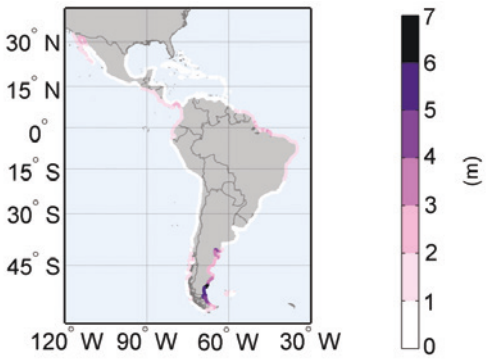

Source: Prepared by the authors.

Annex 1 bibliography

Booij, N., R.C. Ris and L.H. Holthuijsen (1999), "A third-generation wave model for coastal regions, Part I: Model description and validation", *Journal of Geophysical Research,* vol. 104, C4.

Budgell, W.P. (2005), "Numerical simulation of ice-ocean variability in the Barents Sea region", *Ocean Dynamics,* vol. 55, No. 3-4, Springer.

Di Lorenzo, E. (2003), "Seasonal dynamics of the surface circulation in the southern California Current System", *Deep-Sea Research Part II: Topical Studies in Oceanography,* vol. 50, No. 14-16, Amsterdam, Elsevier.

Dinniman, M.S., J.M. Klinck and W.O. Smith Jr. (2003), "Cross shelf exchange in a model of the Ross Sea circulation and biogeochemistry", *Deep-Sea Research Part II: Topical Studies in Oceanography,* vol. 50, No. 22-26, Amsterdam, Elsevier.

Egbert, G.D., A.F. Bennett and M.G.G. Foreman (1994), "TOPEX/POSEIDON tides estimated using a global inverse model", *Journal of Geophysical Research,* vol. 99, No. C12.

Egbert, G.D. and S.Y. Erofeeva (2002), "Efficient inverse modeling of barotropic ocean tides", *Journal of Atmospheric and Oceanic Technology,* vol. 19, No. 2, American Meteorological Society.

GEBCO (General Bathymetric Chart of the Oceans" [online] http://www.gebco.net/.

Haidvogel, D.B. and others (2000), "Model evaluation experiments in the North Atlantic Basin: simulations in nonlinear terrain-following coordinates", *Dynamics of Atmospheres and Oceans,* vol. 32, No. 3-4, Amsterdam, Elsevier.

Marchesiello, P., J.C. McWilliams and A. Shchepetkin, (2003), "Equilibrium structure and dynamics of the California Current System", *Journal of Physical Oceanography,* vol. 33, No. 4, American Meteorological Society.

Mínguez, R. and others (2011), "Directional calibration of wave reanalysis databases using instrumental data", *Journal of Atmospheric and Oceanic Technology,* vol. 28, No. 11, American Meteorological Society.

Pawlowicz, R., B. Beardsley and S. Lentz (2002), "Classical tidal harmonic analysis including error estimates in MATLAB using T_TIDE", *Computers and Geosciences,* vol. 28, No. 8, Amsterdam, Elsevier.

Peliz, A. and others (2003), "Generation and unstable evolution of a density-driven Eastern Poleward Current: The Iberian Poleward Current", *Journal of Geophysical Research,* vol. 108, No. C8.

The WAMDIG Group (1988), "The WAM model - A third generation ocean wave prediction model", *Journal of Physical Oceanography,* vol. 18, No. 12.

Tolman, H.L. (2003), "Treatment of unresolved islands and ice in wind wave models", *Ocean Modelling,* vol. 5, No. 3, Amsterdam, Elsevier.

_____ (2002), "Limiters in third-generation wind wave models", *Journal of Atmospheric and Ocean Science,* vol. 8, No. 1, Taylor & Francis.

_____ (1999), "User manual and system documentation of WAVEWATCH-III version 1.18", *Technical Note,* No. 166.

_____ (1997), "User manual and system documentation of WAVEWATCH-III version 1.15", *Technical Note,* No. 151.

_____ (1989), "The numerical model WAVEWATCH: a third generation model for the hindcasting of wind waves on tides in shelf seas", *Communications on Hydraulic and Geotechnical Engineering,* Delft University of Technology.

United States Army Corps of Engineers (1984), *Shore Protection Manual,* Coastal Engineering Research Center.

Warner, J.C. and others (2005), "Performance of four turbulence closure methods implemented using a generic length scale method", *Ocean Modelling,* vol. 8, No. 1-2, Amsterdam, Elsevier.

Warner, J.C., W.R. Geyer and J.A. Lerczak (2005), "Numerical modeling of an estuary: a comprehensive skill assessment", *Journal of Geophysical Research,* vol. 110, No. C5.

Wilkin, J.L. and others (2005), "A regional ocean modeling system for the long-term ecosystem observatory", *Journal of Geophysical Research,* vol. 110, No. C6.

Annex 2

Hurricanes

A2.1 Introduction

Currently, the numerical reanalyses (GOW and GOS, 1948-2008) generated using numerical models (WW3 and ROMS), which simulate the parameters associated with swells and variations in sea level as a function of wind and atmospheric pressure fields, do not capture the extreme events associated with tropical storms and hurricanes because the resolution for the forcings (wind and pressure fields) of the NCEP/NCAR reanalysis is not high enough. The spatial and temporal definition of this reanalysis is valid for defining usual wave and storm surge conditions (mean climate), but in order to define extreme events associated with tropical storms and hurricanes occurring at a greater resolution (around 5 km per hour), more detailed wind and pressure fields have to be defined. Figure 1.205 depicts one of the discrepancies observed for waves and winds at one buoy during Hurricane Katrina (2005).

FIGURE 1.205
WIND SPEED AND PRESSURE SERIES OF THE FORCING USED IN THE WW3 MODEL (GOW DATABASE, TRIANGLES), AND DATA MEASUREMENTS OF THE NOAA-42001 BUOY STATION (DOTS) FOR HURRICANE KATRINA (2005)

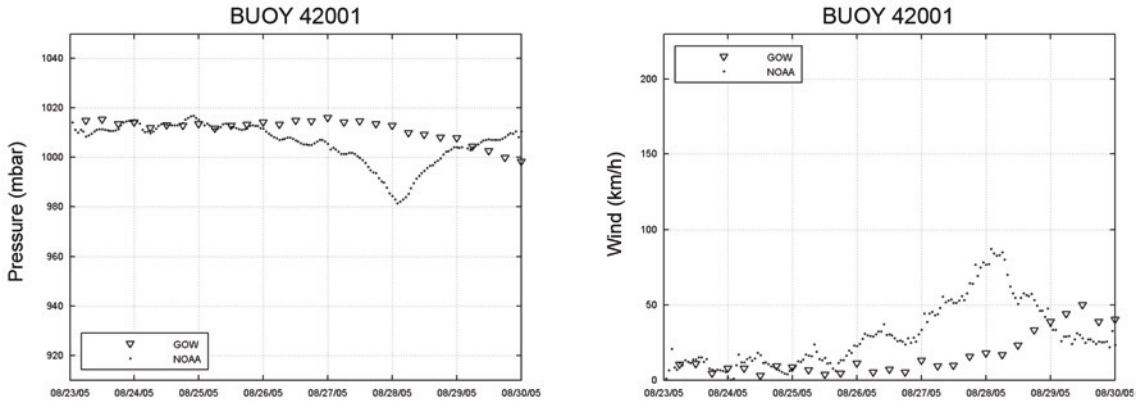

Source: Prepared by the authors.

In order to overcome this problem, extreme atmospheric events have to be identified in the reanalysis in order to obtain higher-resolution forcings, and the numerical models then need to be run again in order to refine the swell and sea level statistics for extreme events, hour by hour and sea state by sea state.

This is one of the best approaches for improving the database on extreme events associated with hurricanes. It can, however, become a tedious exercise in numerical simulation that can take an enormous amount of computer time to conduct and entail a huge effort in terms of the post-processing of data on each sea state associated with high-energy atmospheric events. Such an effort would be justified only in order to obtain an hourly evaluation of each sea state during a limited period of time (e.g., a single hurricane, one month in the hurricane season of a particular year, etc.), not for each hour during the 54-year reanalysis period. An undertaking of this sort would call for a specific study of its own, given the complexity of the task.

Another way of conducting a statistical evaluation of hourly variations in waves and storm surge for the entire 54-year period is to use analytical models that provide a fast, simple, computationally efficient and quantitatively reasonable means of obtaining those parameters for each hour of the entire reanalysis period. The results can then be dealt with statistically.

It is important to point out that these analytical models are based on large simplifications (linear, parametric, one-dimensional models, no energy dissipation processes, etc.) and may sometimes yield quantitatively disappointing results as compared to those of the WW3 and ROMS numerical models for hourly changes in each sea state associated with hurricane-related events over the entire 54-year time series (1955-2008).

Analytical models can provide satisfactory results, however, if we look at the statistical data for most of the events associated with tropical storms and hurricanes, and they can provide us with a very accurate picture of the magnitude of the extreme hurricane-generated wave and storm surge events. The results in terms of maximum significant wave height, peak period of the sea state, storm surge, and pressure and wind can then be mapped in ways that are highly useful for coastal and port engineering design and management purposes.

This chapter presents a reanalysis of wind and pressure fields using historical data for hurricanes and tropical storms in order to force different analytical and parametric models that can then yield the statistical behaviour of the parameters associated with waves and storm surges for the 54-year period for which data are available on hurricanes in the northern Atlantic, Caribbean Sea, Gulf of Mexico and north-eastern Pacific (see figure 1.206).

FIGURE 1.206
POSITIONS AND INTENSITIES OF HURRICANES OVER A 54-YEAR PERIOD

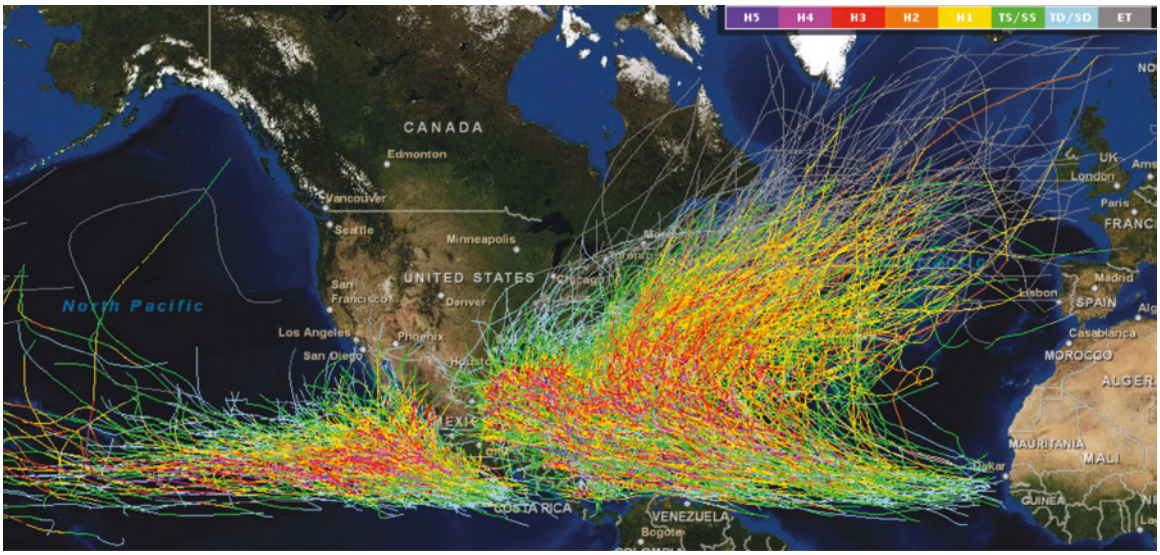

Source: National Hurricane Center, NOAA.
http://www.csc.noaa.gov/beta/hurricanes/#app=2b16&3722-selectedIndex=0.

The wind and pressure fields generated by these models have been checked and found to be in alignment with the instrumental data and to represent both variables satisfactorily. These parametric models are less accurate for waves and storm surges owing to the generation of shadowed areas and to the presence of characteristics that have not been taken into account in the models. However, the results for the buoy stations that were studied are very satisfactory, and the confidence level for the results in zones in which the coastal sheltering effect can be ignored is quite high. In addition, for the statistical analysis of the results to determine coastal impacts under the risk-analysis scenarios being used, the maximum values of the series are what are taken into consideration; thus, the sheltering effect of islands can be discounted, since the maximums will be conditioned by the event having the most direct impact. The statistical distribution of the results obtained using this technique will not be suitable, since certain points and times will be poorly modelled, but the confidence level of the maximum values will be higher than the confidence level of the distribution.

A2.2. Objective and methodology

The objective of this chapter is to map the historical data on pressure, waves, winds and storm surges during hurricanes using analytical and parametric models.

The overall objective can be broken down into the following components, which will be discussed in the following sections:

a) Evaluation and validation of hurricane **pressure fields.**

b) Evaluation and validation of hurricane **wind fields.**

c) Evaluation and validation of hurricane-generated **waves** (significant wave height *Hs* and peak period *Pp).*

d) Evaluation of hurricane-generated **storm surges.**

e) **Statistical mapping** of the variables analysed over the 61-year reanalysis period for hurricane events.

The methodology used for this purpose involves the sequential application of the results obtained from the pressure model as inputs for the wind model, then the application of the wave model and then, finally, the application of the results of the wind and pressure models as inputs for the storm surge model.

A2.3. Evaluation and validation of pressure fields

The atmospheric pressure fields generated by the passage of a tropical storm or hurricane can be modelled based on the Hydromet-Rankin Vortex (1980) and can be easily estimated using the following expression:

$$P_r = P_0 + (P_N - P_0) \cdot e^{\left(-\frac{R}{r}\right)} \qquad \text{(A2.1)}$$

Where,

P_0 is the pressure at the eye of the hurricane in mbar.
P_r is the pressure at a radial distance r in km.
P_N is the pressure in the area unaffected by the hurricane (normally 1013 mbar).
R is the radius of maximum cyclostrophic winds in km.

Figure 1.207 shows the configuration of a typical pressure map for the parameters R=31.95 km and P_0=930 mbar for a domain measuring 1,200 km x 1,200 km.

FIGURE 1.207
EXAMPLE OF A PRESSURE FIELD OBTAINED USING THE HYDROMET-RANKIN VORTEX MODEL (1980)

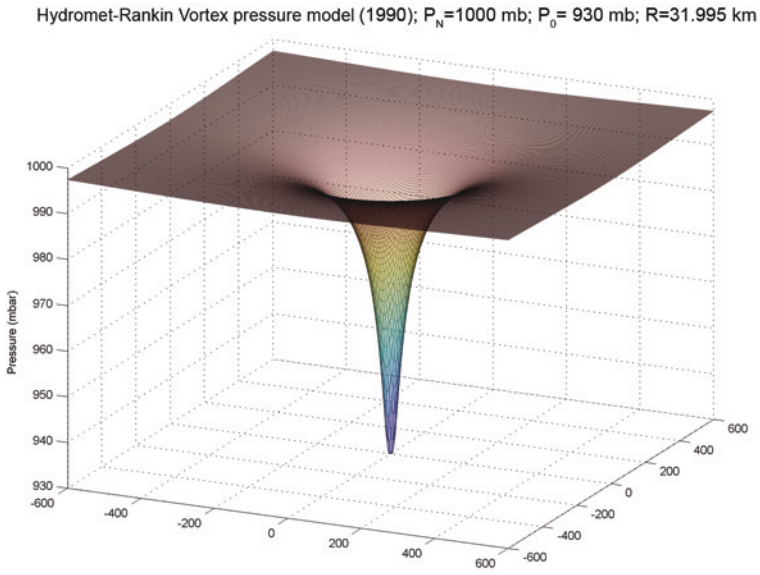

Source: Prepared by the authors.

Consequently, in order to undertake a spatial and temporal evaluation of atmospheric pressure fields showing the changes generated by the passage of a hurricane, the values at each point in time must be known for the pressure at the centre, the radius of cyclostrophic winds, the geographical position of the eye of the hurricane and the positions or numerical domains on the map to be evaluated (values of the radius *r).*

Information on the spatial and temporal position of hurricane-related events and data on the atmospheric pressure at the centre, as well as the name and dates of the hurricane, can be obtained from the web services of NOAA and the National Hurricane Center of the United States.

A total of 40,450 hurricane advisories (providing data on longitude, latitude, dates, name and central pressure values every six hours) have been downloaded for this study for the northern Atlantic, Caribbean Sea and the Gulf of Mexico; a total of 21,705 advisories have been downloaded for the north-eastern Pacific.

This information spans the years since 1851 for the Atlantic Ocean and since 1949 for the Pacific Ocean. However, the data do not begin to form a homogenous dataset for central hurricane pressure fields until the 1950s in both cases.

The NOAA databases do not include information on the cyclostrophic radius at six-hour intervals. In fact, this information is provided only occasionally in NOAA bulletins referring to particularly strong hurricanes.

In order to assess the cyclostrophic radius, the following linear expression, which relates the cyclostrophic radius to the central pressure field on the basis of the observations and spatial measurements of 26 hurricanes provided by Silva *et al.* (2002), has therefore been used.

$$R=0.4785 \cdot P_0-413.01 \quad \text{(A2.2)}$$

Finally, in order to evaluate the different fields of historical data for hurricanes over the 60-year reanalysis period, an area measuring 20 x 20 geographic degrees has been defined; this area has then had to be converted to UTM coordinates for each point in time while interpolating the data provided in hurricane bulletins that were originally issued at six-hour intervals after converting that information into hourly data.

Figure 1.208 and figure 1.209 show examples of pressure fields for two high-energy hurricanes: Hurricane Katrina (2005) in the Atlantic Ocean and Hurricane Kenna (2002) in the Pacific Ocean.

FIGURE 1.208
ATMOSPHERIC PRESSURE FIELD FOR HURRICANE KATRINA
(27 AUGUST 2005 AT 17:00 HOURS)
(Mbar)

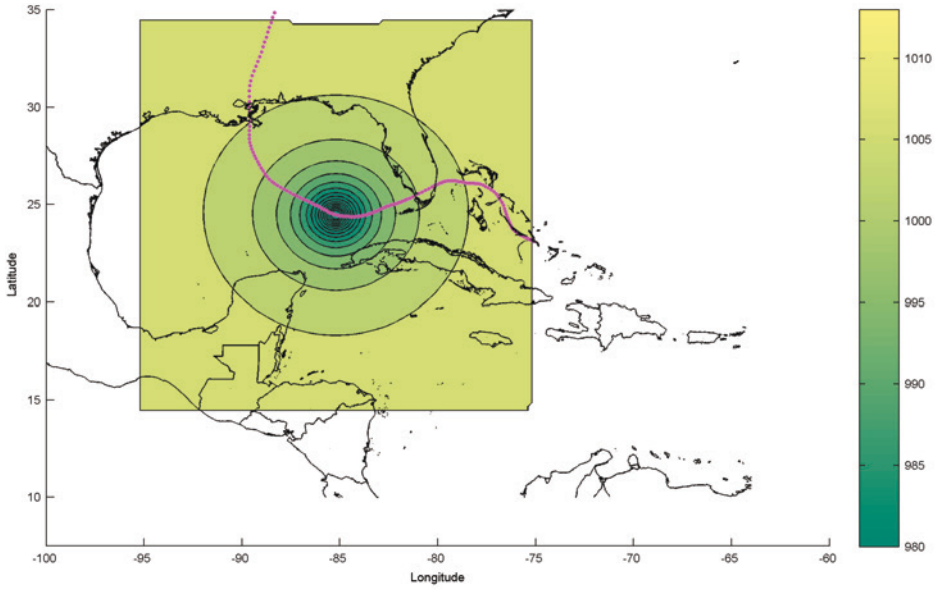

Source: Prepared by the authors on the basis of data from NOAA and the National Hurricane Center

FIGURE 1.209
ATMOSPHERIC PRESSURE FIELD FOR HURRICANE KENNA
(24 OCTOBER 2002 AT 09:00 HOURS)
(Mbar)

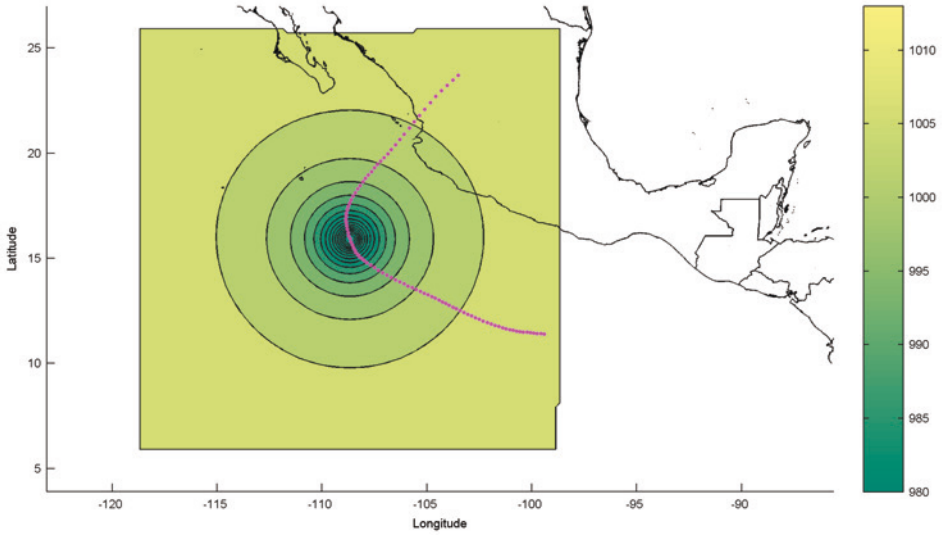

Source: Prepared by the authors on the basis of data from NOAA and the National Hurricane Center.

The pressure fields obtained from this model have then been validated on the basis of the instrumental data derived from the measurements taken at the 58 NOAA National Data Buoy Center stations in the Atlantic and Gulf of Mexico (see figure 1.210), which provide hourly data on pressure, wind force, wind direction, signifi ant wave height and peak period (among others) since around 1990.

FIGURE 1.210
POSITIONS AND NAMES OF NOAA NATIONAL DATA BUOY CENTER STATIONS

Source: http://www.ndbc.noaa.gov/.

Once the pressure fields were generated with the help of the model, measurement data and numerical data were cross-checked with the Hydromet-Rankin Vortex model (1990) for the hurricanes shown in the following figures. The coordinates of the NOAA buoys used in this study are given in table 1.11.

TABLE 1.11
GEOGRAPHIC COORDINATES OF NOAA BUOYS IN THE ATLANTIC OCEAN AND CARIBBEAN SEA

ID	Long	Lat	ID	Long	Lat	ID	Long	Lat
41008	-80.871	31.402	44018	-69.305	41.255	42041	-90.462	27.504
41003	-80.1	30.4	44011	-66.58	41.111	42038	-92.555	27.421
41012	-80.533	30.041	44008	-69.247	40.503	42002	-93.666	25.79
41009	-80.166	28.519	44017	-72.046	40.691	42019	-95.36	27.913
41006	-77.4	29.3	44025	-73.166	40.25	42035	-94.413	29.232
41010	-78.471	28.906	44004	-70.433	38.484	42020	-96.695	26.966
41016	-76.5	24.6	44001	-73.6	38.7	42016	-88.1	30.2
42025	-80.4	24.9	44012	-74.6	38.8	42007	-88.769	30.09
42080	-81.934	24.396	44009	-74.702	38.464	41041	-46.008	14.357
42036	-84.517	28.5	44014	-74.836	36.611	41040	-53.008	14.477
42039	-86.008	28.791	44006	-75.4	36.3	41043	-65.014	29.989
42005	-85.9	30	41001	-72.734	34.704	42059	-67.496	15.006
42009	-87.5	29.3	41036	-76.953	34.211	41018	-75	15
42040	-88.205	29.205	41002	-75.415	32.382	42055	-94.046	22.017
42015	-88.2	30.1	41004	-79.099	32.501	42056	-85.059	19.874
44027	-67.314	44.273	41048	-69.649	30.978	42057	-81.501	16.834
44007	-69.247	40.503	41047	-71.491	27.469	42058	-75.064	15.093
44005	-69.14	43.189	41046	-70.87	23.867	41044	-58.695	21.652
44013	-70.651	42.346	10000	-88	27.5	41049	-63	27.5
			42001	-89.667	25.9			

Source: Prepared by the authors on the basis of NOAA data.

FIGURE 1.211
COMPARISON OF HOURLY PRESSURE SERIES FOR THE HURAC-HYDROMET-RANKIN VORTEX MODEL (1980) (BLUE DOTS), BUOY DATA (BLACK DOTS) AND NCEP/NCAR REANALYSIS (BLACK TRIANGLES) FOR HURRICANE KATRINA (2005)

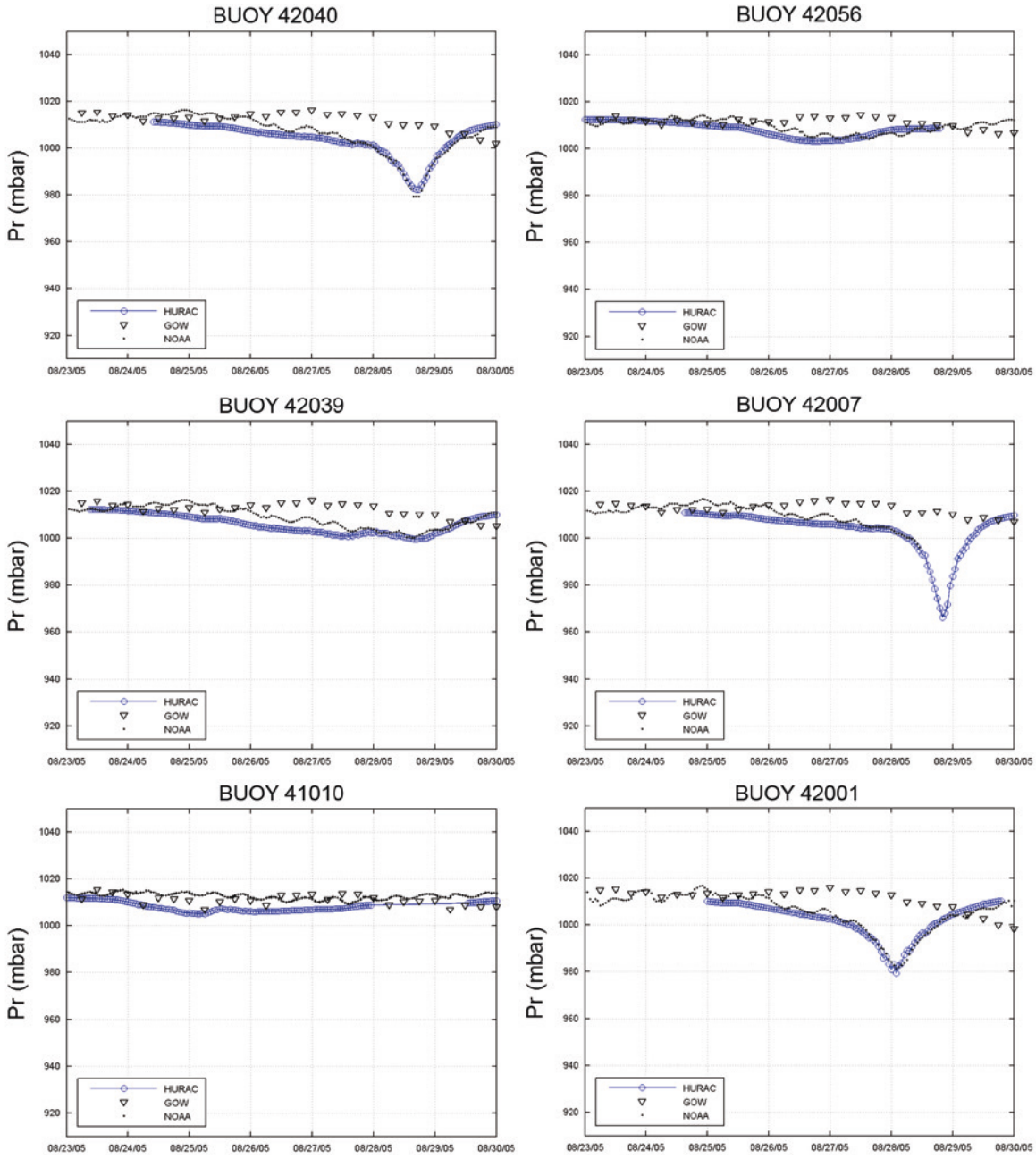

Source: Prepared by the authors.

FIGURE 1.212
COMPARISON OF HOURLY PRESSURE SERIES FOR THE HURAC-HYDROMET-RANKIN VORTEX MODEL (1980) (BLUE DOTS), BUOY DATA (BLACK DOTS) AND NCEP/NCAR REANALYSIS (BLACK TRIANGLES) FOR HURRICANE GILBERT (1988)

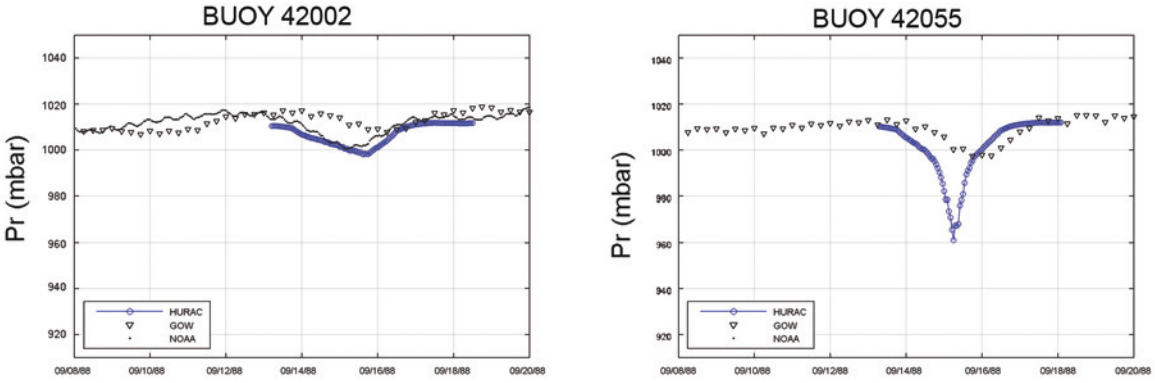

Source: Prepared by the authors.

FIGURE 1.213
COMPARISON OF HOURLY PRESSURE SERIES FOR THE HURAC-HYDROMET-RANKIN VORTEX MODEL (1980) (BLUE DOTS), BUOY DATA (BLACK DOTS) AND NCEP/NCAR REANALYSIS (BLACK TRIANGLES) FOR HURRICANE MITCH (1998)

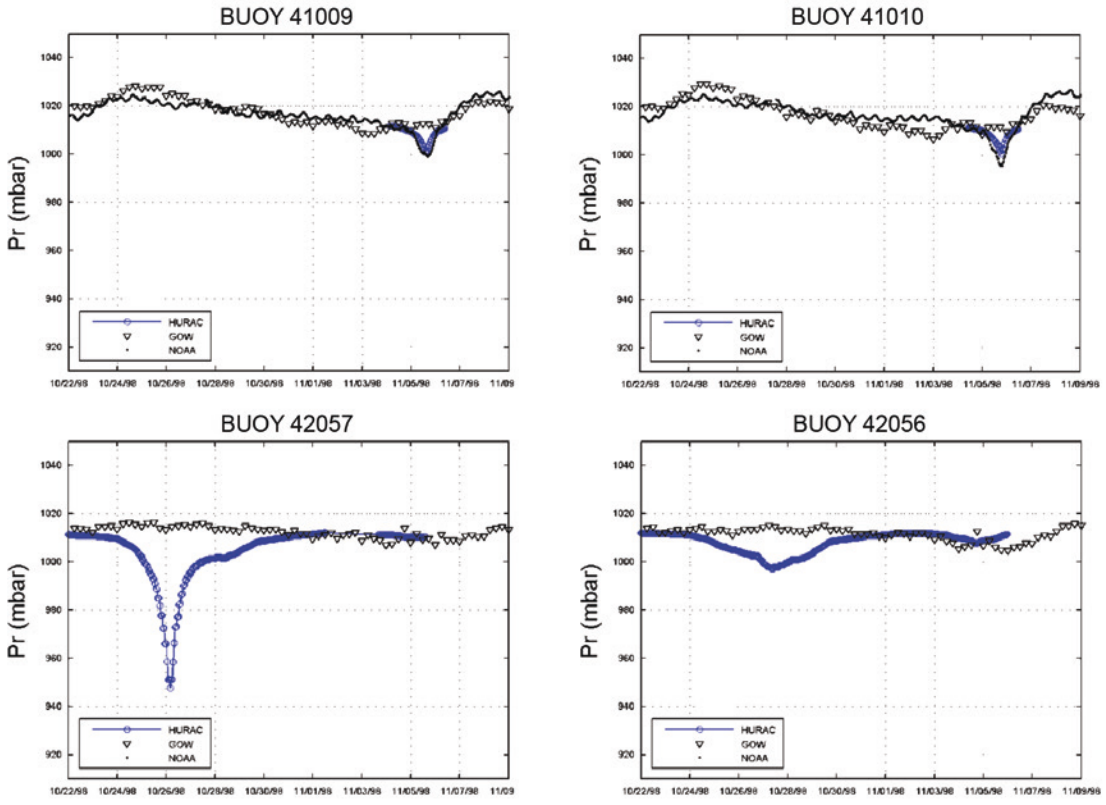

Source: Prepared by the authors.

FIGURE 1.214
COMPARISON OF HOURLY PRESSURE SERIES FOR THE HURAC-HYDROMET-RANKIN VORTEX MODEL (1980) (BLUE DOTS), BUOY DATA (BLACK DOTS) AND NCEP/NCAR REANALYSIS (BLACK TRIANGLES) FOR HURRICANE WILMA (2005)

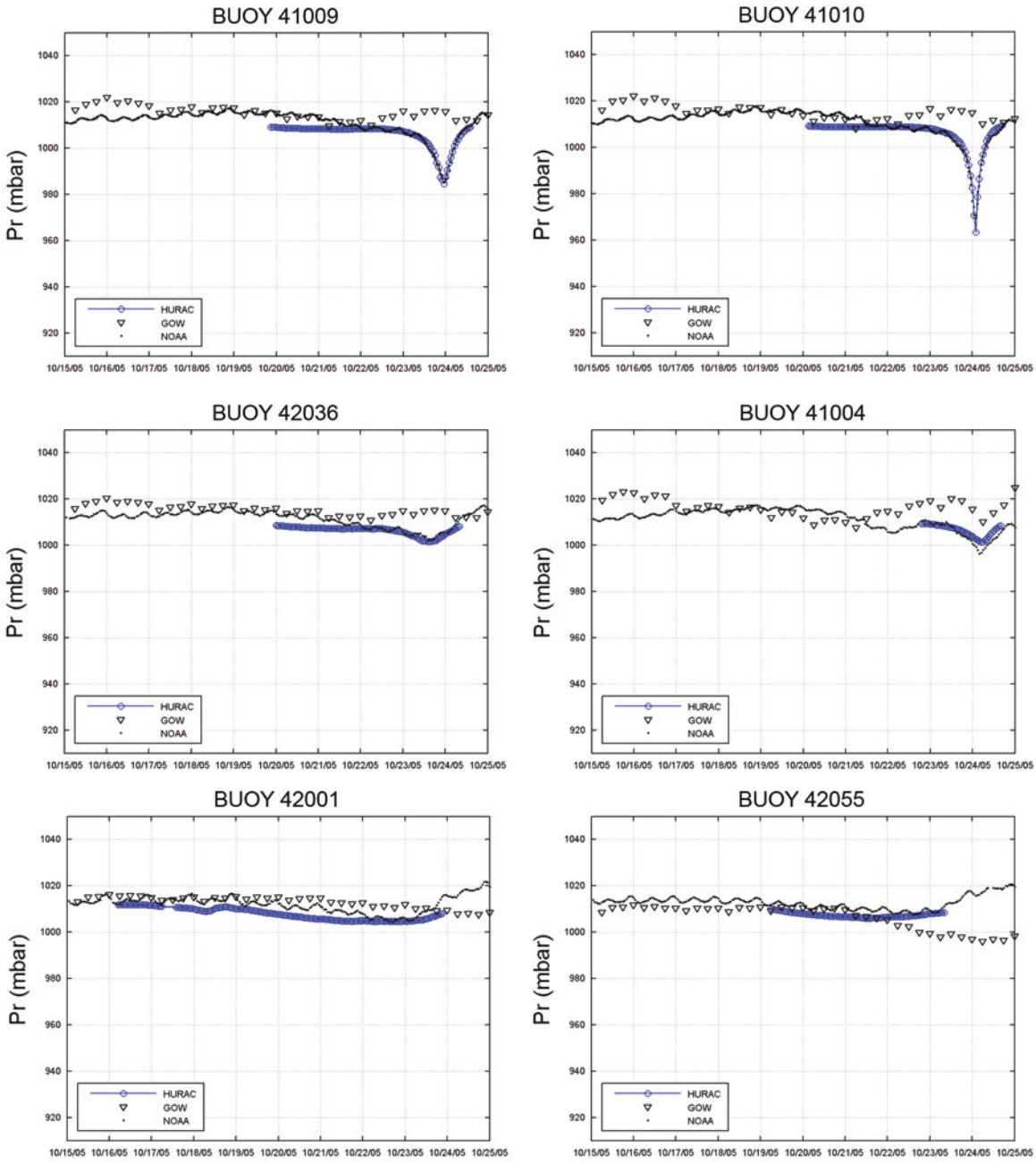

Source: Prepared by the authors.

FIGURE 1.215
COMPARISON OF HOURLY PRESSURE SERIES FOR THE HURAC-HYDROMET-RANKIN VORTEX MODEL (1980) (BLUE DOTS), BUOY DATA (BLACK DOTS) AND NCEP/NCAR REANALYSIS (BLACK TRIANGLES) FOR HURRICANE IKE (2008)

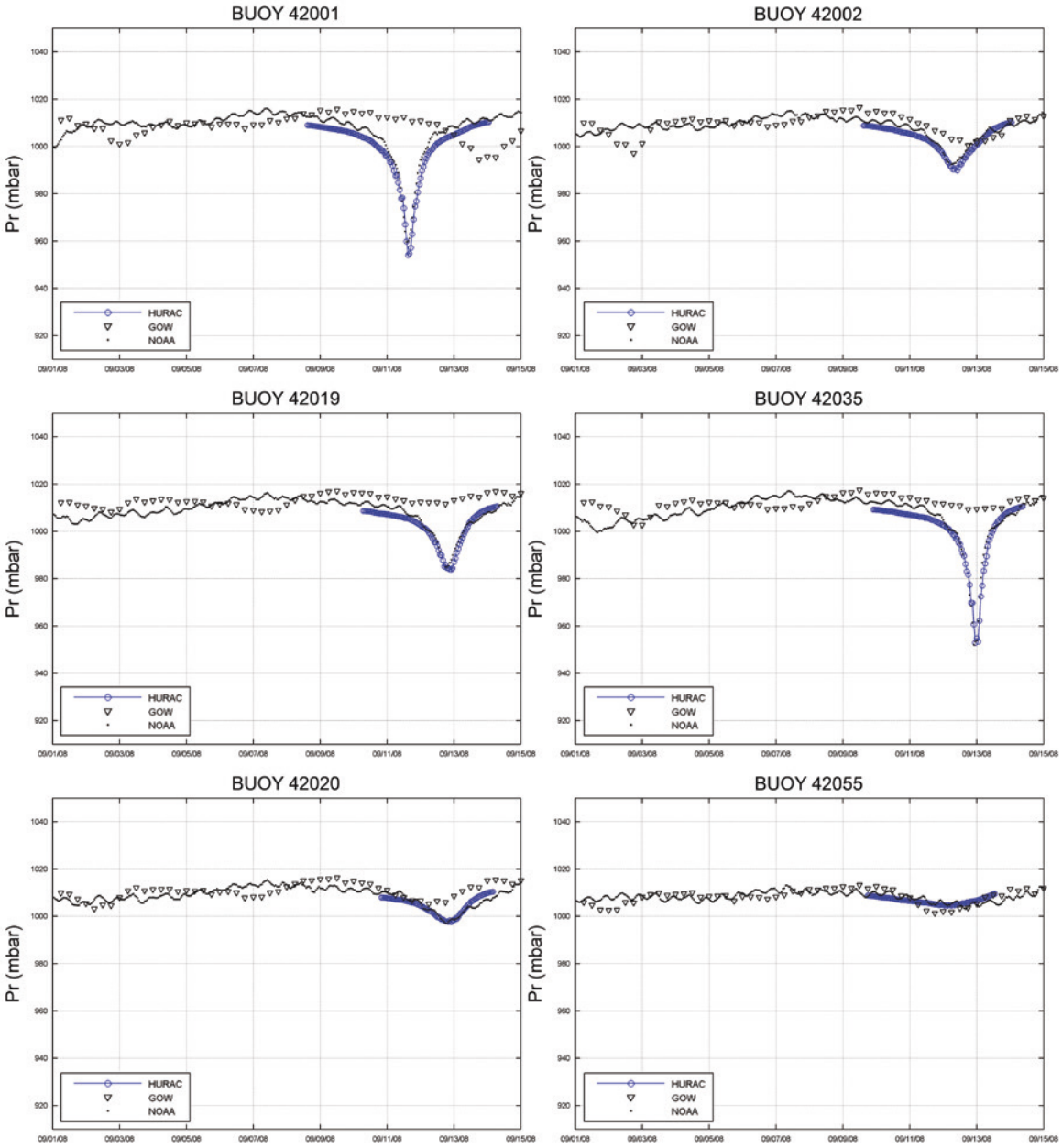

Source: Prepared by the authors.

The above figures reflect a very good fit between the atmospheric pressure data obtained from NOAA buoy measurements and those yielded by the analytical model.

A2.4. Evaluation and validation of wind fields

Wind vector magnitudes associated with the passage of tropical storms or hurricanes can be modelled by applying the Hydromet-Rankin Vortex and the Bretschneider model (1990), which makes it possible to determine the maximum gradients of the wind fields and speeds at 10 m above sea level.

The maximum gradient U_R (in km/h) for a stationary cyclone can be determined using the following equation:

$$U_R = 21.8 \cdot \sqrt{P_N - P_0} - 0.5 \cdot f \cdot R \qquad \text{(A2.3)}$$

Where,

f is the Coriolis parameter $f = 2\omega \sin(\Phi)$

As a function of the velocity relative to the land $\omega = 0.2618 rad/h$, while Φ is the latitude in degrees.

This information can be used to gauge the wind speed (in km/h) at a height of 10 metres above sea level for a hurricane in movement and at a radial distance r as measured from the centre of the atmospheric disturbance.

$$W = 0.886 \left(F_V \cdot U_R + 0{,}5 \cdot V_F \cos(\theta + \beta)\right) \qquad \text{(A2.4)}$$

Where $\theta + \beta$ represents the total angle between the translational velocity V_F (speed of movement of the hurricane in km/h) and the wind speed at a radial distance U_R (in km/h). F_V is the buffer and is evaluated on the basis of the following:

$$F_V = 1 - 0.971 \cdot \exp\left(-6.826\left(\frac{r}{R}\right)^{4.798}\right) \quad \text{for } \frac{r}{R} < 1 \text{ (towards the centre of the hurricane)}$$

$$F_V = \exp\left(A \cdot 1n^3\left(\frac{r}{R}\right) \cdot \exp\left(B \cdot 1n\left(\frac{r}{R}\right)\right)\right) \quad \text{for } \frac{r}{R} \geq 1 \text{ (towards the outer bounds of the hurricane)} \qquad \text{(A2.5)}$$

Where,

$$A = -0.99 \cdot \left(1.066 - \exp\left(-1.936 \cdot \left(\frac{f \cdot R}{U_R}\right)\right)\right)$$

$$B = -0.357 \cdot \left(1.4456 - \exp\left(-5.2388 \cdot \left(\frac{f \cdot R}{U_R}\right)\right)\right)$$

Figure 1.216 depicts a typical wind map for the parameters R=31.95 km and P_0=930 mbar for a domain measuring 1,200 km x 1,200 km.

FIGURE 1.216
EXAMPLE OF A WIND FIELD OBTAINED USING THE BRETSCHNEIDER MODEL (1990)

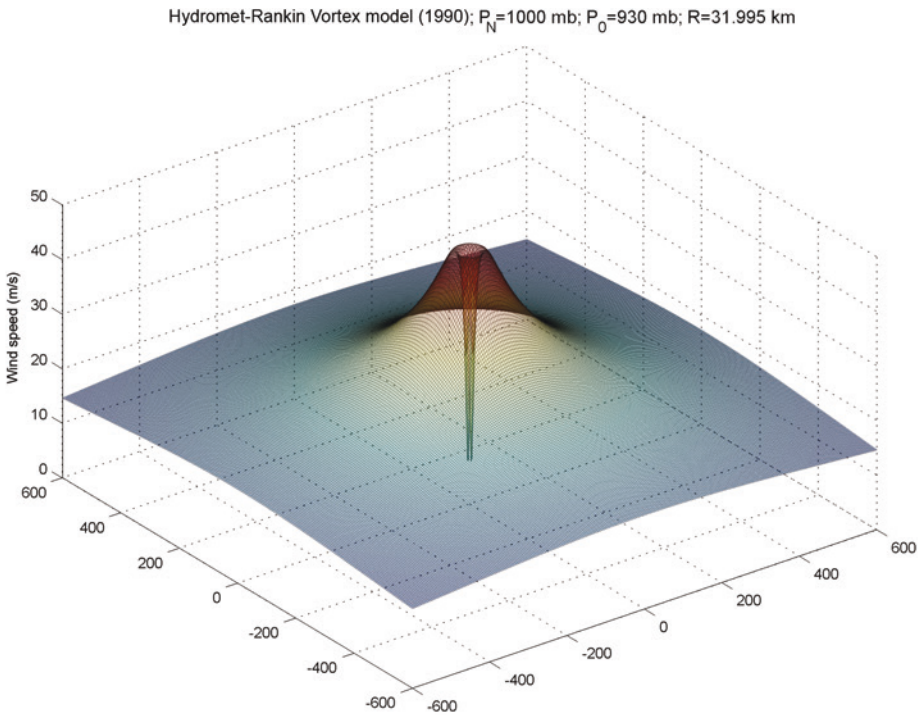

Source: Prepared by the authors.

As in the case of the pressure model, a validation exercise based on the Bretschneider (1990) wind model is performed for the different Atlantic hurricanes of interest.

The spatial and temporal positions of the hurricane-related events are used here too, with the data being drawn from the NOAA database for the Pacific Ocean and Atlantic Ocean, along with the cyclostrophic radiuses for each hurricane for each hour; the equations are evaluated on the basis of an area measuring 20 x 20 degrees.

Figure 1.217 and figure 1.218 give examples of the wind fields (magnitude and direction) obtained for two major hurricanes (Katrina in 2005 in the Atlantic Ocean and Kenna in 2002 in the Pacific Ocean). These fields correlate with the fields shown in figure 1.208 and figure 1.209 above.

FIGURE 1.217
FIELD OF WIND VARIATIONS: HURRICANE KATRINA
(27 AUGUST 2005 AT 17:00 HOURS)
(Km/metres)

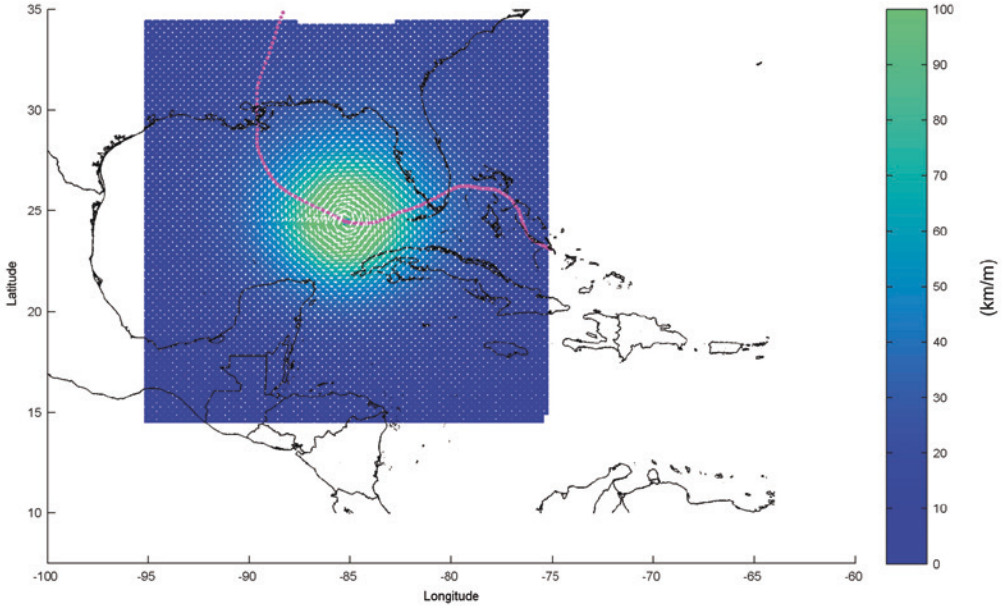

Source: Prepared by the authors.

FIGURE 1.218
FIELD OF WIND VARIATIONS: HURRICANE KENNA
(24 OCTOBER 2002 AT 11:00 HOURS)
(Km/metres)

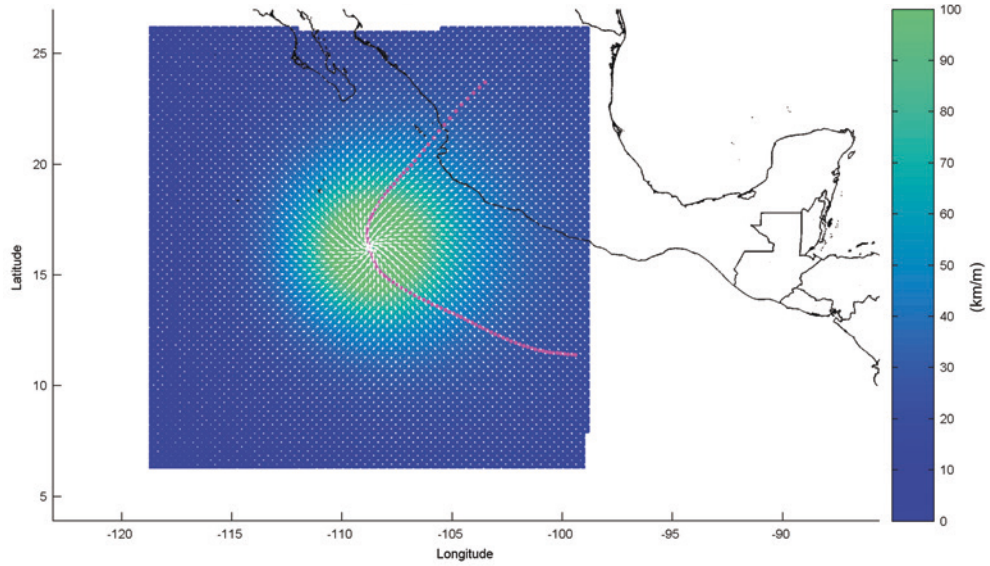

Source: Prepared by the authors.

The following figures show the results of the validation exercises conducted for the wind data obtained using the Bretschneider model (1990) (velocity at 10 m above sea level) for various hurricanes as compared to the instrumental data obtained from measurements taken at the 58 NOAA National Data Buoy Center stations in the Atlantic Ocean and the Gulf of Mexico.

The comparisons show that the wind model that has been used yields satisfactory spatial and temporal results that exhibit a good fit with the NOAA buoy measurements. There are, however, overestimates of the velocity module values of about 15% in some cases.

FIGURE 1.219
COMPARISON OF THE HOURLY SERIES FOR THE HURAC-BRETSCHNEIDER MODEL (1990) (BLUE DOTS), BUOY DATA (BLACK DOTS) AND NCEP/NCAR REANALYSIS (BLACK TRIANGLES) FOR HURRICANE KATRINA (2005)

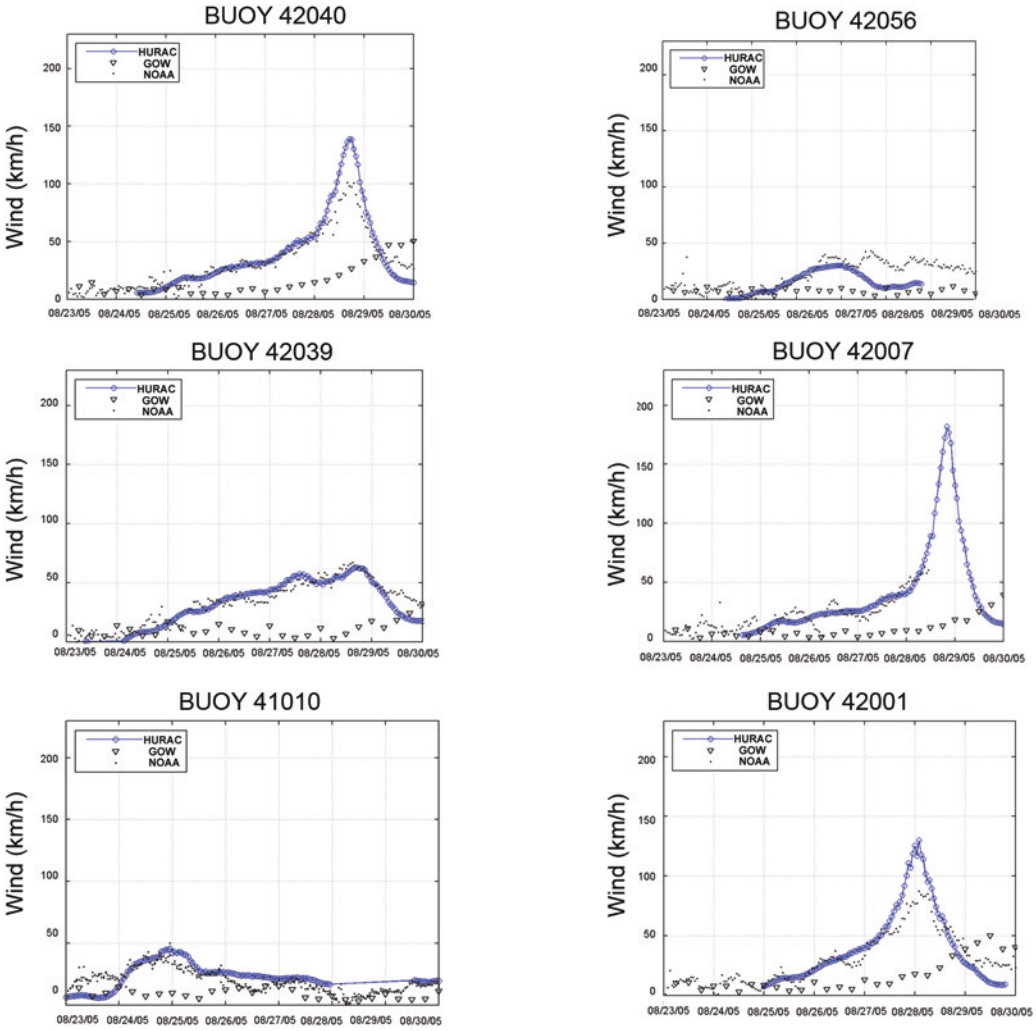

Source: Prepared by the authors.

FIGURE 1.220
COMPARISON OF THE HOURLY SERIES FOR THE HURAC-BRETSCHNEIDER MODEL (1990) (BLUE DOTS), BUOY DATA (BLACK DOTS) AND NCEP/NCAR REANALYSIS (BLACK TRIANGLES) FOR HURRICANE GILBERT (1988)

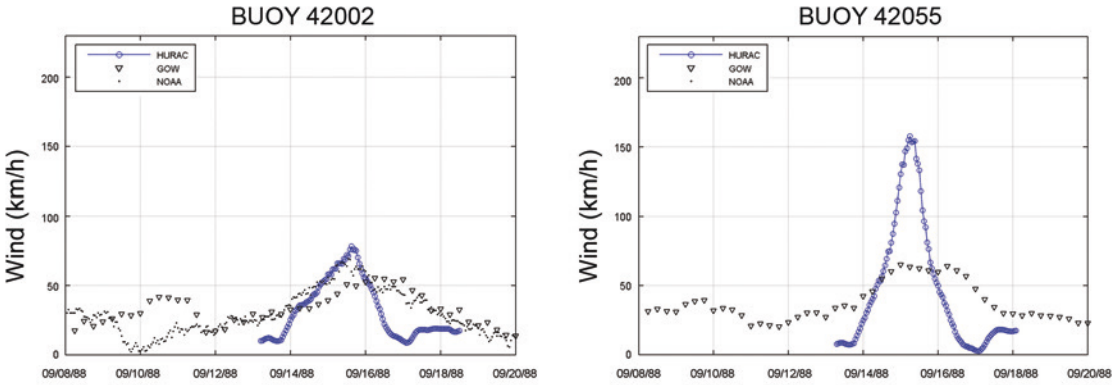

Source: Prepared by the authors.

FIGURE 1.221
COMPARISON OF THE HOURLY SERIES FOR THE HURAC-BRETSCHNEIDER MODEL (1990) (BLUE DOTS), BUOY DATA (BLACK DOTS) AND NCEP/NCAR REANALYSIS (BLACK TRIANGLES) FOR HURRICANE MITCH (1998)

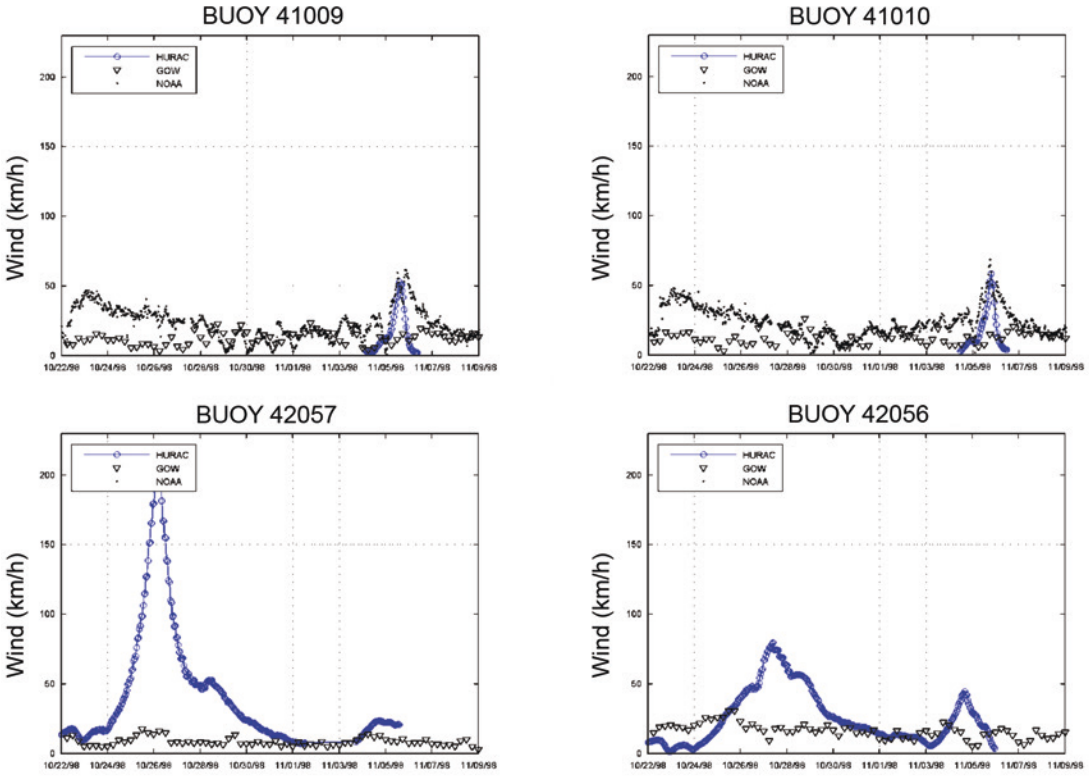

Source: Prepared by the authors.

FIGURE 1.222
COMPARISON OF THE HOURLY SERIES FOR THE HURAC-BRETSCHNEIDER MODEL (1990) (BLUE DOTS), BUOY DATA (BLACK DOTS) AND NCEP/NCAR REANALYSIS (BLACK TRIANGLES) FOR HURRICANE WILMA (2005)

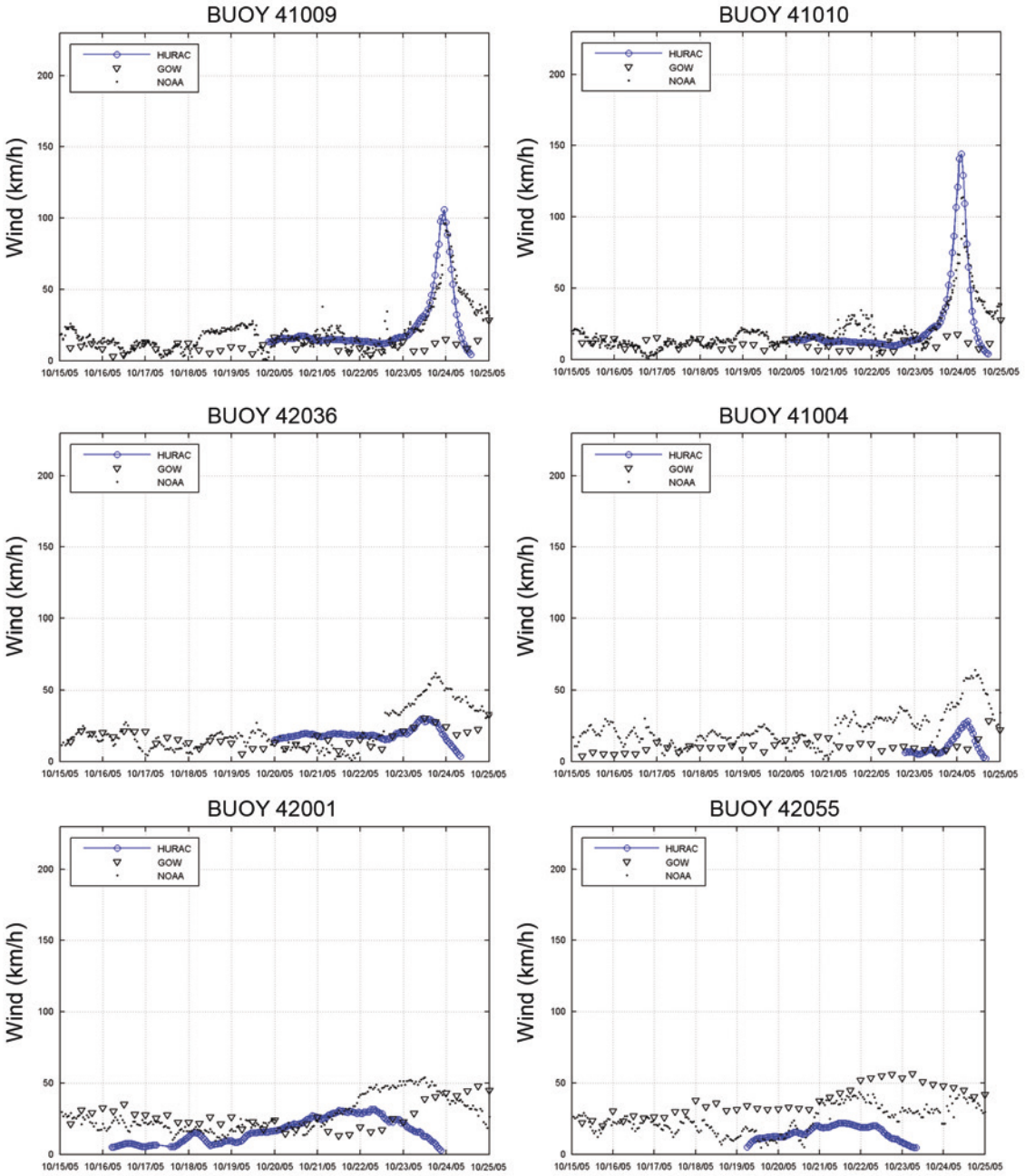

Source: Prepared by the authors.

FIGURE 1.223
COMPARISON OF THE HOURLY SERIES FOR THE HURAC-BRETSCHNEIDER MODEL (1990) (BLUE DOTS), BUOY DATA (BLACK DOTS) AND NCEP/NCAR REANALYSIS (BLACK TRIANGLES) FOR HURRICANE IKE (2008)

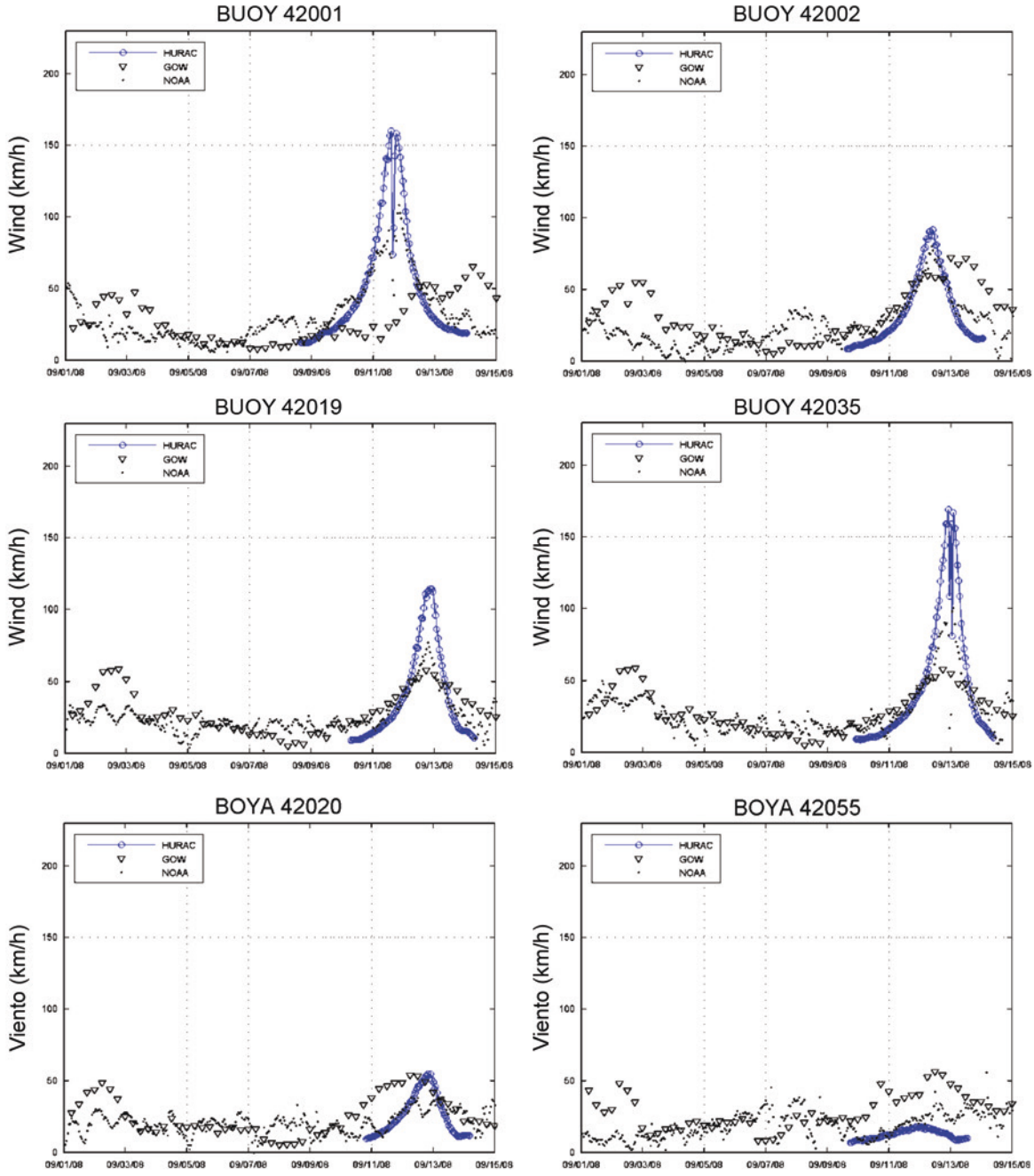

Source: Prepared by the authors.

A2.5. Evaluation and validation of wave fields

Once the pressure and wind maps have been evaluated using the Holland (1980) and Bretschneider (1990) models, respectively, the next step is to calculate the sea state parameters: significant wave height *(Hs)* and peak period *(Pp),* along with the corresponding spatio-temporal variations during the passage of the hurricane.

Earlier sections have discussed the possibility of numerically modelling wave parameters based on wind mapping using latest-generation numerical models. This approach makes it possible to develop high-quality wave fields that incorporate realistic estimates of the different wave-propagation processes, interactions with orographic and bathymetric contours and energy dissipation effects.

The approach entails complex pre- and post-processing tasks, however, and is an inefficient and perhaps unfeasible way of compiling large volumes of data, such as those involved in a 54-year reanalysis of hurricane events.

In order to obtain the statistical parameters for wave activity during the hurricane-related events in the 61-year reanalysis period, the chosen methodology therefore focuses on a state-of-the-art review of three different analytical models that can be used to obtain significant wave height and peak period fields during hurricane events.

The wave models used in this study are (see the examples of fields derived from the three models in figure 1.217, figure 1.224, figure 1.225 and figure 1.227):

The **Bretschneider wave model** (1990) for the evaluation of significant wave height *Hs,* in a non-stationary cyclone in waters in an undefined area.

$$Hs = 0.2557 \cdot F_h \left(1 - \frac{6.69 \cdot N_C}{1 + 10.3 \cdot N_C - 3.25 \cdot N_C^2}\right) \cdot \sqrt{R \cdot (P_N - P_0)} \cdot \left(1 + \frac{V_F \cdot \cos(\theta+\beta)}{2 \cdot U_R \cdot F_V}\right)^2$$

$$Ts = 12.1 \sqrt{\frac{Hs}{g}} \qquad \text{(A2.6)}$$

Where,

$\theta + \beta$ represents the total angle for translational velocity;
g is the gravitational acceleration in m/s²;
N_C is the Coriolis cyclostrophic number;
F_h is calculated by:

For $\frac{r}{R} < 1$ (towards the centre of the hurricane):

$$F_h = \frac{1 - 0.8974 \cdot \left(\cdot \frac{r}{R} - 1\right)}{1.0742 \cdot \left(\cdot \frac{r}{R} - 1\right) + 0.07382 \cdot \left(\cdot \frac{r}{R} - 1\right)^2}$$

For $\frac{r}{R} \geq 1$ (towards the outer bounds of the hurricane):

$$F_h = \frac{1 - 0.8974 \cdot \left(\cdot \frac{r}{R} - 1\right)}{1.0742 \cdot \left(\cdot \frac{r}{R} - 1\right) + 0.07382 \cdot \left(\cdot \frac{r}{R} - 1\right)^2} - \frac{N_C \cdot \left(\cdot \frac{r}{R} - 1\right)}{1 + C \cdot \left(\cdot \frac{r}{R} - 1\right) + \frac{N_C}{10}\left(\cdot \frac{r}{R} - 1\right)^2}$$

And, finally, $C = \frac{0.37 \cdot N_C^{2.55}}{0.13 + N_C^{2.55}}$

FIGURE 1.224
SIGNIFICANT WAVE HEIGHT FIELD FOR HURRICANE KATRINA, BRETSCHNEIDER MODEL (1990) (27 AUGUST 2005 AT 17.00 HOURS)
(Metres)

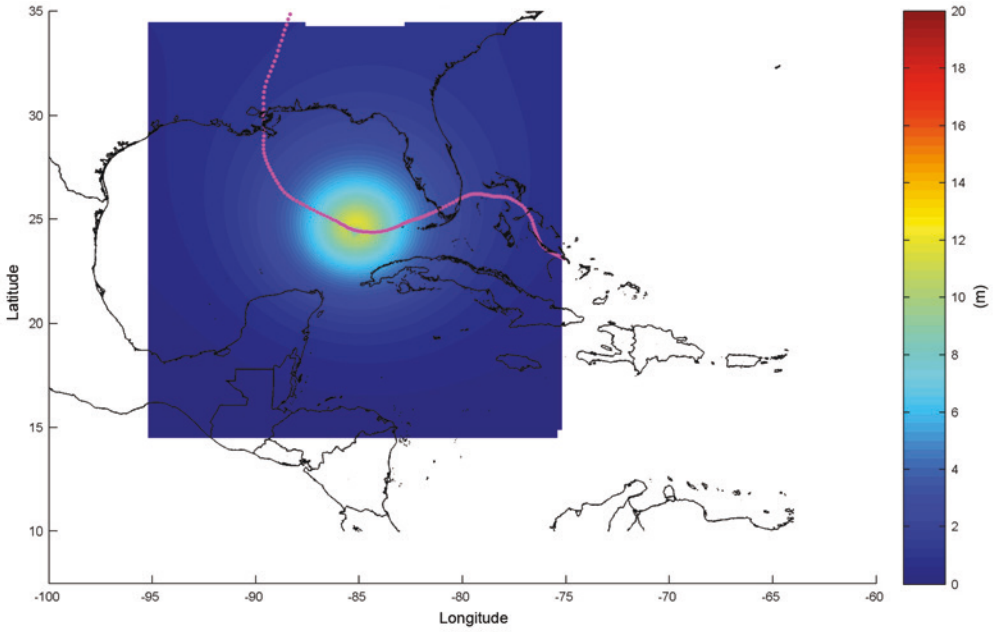

Source: Prepared by the authors.

The **Young wave model** (1988), based on maximum significant wave heights and their fit to synthetic diagrams derived from a numerical model for application in deep water.

$$\frac{g \cdot H_S^{\max}}{V_{\max}^2} = 0.0016 \left(\frac{g \cdot x}{V_{\max}^2} \right)^{0.5}$$

$$\frac{g \cdot Tp^{\max}}{2\pi \cdot V_{\max}^2} = 0.045 \left(\frac{g \cdot x}{V_{\max}^2} \right)^{0.33} \qquad \text{(A2.7)}$$

Where,

$$\frac{x}{R'} = \psi(a \cdot V_{max}^{\ 2} + b \cdot V_{max} \cdot V_F + c \cdot V_F^{\ 2} + d \cdot V_{max} + e \cdot V_F + f)$$

$R' = 22.5x10^3 \cdot \log(R) - 70.8x10^3$

$a = -2.175x10^{-3}$

$b = 1.506x10^{-2}$

$c = -1.223x10^{-1}$

$d = 2.190x10^{-1}$

$e = 6.737x10^{-1}$

$f = 7.980x10^{-1}$

$\psi = -0.015 \cdot V_{max} + 0.0431 \cdot V_F + 1.30$

FIGURE 1.225
SIGNIFICANT WAVE HEIGHT FIELD FOR HURRICANE KATRINA, YOUNG MODEL (1988) (27 AUGUST 2005 AT 17.00 HOURS)
(Metres)

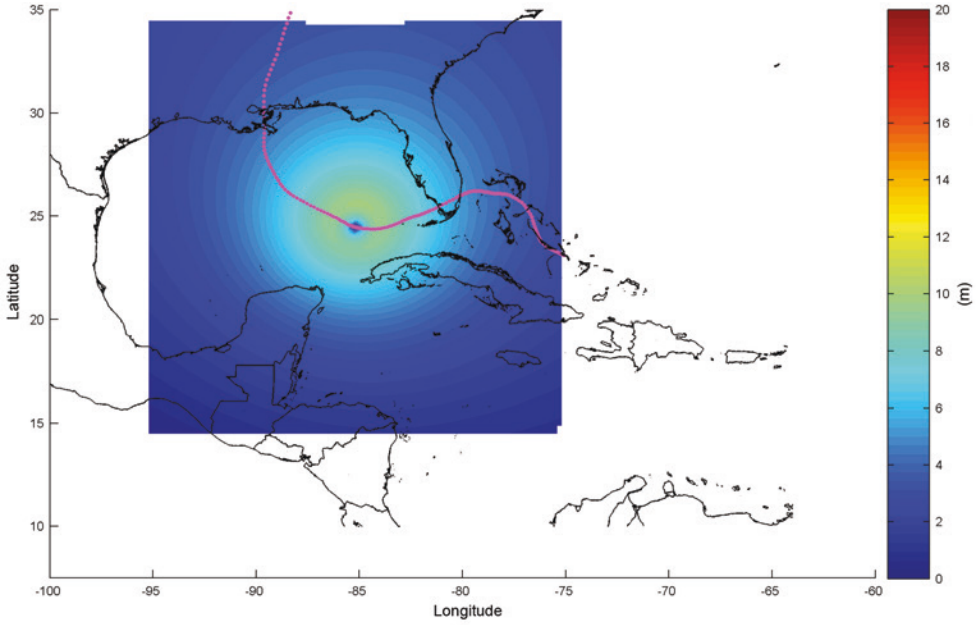

Source: Prepared by the authors.

Wind-generated wave model as presented in the Shore Protection Manual (SPM 1984), modified to take account of the wave effects propagated by the hurricane (intermediate or shallow depths).

$$\frac{g \cdot H_S}{U_A^2} = 0.25 \cdot \tanh\left[0.6\left(\frac{g \cdot h}{U_A^2}\right)^{0.75}\right] \cdot \tanh^{0.5}\left\{\frac{4.3x10^{-5}\left(\frac{g \cdot 2F}{U_A^2}\right)}{\tanh^2\left[0.6\left(\frac{g \cdot h}{U_A^2}\right)^{0.75}\right]}\right\}$$

$$\frac{g \cdot Tp}{U_A} = 8.3 \cdot \tanh\left[0.76\left(\frac{g \cdot h}{U_A^2}\right)^{0.375}\right] \cdot \tanh^{1/3}\left\{\frac{4.1x10^{-5}\left(\frac{g \cdot 2F}{U_A^2}\right)}{\tanh^3\left[0.76\left(\frac{g \cdot h}{U_A^2}\right)^{0.375}\right]}\right\} \quad \text{(A2.8)}$$

U_A is the velocity generated by the hurricane at a height of 10 metres above sea level in m/s.
h is the depth in metres associated with each U_A.
F is the fetch, or the distance over which the wind blows.

In order to evaluate the depth of h throughout the domain of interest, the bathymetric measurements published in the *General Bathymetric Chart of the Oceans* (GEBCO) (http://www.gebco.net/) have been used (with a grid resolution of 30 geographic seconds).

The bathymetric grids used for the Pacific Ocean and Atlantic Ocean domains are shown in figure 1.226.

FIGURE 1.226
BATHYMETRY FOR THE MODIFIED SPM MODEL (1984)

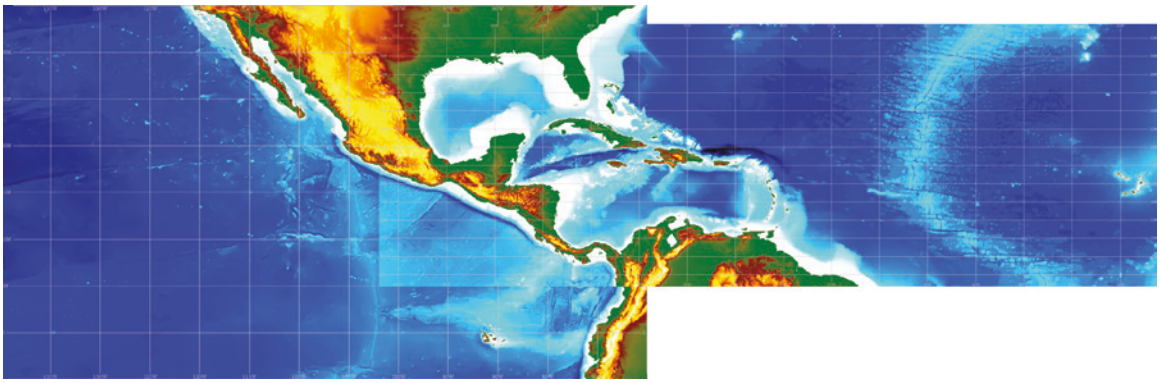

Source: GEBCO.

FIGURE 1.227
SIGNIFICANT WAVE HEIGHT FIELD FOR HURRICANE KATRINA, MODIFIED SPM MODEL (1984) (27 AUGUST 2005 AT 17.00 HOURS)
(Metres)

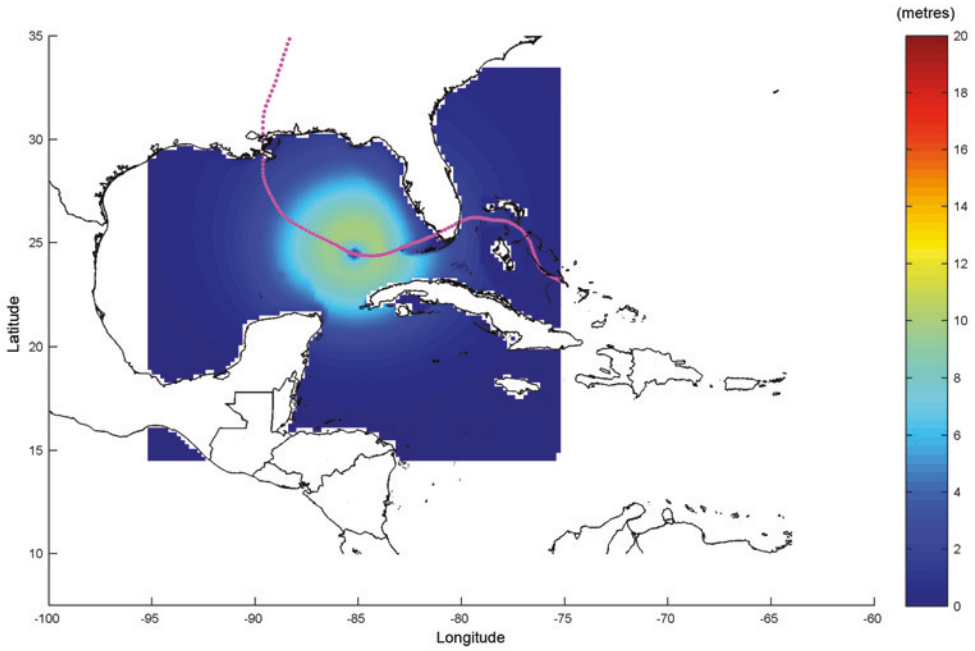

Source: Prepared by the authors.

Comparisons are shown below of the *Hs* and *Pp* for the three wave models used in this study, the measurements recorded by the NOAA buoys, and the *Hs* and *Pp* measurements obtained from the GOW database.

These comparisons show that the modified SPM model yields results that are closer to the NOAA buoy measurements, both for significant wave height and for the peak period. These results provide a satisfactory simulation of the upward trend in wave height and period following a hurricane's passage, as well as for the post-passage decline of this atmospheric phenomenon in terms of both time and space. Figure 1.227 also shows how the modified SPM model fits the bathymetric contour and alters the spatial values for Hs based on the information provided by the General Bathymetric Chart of the Oceans.

The Young model (1988) is the worst predictor of wave activity, as it overestimates the value of Hs in many cases and underestimates it in others without registering any well-defined trend or behaviour. This may be due to the fact that this model has been constructed specifically for application at deep water, whereas the focus of interest in this study is the evaluation of how hurricane-related wave parameters behave at shallow and intermediate depths, rather than only at undetermined ones.

The Bretschneider wave model (1990) performs well in terms of the buoys located in deeper waters, but it tends to yield increasingly erroneous underestimates for wave values occurring after a hurricane has passed for shallower waters (the position of each NOAA buoy) and fails to provide a suitable simulation of the peak period for wave activity.

FIGURE 1.228
COMPARISON OF HOURLY SERIES FOR HS AND PP FOR THE BRETSCHNEIDER (1990) (BLUE DOTS), YOUNG (1988) (GREEN DOTS), AND MODIFIED SPM (RED DOTS) MODELS, BUOY DATA (BLACK DOTS) AND GOW DATABASE (BLACK TRIANGLES) FOR HURRICANE KATRINA (2005)

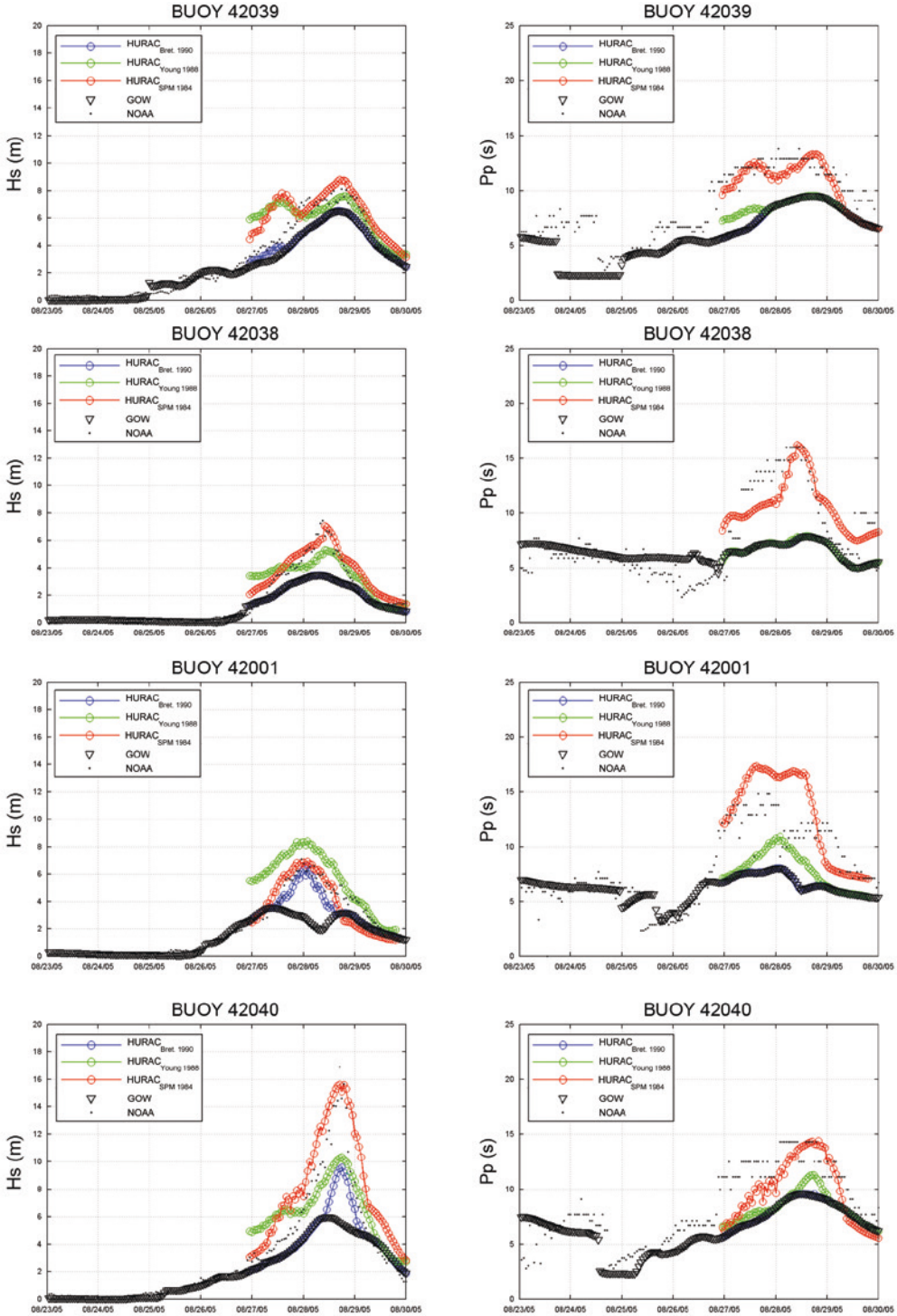

Source: Prepared by the authors.

FIGURE 1.229
COMPARISON OF HOURLY SERIES FOR HS AND PP FOR THE BRETSCHNEIDER (1990) (BLUE DOTS), YOUNG (1988) (GREEN DOTS), AND MODIFIED SPM (RED DOTS) MODELS, BUOY DATA (BLACK DOTS) AND GOW DATABASE (BLACK TRIANGLES) FOR HURRICANE GILBERT (1988)

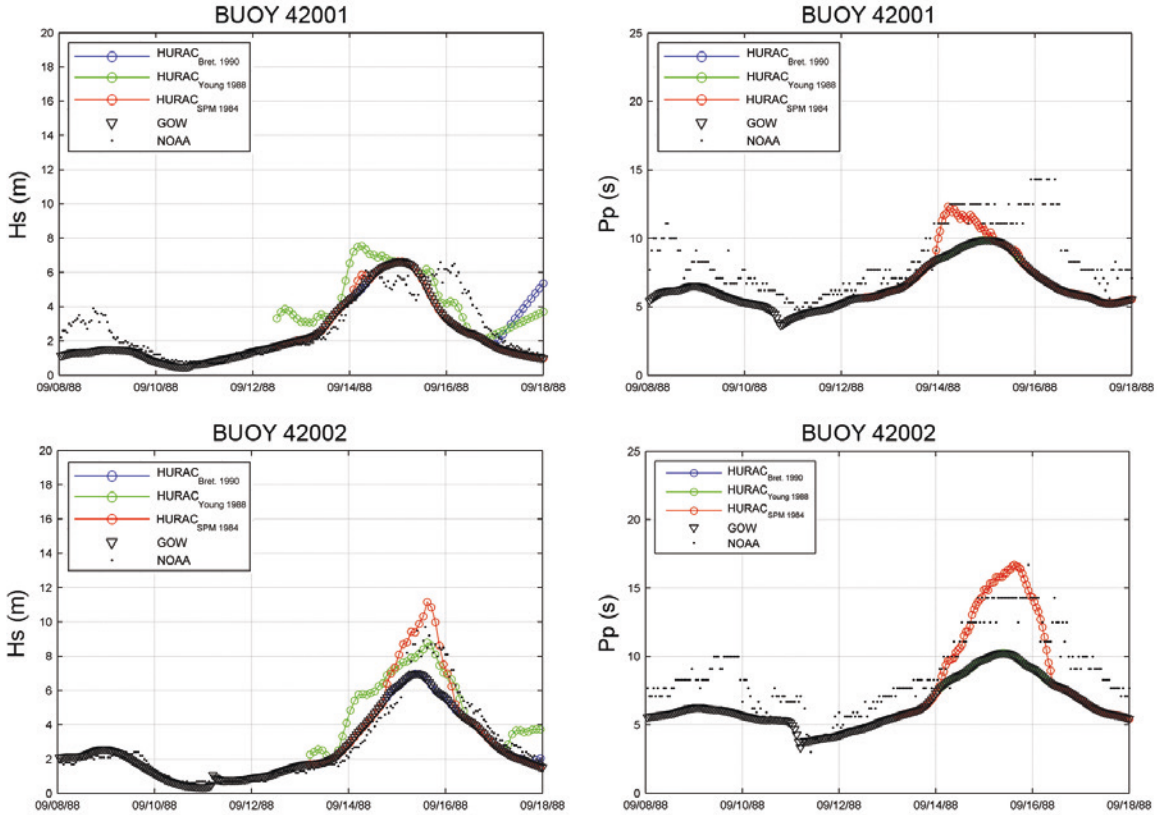

Source: Prepared by the authors.

FIGURE 1.230
COMPARISON OF HOURLY SERIES FOR HS AND PP FOR THE BRETSCHNEIDER (1990) (BLUE DOTS), YOUNG (1988) (GREEN DOTS), AND MODIFIED SPM (RED DOTS) MODELS, BUOY DATA (BLACK DOTS) AND GOW DATABASE (BLACK TRIANGLES) FOR HURRICANE CHARLEY (2004)

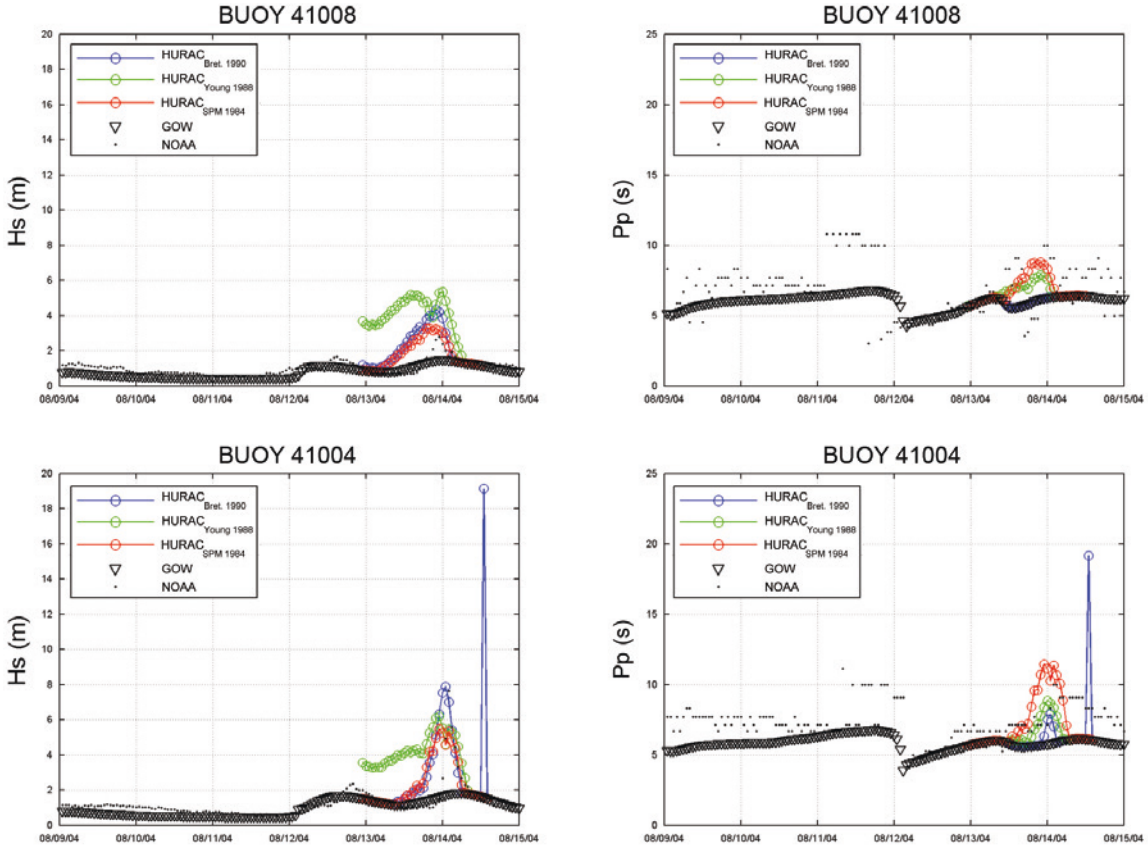

Source: Prepared by the authors.

FIGURE 1.231
COMPARISON OF HOURLY SERIES FOR HS AND PP FOR THE BRETSCHNEIDER (1990) (BLUE DOTS), YOUNG (1988) (GREEN DOTS), AND MODIFIED SPM (RED DOTS) MODELS, BUOY DATA (BLACK DOTS) AND GOW DATABASE (BLACK TRIANGLES) FOR HURRICANE WILMA (2005)

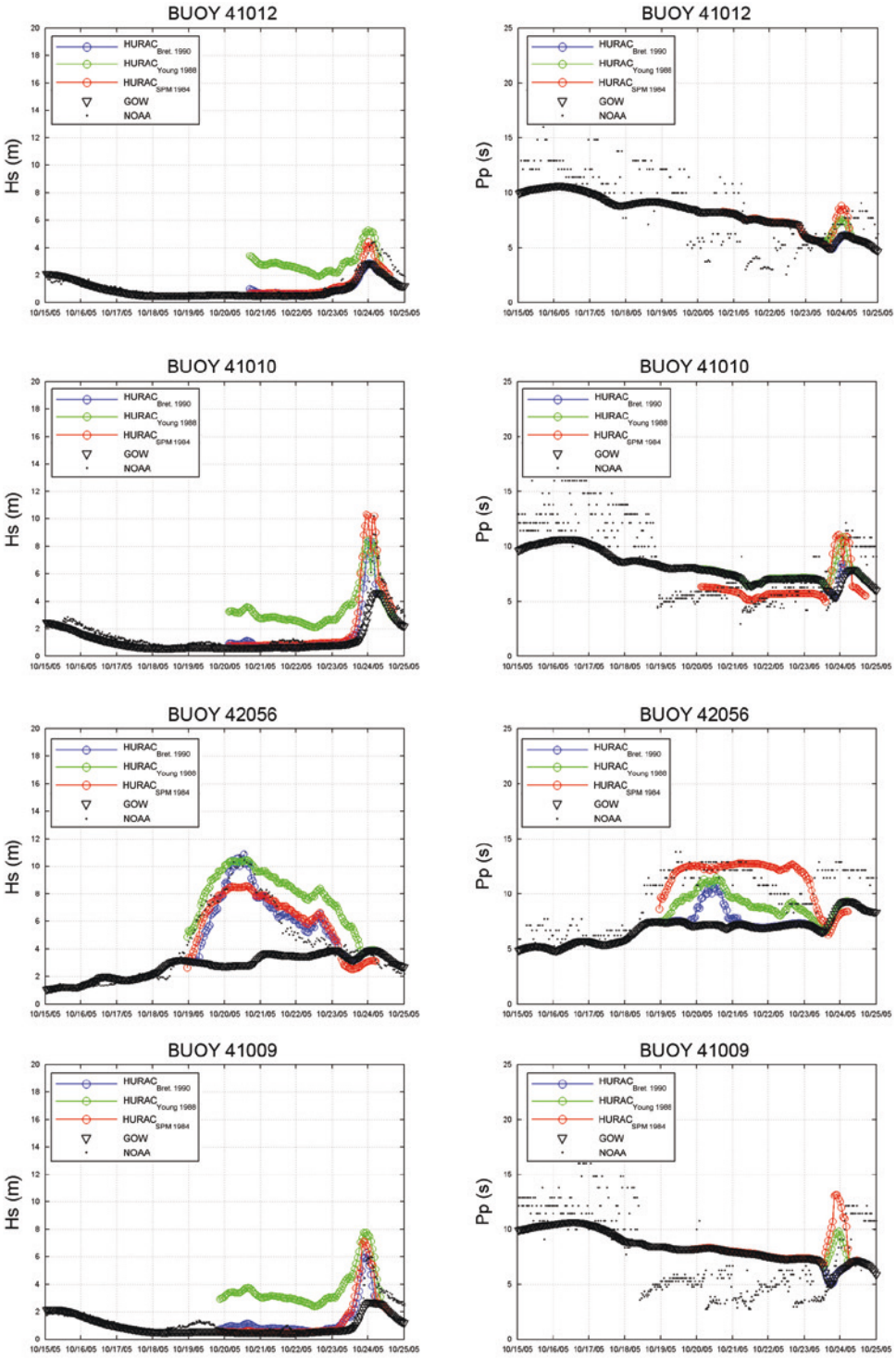

Source: Prepared by the authors.

FIGURE 1.232
COMPARISON OF HOURLY SERIES FOR HS AND PP FOR THE BRETSCHNEIDER (1990) (BLUE DOTS), YOUNG (1988) (GREEN DOTS), AND MODIFIED SPM (RED DOTS) MODELS, BUOY DATA (BLACK DOTS) AND GOW DATABASE (BLACK TRIANGLES) FOR HURRICANE IKE (2008)

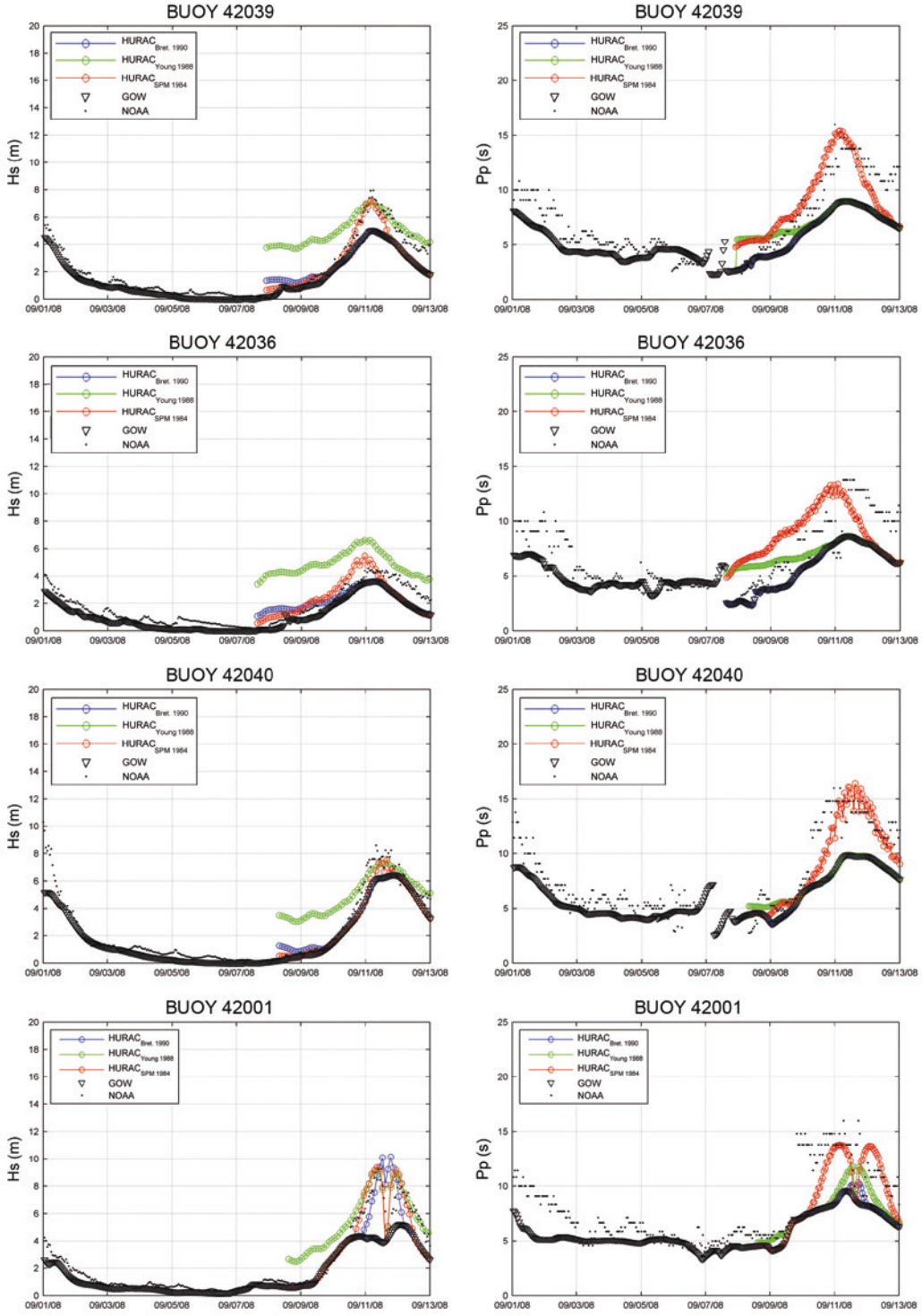

Source: Prepared by the authors.

None of the three wave models covers the wave transformation and dissipation associated with such phenomena as refraction, diffraction, reflection, breaking and shoaling in cases where the combined effects of diffraction and refraction in areas sheltered by given land formations interfere with the possibility of obtaining accurate results (the modified SPM model is the only one that is designed to correct wave parameters for shoaling).

It seems reasonable to conclude that the wave model's goodness of fit depends in large part on the possibility of taking physical and bathymetric contours into consideration. The decision was therefore made to use the modified SPM model (1984) for the reanalysis of the 54 years of hurricane data that are available, since the study's control points are located at intermediate and shallow depths along the coast.

A2.6. Evaluation and validation of storm surge maps

The storm surges generated by hurricanes or tropical cyclones are one of the most destructive and deadly natural phenomena on Earth. In 1900, the population of Galveston, Texas, was hit by a storm surge that killed 6,000 people and levelled the city.

Hurricane-generated storm surges pose a serious threat to ships on the high seas and in harbours, as well as to marine platforms and port and coastal structures.

Marine structures suffer damage due to the constant battering of the waves and the flooding of the lower sections of these facilities. Damage takes the form of the erosion of building foundations, damage to retaining walls, the erosion of beaches and coastlines, the sinking or damage of ships and boats, the destruction of port facilities and the destruction of beach facilities.

FIGURE 1.233
AN AUTOMOBILE CARRIED AWAY BY A STORM SURGE DURING HURRICANE GUSTAV IN THE UNITED STATES IN 2008

Source: www.elespectador.com/imagen-gustav-sigue-causando-daños.

Storms surges associated with hurricanes are usually analysed on the basis of two main forcings: (a) sea level variation generated by wind action (far from the hurricane itself), and (b) sea level variations that occur locally owing to the drop in atmospheric pressure (close to the hurricane).

Sophisticated numerical models are available that can be used to evaluate hurricane-related storm surges. These models are derived from pressure and wind fields and provide realistic depictions of spatial and temporal variations in sea levels that take into account the bathymetric depth, long-wave propagation, wave friction with the sea floor, etc. (e.g., ROMS model, H2D (shallow water equations) model, the NOAA SLOSH model: http://www.nhc.noaa.gov/HAW2/english/surge/slosh.shtml), etc.).

FIGURE 1.234
EXAMPLE OF A TWO-DIMENSIONAL HURRICANE-RELATED BEACH EVENT AND THE ASSOCIATED EFFECT OF STORM SURGES AND WAVES

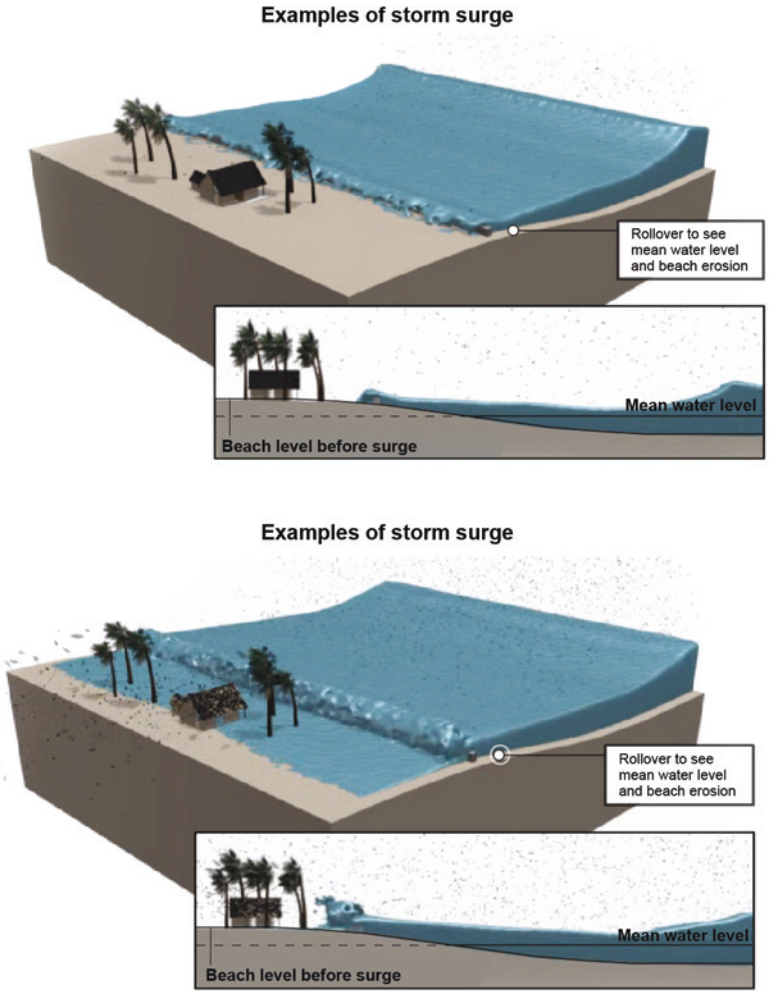

Source: NOAA.

As noted earlier in relation to the numerical models for wave generation and propagation in connection with hurricane events, the use of this type of model and the efficiency of its use in terms of the time required for its application can be problematical in a study such as this, where the objective is to conduct a reanalysis of the GOS database and to supplement those data.

Accordingly, in this study a straightforward approach is used to analyse storm surge data based on the information provided by pressure and wind fields and a number of simplifying hypotheses, as detailed below:

For wind-driven storm surges:

• A transect drawn from the centre of the hurricane to the point of analysis on the coast (see figure 1.235);

• The bathymetric measurements along the entire transect are taken into consideration;

• A stationary maximum constant wind speed for the transect is used for each hourly hurricane event;

• The relative angle between the direction of the maximum wind speed and the geographic orientation of the transect is factored in;

• Friction along the sea floor is not taken into account;

• The two-dimensional effects (the transect is 2DV) of the spatial/temporal propagation of the long-period waves associated with the storm surge are not taken into account;

• Topographic and bathymetric terrain is not factored into the two-dimensional scheme (2DH).

FIGURE 1.235
BATHYMETRIC AND STORM SURGE CROSS-SECTION ALONG THE TRANSECT

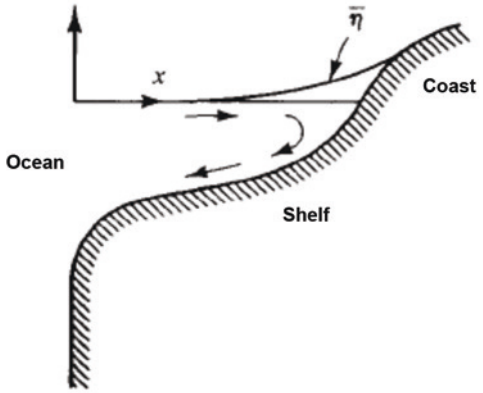

Source: Dean and Dalrymple (1984).

The one-dimensional model proposed by Dean and Darlymple (1984) has therefore been used to evaluate the long-wave equations for bodies of water having variable sea floor depths that are forced by a constant wind factor.

Since the main forcing of the system is the tangential tension acting on the surface as a function of the prevailing winds, such that:

$$\tau_W = \rho \cdot k \cdot U_{\max} |U_{\max}| \qquad \text{(A2.9)}$$

Where,

ρ is the density of the water in kg/m³;

U_{max} is the hurricane's maximum wind speed at 10 m above sea level as measured along the entire transect at m/s;

k is a factor for friction on the order of 106 as proposed and analysed by Van Dorn (1953);

$$k = 1.2x10^{-6} \qquad \text{for } |U_{max}| \leq 5.6$$

$$k = 1.2x10^{-6} + 2.25x10^{-6}\left(1 - \frac{5.6}{|U_{max}|}\right) \qquad \text{for } |U_{max}| > 5.6$$

In order to incorporate the relative angle between the wind direction and the geographic direction of the transept θ, the shear value has to be corrected as follows:

$$\tau_{wx} = |\tau_w| cos\theta$$

Using the above parameters and the parameter n (between 1.15 and 1.30, SPM, (1977)), the following differential equation can be used to resolve the wind-driven storm surge generated by wind η_w, as a function of the shearing associated with factor n and the depth along the entire transect h:

$$\frac{\partial \eta_w}{\partial x} = \frac{n \cdot \tau_{zx}(\eta_w)}{\rho \cdot g\,(h + \eta_w)}$$

Figure 1.236 and figure 1.237 provide examples of the results obtained for the two forced transects for wind fields obtained for Hurricane Katrina for 28 August 2005 at 17:00 hours.

In the analysis of storm surges associated with changes in atmospheric pressure:

a) It is assumed that spatial variations are stationary and symmetrical and are determined solely by pressure gradients.

b) Surge levels generated by atmospheric pressures are added as a linear term in the spatial dimension (along the entire transect) to the effect generated by the wind for each hourly point in time.

The model used to evaluate the variation in sea levels generated by oscillations in atmospheric pressure during hurricanes uses the follow equation, which has been derived from the work of Dean and Dalrymple (1984).

$$\eta_{vp} = \frac{(p_n - p_o)}{\rho g}\left(1 - e^{-\frac{(R-r)}{r}}\right) \qquad \text{(A2.10)}$$

Where:

η_{vp} is the variation in the mean level measured in metres;

P_n is the pressure at the periphery of the low-pressure system in mbar;

P_0 is the pressure at the centre of the low-pressure area in mbar;

P is the water density (1025 kg/m³);

R is the cyclostrophic radius of the hurricane in km;

r is the radial distance from the reference point at the centre of the low-pressure area in km.

Figure 1.238 maps the storm surge associated with Hurricane Katrina on 27 August 2005 at 22:00 hours.

FIGURE 1.236

WIND FIELD FOR HURRICANE KATRINA ON 28 AUGUST 2005 AT 17:00 HOURS AND BATHYMETRIC, WIND AND WIND-DRIVEN STORM SURGE DATA FOR THE ENTIRE TRANSECT (RED LINE) STARTING FROM THE CONTROL POINT (WHITE POINT)

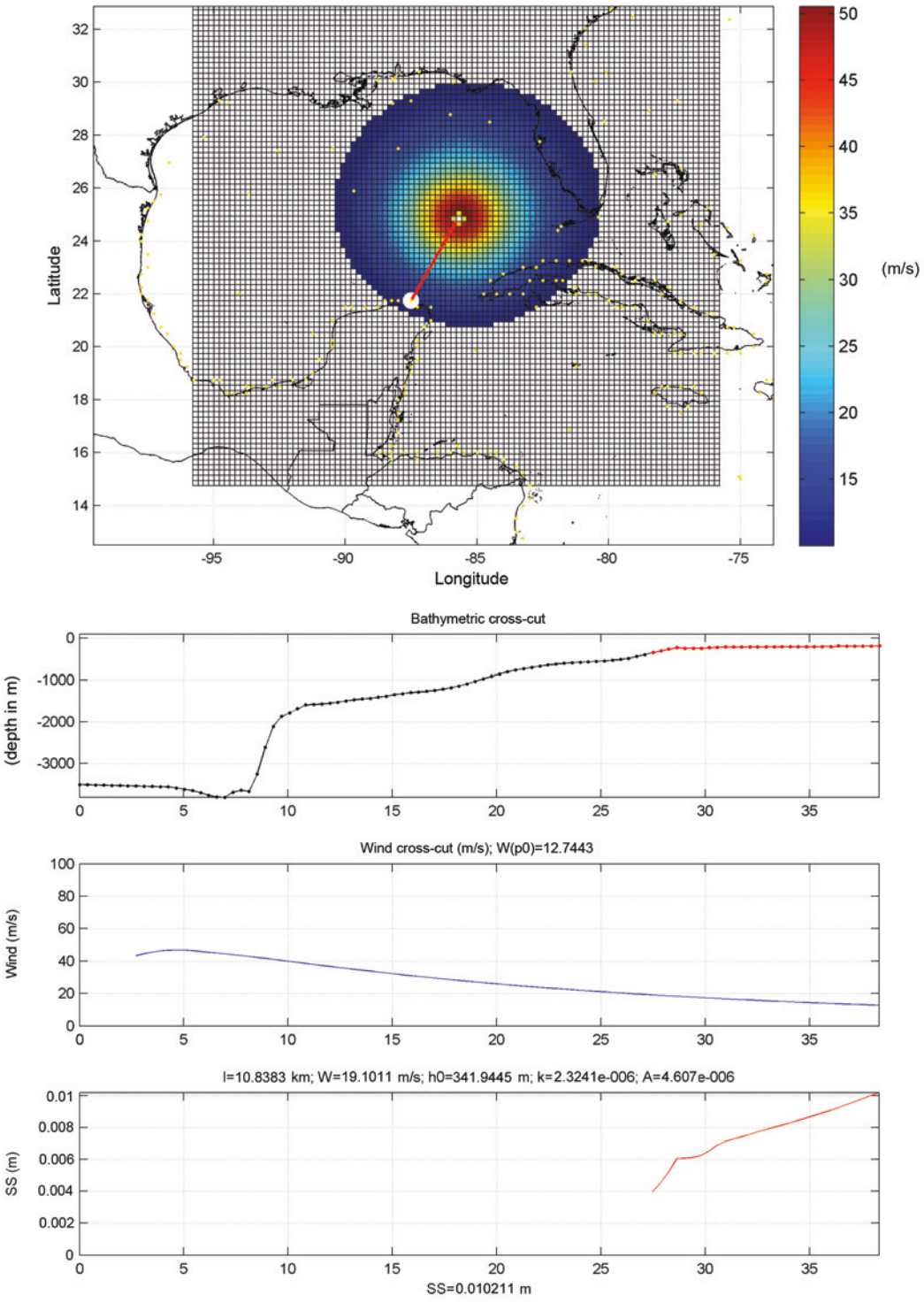

Source: Prepared by the authors.

FIGURE 1.237

WIND FIELD FOR HURRICANE KATRINA ON 28 AUGUST 2005 AT 17:00 HOURS AND BATHYMETRIC, WIND AND WIND-DRIVEN STORM SURGE DATA FOR THE ENTIRE TRANSECT (RED LINE) STARTING FROM THE CONTROL POINT (WHITE POINT)

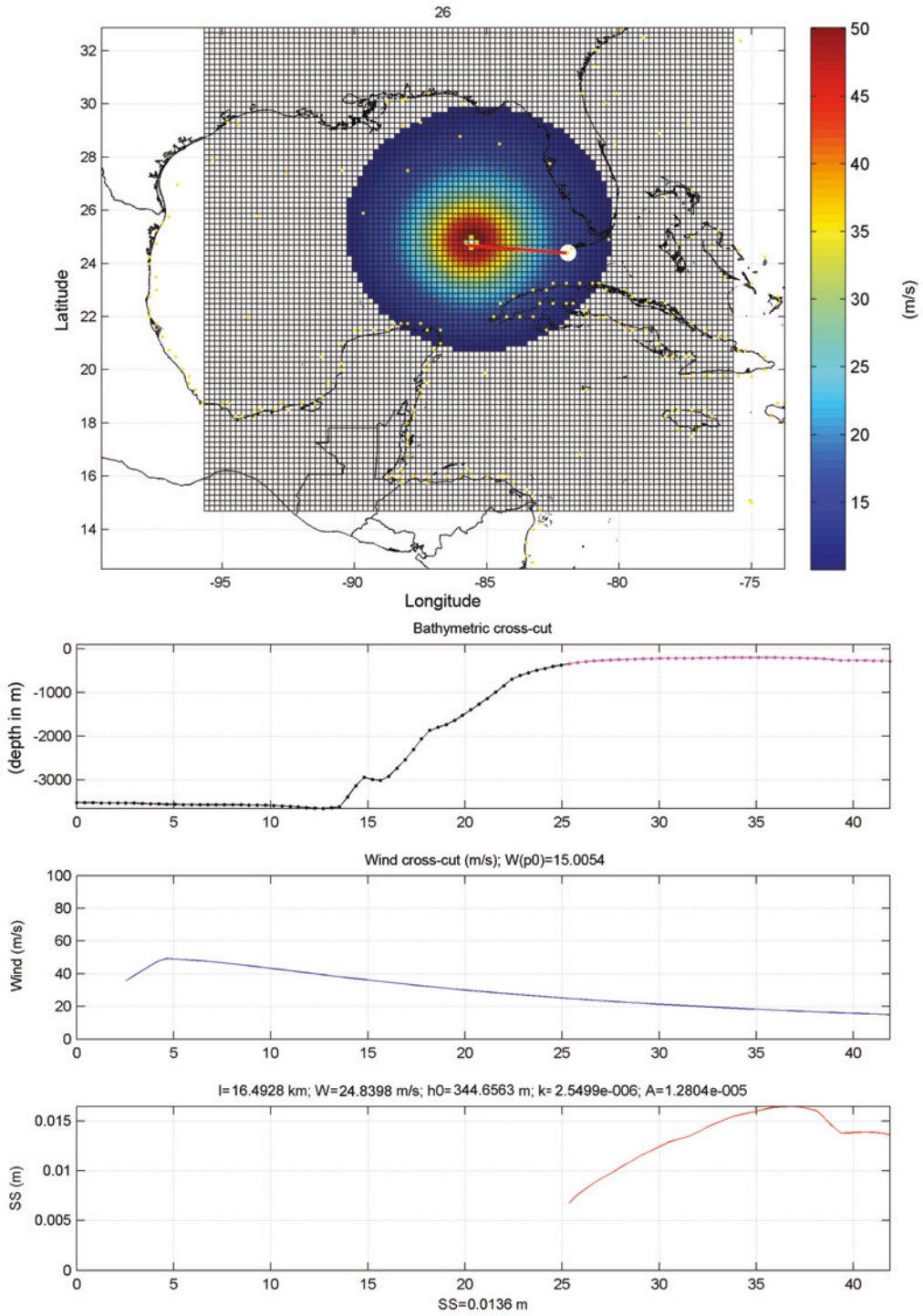

Source: Prepared by the authors.

FIGURE 1.238
STORM SURGE FIELD GENERATED BY CHANGES IN ATMOSPHERIC PRESSURE ASSOCIATED WITH HURRICANE KATRINA ON 27 AUGUST 2005 AT 22:00 HOURS
(Metres)

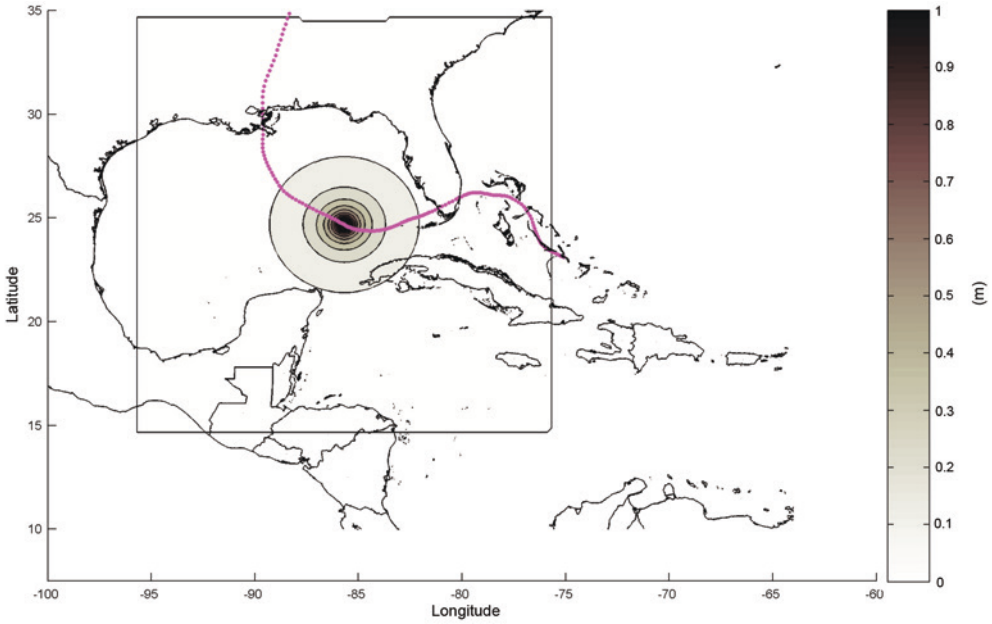

Source: Prepared by the authors.

The validation of the storm surge models covered in this section has been conducted using instrumental data from the Global Extreme Sea Level Analysis (GESLA), which have been compiled from the measurements taken by sea-level gauges.

The validation of the wind- and pressure-driven storm surge for this study yielded suitable results, as shown in figures 1.239, 1.240 and 1.241.

FIGURE 1.239
COMPARATIVE SERIES ON STORM SURGES OBTAINED USING THE ANALYTICAL MODEL AND GESLA NO. 242 GAUGE DATA FOR HURRICANE KATRINA (2005)

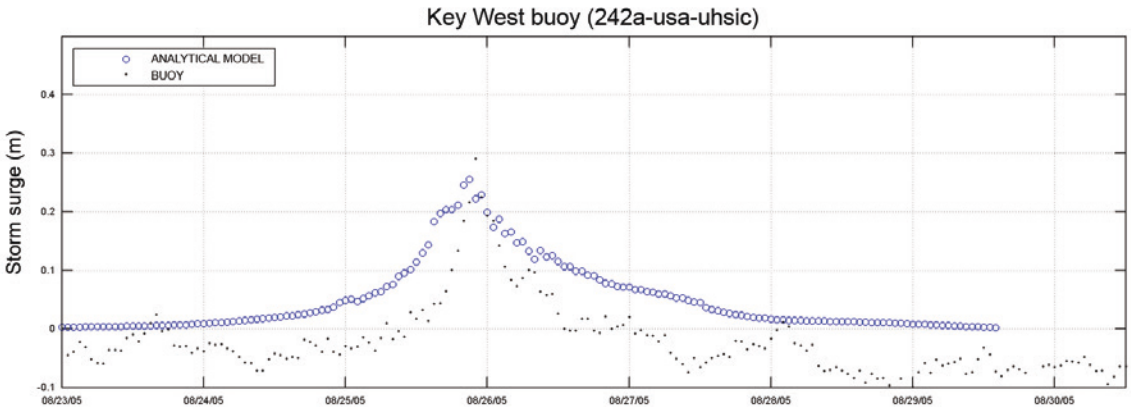

Source: Prepared by the authors.

FIGURE 1.240
COMPARATIVE SERIES ON STORM SURGES OBTAINED USING THE ANALYTICAL MODEL AND GESLA NO. 752 AND 242 GAUGE DATA FOR HURRICANE CHARLEY (2004)

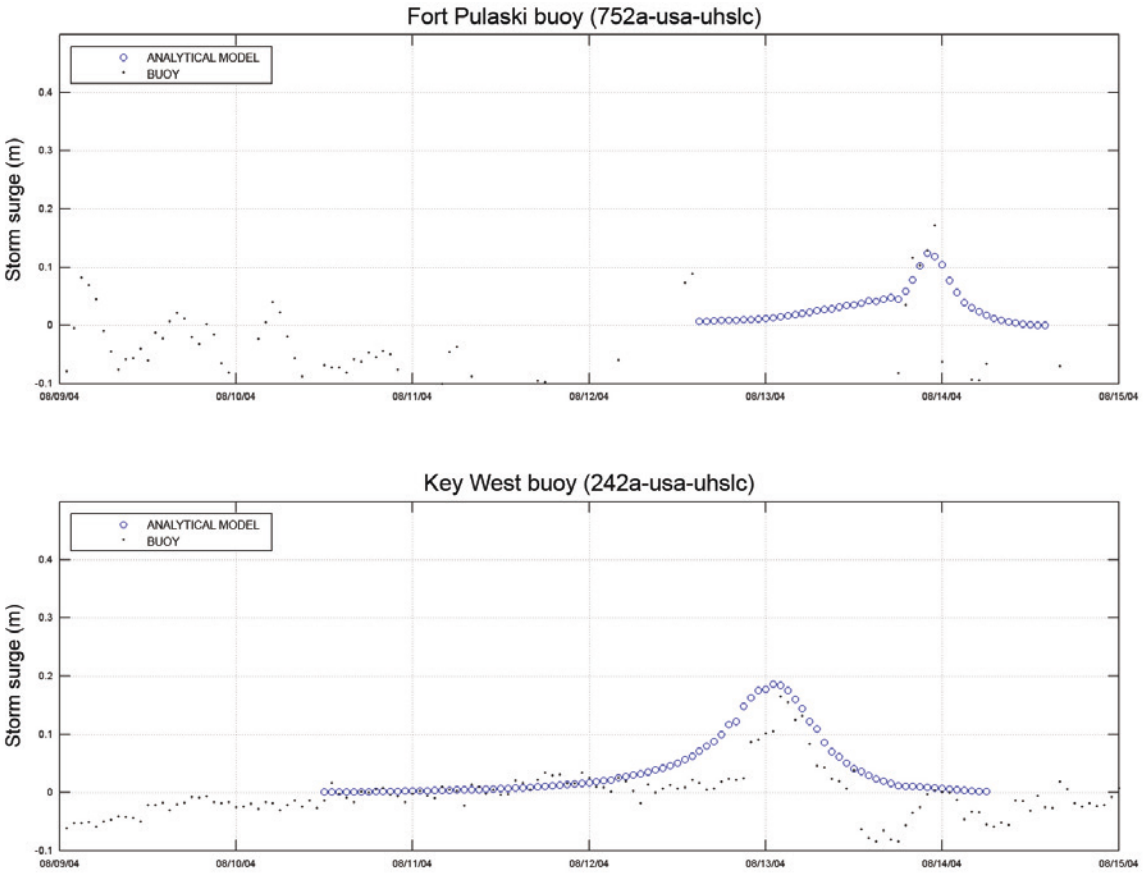

Source: Prepared by the authors.

FIGURE 1.241
COMPARATIVE SERIES ON STORM SURGES OBTAINED USING THE ANALYTICAL MODEL AND GESLA NO. 242 AND 246 GAUGE DATA FOR HURRICANE FRANCES (2003)

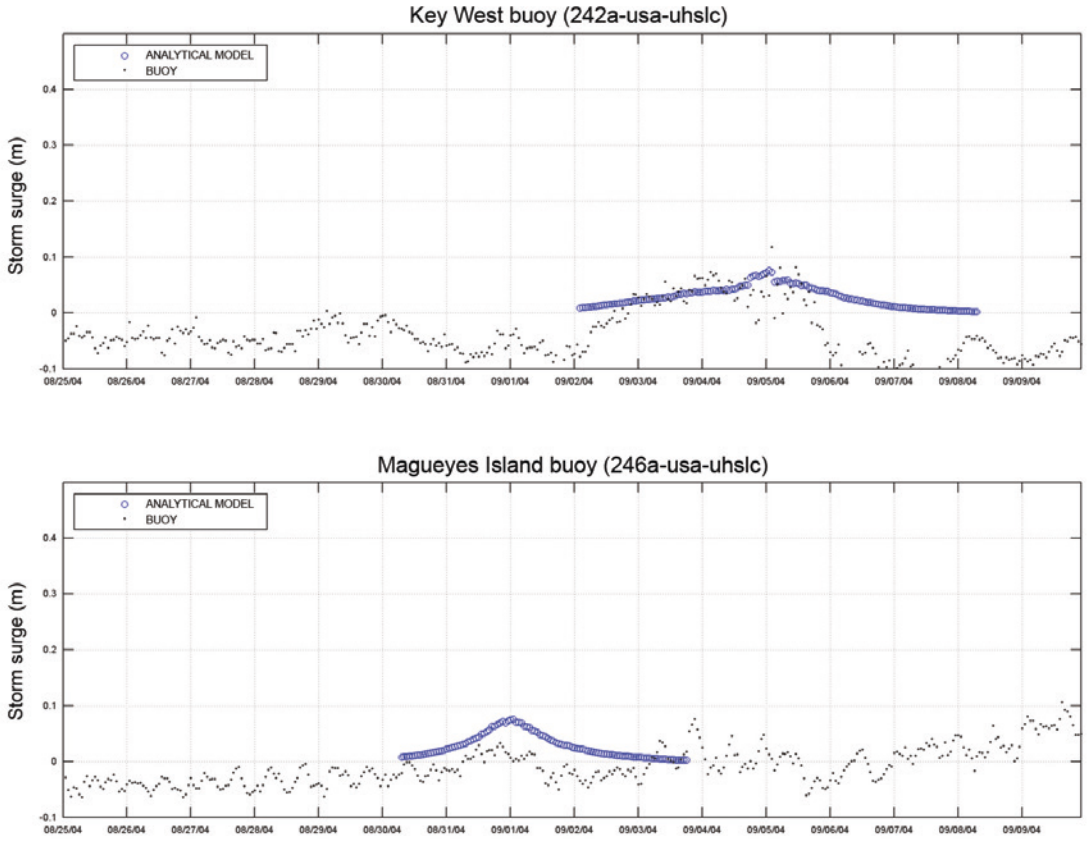

Source: Prepared by the authors.

A2.7. Statistical analysis of parameters for hurricane events

Once the various air pressure, wind, wave and storm surge models for the different hurricane events have been run, analysed and validated, and once it has been determined that they yield reliable results, the hourly figures generated by these models for the 54-year period for which hurricane data are available can be presented.

The purpose of this analysis is to define and supplement the statistical storm surge and wave maps generated by the GOS and GOW models for the 60-year reanalysis for the Atlantic and Pacific coasts with the use of maps that depict the potential maximum wave heights and storm surges during hurricanes for the same locations.

This information is of crucial importance for two reasons: first, it provide an idea of the order of magnitude of the maximum wave heights and storm surges occurring during high-energy events such as hurricanes, which can then be used to gauge the behaviour and limitations of the GOW and GOS databases; and, second, it makes it possible to draw up historical maps of potential maximums that can be used to provide inputs for the engineering designs of coastal and port buffers and other structures along the Pacific and Atlantic coasts of North America (Mexico), Central America and South America.

In all, 369 control points along the Atlantic coast and 257 control points along the Pacific coast have been used to generate these data (see figure 1.242).

FIGURE 1.242
CONTROL POINTS (RED DOTS) ANALYSED FOR THIS STUDY AND WIND AND WAVE FIELDS FOR HURRICANES KENNA (2001) AND KATRINA (2005)

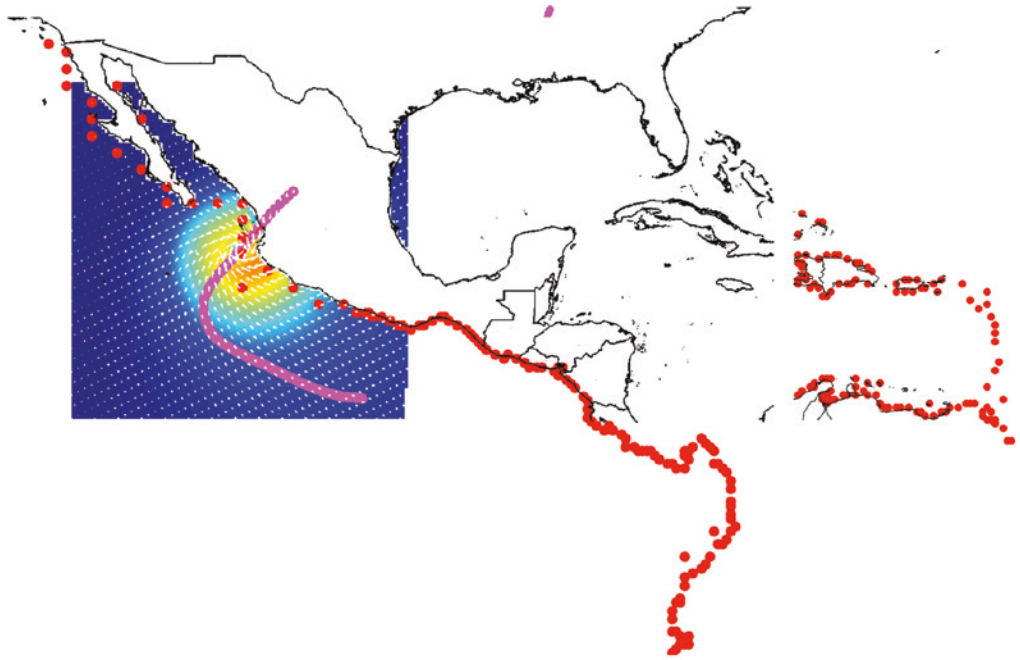

Source: Prepared by the authors.

The models have been run for each of the control points, and the annual maximums (for the 54-year period) have been obtained for pressure, wind speed, significant wave height, peak period, wind-driven storm surge, pressure-driven storm surge and dual-factor storm surge. The results are shown in the following figures.

FIGURE 1.243
MAP OF MINIMUM ATMOSPHERIC PRESSURE LEVELS (54 YEARS OF HURRICANE DATA) FOR THE CONTROL POINTS USED IN THIS STUDY
(Mbar)

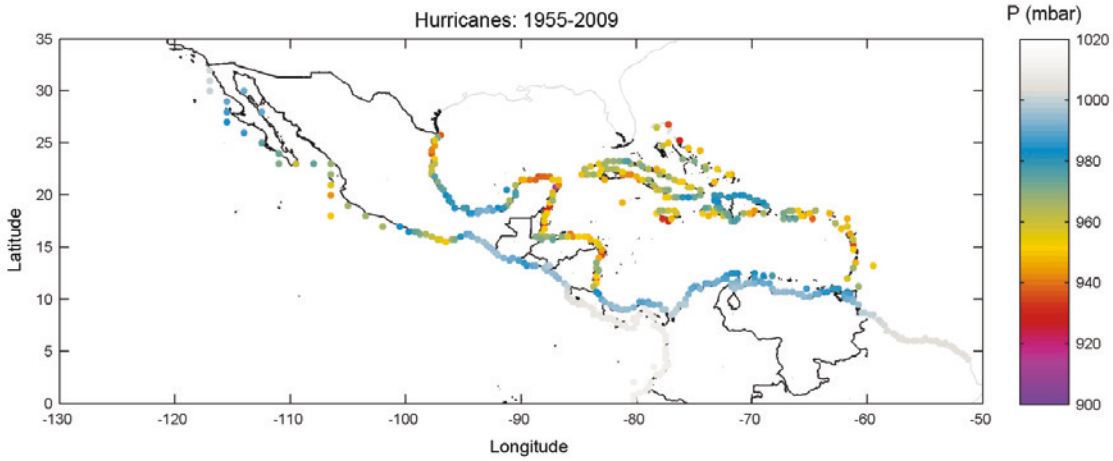

Source: Prepared by the authors.

FIGURE 1.244
MAP OF MAXIMUM WIND SPEEDS (54 YEARS OF HURRICANE DATA) AT THE CONTROL POINTS USED IN THIS STUDY
(Kilometres/hour)

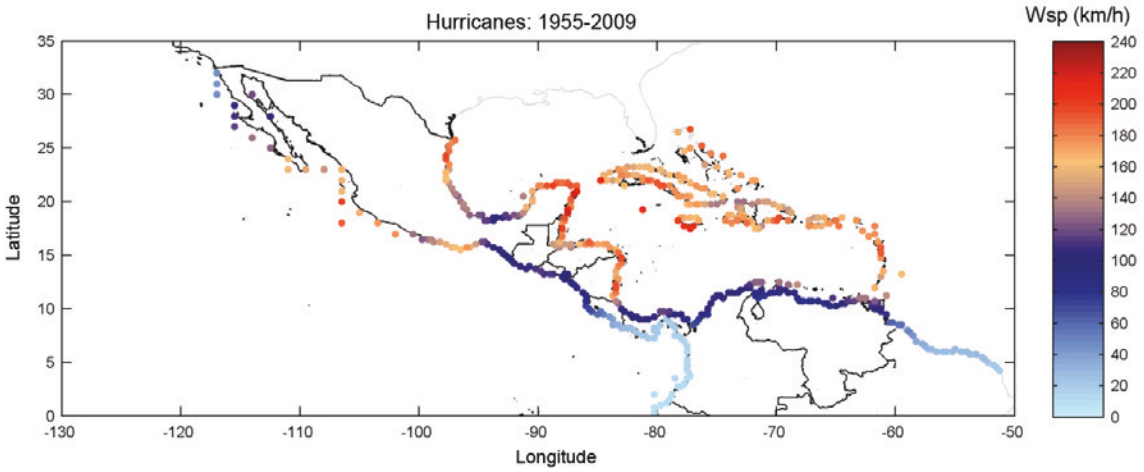

Source: Prepared by the authors.

FIGURE 1.245
MAP OF MAXIMUM SIGNIFICANT WAVE HEIGHTS (54 YEARS OF HURRICANE DATA) AT THE CONTROL POINTS USED IN THIS STUDY
(Metres)

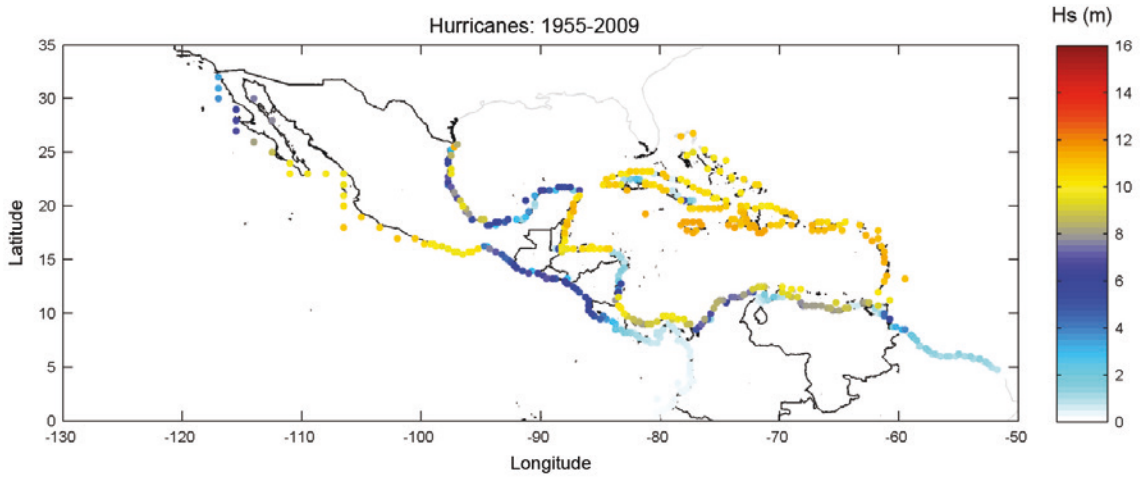

Source: Prepared by the authors.

FIGURE 1.246
MAP OF MAXIMUM SWELLS (54 YEARS OF HURRICANE DATA) AT THE CONTROL POINTS USED IN THIS STUDY
(Seconds)

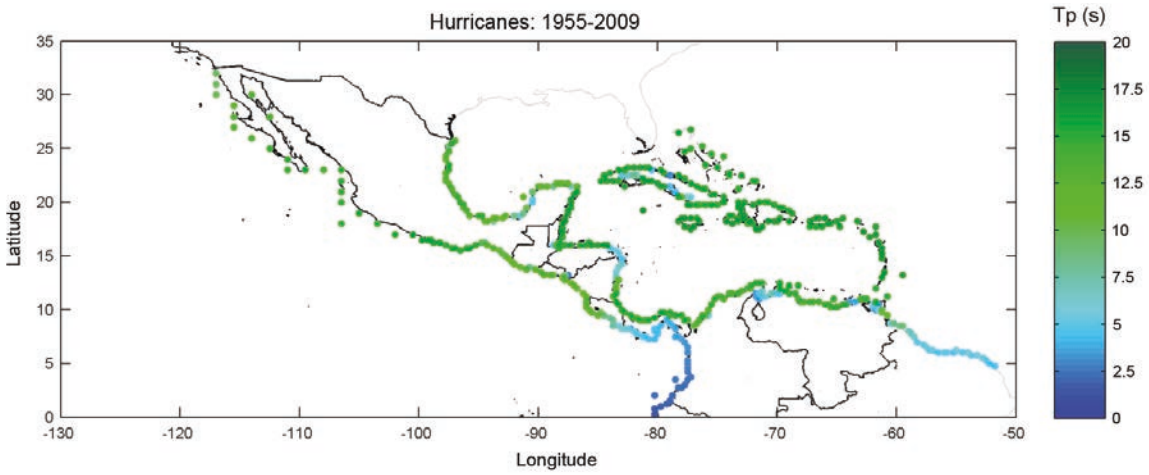

Source: Prepared by the authors.

FIGURE 1.247
MAP OF MAXIMUM PRESSURE-DRIVEN STORM SURGES (54 YEARS OF HURRICANE DATA) AT THE CONTROL POINTS USED IN THIS STUDY
(Metres)

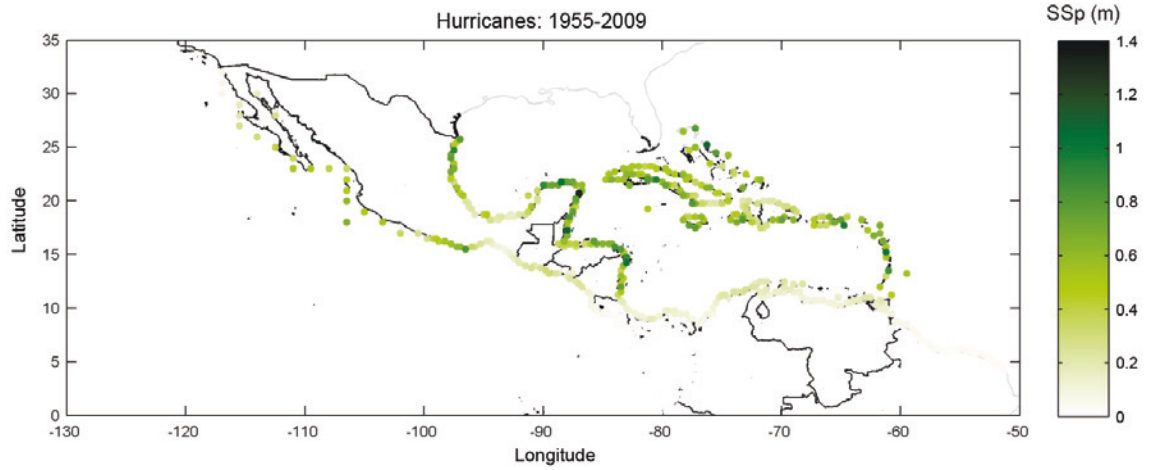

Source: Prepared by the authors.

FIGURE 1.248
MAP OF MAXIMUM WIND-DRIVEN STORM SURGES (54 YEARS OF HURRICANE DATA) AT THE CONTROL POINTS USED IN THIS STUDY
(Metres)

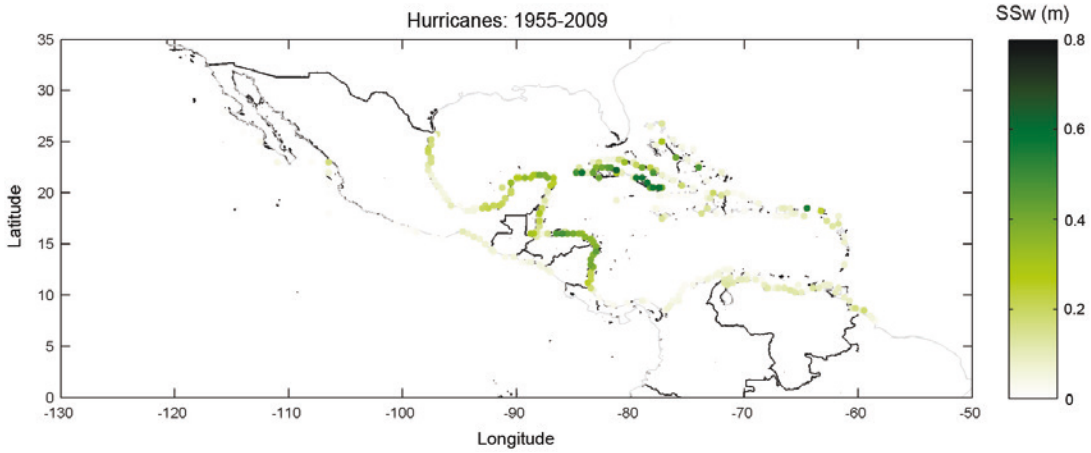

Source: Prepared by the authors.

FIGURE 1.249
MAP OF MAXIMUM DUAL-CAUSE (LINEAR SUM: $SS_{PRESSURE}$+SS_{WIND}) STORM SURGES (54 YEARS OF HURRICANE DATA) AT THE CONTROL POINTS USED IN THIS STUDY
(Metres)

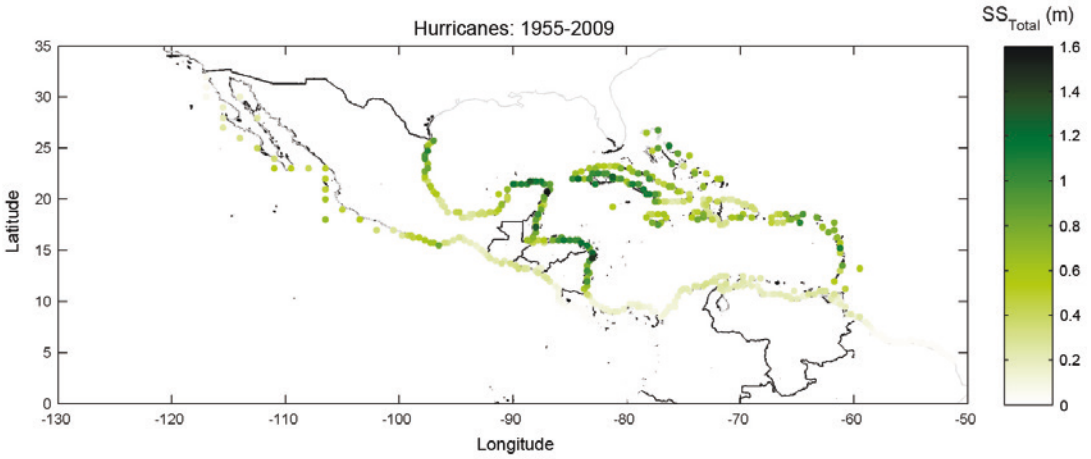

Source: Prepared by the authors.

A2.8. Conclusions

The analysis of hurricanes conducted in this study is descriptive of the situation as it stands today. A deeper analysis of the historical wave and sea level events and the changes occurring in those phenomena, together with their implications for coastal areas, can only be addressed by means of a more targeted study. The factors involved in these shifts are far too complex to be covered in detail at this stage. Nonetheless, the information provided by simplified models, so long as they are validated by the measurements taken at weather buoys, is extremely useful, especially in the absence of in-depth studies on these topics. The maps provided for this purpose cover pressure, wind, wave and storm surge data.

Annex 2 bibliography

Bretschneider, C.L.(1990), Tropical cyclones. *Handbook of Coastal and Ocean Engineering.* vol. 1. Houston, Gulf Publishing Co., pp. 249-370.

Dean, R., Dalrymple, R. (1984), *Water Wave Mechanics for Engineers and Scientists,* Prentice-Hall Inc., Englewood Cliffs, New Jersey.

Harper, B.A. Holland G.J., (1999), An updated parametric model of the tropical cyclone. Proceedings of the 23rd Conference Hurricanes and Tropical Meteorology, American Meteorological Society, Dallas, 10-15 January.

Holland, G.J., (2002), "Tropical cyclone reconnaissance using the Aerosonde UAV", *Bulletin of the World Meteorological Organization,* 51 (3).

Holland, G.J., (1984), "On the climatology and structure of tropical cyclones in the Australian/southwest Pacific region: I. Data and tropical storms", *Australian Meteorological Magazine,* 32.

Holland, G.J., (1981), "On the quality of the Australian tropical cyclone data base", *Australian Meteorological Magazine,* 29.

Holland, G.J., (1980), "An analytical model of the wind and pressure profiles in hurricanes", *Monthly Weather Review,* 108, 1212–1218.

Janssen, P.A.E.M., (1989), "Wave-induced stress and the drag of air flow over sea waves", *Journal of Physical Oceanography,* 19, pp. 745-754.

Pérez, D.M. (2005), Verificación de un modelo de tercera generación para estimar oleaje en la vertiente atlántica mexicana, Tesis de maestría en Ingeniería, México, D.F., UNAM, 79 pp.

Pérez, D.M., Bolaños, R. and Silva, R. (2005), "Predicción del oleaje generado por dos hurricanes en las costas mexicanas del Golfo de México", *Ingeniería hidráulica en México,* 23 (2). 5-20.

Sánchez, C., Silva, R., Govaere, G., and Contreras, A (1998), *Comparison of 4 wave prediction models,* 5th International Workshop on Wave Hindcasting and Forecasting, Melbourne, 134-145.

Silva, R., Díaz, G., Contreras, A., Bautista, G. and Sánchez, C., (2000), "Determination of oceanographic risk for hurricanes on the Mexican coast", *6th International Workshop on Wave Hindcasting and Forecasting,* Melbourne, 137-151.

Silva, R., Govaere, G., Salles, P., Bautista, G. and Díaz, G. (2002), Oceanographic vulnerability to hurricanes on the Mexican coast. Proc. *28th International Conference on Coastal Engineering.* World Scientific. Singapur.

Silva R., Ruiz G., Perez D., Posada G. Bautista E., (2009), "Modelo híbrido para la caracterización del oleaje", *Ingeniería Hidráulica en México,* 24,(3),5-22.

Young, I.R., (1988), "Parametric hurricane wave prediction model". J. *Waterway, Port, Coastal, Ocean Engeneering,* 114 (5), 639–652.

Van Dorn, W.C. (1953), "Wind Stress on an Artificial Pond," *Journal of Marine Research,* Volume 12.

This document is the first in a series prepared in the framework of the Regional Study on the Economics of Climate Change in Latin America and the Caribbean (ERECC) initiative. The study area has a total longitude of approximately 72,182 km distributed in four geographical areas: North America, Central America, South America and the Caribbean islands. The study analysed the changes detected in coastal dynamics and climate variability and a range of information on the vulnerability of coastal areas, encompassing the physical and socioeconomic environment, the physical configuration of coasts and the foreseeable impacts and risks.

This volume provides an atlas of current physical conditions and the changes detected in coastal variables such as average sea level, surface temperature, salinity, swell, tides, air temperature anomalies, wind and hurricanes. This description, which is based on the information available for the region, is the first step towards a study of how the different variables have changed and what effects may be expected on coasts in the future. This is vital knowledge for coastal and port engineering, for analysis of the vulnerability of human settlements in coastal areas, and for the integrated environmental management of coastal areas, among other factors. The document also analyses possible trend changes in the different variables in the future, taking as cut-off years 2040, 2050 and 2070 and establishing mean values and the degree of uncertainty or variability to be expected, including an analysis of extreme events associated with some variables. Patterns of inter-annual climate variability, such as the El Niño Southern Oscillation (ENSO) phenomenon, are also examined. This study thus represents the first analysis in the region for a broad range of climate dynamics and patterns.

The information provided in this volume provides the starting point for analysis of the vulnerability and exposure of Latin American and Caribbean coastal areas to the effects of climate change and the impacts that may be expected, which will be reported in detail in the following documents.

ECLAC

Economic Commission for Latin America and the Caribbean (ECLAC)
Comisión Económica para América Latina y el Caribe (CEPAL)
www.eclac.org